



The University of
Nottingham

Department of Mechanical, Materials and Manufacturing Engineering

Investigations into fibre laser cutting

By:

Majid Hashemzadeh, M.Sc.

Thesis submission for degree of Doctor of Philosophy

Supervisors:

Dr Katy Voisey

Prof John Powell

February 2014

Preface

This thesis is submitted to fulfil the requirement for degree of doctorate of philosophy at the University of Nottingham. The research work was carried out under the supervision of Dr Katy Voisey and Prof John Powell. It is certified that the work presented in this research is original and references are made from any work discussed in the literature and result discussion.

The following publication has been produced from the content of this thesis:

- M. Hashemzadeh, J. Powell, K.T. Voisey. Piercing in fibre laser cutting. Proceedings of the 3rd UK industrial laser applications symposium (ILAS), Nottingham, 2013.
- M. Hashemzadeh, J. Powell, K.T. Voisey. Fibre laser piercing of mild steel - The effects of power intensity, gas type and pressure. Journal of Optics and Lasers in Engineering. 2014, 55, 143-149.

Accepted paper to publish:

- M. Hashemzadeh, W.J. Suder, K.T. Voisey, J. Powell, S.W. Williams. Application of specific point energy analysis approach to fibre laser cutting, 8th International Conference On photonic Technologies (LANE 2014), Furth, Germany, September 8-11, 2014.

Acknowledgment

I would like to express my deep appreciation to my supervisors Dr Katy Voisey and Professor John Powell for their support and encouragement. Their experience and enthusiasm were the main motivation of this project. Their kindness, friendly atmosphere, constructive discussion and advice in our meetings caused me to move forward in my research. I have learned many things from them.

Sincere thanks to my examiners, Dr Adam Clare and Professor W. O'Neill, for their friendly and constructive questions during my viva.

I also appreciate Dr W. Suder and Professor S. Williams from Cranfield University for their valuable discussions and friendly cooperation in applying the novel method of the SPE in laser cutting.

I would also like to thank all of the technicians from the Wolfson Building, Manufacturing Engineering and the Laser labs, in particular Mr. Stuart Branston, Mr. Mark Daine, Mr. Graham Malkinson, Dr Nigel Neate, Martin Roa, Mrs. Julie Thompson, Mr. Keith Dinsdale, Mr. Thomas Buss for their patience, tolerance and willingness to solve various engineering issues, as well as for being good friends.

To all my friends from the University and Wolfson building, I thank them for their friendship and cheerful attitude, in particular Dr Andy Patman, Jaimie Daure, Matthew Moles and his wife Dr Xuanly, Hao Chen, Chunling Li, Dr Akbar Niaz, Dr Mariem Meggouh, Marwa Abbas and Dr Amir Pourabdelah.

Special thanks from the bottom of my heart to my wife (Parisa) and my honey daughter (Sormeh) for their tolerance and patience during hard times, when I was studying a PhD far from them. Also, thanks to my parent in law (Dr N. Hajian and Parvin) for taking care of my wife and my daughter.

At the end, I would like to express the greatest appreciation to my parents, who have supported me in all my life.

Abstract

Fibre laser cutting of mild steel using oxygen and nitrogen is widely used in industries throughout the world. An IPG YLR-2000 Ytterbium fibre machine with a maximum power of 2 kW and a wavelength of 1.06 μm is used throughout this research. The effects of oxygen and nitrogen as assist gases on the feature of laser cutting process are different in terms of kerf width, surface roughness, heat affected zone and striation pattern. The kerf width in oxygen laser cutting is wider than that for nitrogen. The striation pattern on oxygen cut edge is smoother than that for the nitrogen cut edge. When using oxygen, the cut edge is covered by a fragile oxide layer while this feature is not seen on the nitrogen cut edge. After laser cutting with oxygen, the cut edge is dross free whilst nitrogen cut edge is drossy.

Laser piercing is used to generate a starting point for laser cutting. The pierced hole is normally larger than the kerf width, which means that it cannot lie on the cutline. An experimental programme investigating the piercing process as a function of laser and assist gas parameters is presented. Oxygen and nitrogen were used as assist gases, with pressures ranging from 0.3 to 12 bar. The sizes, geometries and piercing time of the holes produced have been analysed. The pierced hole size decreases with increasing gas pressure and increasing laser power. Oxygen assist gas produced larger diameter holes than nitrogen. A new technique is presented which produces pierced holes no larger than the kerf width and would allow the pierced hole to lie on the cut line of the finished product – allowing better material usage. This uses an inclined jet of nitrogen when piercing prior to oxygen assisted cutting.

Specific point energy (SPE) is a concept that has been successfully used in laser welding where SPE and power density determine penetration depth. This analysis allows welding carried out by different laser systems to be directly compared. This work investigates if the SPE concept can be applied to laser cutting. Laser cutting of various thicknesses of mild steel, two different optical set ups and three different delivery fibres with a range of powers and translation speeds is done to gain results for numerous different parameter combinations. It is found that the SPE concept is applicable to laser cutting and the following effects noted: for given material thickness and any given value of SPE, cost is decreased by using a larger beam

diameter; for given cut sheet thickness, cutting efficiency increases with SPE; for given value of SPE, cutting efficiency increases as material thickness decreases.

Contents

Contents	V
List of figures	X
List of tables.....	XXVI
List of symbols.....	XXIX
Abbreviation.....	XXX
1 Introduction.....	1
1.1 General background	1
1.2 Aims and objectives	1
1.3 Overview	2
2 Literature review.....	4
2.1 Introduction to laser beam.....	4
2.2 Laser beam characteristics.....	5
2.2.1 Wavelength	6
2.2.2 Polarisation.....	7
2.2.3 Laser beam interaction	8
2.2.4 Pulsed and Continues Wave (CW) modes	11
2.2.5 Power	12
2.2.6 Power density	12
2.2.7 Beam quality	13
2.3 Fibre lasers	15
2.3.1 Fibre laser systems	16
2.3.2 Fibre laser benefits	18
2.4 Laser Cutting process	18
2.4.1 Kerf width	19
2.4.2 Cut front geometry	20
2.4.3 Beam behaviour inside the cut zone.....	24
2.4.4 Depth of cut.....	25
2.4.5 Cut edge quality	26
2.4.6 Energy losses.....	29
2.5 Laser cutting machine parameters	31
2.5.1 Cutting head parameters.....	31
2.5.2 Assist gas and pressure.....	37
2.5.3 Cutting speed.....	37

2.6	Laser-oxygen cutting process	39
2.7	Laser-nitrogen cutting process	43
2.8	Laser piercing	45
2.8.1	Definition	45
2.8.2	Laser piercing mechanism.....	47
2.8.3	Piercing quality characteristics	48
2.8.4	Rapid laser piercing.....	48
2.9	Thermal lensing	49
2.10	Summary	51
3	Equipment and experimental procedures.....	53
3.1	Introduction	53
3.2	Material	53
3.3	Fibre laser cutting machine	54
3.3.1	Optical system of cutting head.....	54
3.4	Output power measurement.....	54
3.5	Laser beam characterisation	57
3.5.1	Finding the focal point by focus monitor.....	59
3.6	Beam monitoring results	60
3.6.1	Cutting head with focal distance of 120 mm	60
3.6.2	Cutting head with focal distance of 80 mm	62
3.6.3	Comparison of focussed beams with different focal length.....	63
3.6.4	Focal point distance and focused beam diameter.....	69
3.6.5	Focal point position adjustment	70
3.6.6	Machine setup	73
3.7	Oxygen- fibre laser cutting.....	74
3.7.1	Experiment parameters.....	74
3.8	Nitrogen-fibre laser cutting	74
3.8.1	Initial experiment	74
3.8.2	Cutting with maximum cutting speed	75
3.9	Kerf width measurement	78
3.10	Surface roughness measurement	80
3.11	Laser piercing	82
3.11.1	Experimental method	83
3.11.2	Nitrogen laser piercing.....	83
3.11.3	Oxygen laser piercing	84

3.11.4	Sample preparing	84
3.11.5	Mapping of hole growth.....	86
3.12	Piercing with nitrogen – cutting with oxygen	88
4	Preliminary laser cutting results	90
4.1	Overview	90
4.2	Kerf width.....	90
4.2.1	Fibre laser-oxygen cutting.....	91
4.2.2	Fibre laser-nitrogen cutting	97
4.2.3	Comparison of kerf width in oxygen and nitrogen laser cutting.....	100
4.3	Heat affected zone (HAZ) and oxidation mark	101
4.3.1	Fibre laser oxygen cutting.....	101
4.3.2	Fibre laser nitrogen cutting	107
4.3.3	Comparison of the HAZ between oxygen and nitrogen laser cutting	111
4.4	Surface roughness results	112
4.4.1	Fibre laser-oxygen cutting.....	112
4.4.2	Fibre laser-nitrogen cutting.....	118
4.5	Cut surface characterisation	120
4.5.1	Cut edge comparison between oxygen and nitrogen laser cutting.....	122
4.6	Striation pattern observation	122
4.6.1	Fibre laser-oxygen cutting.....	122
4.6.2	Fibre laser-nitrogen cutting.....	128
4.6.3	Comparison between oxygen and nitrogen striations pattern	131
4.7	Summary	132
5	Piercing process	134
5.1	Overview	134
5.2	The importance of study on piercing.....	134
5.3	Basic mechanism of piercing.....	135
5.4	Piercing in comparison with cutting.....	136
5.5	Kerf width results	137
5.6	Definition of hole structure	137
5.7	Quality requirement in laser piercing	138
5.8	Mapping of hole growth	138
5.9	Piercing with low and moderate nitrogen pressure	140
5.9.1	2 bar pressure of nitrogen.....	140
5.9.2	0.3 bar pressure of nitrogen.....	143

5.9.3	Comparison of results	148
5.9.4	Discussion of results	149
5.10	Piercing with low and moderate oxygen pressure	152
5.10.1	With 2 bar pressure of oxygen	152
5.10.2	With 0.3 bar pressure of oxygen	157
5.10.3	Comparison of results	162
5.10.4	Discussion of results	163
5.11	Comparison of O ₂ and N ₂ piercing in low and moderate pressure	167
5.12	High power piercing with moderate and high pressure of nitrogen	172
5.12.1	With 2 bar nitrogen pressure	172
5.12.2	With 4 bar nitrogen pressure	174
5.12.3	With 8 bar nitrogen pressure	177
5.12.4	With 12 bar nitrogen pressure	180
5.12.5	Comparison of results	183
5.12.6	Discussion of results	184
5.13	High power piercing with moderate and high pressure of oxygen	187
5.13.1	With 2 bar pressure of oxygen	187
5.13.2	With 4 bar oxygen pressure	189
5.13.3	With 8 bar oxygen pressure	192
5.13.4	Comparison of the results	193
5.13.5	Discussion of results	194
5.14	Hole characteristics	197
5.15	Summary of piercing results	199
5.15.1	General results	199
5.15.2	Nitrogen piercing results	200
5.15.3	Oxygen piercing results	201
5.16	Piercing with nitrogen - cutting with oxygen	201
5.16.1	Results	203
6	Specific Point Energy	207
6.1	Introduction	207
6.2	Basic laser material interaction parameters	208
6.2.1	Power density	208
6.2.2	Interaction time	208
6.2.3	Energy density	209
6.2.4	Specific point energy	209

6.3	Cutting with maximum speed.....	211
6.3.1	Kerf width	212
6.4	Thermal lensing	214
6.5	The effect of beam diameter on kerf width	216
6.6	Effect of power density on kerf width.....	217
6.7	Effect of power density and SPE on the cut sheet thickness.....	218
6.8	Comparison of cutting and welding	221
6.9	Discussion	222
7	Summary and conclusions	225
7.1	Characterisation of fibre laser cutting:	225
7.2	Piercing.....	226
7.3	Specific point energy (SPE) analysis:	226
8	Future Work.....	228
9	References.....	230
10	Appendix	240

List of figures

Figure 2.1- The absorption of input energy by an electron and moving from a lower-energy orbit to higher-energy orbit.	4
Figure 2.2- The excited electron decays and emits a light photon.....	4
Figure 2.3- Stimulated emission: photons encounter other excited atoms.....	5
Figure 2.4-The simple structure of a laser device showing the excited state [13].	5
Figure 2.5- Stimulated photons travelling through the mirror are termed a laser beam [13].	5
Figure 2.6- Laser absorptivity by metals as a function of wavelength [15].	7
Figure 2.7- The effect of S polarization (perpendicular) and P polarization (parallel) on absorptivity of CO ₂ laser [18].	7
Figure 2.8- Cutting speed in radial and circular polarization of CO ₂ laser for 2mm X5CrNi18-10 [18].	8
Figure 2.9- Diagram defining the reflection and absorption of a laser beam.	8
Figure 2.10- Absorptivity of unpolarised laser radiation from CO ₂ (10.6 μm) and solid state (1.06 μm) of a molten iron surface as a function of incidence angle [21].	10
Figure 2.11- Left: Concept of glancing angle. Right: Absorptivity as a function of glancing angle [22].	10
Figure 2.12- Absorptivity coefficient for CO ₂ laser of steel using oxygen as a function of material thickness. Power was increased from 1000 W to 3000 W with increasing thickness [26].	11
Figure 2.13- Comparison between CO ₂ and fibre laser cutting of 3mm-thick mild steel and the effect of power on the cutting speed [31].	12
Figure 2.14- Focused laser beam geometry[31].	13
Figure 2.15- Geometrical definition of M2 and its effect on the beam diameter. The equations have been derived from equation 2.5.	14
Figure 2.16-Effect of beam parameter product on the focused beam profile [34].	14
Figure 2.17- Measured intensity distribution for (a) CO ₂ and (b) disk laser beam [36, 37].	15
Figure 2.18- Effect of beam parameter product (BPP) on beam diameter and power density [11].	15
Figure 2.19- Schematic showing the solid state laser designs. (a) Side pumped rod laser, (b) thin disc laser and (c) fibre laser [38].	16
Figure 2.20 - Schematic showing a single emitter fibre laser machine.	16
Figure 2.21- Multi mode (modular) fibre laser structure [42].	17
Figure 2.22- Schematic structure of multimode fibre laser beam.	17
Figure 2.23- Definition of laser cutting [48].	19

Figure 2.24- Showing typical kerf. Left: upper kerf, Right: lower kerf (focused beam diameter of 0.2 mm on the top surface, 1000 W, 6000 mm/min, 2 bar oxygen, 1.6 mm thick mild steel).....	19
Figure 2.25- Kerf width versus cutting speed in CO ₂ laser cutting [50].....	20
Figure 2.26- The effect of assistant gas type and pressure on the kerf width [30]. ...	20
Figure 2.27- Cut front inclination as a function of beam geometry and sheet thickness [59]......	21
Figure 2.28- Cut front-laser beam interaction geometries at; (a) slow cutting speeds, (the cut front is and almost vertical, straight line of fluctuating position), (b) moderate cutting speeds (the cut front is straight line inclined at θ), (c) higher cutting speeds (the cut front can be approximated to upper and lower lines inclined θ_U and θ_L), and (d) very high cutting speeds (the cut front becomes extended in the direction of cutting and the reflected beam interacts more with the lower part of cut front) [22]......	21
Figure 2.29- Observation result for different cutting velocities V. (a) V=1 m/min, (b) V=3 m/min, and (c) V=6 m/min [53]......	22
Figure 2.30- Observation results of 2D melting experiments for different velocities V. (a) V=1 m/min, (b) V=2 m/min, and (c) V=3 m/min [53]......	22
Figure 2.31- Lower part of cut front become curved (CO ₂ laser, V _{max} =1.2 m/min, 5mm thickness, focal point at 33% of thickness below the upper surface) [62]......	23
Figure 2.32- Cut front inclination as a function of cutting speed and laser source is shown for thickness of 5mm and focal position of -1.65mm. A) CO ₂ , B) Disk laser [37]......	24
Figure 2.33- Comparison of cut front inclination between the experimental profile obtained at maximum cutting velocity and theoretical calculation as a function of focal position when thickness is 5mm. A) Focal position of -1.65mm, B) Focal position of -3.3mm [37].	24
Figure 2.34- Laser cutting simulation of the cutting front with CALCut [58].	25
Figure 2.35- Striation pattern, A) 15mm mild steel, 4 kW power, 18 bar oxygen, 0.8 m/min cutting speed, 190.5 mm focal length, focal position 4 mm above top surface. B) 10 mm stainless steel, 4 kW power, 4bar nitrogen, 1.0 m/min cutting speed, 190.5 mm focal length, focal position 8 mm below the top surface [45].	27
Figure 2.36- Mean height of the profile (Rz) as a function of cut thickness [68]......	28
Figure 2.37- Deviation of perpendicularity (u) of a vertical cut; a is the workpiece thickness and Δa is the thickness reduction for determination of perpendicularity tolerance [68].	29
Figure 2.38- Perpendicularity tolerance (u) as a function of cut thickness [68]......	29
Figure 2.39- Schematic diagram of the power contributions and energy losses collecting [36].	30
Figure 2.40- YK52 cutting head components as used in this research [72]......	31
Figure 2.41- Kerf widths for varying focal positions compared to the theoretical laser beam diameter (2.2kW, fibre laser, 6mm thick stainless steel, nitrogen) [10].	32

Figure 2.42- Showing a geometrical definition of focusing system. Left: focusing of laser beam. Right: geometrical definition of Rayleigh length.	33
Figure 2.43- Focus position and quality of cut [80].....	34
Figure 2.44- Nozzle diameter and stand-off distance [31].....	35
Figure 2.45- Alignment and misalignment of laser beam and nozzle (drawn by author).	36
Figure 2.46- Showing a poor quality cut edge obtained when there was a nozzle-beam misalignment [1].....	36
Figure 2.47- Showing 1 mm nozzle damaged by misaligned laser beam. A) Outside of the tip, B) Inside. Focused beam size was 0.2 mm.....	36
Figure 2.48- laser power versus cutting speed for different laser source and material [51].	38
Figure 2.49- Maximum cutting speed with the corresponding required laser power (fibre laser, nitrogen, 14 bar for aluminium and 19 bar for stainless steel) [65].	38
Figure 2.50- Brittle oxide layer on the cut edge [9].....	39
Figure 2.51- The relationship between viscosity and temperature [89].....	40
Figure 2.52- Cutting speed as a function of oxygen purity (CO ₂ , 400 W, 0.35 MPa, 2 mm thick mild steel) [8].....	40
Figure 2.53- Kerf width per spot size versus different power for various thickness of mild steel sheet in fibre laser-oxygen cutting [52].....	41
Figure 2.54- Surface roughness graph (left) and striation free on the cut edge (right), (2bar oxygen, 1000 W, 5500 mm/min) [22, 52].	41
Figure 2.55- Boundary layer separation point (BLS) in 10 mm stainless steel (4 kW, 4 bar nitrogen, 1.0 mm/min cutting speed, 190.5 mm focal length, focal point position 8 mm below upper surface) [45].	44
Figure 2.56- Kerf width and dross attachment with 1.0 bar oxygen pressure. Kerf width is about 1mm (15 mm mild steel, 3 kW, 0.8 mm/min, 2 mm nozzle diameter, - 10 mm focal length) [51].....	46
Figure 2.57- Decreases in the start-up hole by PRPM cutting. A) Normal pulsed mode, B) PRPM laser C) cutting with normal pulsed laser D) cutting with PRPM laser [93].....	48
Figure 2.58 - A 3D cross section of a hole pierced by CW laser beam.	49
Figure 2.59- Relatively focus shift as a function of irradiation time [101].....	50
Figure 3.1- Schematic of calorimetric power meter [103].....	55
Figure 3.2- Indicating the setup for power calibration with power meter.	55
Figure 3.3- Power meter's software window indicates the measured power for the target power of 1200 W with fibre of 200 µm and the focal length of 120 mm as the time increases.	56
Figure 3.4- Indicating the trend of actual power versus target power using different lenses with focal length of 120 mm and 80 mm. The cone without nozzle had been set up on the cutting head.....	56

Figure 3.5- Primes GmbH focus monitor [103, 109].	58
Figure 3.6- The experimental setup for monitoring the laser beam.	58
Figure 3.7- Adjustment plate on the focus monitor. Arrow shows the red guide beam path. Measuring tip has been rotated to avoid any crash with adjustment plate [99].	58
Figure 3.8- Showing the geometrical position of focus monitoring with cutting head. A) Usual setup of the focus monitor for focal length of 120 mm. B) Due to some space limitation between the focus monitor and the cutting head when monitoring the beam focussed by 80 mm-lens, the focus monitor was setup upside down with the inverted pinhole.	59
Figure 3.9- Focussed beam profile for fibre of 200 μm with focal length of 120 mm (600 W).	61
Figure 3.10- Energy distribution at the position of focus point and power of 600 W with focal length of 120 mm for different fibres.	61
Figure 3.11- Superposition of beam profile with a pierced hole (Fibre diameter of 200 μm , focal length of 120 mm, irradiation time of 8 ms, power of 1.7 kW with 2 bar oxygen).	62
Figure 3.12- Focussed beam profile for fibre of 200 μm with focal length of 80 mm (400 W).	63
Figure 3.13- Energy distribution at the focus point with power of 400 W for different fibres with focal length of 80 mm.	63
Figure 3.14- A comparison of four beams with fibres of 200 μm and 400 μm focussed by two different lenses with focal distance of 120 mm and 80 mm. This figure was carefully drawn in AutoCAD with using the geometric information which had been obtained by the focus monitoring tests.	64
Figure 3.15- Showing a comparison of employed fibres in terms of power intensity distribution throughout the focal point position (focal length of 120 mm with power of 600 W).	66
Figure 3.16- Power intensity as a function of fibre diameter at focal point and Rayleigh length for power of 600 W and focal distance of 120 mm.	67
Figure 3.17- Indicating a comparison of two employed fibres in terms of power intensity distribution throughout the focal point position with different powers (focal length of 80 mm).	67
Figure 3.18- Power intensity distribution for different fibres, focal lengths and powers.	68
Figure 3.19- Dimensions of employed cutting heads. A) Focal length of 80 mm, B) 120 mm.	68
Figure 3.20- Showing two employed cutting heads are setup on the sheet ready to cut.	69
Figure 3.21- Focused beam diameter as a function of power for fibre of 200 μm at the constant relative focal length of $FR = 218$ mm.	69
Figure 3.22- Relative focal point position (FR) as a function of power for fibre of 200 μm .	70

Figure 3.23- Focal point adjustment tool for YK52 cutting head.	71
Figure 3.24- Focal point position adjustment. A) Before adjustment, B) After adjustment.	71
Figure 3.25- Kerf width versus lens position for different fibres (focal length of 120 mm, 1 mm thick mild steel, 12 bar nitrogen, V = 500 mm/min, P = 250 W).	72
Figure 3.26- Comparison of employed fibres and optical systems in terms of lens position and kerf width (1 mm thickness, 12 bar nitrogen, V = 500 mm/min, P = 250 W).	72
Figure 3.27- Minimum power at maximum cutting speed versus thickness for different fibres. The cutting speed range has given in Table 3.14.	76
Figure 3.28- Minimum energy per unit length versus thickness for different fibres, 12 bar N ₂	76
Figure 3.29- Maximum cutting speed experiment flowchart.	77
Figure 3.30- Illustrating the plan of kerf width measuring position on the cut sheet (mm).	79
Figure 3.31- Keyence VHX-100 Series Digital Microscope used to measure the kerf width [52].	79
Figure 3.32- Showing the top kerf and the measurement positions.	79
Figure 3.33- Workpiece was engraved before chopping up.	80
Figure 3.34- Showing the positions of surface roughness scan lines. (2 mm, 2 bar oxygen, 1000 W, 5 m/min).	80
Figure 3.35- Hobson precision CLI 100 profilometer.	81
Figure 3.36- A definition of surface roughness Ra [112].	81
Figure 3.37- A definition of surface roughness Rz [112].	81
Figure 3.38- Indicating a result of surface roughness measured in the middle of cut edge shown in Figure 3.34. The length of sample is 17 mm. A) Surface roughness + waviness profile. The profile was calculated after a Gaussian filtering of 0.8 mm. B) Illustrating the waviness profile, the pitch of waviness= 2.5 mm. C) Showing the surface roughness, Ra = 2.2 μ m.	82
Figure 3.39- Engraving of workpiece.	84
Figure 3.40- The upper and lower surface of the holes were observed and measured under an optical microscope.	84
Figure 3.41- Indicating the top view of a sample with inclined grinding lines.	85
Figure 3.42- 3D view of a ground sample. A) Beginning of grinding, B) continuing of grinding.	85
Figure 3.43- Etched cross section of holes pierced by 2000 W, 8 bar nitrogen at 8 ms irradiation time.	86
Figure 3.44- Showing a micro photo of the cross sectioned hole in AutoCAD.	87
Figure 3.45- Indicating results brief from the AutoCAD.	87
Figure 3.46- Three sorts of hatch were used in the maps.	88

Figure 3.47- Machine setup. Piercing nozzle angle is 40° from the horizontal.	89
Figure 3.48- Showing the position of piercing nozzle in relation to the main nozzle in two views.	89
Figure 4.1- Upper and lower kerf width (2 mm, 1000 W, 2 bar oxygen).	91
Figure 4.2- Upper and lower kerf width (2 mm, 1500 W, 2 bar oxygen).	91
Figure 4.3- Upper and lower kerf width (1.6 mm, 1000 W, 2 bar oxygen).	92
Figure 4.4- Upper and lower kerf width (1.6 mm, 1500 W, 2 bar oxygen).	93
Figure 4.5- Upper and lower kerf width (1 mm, 1000 W, 2 bar oxygen).	93
Figure 4.6- Upper and lower kerf width (1 mm, 1500 W, 2 bar oxygen).	93
Figure 4.7- Comparison of upper kerf widths for different thicknesses and powers. The range of kerf width is shown by two lines between 0.4 mm to 0.6 mm. Focused spot size is 0.2 mm on the surface of sheet (2 bar oxygen).	94
Figure 4.8- Upper and lower kerf width per spot size vs cutting speed (2 mm, 2 bar oxygen).	95
Figure 4.9- Upper and lower kerf width per spot size vs cutting speed (1.6mm, 2 bar oxygen).	95
Figure 4.10- Upper and lower kerf width per spot size vs cutting speed (1 mm, 2 bar oxygen).	96
Figure 4.11- Kerf width profile when cutting 1 mm (1000 W, 6000 mm/min) and 2 mm (1000 W, 4000 mm/min) with 2 bar oxygen.	96
Figure 4.12- Upper and lower kerf width (2 mm, 1000 W, 12 bar nitrogen).	98
Figure 4.13- Upper and lower kerf width (2 mm, 1500 W, 12 bar nitrogen).	98
Figure 4.14- Upper and lower kerf width (1 mm, 1000 W, 12 bar nitrogen).	98
Figure 4.15- Upper and lower kerf width (1 mm, 1500 W, 12 bar nitrogen).	98
Figure 4.16- Comparison of upper kerf width for a variety of thicknesses and powers, with 12 bar N ₂ . The range of kerf width is shown by two lines between 0.24 mm to 0.37 mm. Focused beam size is 0.2 mm on the surface of sheet (12 bar nitrogen). ..	99
Figure 4.17- Upper and lower kerf width per spot size vs cutting speed (2 mm, 12 bar nitrogen).	100
Figure 4.18- Upper and lower kerf width per spot size vs cutting speed (2 mm, 12 bar nitrogen).	100
Figure 4.19- Upper kerf width versus power for different assist gas and cutting speed (1 mm, 2 bar oxygen, 12 bar nitrogen).	101
Figure 4.20- Upper kerf width versus power for different assist gas and cutting speed (1 mm, 2 bar oxygen, 12 bar nitrogen).	101
Figure 4.21- Oxidation mark. A) Upper kerf. B) Lower kerf. (2 mm-thick sheet, 1500 W, 6000 mm/min, 2bar oxygen).	102
Figure 4.22- EDS examination of the dark zone on the upper surface of sheet close to the cut edge (2 mm- thick sheet, 1500 W, 4000 mm/min, 2 bar oxygen).	102

Figure 4.23- EDX examination of the dark zone on the lower surface of sheet close to the cut edge. Dark width position is shown. (2 mm-thick sheet, 1500 W, 4000 mm/min, 2 bar oxygen).....	102
Figure 4.24- Oxidation width versus cutting speed for different powers (2 mm, 2 bar oxygen).....	103
Figure 4.25- Oxidation width versus cutting speed for different powers (1.6 mm, 2 bar oxygen).....	103
Figure 4.26- Oxidation width versus cutting speed for different powers (1 mm, 2 bar oxygen).....	103
Figure 4.27- The dark thin width on the right edge of the samples indicates the HAZ. Black line added to indicate edge of the HAZ (1000 W, 4000 mm/min, 2 bar oxygen).....	104
Figure 4.28- Width of HAZ versus cutting speed (2 mm, 2 bar oxygen).	105
Figure 4.29- Width of HAZ versus cutting speed (1.6 mm, 2 bar oxygen).	105
Figure 4.30- Width of HAZ versus cutting speed (1 mm, 2 bar oxygen).	105
Figure 4.31- EDS examination qualitatively shows the presence of oxygen on the surface of cut sample (1500 W, 800 mm/min, 12 bar nitrogen).	107
Figure 4.32- Upper and lower kerf width when laser cutting of 1mm thick mild steel sheet with 12 bar nitrogen. A) 250 W, 200 mm/min. B) 400 W, 800 mm/min. C) 600 W, 2400 mm/min.	108
Figure 4.33- Heat affected zone in nitrogen laser cutting for three different thicknesses (1200 W, 1000 mm/min).....	108
Figure 4.34- Width of HAZ when cutting 3 mm thick mild steel with 12 bar nitrogen.	109
Figure 4.35- Width of HAZ when cutting 2 mm thick mild steel with 12 bar nitrogen.	109
Figure 4.36- Width of HAZ when cutting 1 mm thick mild steel with 12 bar nitrogen.	109
Figure 4.37- Showing the positions of surface roughness scan lines. (2 mm, 0.2 mm spot size, 2 bar oxygen, 1000 W, 5000 mm/min).	112
Figure 4.38- The surface roughness (Ra) versus cutting speed at different position on the cut edge (1500 W, 2 bar oxygen, 2 mm thick sheet).....	113
Figure 4.39- The surface roughness (Ra) versus cutting speed at different position on the cut edge (1000 W, 2 bar oxygen, 2 mm thick sheet).....	113
Figure 4.40- The surface roughness (Ra) versus cutting speed at different position on the cut edge (1500 W, 2 bar oxygen, 1.6 mm thick sheet).....	113
Figure 4.41- The surface roughness (Ra) versus cutting speed at different position on the cut edge (1000 W, 2 bar oxygen, 1.6 mm thick sheet).....	114
Figure 4.42- The surface roughness (Ra) versus cutting speed at different position on the cut edge (1500 W, 2 bar oxygen, 1 mm thick sheet).....	114

Figure 4.43- The surface roughness (Ra) versus cutting speed at different position on the cut edge (1000 W, 2 bar oxygen, 1 mm thick sheet).....	114
Figure 4.44- Comparison of surface roughness for different thicknesses with increasing cutting speed (1000 W, 2 bar oxygen).....	115
Figure 4.45- Photos of the cut edges for different powers and cutting speeds. Sheet thickness is 2 mm, 2 bar oxygen.	116
Figure 4.46- Micrographs of the cut edges from 2 mm, 1.6 mm and 1 mm thick sheet. A severe melting influence is observed on the lower surface of the 2 mm sheet. Three dash lines show the position of surface roughness examinations at distances of 0.2, 0.8 and 1.4 mm from the upper surface of the sheet (2 bar oxygen, 200 μ m, 1000 W, 4000 mm/min).....	116
Figure 4.47- Surface roughness versus thickness as a function of distance from the upper surface of the sample (2 bar oxygen, 200 μ m, 1000 W, 4000 mm/min).	117
Figure 4.48- Surface roughness (Ra) versus cutting speed (2 mm, 1000 W, 12 bar nitrogen).....	118
Figure 4.49- Surface roughness (Ra) versus cutting speed (2 mm, 1500 W, 12 bar nitrogen).....	118
Figure 4.50- The surface roughness (Ra) versus cutting speed (1 mm, 1000 W, 12 bar nitrogen).....	118
Figure 4.51- The surface roughness (Ra) versus cutting speed (1 mm, 1500 W, 12 bar nitrogen).....	118
Figure 4.52- The cut surface after nitrogen laser cutting. Dross can be seen at lower cut edge. Dash lines show the position of surface roughness analysis (1000 W, 400 mm/min, 12 bar nitrogen).	119
Figure 4.53- Surface roughness versus thickness as a function of distance from the upper surface of sample (12 bar nitrogen, 200 μ m, 1000 W, 400 mm/min).....	120
Figure 4.54- XRD of 2mm thick cut edge (fibre laser oxygen cut at 4000 mm/min and 1500 W).....	120
Figure 4.55- EDS line scan of a cut surface at which a piece of oxide layer was broken off the cut surface. EDS qualitatively confirms the presence of oxide on the cut edge (1500 W, 4000 mm/min, 2 bar oxygen).	121
Figure 4.56- The EDS line scan of a fibre laser-nitrogen cut surface. a) The line is located on the cut surface and attached dross at the bottom of kerf. b) Iron, oxygen and carbon can qualitatively be observed. The position of cut surface and dross are shown on the top of the figure. As the EDS line-scan crosses a solidified streak, a big ripple was placed on the interface of the cut edge and dross. It is probably due to a hole formed on the streak during solidification (1500 W, 1000 mm/min, 12 bar nitrogen pressure).....	121
Figure 4.57- Left: presence of oxide layer on the top of the cut edge (1500 W, 6000 mm/min, 2 bar oxygen). Right: A cross section of the sample to see the thickness of oxide layer.....	122
Figure 4.58- The cut surface with three kinds of striation: smooth, moderate and coarse (1000 W, 4000 mm/min, 2 bar oxygen).....	123

Figure 4.59- Left: some smooth striations initiated below the edge. Right: Magnified marked striation is shown (1000 W – 4000 mm/min – 2 bar oxygen).....	124
Figure 4.60- Left: some smooth and moderate striations initiated at the edge. Right: magnified marked striation is shown (1500 W – 4000 mm/min – 2 bar oxygen). ..	124
Figure 4.61- The cut surface reprinted from Figure 4.58 (1000 W, 4000 mm/min, 2 bar oxygen).....	124
Figure 4.62- Explanation of melt build-up ejection cycle. The numbers are matched with numbers in Figure 4.61.	125
Figure 4.63- Waveguiding effect and multiple reflections explanations in the kerf and cut front.	126
Figure 4.64- Left: Schematic showing the thicker oxidation generation. Right: Thick oxide layer on the upper cut edge (2 bar oxygen, 1000 W, 5000 mm/min).....	127
Figure 4.65- A: showing the thickness of the melt and the oxide layers with a chemical gradient in the cutting front. B: Diagram showing a gently sectioned and polished cut edge. A relatively thick porous oxide + iron layer is observed on the cut edge. Several photos with high magnification were taken with an optical microscope and then aligned together carefully. The thicker part of the oxide + iron layer is shown in a higher magnification inset in the diagram. The shape of the oxide + iron layer is also drawn for clarity (1500 W, 4000 mm/min, 2 mm).....	128
Figure 4.66- Relatively thick dross clinging to the lower surface of the sheet (12 bar nitrogen).	128
Figure 4.67- Left: a cut edge with dross clinging to the lower surface of the sample, three areas can be observed as shown with A1 to A3. Right: the boundary of areas has been presented in magnification. Re-cast melt layers and chaotic striation pattern can be seen (1000 W, 1000 mm/min, 2 mm, 8 bar nitrogen).....	130
Figure 4.68- Indicating the inclination of striations in area 1 and 2.	130
Figure 4.69- Left: Downstream region at the bottom of area 2, Re-solidified melt flow and dross generation can be seen. Right: Different view of dross attachment and integration of dross layers (1000 W, 1000 mm/min, 8 bar nitrogen).....	130
Figure 4.70- Superposition of laser beam with striation. Multiple reflections irradiate the lowest melt layers (1000 W, 1000 mm/min, 2 mm, 8 bar nitrogen).	131
Figure 5.1- Showing how the initial hole affects the shape of cut kerf. Photo (A) shows usual initial hole shape which is seen at the beginning of a traditional laser cut (1000W, 4000 mm/min, 2 bar oxygen). Photo (B) is a schematic diagram of the ideal shape of the initial part of the kerf.	134
Figure 5.2- Illustrating how initial hole and cut path increase wastage of material in traditional laser cutting. Initial holes are arranged at regions outside the product area.	135
Figure 5.3- Showing the basic mechanism of piercing.	135
Figure 5.4- Upper kerf width versus cutting speed for different powers (2 mm thick mild steel, 2 bar oxygen, spot size of 0.2 mm on the upper surface of sheet, focal length of 120 mm).	137

Figure 5.5- Upper kerf width versus cutting speed for different powers (2 mm thick mild steel, 12 bar nitrogen, spot size of 0.2 mm on the upper surface of sheet, focal length of 120 mm).....	137
Figure 5.6- Indicating hole structure terms (1000 W, 2 bar nitrogen, irradiation time of 12 ms).	138
Figure 5.7- Showing hole growth with increasing irradiation time. The first row was often observed; the second one was rarely seen (1000 W, 2 bar nitrogen).....	139
Figure 5.8- Indicating the hole growth map of Figure 5.7. Much information can be shown in the map.	139
Figure 5.9- Piercing results for 1000 W with 2 bar nitrogen. A) Map of hole growth. B) Depth of hole and melt versus irradiation time. C) Volume of hole, melt total and HAZ versus irradiation time. D) Width of hole versus irradiation time. Solid circles indicate the through holes. Dash circles indicate the sporadic through holes.....	140
Figure 5.10- Piercing results for 1200 W with 2 bar nitrogen. A) Map of hole growth. B) Depth of hole and melt versus irradiation time. C) Volume of hole, melt total and HAZ vs irradiation time. D) Width of hole vs irradiation time. Solid circles indicate the through holes. Dash circles indicate the sporadic through holes.	141
Figure 5.11- Piercing results for 1400 W with 2 bar nitrogen. A) Map of hole growth. B) Depth of hole and melt versus irradiation time. C) Volume of hole, melt total and HAZ versus irradiation time. D) Width of hole versus irradiation time. Solid circles indicate the through holes.	142
Figure 5.12- Piercing results for 800 W with 0.3 bar nitrogen. A) Map of hole growth. B) Depth of hole and melt vs irradiation time. C) Volume of hole, melt total and HAZ vs irradiation time. D) Width of hole vs irradiation time. Solid circles indicate the through holes. Dash circles indicate the sporadic through holes.....	143
Figure 5.13- Piercing results for 1000 W with 0.3 bar nitrogen. A) Map of hole growth. B) Depth of hole and melt vs irradiation time. C) Volume of hole, melt total and HAZ vs irradiation time. D) Width of hole vs irradiation time. Solid circles indicate the through holes. Dash circles indicate the sporadic through holes.....	144
Figure 5.14- Piercing results for 1200 W with 0.3 bar nitrogen. A) Map of hole growth. B) Depth of hole and melt vs irradiation time. C) Volume of hole, melt total and HAZ vs irradiation time. D) Width of hole vs irradiation time. Solid circles indicate the through holes. Dash circles indicate the sporadic through holes.....	145
Figure 5.15- Piercing results for 1400 W with 0.3 bar nitrogen. A) Map of hole growth. B) Depth of hole and melt vs irradiation time. C) Volume of hole, melt total and HAZ vs irradiation time. D) Width of hole vs irradiation time. Solid circles indicate the through holes. Dash circles indicate the sporadic through holes.....	146
Figure 5.16- The effect of nitrogen pressure on the hole and melt volumes. A) Sufficient gas pressure. B) Inadequate gas pressure. C) 1400 W, 2 bar, 10 ms. D) 1400 W- 0.3 bar , 48 ms.....	150
Figure 5.17- Piercing results for 600 W with 2 bar oxygen. A) Map of hole growth. B) Depth of hole and melt versus irradiation time. C) Volume of hole, melt total and HAZ versus irradiation time. D) Width of hole versus irradiation time. Solid circles indicate the through holes.	152

Figure 5.18- Piercing results for 800 W with 2 bar oxygen. A) Map of hole growth. B) Depth of hole and melt vs irradiation time. C) Volume of hole, melt total and HAZ vs irradiation time. D) Width of hole vs irradiation time. Solid circles indicate the through holes. Dash circles indicate the sporadic through holes. 153

Figure 5.19- Piercing results for 1000 W with 2 bar oxygen. A) Map of hole growth. B) Depth of hole and melt versus irradiation time. C) Volume of hole, melt total and HAZ versus irradiation time. D) Width of hole versus irradiation time. Solid circles indicate the through holes. 154

Figure 5.20- Piercing results for 1200 W with 2 bar oxygen. A) Map of hole growth. B) Depth of hole and melt versus irradiation time. C) Volume of hole, melt total and HAZ versus irradiation time. D) Width of hole versus irradiation time. Solid circles indicate the through holes. Dash circles indicate the sporadic through holes..... 155

Figure 5.21- Piercing results for 1400 W with 2 bar oxygen. A) Map of hole growth. B) Depth of hole and melt versus irradiation time. C) Volume of hole, melt total and HAZ versus irradiation time. D) Width of hole versus irradiation time. Solid circles indicate the through holes. 156

Figure 5.22- Piercing results for 600 W with 0.3 bar oxygen. A) Map of hole growth. B) Depth of hole and melt versus irradiation time. C) Volume of hole, melt total and HAZ versus irradiation time. D) Width of hole versus irradiation time. Solid circles indicate the through holes. Dash circles indicate the sporadic through holes..... 157

Figure 5.23- Piercing results for 800 W with 0.3 bar oxygen. A) Map of hole growth. B) Depth of hole and melt versus irradiation time. C) Volume of hole, melt total and HAZ versus irradiation time. D) Width of hole versus irradiation time. Solid circles indicate the through holes. 158

Figure 5.24- Piercing results for 1000 W with 0.3 bar oxygen. A) Map of hole growth. B) Depth of hole and melt versus irradiation time. C) Volume of hole, melt total and HAZ versus irradiation time. D) Width of hole versus irradiation time. Solid circles indicate the through holes..... 159

Figure 5.25- Piercing results for 1200 W with 0.3 bar oxygen. A) Map of hole growth. B) Depth of hole and melt versus irradiation time. C) Volume of hole, melt total and HAZ versus irradiation time. D) Width of hole versus irradiation time. Solid circles indicate the through holes..... 160

Figure 5.26- Piercing results for 1400 W with 0.3 bar oxygen. A) Map of hole growth. B) Depth of hole and melt versus irradiation time. C) Volume of hole, melt total and HAZ versus irradiation time. D) Width of hole versus irradiation time (printed in the next page). Solid circles indicate the through holes. 161

Figure 5.27- Volumes of melt, hole and the NEM versus power at breakthrough for different oxygen pressure..... 166

Figure 5.28- Hole and melt depth versus irradiation time at 1000 W for different gases and pressures. Circles show through holes. Dash circles indicate sporadic through holes..... 167

Figure 5.29- Melt total volume versus irradiation time at power of 1000 W for different gases and pressures. Through holes are shown by circles. Dash circles show sporadic through holes. 168

Figure 5.30- Hole volume versus irradiation time at power of 1000 W for different gases and pressures. Circles indicate through holes. Dash circles show sporadic through holes.....	168
Figure 5.31- A comparison of oxygen and nitrogen in terms of melt total and hole volumes when piercing with 1000W and 2 bar pressure. Circles indicate through holes. Dash circles show sporadic through holes.....	169
Figure 5.32- A comparison between 2 bar and 0.3 bar nitrogen pressure in terms of melt and hole volumes versus irradiation time. Circles indicate through holes. Dash circles show sporadic through holes.	169
Figure 5.33- Depth of melt versus irradiation time for different powers in 2 bar oxygen and nitrogen.....	170
Figure 5.34- Depth of hole versus irradiation time for different powers and gases with 2 bar pressure.	170
Figure 5.35- The melt and hole volumes versus power for different gases and pressures.....	171
Figure 5.36- Showing hole diameter versus power for different employed gases...	171
Figure 5.37- Showing the time when through hole appears at each power intensity.	171
Figure 5.38- Piercing results for 1700 W with 2 bar nitrogen. A) Map of hole growth. B) Depth of hole and melt vs irradiation time. C) Volume of hole, melt total and HAZ vs irradiation time. D) Width of hole vs irradiation time. Solid circles indicate the through holes. Dash circles indicate the sporadic through holes.	172
Figure 5.39- Piercing results for 2000 W with 2 bar nitrogen. A) Map of hole growth. B) Depth of hole and melt versus irradiation time. C) Volume of hole, melt total and HAZ vs irradiation time. D) Width of hole vs irradiation time. Solid circles indicate the through holes. Dash circles indicate the sporadic through holes.	173
Figure 5.40- Piercing results for 1400 W with 4 bar nitrogen. A) Map of hole growth. B) Depth of hole and melt vs irradiation time. C) Volume of hole, melt total and HAZ vs irradiation time. D) Width of hole vs irradiation time. Solid circles indicate the through holes. Dash circles indicate the sporadic through holes.	174
Figure 5.41- Piercing results for 1700 W with 4 bar nitrogen. A) Map of hole growth. B) Depth of hole and melt vs irradiation time. C) Volume of hole, melt total and HAZ vs irradiation time. D) Width of hole vs irradiation time. Solid circles indicate the through holes. Dash circles indicate the sporadic through holes.	175
Figure 5.42- Piercing results for 2000 W with 4 bar nitrogen. A) Map of hole growth. B) Depth of hole and melt vs irradiation time. C) Volume of hole, melt total and HAZ vs irradiation time. D) Width of hole vs irradiation time. Solid circles indicate the through holes. Dash circles indicate the sporadic through holes.	176
Figure 5.43- Piercing results for 1400 W with 8 bar nitrogen. A) Map of hole growth. B) Depth of hole and melt vs irradiation time. C) Volume of hole, melt total and HAZ vs irradiation time. D) Width of hole vs irradiation time. Solid circles indicate the through holes. Dash circles indicate the sporadic through holes.	177
Figure 5.44- Piercing results for 1700 W with 8 bar nitrogen. A) Map of hole growth. B) Depth of hole and melt vs irradiation time. C) Volume of hole, melt total and	

HAZ vs irradiation time. D) Width of hole versus irradiation time. Solid circles indicate the through holes. Dash circles indicate the sporadic through holes.....	178
Figure 5.45- Piercing results for 2000 W with 8 bar nitrogen. A) Map of hole growth. B) Depth of hole and melt vs irradiation time. C) Volume of hole, melt total and HAZ vs irradiation time. D) Width of hole vs irradiation time. Solid circles indicate the through holes. Dash circles indicate the sporadic through holes.	179
Figure 5.46- Piercing results for 1400 W with 12 bar nitrogen. A) Map of hole growth. B) Depth of hole and melt vs irradiation time. C) Volume of hole, melt total and HAZ vs irradiation time. D) Width of hole vs irradiation time. Solid circles indicate the through holes. Dash circles indicate the sporadic through holes.....	180
Figure 5.47- Piercing results for 1700 W with 12 bar nitrogen. A) Map of hole growth. B) Depth of hole and melt vs irradiation time. C) Volume of hole, melt total and HAZ vs irradiation time. D) Width of hole vs irradiation time. Solid circles indicate the through holes.	181
Figure 5.48- Piercing results for 2000 W with 12 bar nitrogen. A) Map of hole growth. B) Depth of hole and melt versus irradiation time. C) Volume of hole, melt total and HAZ versus irradiation time. D) Width of hole versus irradiation time. Solid circles indicate the through holes.....	182
Figure 5.49- Breakthrough time as a function of power and nitrogen pressure.....	185
Figure 5.50- Breakthrough time versus nitrogen pressure for different powers.....	185
Figure 5.51- Showing the upper diameter of the through hole versus power intensity for variety of nitrogen pressure.	186
Figure 5.52- The volumes of melt and hole (at breakthrough) vs power for nitrogen pressures.....	186
Figure 5.53- The melt and hole volumes versus irradiation time for a moderate power-pressure (1000 W, 2 bar nitrogen) and a relatively high power-pressure nitrogen piercing (2000 W, 12 bar). Circles show through holes. Dash circles show sporadic penetration.	186
Figure 5.54- Piercing results for 1700 W with 2 bar oxygen. A) Map of hole growth. B) Depth of hole and melt versus irradiation time. C) Volume of hole, melt total and HAZ versus irradiation time. D) Width of hole versus irradiation time. Solid circles indicate the through holes.	187
Figure 5.55- Piercing results for 2000 W with 2 bar oxygen. A) Map of hole growth. B) Depth of hole and melt versus irradiation time. C) Volume of hole, melt total and HAZ versus irradiation time. D) Width of hole versus irradiation time. Solid circles indicate the through holes.	188
Figure 5.56- Piercing results for 1400 W with 4 bar oxygen. A) Map of hole growth. B) Depth of hole and melt versus irradiation time. C) Volume of hole, melt total and HAZ versus irradiation time. D) Width of hole versus irradiation time. Solid circles indicate the through holes.	189
Figure 5.57- Piercing results for 1700 W with 4 bar oxygen. A) Map of hole growth. B) Depth of hole and melt versus irradiation time. C) Volume of hole, melt total and HAZ versus irradiation time. D) Width of hole versus irradiation time. Solid circles indicate the through holes.	190

Figure 5.58- Piercing results for 2000 W with 4 bar oxygen. A) Map of hole growth. B) Depth of hole and melt versus irradiation time. C) Volume of hole, melt total and HAZ versus irradiation time. D) Width of hole versus irradiation time. Solid circles indicate the through holes. Dash circles indicate the sporadic through holes.....	191
Figure 5.59- Piercing results for 2000 W with 8 bar oxygen. A) Map of hole growth. B) Depth of hole and melt versus irradiation time. C) Volume of hole, melt total and HAZ versus irradiation time. D) Width of hole versus irradiation time. Solid circles indicate the through holes.	192
Figure 5.60- Breakthrough time as a function of power for variety of oxygen pressures.....	194
Figure 5.61- Pierce breakthrough times for variety of oxygen pressure and laser powers.	195
Figure 5.62- Upper pierce hole diameter for oxygen at a range of powers and gas pressures.....	195
Figure 5.63- The volume of the melted zone and the hole volume versus irradiation time for two oxygen pressures at the power of 2000 W Circles show through holes. Dash circles show sporadic penetration.	196
Figure 5.64- The volumes of melt and hole versus irradiation time when piercing with 2 bar oxygen pressure with powers of 1000 W and 2000 W. Circles show through holes.....	197
Figure 5.65- Indicating a hole accompanied by an oxide layer which is pierced by 100 W fibre laser-oxygen at 50 ms. Cross section of the hole is shown in B. The Gaussian curve to compare with the shape of the hole is shown.	198
Figure 5.66- Showing the line scan EDS results at the edge of hole.	198
Figure 5.67- Showing a hole pierced by nitrogen with the EDS examination at the edge of the hole.	198
Figure 5.68- Upper pierced hole diameter for nitrogen at a range of powers and gas pressures.....	202
Figure 5.69- Upper pierced hole diameter for oxygen at a range of powers and gas pressures.....	202
Figure 5.70- Showing that the kerf width in oxygen laser cutting is in the range of nitrogen piercing.	203
Figure 5.71- A) Showing two holes pierced by inclined nozzle. (3bar pressure of nitrogen, 1500 W, 20 ms). Directional spatter on the sheet is due to inclined nozzle. B) Possibility of decrease in the pressure at the entrance of the hole.	204
Figure 5.72- Showing off axis piercing with an inclined nitrogen nozzle.	205
Figure 5.73- (A) Common laser-oxygen cutting (1500 W-6000 mm/min, 2 bar oxygen). (B) Nitrogen piercing-oxygen cutting method (Piercing parameters: 1500 W, 20 ms, 3 bar nitrogen and cutting parameters: 1500 W, 6000 mm/min, 2 bar oxygen).....	205
Figure 5.74- A hole with nitrogen was pierced at the middle of cut path before cutting by oxygen. (Left: piercing at 1500 W, 20 ms and cutting at 1500 W,	

6000 mm/min – Right: piercing at 1500 W, 20 ms and cutting at 1500 W, 5000 mm/min.	206
Figure 6.1- Schematic of interaction of laser beam with workpiece [12].	208
Figure 6.2- Effect of specific point energy on depth of penetration at low levels of power density: 1.6 MWcm ⁻² (5 kW at 0.63 mm) and 0.4 MWcm ⁻² (2 kW at 0.78 mm) [12].	209
Figure 6.3- Schematic interaction of laser beam with workpiece in laser cutting. ...	211
Figure 6.4- Showing cut front laser beam interaction geometries. (A) Slower cutting speed (steep cut front, some laser beam is lost), (B) Faster cutting speed (steeper cut front, all laser beam interacts with cut edge) [22].	211
Figure 6.5- Kerf width versus power for different fibres (1 mm thick, 120 mm focal length).	213
Figure 6.6- Kerf width versus power for different fibres (4 mm thick, 120 mm focal length).	213
Figure 6.7- Kerf width versus power for different fibres (1 mm thick, 80 mm focal length).	213
Figure 6.8- Kerf width versus power for different fibres (6 mm thick, 80 mm focal length).	213
Figure 6.9- Kerf width widening due to thermal lensing. Kerf width slightly increases along the cut (left to right) from 0.195 mm to 0.22 mm (1 mm thick, fibre of 200 µm, 120 mm focal length, power of 310 W, 2.4 m/min).	214
Figure 6.10- Example of kerf width per spot size ratio (K/S) versus power for different fibres and thicknesses. Kerf width for 200 µm fibre and 6 mm thickness is much bigger than that is achieved for 400 µm-1 mm, confirming thermal lensing (80 mm focal length).	214
Figure 6.11- Schematically showing the effect of thermal lensing on the lens, focal distance and spot size for a lens with original focal length of 80 mm and raw beam diameter of 20 mm after collimation. Before thermal lensing, focused beam size at power of 400 W is 0.15 mm (measured by focus monitor). After thermal lensing, the lens volume increases and focal length decreases so the focussed spot size on the sheet surface increases, giving a bigger kerf width.	215
Figure 6.12- Kerf width versus beam diameter for different interaction times (1 mm-thick).	216
Figure 6.13- Kerf width versus beam diameter for different interaction time (4 mm-thick).	216
Figure 6.14- Showing kerf width slightly increases with interaction time (1 mm thick, 200 µm beam diameter, 120 mm focal length).	217
Figure 6.15- Kerf width versus power for different beam diameter (1mm-thick, power range of 120-950 W, cutting speed range of 0.09-3.6 m/min, SPE range of 1.85-25 J, K/S≤1.30).	217
Figure 6.16- Kerf width versus power for different beam diameter (4mm-thick, power range of 480-1550 W, cutting speed range of 0.15-1.2 m/min, SPE range of 22.8-68.3 J, K/S≤1.3).	218

Figure 6.17- Energy distribution for two focused beams delivered by a fibre of 400µm at two powers of 400 W and 600 W. The energy distribution is not exactly a top hat. The energy density for the cutting threshold indicates that the effective beam diameter increases with power.	218
Figure 6.18- Power density results as a function of data number.	219
Figure 6.19- Showing power density batches used in following results.	219
Figure 6.20- The effect of specific point energy on the cut sheet thickness for different power densities.	220
Figure 6.21- The effect of specific point energy on the cut sheet thickness for different power densities.	220
Figure 6.22- Duplication of Figure 6.2 to show the similarity of welding and cutting processes regarding the effect of SPE on the penetration depth and the cut sheet thickness.	220
Figure 6.23- Weld width is controlled by the interaction time but the kerf width is not substantially change with increasing interaction time. Beam diameter for welding was 0.75 mm and for cutting was 0.2 mm.	222
Figure 6.24- Cost (kJ/m) plotted against SPE (J) showing that data forms straight lines, data point markers correspond to material thickness.	222
Figure 6.25- Cost (kJ/m) plotted against SPE (J) showing that data forms straight lines, with each line corresponding to a different beam diameter.	223
Figure 6.26- Showing Figure 6.21 with the Ceff values for selected data point superposed, units for Ceff are $10^{-8} \text{ m}^2 \text{ J}^{-1}$	224
Figure 8.1- A developed NIPOC head with two coaxial nozzles (designed by the author).	229
Figure 10.1- Power versus maximum cutting speed for different thicknesses (200 µm fibre diameter, 120 mm focal length, 12 bar nitrogen).	242
Figure 10.2- Power versus maximum cutting speed for different thicknesses (400 µm fibre diameter, 120 mm focal length, 12 bar nitrogen).	243
Figure 10.3- Power versus maximum cutting speed for different thicknesses (600 µm fibre diameter, 120 mm focal length, 12 bar nitrogen).	244
Figure 10.4- Power vs max cutting speed for different thicknesses (200 µm, 80 mm focal length, 12 bar nitrogen).	245
Figure 10.5- Power vs max cutting speed for different thicknesses (400 µm, 80 mm focal length, 12 bar nitrogen).	245

List of tables

Table 2.1- Index of refraction and extinction coefficients of iron for different wavelengths and temperatures (melting point, boiling point and average) [21].	9
Table 2.2- - Showing the characteristics of CO ₂ and Disk laser beam utilized in [36, 37].	14
Table 2.3- Comparison between high power commercial lasers [44].	18
Table 2.4- The effect of gas pressure on the maximum cutting speed (mm/s) with a laser power of 1.5 kW [85].	37
Table 3.1- Composition content of mild steel sheet (% of weight) measured using spark emission (Spectrometry, Foundry Master).	53
Table 3.2- General characteristics of the IPG fibre laser cutting machine.	54
Table 3.3- Showing the optical parameters of employed cutting heads.	54
Table 3.4- Showing the numeric values of target power and the actual power for both applied lenses with different focal length of 120 mm and 80 mm with using the output fibre of 200 µm.	56
Table 3.5- Comparison of actual powers with and without cone.	57
Table 3.6- The effect of fibre diameter on the actual power.	57
Table 3.7- Geometrical characteristics of two applied lenses in focus monitoring. ...	60
Table 3.8- Indicating the theoretical and measured spot size using the lens with focal distance of 120 mm (600 W).	61
Table 3.9- Laser beam characteristics for different focal lengths and fibre diameters.	64
Table 3.10- The effect of power on the focussed beam characteristics (Fibre of 400µm and focal distance of 80 mm).	65
Table 3.11- Relative focal length and lens position for different fibres and optical systems.	71
Table 3.12- Laser cutting parameters in oxygen laser cutting.	74
Table 3.13- Experiment parameters for initial laser cutting of mild steel with nitrogen.	75
Table 3.14- Minimum power at relevant maximum cutting speed to cut the applied sheets.	75
Table 3.15- Cutting speed (mm/min) for each employed fibre, focal length and Ti.	78
Table 3.16- Showing a concise table of cutting parameters used in maximum cutting speed experiment. Parameters were capable to cut the sheet, selected for next analysis (fibre diameter of 200 µm, spot size of 0.2 mm, focal length of 120 mm, 4 mm-thick mild steel, 12 bar N ₂).	78
Table 3.17- Briefly shows the laser powers, gas type and gas pressures in piercing experiments.	83
Table 3.18- Parameters for nitrogen laser piercing.	83

Table 3.19- Parameters for oxygen laser piercing.	84
Table 3.20- Parameters of piercing and cutting experiment.	89
Table 4.1- Showing some parameters employed in oxygen and nitrogen cutting.	90
Table 5.1- Indicating some laser piercing parameters.	134
Table 5.2- Breakthrough time and the percentage of hole through, 2 bar nitrogen.	147
Table 5.3- Breakthrough time for different powers and pressures in nitrogen piercing.	148
Table 5.4- The hole and total melt volumes at breakthrough for different powers and pressures in nitrogen piercing.	148
Table 5.5- Upper hole width at breakthrough for different powers and pressures in nitrogen piercing.	148
Table 5.6- The volume of NEM lining the hole surface for different powers and pressures in nitrogen piercing.	149
Table 5.7- Breakthrough time for different powers and pressures in piercing with oxygen.	163
Table 5.8- The volumes of hole, melt and the NEM at breakthrough for different powers and pressures in piercing with oxygen.	163
Table 5.9- Upper hole width at breakthrough for different powers and pressures in piercing with oxygen.	163
Table 5.10- Breakthrough time for 0.3 bar pressure of nitrogen and oxygen.	165
Table 5.11- Percentage of through hole appearance for variety of nitrogen pressure at different irradiation times and powers.	183
Table 5.12- Breakthrough time for different nitrogen pressure with different powers.	183
Table 5.13- The melt and hole volumes at breakthrough time for different powers and nitrogen pressures.	184
Table 5.14- Upper hole width at breakthrough time for different powers.	184
Table 5.15- Breakthrough time for different powers and oxygen pressures.	193
Table 5.16- Melt and hole volumes at breakthrough and afterwards for different powers and oxygen pressures.	193
Table 5.17- Upper hole width at breakthrough time for different powers and oxygen pressures.	194
Table 5.18- Showing a brief comparison between oxygen and nitrogen as assist gas.	199
Table 5.19- The parameters of pre-piercing with 3bar pressure of nitrogen and cutting with 2 bar oxygen pressure (2 mm thick mild steel, 200µm spot size, 120mm optical length).	203
Table 6.1- Cutting parameters which were applied in maximum cutting speed experiments.	212

Table 6.2- Focussed beam diameter for each fibre and focal length (measured at power of 400-600 W).....	212
Table 6.3- Showing the specific point energy for each sheet thickness and different power density range.	219
Table 6.4- Comparison between laser cutting and laser welding.....	221
Table 10.1- The effect of different parameters on the kerf width/spot size for stainless steel [73].	240
Table 10.2- The effect of different parameters on the kerf width/spot size for stainless steel [46].	240
Table 10.3- The effect of different parameters on the kerf width/spot size for zinc steel [30].....	241
Table 10.4- The effect of different parameters on the kerf width/spot size for stainless steel [46].	241

List of symbols

Symbol	Unit	Explanation
R_P	-	Reflection of parallel polarisation
R_S	-	Reflection of perpendicular polarisation
R_{Ave}	-	Average reflection
n	-	Indices of refractive
k	-	Extinction coefficient
ϕ_{in}	$^\circ$	Angle of incidence, inclination angle of the cut front
q_P	$\{Wm^{-2}\}$	Power density.
M^2	-	Beam propagation factor
W_0	mm	Beam waist
d	mm	Focused beam diameter
λ	μm	Wavelength
F, F_{foc}	mm	Focusing focal length
F_{col}	mm	Collimation focal length
D	mm	Raw beam diameter on the surface of lens
D_f	mm	Fibre diameter
P_L, P	W	Power of incident laser beam
P_{FC}	W	Power required to perform a laser cutting
P_{Loss1}	W	Primary power loss
P_{Loss2}	W	Secondary power loss
P_{TP}	W	Power to heat up the volume of material
P_m	W	Power required to melt the volume of material
P_v	W	Power required to vaporise the volume of material
P_{TRANS}	W	Power that directly leaves the cutting zone with no interaction.
P_{REFLE}	W	Power that is reflected from the cutting front surface.
P_{CONV}	W	Power that is lost by convection.
P_{RAD}	W	Power that is lost by radiation.
M	-	Magnification of optical system
A_0, A_S	mm^2	Focused beam area at optical point
A_R	mm^2	Focused beam area at Rayleigh length
W_R	mm	Focused beam diameter at Rayleigh length
ψ_P	-	Thermal power of lens
α	$1/^\circ C$	Thermal coefficient of expansion of lens
Φ	-	Power of the focusing lens
dn/dT	$1/^\circ C$	Temperature coefficient of refractive index of lens
ΔP_{abs}	W	Power that is absorbed by focusing lens
Δf_{abs}	mm	Focal shift due to absorbed power
K_W	$Wm^{-1}K^{-1}$	Material specific thermal conduction
f	mm	Nominal focal length
V	mm/min	Cutting speed
E_L	J	Energy per unit length
T_i	ms	Interaction time
q_E	Jm^{-1}	Energy density
E_{SP}	J	Specific point energy
C_{eff}	mm^2J^{-1}	Cutting efficiency
h, tc	mm	Sheet thickness

Abbreviation

Nd:YAG: Neodymium-Doped Yttrium Aluminium Garnet.

CO₂: Dioxide Carbon.

CNC: Computer Numerical Control.

SPE: Specific Point Energy

SEM: Scanning Electron Microscope.

HAZ: Heat Affected Zone.

CW: Continues Wave.

BPP: Beam Parameter Product.

FeO: Iron Oxide.

K/S: Ratio of kerf width to laser spot size.

BLS: Boundary Layer Separation.

PRPM: Power Ramped Pulse Mode.

RL: Rayleigh Length.

RSZ: Re-solidified Zone.

XRD: X Ray Diffraction.

EDS: Energy-Dispersive X-ray Spectroscopy.

OHD: Open Hole Depth.

MPD: Melt Penetration Depth.

NEM: Non Ejected Melt.

1 Introduction

1.1 General background

Laser cutting has become one of the most reliable advanced manufacturing technologies for industrial productions and has undergone many improvements since its beginning in the 1970s [1, 2]. The cost effectiveness of the laser cutting process is evident in its wide scope of application [3]. The cutting process is CNC programmable and so can be flexible. Lasers have undertaken those tasks that carried out by CNC flame cutting [4]. It can be also an alternative to mechanical cutters and is used in wide variety of industries. Almost all materials can be cut by laser [1]. Metal plates, hollow section metal and polymers can be cut by laser [3]. The maximum metal sheet thickness is limited depending on the type of laser, material, assist gas and other cutting parameters [3, 4]. It is believed that the laser cutting process has the potential to be optimised to a greater extent of efficiency than at present [5, 6].

Laser cutting is a non-contact process so there is no force mechanically applied to the workpiece except for that from the pressure of the assistant gas. Therefore, strong clamping fixtures are not necessary and hence, thin or delicate sheets can be cut without any mechanical damage [1, 2].

Nowadays, two types of laser are most commonly used in laser cutting: CO₂, and disk/rod/fibre Nd:YAG lasers. Both generate high intensity beams of infrared light. CO₂ laser with a wavelength of 10.6µm and disk/fibre laser with wavelength of 1.06µm has its own applications. The general principles of cutting are similar for both types of laser. Most organic materials cannot be cut properly by disk/fibre lasers [3, 7]. In general cutting applications, CO₂ lasers are most effective. However, It has been reported that the disk/fibre laser has some advantages over the CO₂ laser [3, 6]. The performance of the fibre laser, when laser cutting mild steel sheet, is the subject of this research.

1.2 Aims and objectives

One of the most common metals to be cut by laser is thin mild steel sheet using oxygen or nitrogen as assist gases. The presence of oxygen in the cutting zone

creates an exothermic reaction with Fe and the energy released by this reaction enhances the cutting process [1, 8, 9]. However, nitrogen does not react with iron and only used to remove the molten material from the cutting zone [1, 2, 10].

To date, there are few published articles on fibre laser cutting of mild steel. These have focused on the effects of laser cutting parameters on the cut quality compared with CO₂ laser cutting. There are still many questions to be answered regarding the details of fibre laser cutting of mild steel when using oxygen and nitrogen as assist gases. Those addressed in this thesis are as following:

- 1- The first purpose of this report is to study fibre oxygen/nitrogen laser cutting of mild steel, in terms of kerf width, heat affected zone, surface roughness and the phenomenon of striation generation. The aim in this section is to characterise these aspects of fibre laser cutting.
- 2- In laser cutting of mild steel, the use of oxygen creates an exothermic reaction with iron releasing additional energy which can enhance the process. However, to start the laser cut, the laser has to pierce a hole in the workpiece from where the cut proceeds. This start-up hole has a larger width than the rest of the cut so piercing has to be carried out away from the final cut surface, leading to material wastage. Better understanding of laser piercing is needed to be able to minimise the amount of material wastage in laser cutting. How can laser cutting process be optimised?
- 3- A novel research method has been developed by Cranfield University [11, 12] on laser welding. They describe the welding process uniquely using basic laser material interaction parameters such as specific point energy (SPE) and power density. It is of interest if this approach is applicable in laser cutting. Does the SPE and power density control the cut sheet thickness possible? Does the interaction time control the kerf width?

1.3 Overview

In order to begin the investigations into fibre laser cutting, chapter 2 presents a background to the field of laser cutting of metals considering the relevant published work. The experimental methods, samples preparation, samples observation and the relevant equipment applied throughout this research are explained in detail in

chapter 3. The preliminary laser cutting results from the oxygen and nitrogen laser cutting of mild steel sheets are introduced in chapter 4. This chapter contains a comparison between oxygen and nitrogen laser cutting in terms of kerf width, surface roughness, heat affected zone and striation pattern. Chapter 5 concentrates on fibre laser piercing of mild steel. The effects of power intensity, assist gas type and pressure on the laser piercing are investigated. A new technique is presented which pierces the start-up holes no larger than the kerf width and would allow the pierced hole to lie on the cut line of the finished product – leading better material usage. In chapter 6, the effects of basic laser material interaction parameters such as specific point energy, power density and interaction time on the fibre laser cutting are studied. A summary and conclusion of the thesis is presented in chapter 7. Finally, the relevant suggestions for future study are given in chapter 8.

2 Literature review

2.1 Introduction to laser beam

The purpose of this section is to briefly review what the laser beam is. Light Amplification by Stimulated Emission of Radiation (LASER), which has some unique properties including being monochromatic, coherent and having a very low divergence, is a classic interpretation of the atomic excitation. This atomic excitation can be divided into two stages:

- 1- The absorption of energy (heat, light, electricity) by the atom and
- 2- Moving from a lower energy orbit to a higher energy orbit (Figure 2.1).

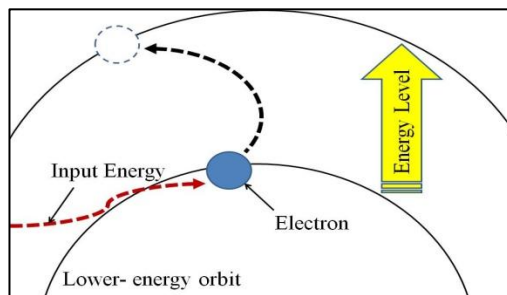


Figure 2.1- The absorption of input energy by an electron and moving from a lower-energy orbit to higher-energy orbit.

Naturally, an excited electron tends to relax back to the ground state and relieves itself of some photonic energy (Figure 2.2). Such photons are not laser light yet, but can produce laser light by stimulated emission. This happens when these photons encounter other excited atoms (Figure 2.3). The incident photon causes the excited atom to release a photon, of the same energy, which is in phase with the original photon. So, one excited atom and one photon results in one released atom plus two photons. In order to increase the probability of this scenario, photons are repeatedly reflected through the laser medium.

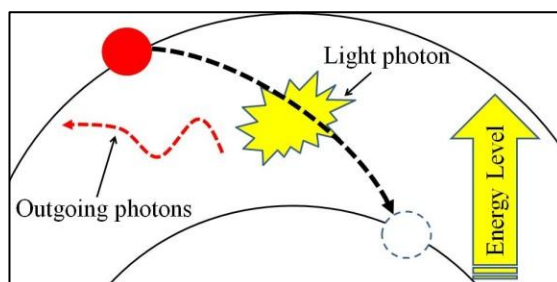


Figure 2.2- The excited electron decays and emits a light photon.

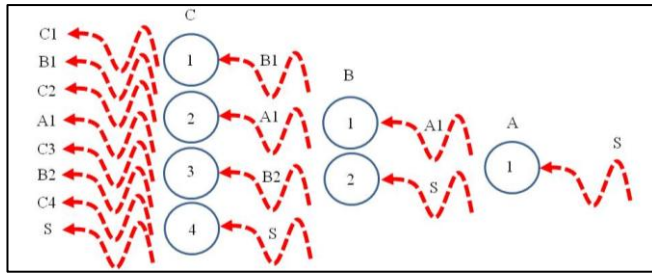


Figure 2.3- Stimulated emission: photons encounter other excited atoms.

Existing atoms in the medium are excited by a flash tube (Figure 2.4). Photons reflect between two mirrors and emission of more photons will be stimulated, building up the laser beam (Figure 2.5); the beam exits through the partially reflected mirror.

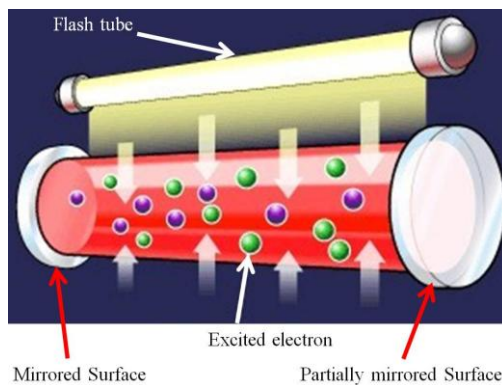


Figure 2.4-The simple structure of a laser device showing the excited state [13].

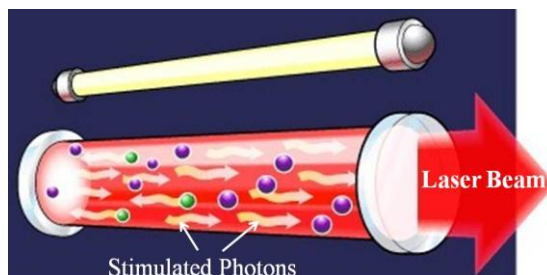


Figure 2.5- Stimulated photons travelling through the mirror are termed a laser beam [13].

The classification of lasers can depend on the kind of medium involved. Gas, solid, liquid or semiconductor laser medium can be used [13].

2.2 Laser beam characteristics

The properties of the laser beam, which directly affects the beam quality and absorptance, are characterised in terms of the wavelength, wave mode, power intensity, polarisation and beam quality. When the laser beam is applied as a heating

tool in material processing applications such as welding and cutting, the beam quality and absorptance can directly affect the quality of process, as if a fibre/disk laser is providing significant advantage to the users in terms of higher speed with lower power in comparison with CO₂ laser [6].

2.2.1 Wavelength

The wavelength of a particular laser depends on the energy levels of atoms in the laser medium and transitions in the process of stimulated emission [2]. In laser material processing, a laser beam should penetrate the surface of the workpiece, in order to melt the material [14]. With regard to the physical mechanism of laser interaction with the surface of material, the wavelength of laser has a decisively important effect on the material's surface absorptivity (Figure 2.6) [15]. The maximum absorption of laser energy with lowest reflection can be obtained with a certain wavelength for a specific material type. The two most common commercial lasers are CO₂ lasers with a wavelength of 10.6 μm and Nd:YAG with 1.06 μm, both of which are used in cutting and welding processes. Due to the shorter wavelength, fibre/disk/Nd:YAG have some advantages over CO₂. The absorption of fibre lasers in metallic materials is higher than that is in CO₂ lasers as shown in Figure 2.6. The reasons for the different performances between fibre/disk and CO₂ laser cutting are not yet completely realised and there are debatable discussions in literatures.

The energy of photons is inversely proportional to the wavelength so the majority of energetic photons with a short wavelength can penetrate into the bound electrons of the material surface atoms, resulting in reflection reduction and absorption enhancement [1, 15, 16]. The relatively low wavelength of fibre, Nd:YAG and disk lasers, due to lack of interaction with silica glass, enables their delivery through optical fibres for flexible laser applications.

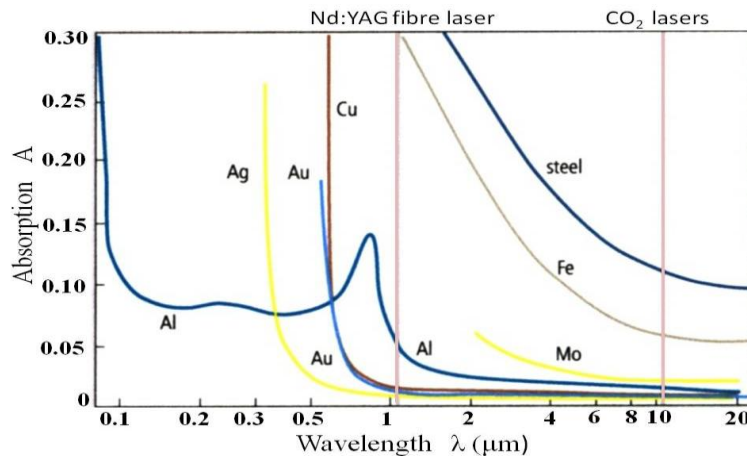


Figure 2.6- Laser absorptivity by metals as a function of wavelength [15].

2.2.2 Polarisation

Any laser beam has two fields: electrical and magnetic, caused by an electromagnetic oscillation and the polarisation of one beam can be linear, circular, and random. For instance, polarization in the fibre lasers is random. Noteworthy is the report that polarisation of laser beam can affect laser processing [17-19]. Niziev et al. [17] concluded by 3D modelling that laser polarisation influences cutting efficiency, depth of cut and cut edge quality. Weber et al. [18] believe that polarised CO₂ laser beams show very specific absorbed intensity behaviour, which is of importance in industrial and scientific applications. The absorptivity of the perpendicular polarised beam is less than that for others (Figure 2.7).

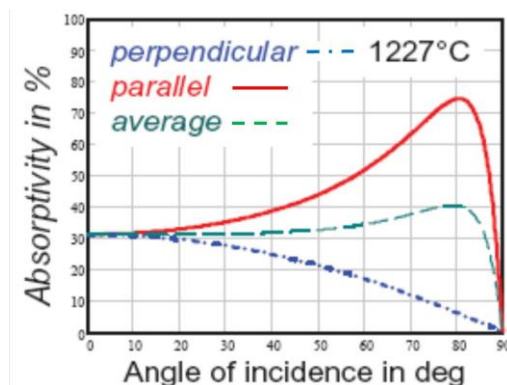


Figure 2.7- The effect of S polarization (perpendicular) and P polarization (parallel) on absorptivity of CO₂ laser [18].

Using a radially polarised CO₂ laser beam, Weber et al. could increase the cutting efficiency up to 36% and the maximum cutting speed up to 37.5% in cutting of 2 mm stainless steel (Figure 2.8) [18]. They also found that using the tangentially polarised laser beam in deep welds at low welding velocity, the spatter significantly decreased

below 40% in comparison with random polarised beam. They also realised that the drilling efficiency increases using radial polarisation in the case of shallow hole depths, while for deep drilling tangential polarisation has more efficiency [18]. In this thesis the polarisation is random.

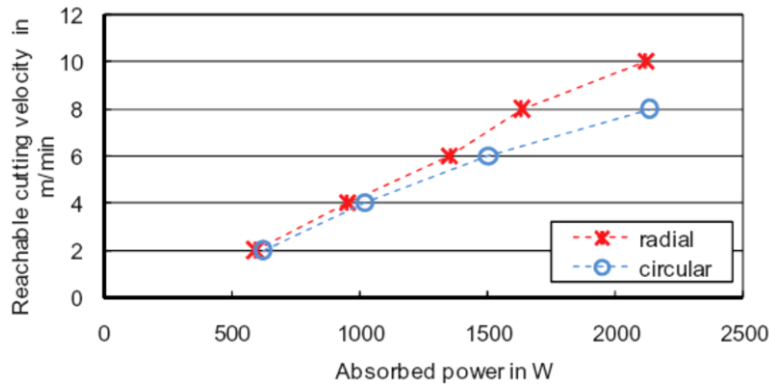


Figure 2.8- Cutting speed in radial and circular polarization of CO₂ laser for 2mm X5CrNi18-10 [18].

2.2.3 Laser beam interaction

When the laser beam encounters a surface at an incidence angle, some of the beam is reflected while the rest is refracted and/or absorbed into the surface [20]. Figure 2.9 schematically shows the reflection and absorption definition of an incident laser beam.

Brewster angle is a special angle of incidence at which an unpolarised beam is reflected from the surface perfectly polarised (perpendicularly) while the absorbed ray is partially polarised.

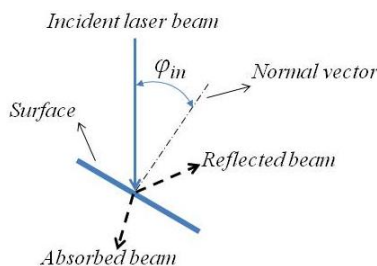


Figure 2.9- Diagram defining the reflection and absorption of a laser beam.

In the laser material applications such as cutting and welding, the values of absorption and reflection significantly affect the process quality. As has been reported by Mahrle and Beyer [21], the reflection values can be calculated using

Fresnel formulations in fibre laser cutting process for a polarised laser beam as shown by equations 2.1 and 2.2:

$$R_P = \frac{(n \cdot \cos \varphi_{in} - 1)^2 + (k \cdot \cos \varphi_{in})^2}{(n \cdot \cos \varphi_{in} + 1)^2 + (k \cdot \cos \varphi_{in})^2} \quad 2.1$$

$$R_S = \frac{(n - \cos \varphi_{in})^2 + k^2}{(n + \cos \varphi_{in})^2 + k^2} \quad 2.2$$

Where R_P is the reflection for parallel and R_S is the reflection of perpendicular polarised laser radiations, φ_{in} is the inclination angle, n is the refractive index and k is the extinction coefficient.

For circular polarised or un-polarised radiation the average of R_P and R_S is used as shown by equation 2.3 [21]:

$$R_{Ave} = \frac{R_P + R_S}{2} \quad 2.3$$

The indices of reflection (n) and absorption (k) vary slightly with temperature; however, they are strongly dependent on the wavelength. Table 2.1 shows the indices of refraction and extinction coefficients of molten iron for different wavelengths and temperatures.

Table 2.1- Index of refraction and extinction coefficients of iron for different wavelengths and temperatures (melting point, boiling point and average) [21].

Temperature (K)	Wavelength = 1.07 μm		Wavelength = 10.6 μm	
	n	k	n	k
1800	5.46	3.96	15.5	15.1
3000	5.14	3.68	14.6	14.1
2400	5.30	3.82	15.0	14.6

Figure 2.10 illustrates the theoretical absorptivity for different un-polarised laser beam wavelengths of 10.6 μm (CO_2) and 1.06 μm (fibre/disk) as a function of the incident angle. The absorptivity reaches a maximum at a distinct angle of incidence which is referred as the Brewster angle. After exceeding this angle the absorptivity strongly diminishes with subsequent increased values of the inclination angle.

The fibre or disk laser (1.06 μm) has a maximum absorptivity at the Brewster angle of 79.6° while for CO_2 (10.6 μm) it is 87.3°. Theoretically at the angle of 85.9° the absorptivity is the same for both wavelengths.

In some published work [22-24], they used absorption as a function of glancing angle (complementary angle for incidence angle) as shown in Figure 2.11 which is consistent with Figure 2.10. Petring et al. [25] reported that thick plates benefit from a larger Brewster angle at the 10.6 μm wavelength of CO₂ lasers due to an increased absorptance in metal at glancing angle.

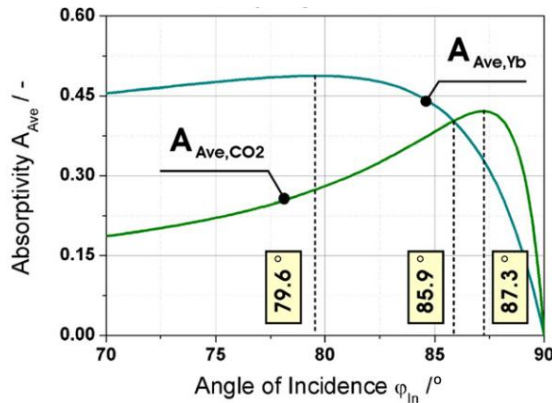


Figure 2.10- Absorptivity of unpolarised laser radiation from CO₂ (10.6 μm) and solid state (1.06 μm) of a molten iron surface as a function of incidence angle [21].

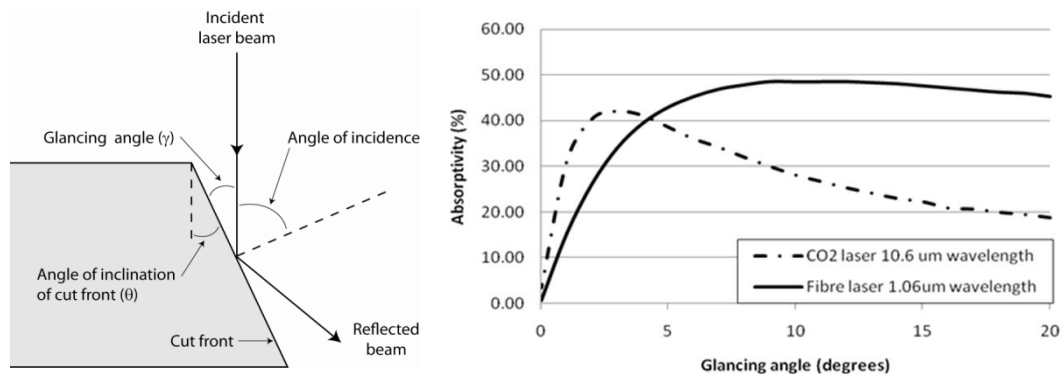


Figure 2.11- Left: Concept of glancing angle. Right: Absorptivity as a function of glancing angle [22].

Bergstrom et al. [16] investigated the absorptance of steels with respect to Nd:YAG laser light. They found that surface oxides, surface contamination, surface roughness and the presence of alloying elements can increase the laser absorption. In stainless steel samples, a trend of increasing absorptance could be seen for surface roughness values above 1.5 μm . For mild steel there was no clear roughness-absorptance correlation below the roughness value of 6 μm . Kaplan [23] found that ripples on the melt surface causes a complex absorptivity distribution during processes like welding, drilling or cutting when using fibre/disk lasers. He concluded that absorptivity for rather smooth melt surface remains quite steady; but for higher

roughness levels, a complex and nonlinear absorptivity modulation (in average 33%) happens across the surface which is proportionally lowered by the presence of local absorptivity as shadow domains. Fomin et al. [26, 27] restated that in CO₂ laser cutting of steel using oxygen, the absorbance coefficient in the cut zone increases with sheet thickness as shown in Figure 2.12. In contrast with CO₂, the absorptivity in fibre/disk lasers decreases for thicker material [21].

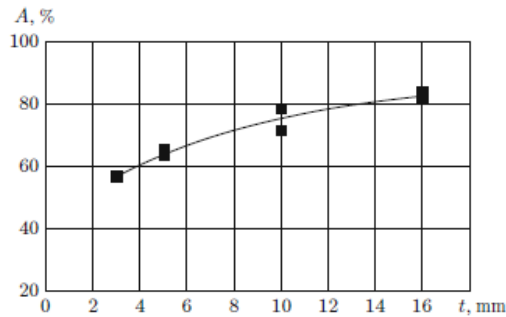


Figure 2.12- Absorptivity coefficient for CO₂ laser of steel using oxygen as a function of material thickness. Power was increased from 1000 W to 3000 W with increasing thickness [26].

2.2.4 Pulsed and Continues Wave (CW) modes

Both continuous and pulsed lasers can be used in laser cutting process. The cutting speed is specified by the average power intensity. The higher the average power is, the higher the cutting speed is. Hence, a high power CW laser is more suitable in laser cutting [1]. In laser cutting around sharp corners, due to the reduction of speed, the heat conduction increases resulting in inferior cut quality so pulsed lasers are more appropriate.

In contrast, the cutting speed of pulsed laser is lower than CW laser. A high power CW is useful for thicker material to achieve the high cut quality and high cutting speed. However, removing the molten material from a narrow kerf, in a thick sheet at a high average power laser, is much difficult; and the heat is being transferred to the cut front causing a severe heat affected zone (HAZ) and deterioration of the cut quality [28]. Lower energy pulsed lasers are suitable for fine cutting and piercing [2, 29].

2.2.5 Power

One of the main characteristics of the focused laser beam for heating and melting of the workpiece material, is power. Overall, laser machines are sized with maximum output power which refers to the maximum energy per second emitted from the laser system. A high brightness laser (disk/fibre) provides a high output power with a small beam diameter resulting in high power intensity. Hence, in comparison with CO₂ laser, the brightness characterises a given laser in terms of its usefulness as a tool in laser processing [2]. Ghany et al. [30] reported that in laser cutting of zinc-coated steel, Nd:YAG needs less power and attains higher speeds than CO₂ lasers. The benefits of using high power intensity in laser cutting are rapid heating and melting of the material, higher cutting speeds, higher absorptance (fast penetration) and good quality [2]. Xiao [31] compared fibre laser with CO₂ and found that almost with the same power, fibre cuts 3mm-thick mild steel faster than CO₂ laser.

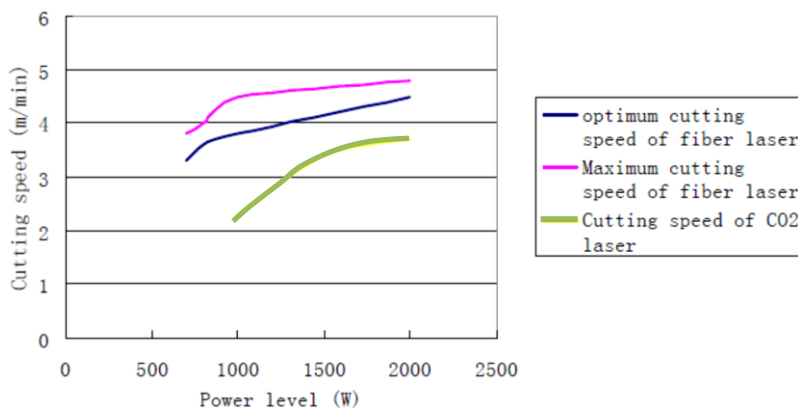


Figure 2.13- Comparison between CO₂ and fibre laser cutting of 3mm-thick mild steel and the effect of power on the cutting speed [31].

2.2.6 Power density

In laser cutting, disregarding the effect of gas type on the fusion, the ability of focused laser beam in melting of the material can basically be described with two terms of power and power density. According to definition, the density of a laser beam equals the power (P) divided by the area (A) over which the power is concentrated as shown in equation 2.4.

$$q_P = \frac{P}{A} \quad \{Wm^{-2}\} \quad 2.4$$

Power density can be changed by either power or beam diameter or both. If the beam diameter is changed by a factor of two, the power density will be changed by a factor of four. The high power density of focused laser beam causes the material to melt rapidly, so that little time is available for heat to spread through the cut front into the surrounding material. The high power density can produce high cutting rates and an excellent quality of cut [32].

2.2.7 Beam quality

There are two definitions of beam quality based on the divergence angle, usually applied: M^2 and BPP.

The M^2 is a definition of the beam quality which is usually used for comparison of lasers with different wavelengths. It corresponds to the quality of a particular laser beam relatively to a perfect beam, as the diffraction limit factor.

$$M^2 = \frac{\pi W_0 \theta}{4\lambda} \quad 2.5$$

Where W_0 is the focused beam diameter (mm), λ is the wavelength (μm) and θ is the divergence angle ($^\circ$). According to equation 2.5, a laser with $M^2=1.2$ will provide a beam diameter 20% larger than a perfect laser beam with $M^2=1$ [2].

When the beam quality is evaluated by BPP (Beam Parameter Product), the focus ability of a particular beam is considered. The lowest amount of BPP ($\frac{\lambda}{\pi}$) is obtained with a diffraction-limited Gaussian beam (TEM_{00}). However, a real laser beam has larger BPP as described by equation 2.6. Figure 2.14 illustrates the focused laser beam geometry.

$$BPP = \theta_0 W_0 = \frac{\lambda}{\pi} M^2 \quad \{mm.mrad\} \quad 2.6$$

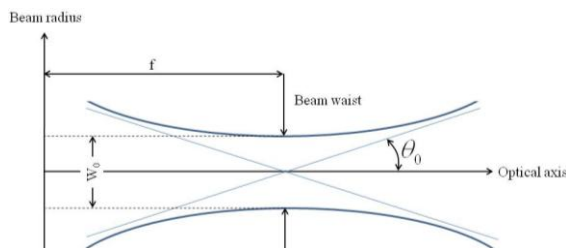


Figure 2.14- Focused laser beam geometry[31].

M^2 shows how much the BPP of the real laser is larger than the BPP of an ideal Gaussian beam. For a Gaussian mode (ideal beam) $M^2 = 1$. Knowing M^2 , many laser beam characteristics can be calculated such as the beam diameter, wave front radius, Rayleigh radius, depth of focus and focused spot size [33]. The effect of M^2 on the beam diameter is illustrated by Figure 2.15.

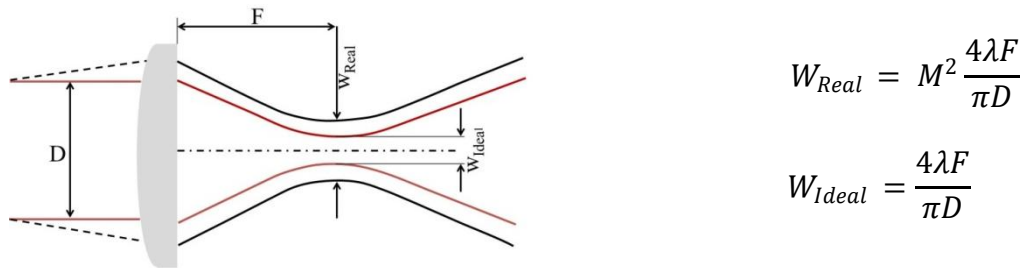


Figure 2.15- Geometrical definition of M^2 and its effect on the beam diameter. The equations have been derived from equation 2.5.

O'Neill demonstrated a practical meaning of the BPP as shown in Figure 2.16 [34]. The lower the BPP of a particular laser the greater the depth of focus. The higher the beam quality (smaller spot size), the lower the value of BPP. Hogle [35] mentioned that in order to evaluate the laser's quality with different wavelength (fibres and diodes), BPP is used; whereas M^2 is more used for lasers with the same wavelength.

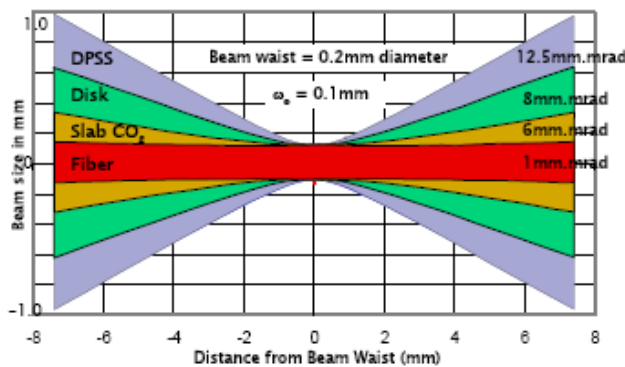


Figure 2.16-Effect of beam parameter product on the focused beam profile [34].

A comparison between CO_2 and disk lasers indicated that the intensity distribution is different for two lasers because the M^2 of these types of laser sources is different. Typical values of beam propagation output parameters measured at 3 kW after the laser beam has passed through the cutting head are shown in Table 2.2 [36, 37].

Table 2.2- - Showing the characteristics of CO_2 and Disk laser beam utilized in [36, 37].

Laser source	Cutting head	M^2	Focus radius	Rayleigh length
CO_2	Precitec HP 1.5"	1.36	76.123 μm	1.27 μm
Disk	High YAG BIMO FSC	14.30	76.171 μm	1.20 μm

As it is seen in Figure 2.17, the intensity profile of the CO₂ laser approximately was a Gaussian distribution. The maximum power intensity of CO₂ was 42.99 MW/cm², about 175% of the one measured for disk laser valued as 24.67 MW/cm² [36, 37].

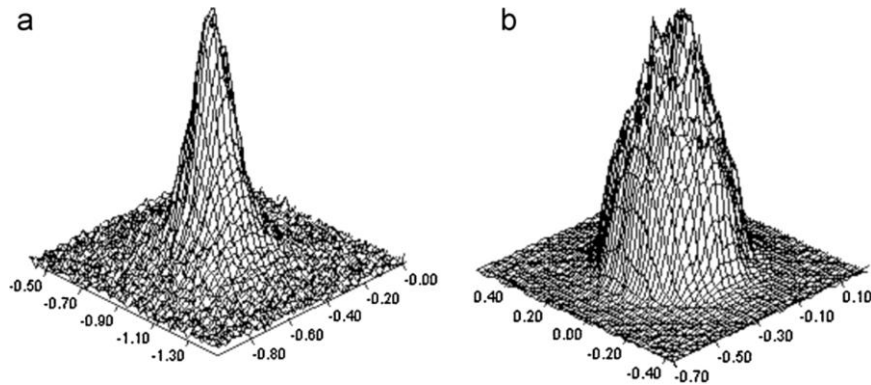


Figure 2.17- Measured intensity distribution for (a) CO₂ and (b) disk laser beam [36, 37].

The relationship between beam diameter and power density with BPP is indicated in Figure 2.18. With using the same optical set-up, an increase in the BPP by a factor of two results in an increase in the beam diameter by a factor of two. This corresponds to a reduction of power density by factor four. Hence, lasers with a lower BPP can be operated at lower powers to achieve the same power density [11].

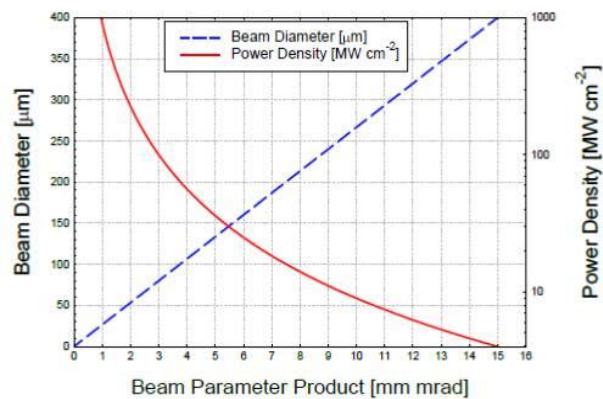


Figure 2.18- Effect of beam parameter product (BPP) on beam diameter and power density [11].

2.3 Fibre lasers

Industrial users of laser technology have demanded laser systems with higher powers. Applications such as cutting, welding, piercing and drilling could be enhanced by the development of more powerful lasers with high beam quality, efficiency and stability. Several solid state laser structures have been developed such as rod, disk and fibre as shown in Figure 2.19. Fibre/disk lasers are designed to

minimise thermal distortion and provide light brightness beam. Both fibre/disk lasers have a $1.06\mu\text{m}$ wavelength [38].

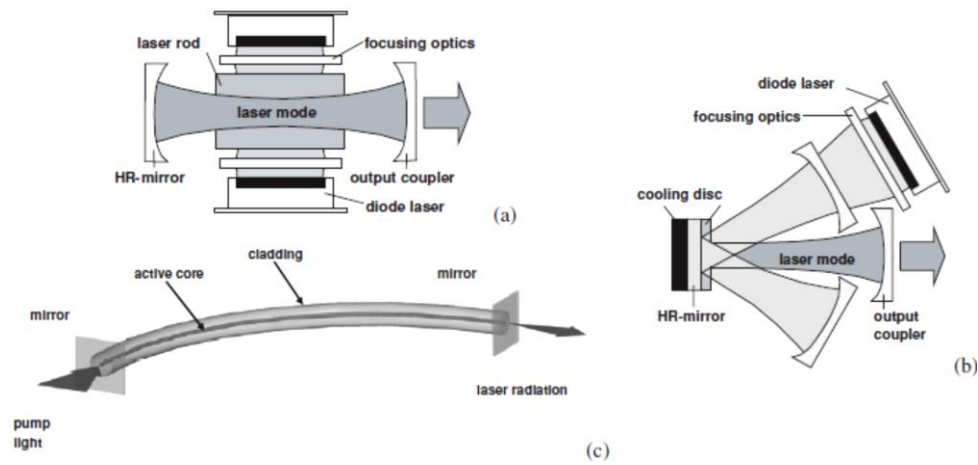


Figure 2.19- Schematic showing the solid state laser designs. (a) Side pumped rod laser, (b) thin disc laser and (c) fibre laser [38].

Likewise several kinds of fibre laser systems in terms of laser source have been developed: single emitter, modular and high power fibre lasers. Regarding optical fibres, single-clad and double-clad fibres have been used.

2.3.1 Fibre laser systems

A single emitter fibre laser, is established using an Ytterbium fibre laser system and has a wavelength from $1.06\ \mu\text{m}$ to $1.08\ \mu\text{m}$, with power output up to 3 kW available by IPG laser company [39]. A single mode fibre has been reported to deliver a laser beam from a typical flash pumped Nd:YAG system for precision machining at peak power of 225 W [40].

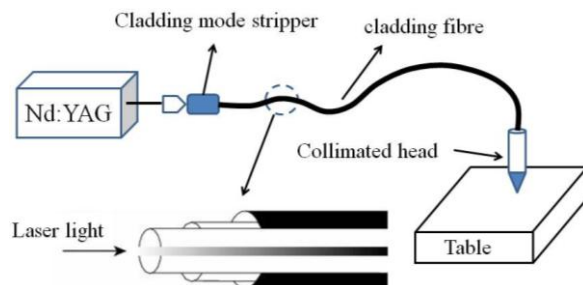


Figure 2.20 - Schematic showing a single emitter fibre laser machine.

In modular fibre lasers, fibre lasers deliver their energy through an integrated flexible optical fibre that can be up to 200 meters long. Each module yields some part of the total power, and a beam combiner combines the outputs of the modules

(Figure 2.21). In contrast with single emitter lasers, the output fibres from the modular can be single or multiple. IPG photonics has developed the modular system up to 10 kW output power [41, 42]. For example the fibre laser cutting machine, which is used in this research, had five modules of 500 W and the maximum output power is 2000 W, with one module reserved as a backup.

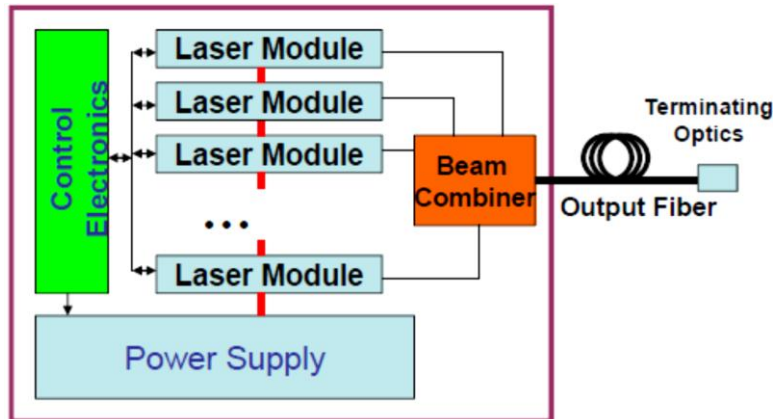


Figure 2.21- Multi mode (modular) fibre laser structure [42].

In contrast, in high power fibre laser systems a double cladding doped fibre (active fibre) and two groups of multimode high power laser diodes are used (Figure 2.22). Two groups of multimode pump diodes are coupled on the both side of an active fibre. A coil of the active fibre with two Bragg gratings form the laser medium. The Bragg gratings reflect particular wavelength of laser and transmit others. [31, 43].

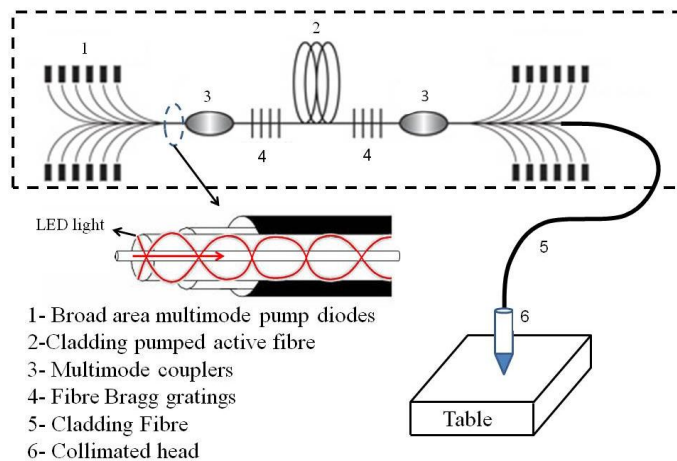


Figure 2.22- Schematic structure of multimode fibre laser beam.

A brief comparison between high power commercial lasers is given in Table 2.3.

Table 2.3- Comparison between high power commercial lasers [44].

Laser Characteristics	CO2	Lamp pumped Nd:YAG	diode- pumped Nd:YAG	Yb-Fibre (multi-mode)	Thin disc Yb-YAG
Lasing medium	Gas mixture	Crystalline rode	Crystalline rode	Doped fibre	Crystalline disc
Wavelength (nm)	10,600	1060	1060	1070	1030
Beam transmission	Mirror lens	Fibre, lens	Fibre, lens	Fibre ,lens	Fibre ,lens
Typical delivery fibre Ø (mm)	-	0.6	0.4	0.1-0.2	0.15-0.2
Output power ^a (kW)	Up to 15	Up to 4	Up to 6	Up to 20	Up to 4
Typical beam quality ^b (mm. mrd)	3.7	25	12	20	7
	3.7	12	<12	1.8	4
Maintenance interval (1000 hours)	2	0.8-1.0	2-5	100 ^c	2.5
Power efficiency (%)	5-8	3-5	10-20	20-30	10-20
Approximate cost per kw, (k\$)	60	130-150	150-180	130-150	130-150
Foot print of the laser source	Large	Medium	Medium	Small	Medium
Laser mobility	low	low	low	high	low

Notes:
a) Commercially available.
b) The top figures are for the max. Available output powers, the bottom figures for the same type of laser but configured for optimum operation at 1kW.
c) Manufacturer's claim.

2.3.2 Fibre laser benefits

The main advantage of the fibre laser is that the quality of the beam is high (low BPP) and has a lower sensitivity against laser-induced plasma [45]. Low BPP results in high brightness, long depth of focus and long working distance when long focal length optics is used [34]. Other benefits can be identified as [42, 46, 47]:

- High power output
- Low cost
- Flexibility in beam delivery
- Acceptable life time
- Multi-output potential
- Beam shaping potential
- Multipurpose machine potential

2.4 Laser Cutting process

In fibre laser cutting of metals, the focused laser beam on the surface of a workpiece makes a melting zone and, at the same time, a gas flow from the nozzle has an effective pressure area on the surface and removes the molten material from the cutting zone through the bottom of the kerf (Figure 2.23). Thus, when the laser beam or workpiece moves at a specified velocity, cutting happens.

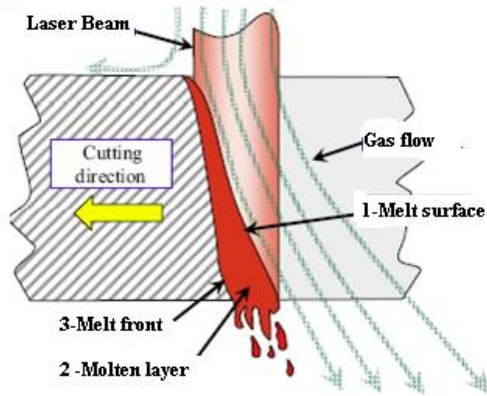


Figure 2.23- Definition of laser cutting [48].

2.4.1 Kerf width

The kerf is narrow cut groove that is produced during thorough cutting [2]. The width of kerf is the distance between the two kerf walls. In this case there are two kerf widths: upper and lower kerf width which are measured on the top and bottom surface of the sheet respectively.

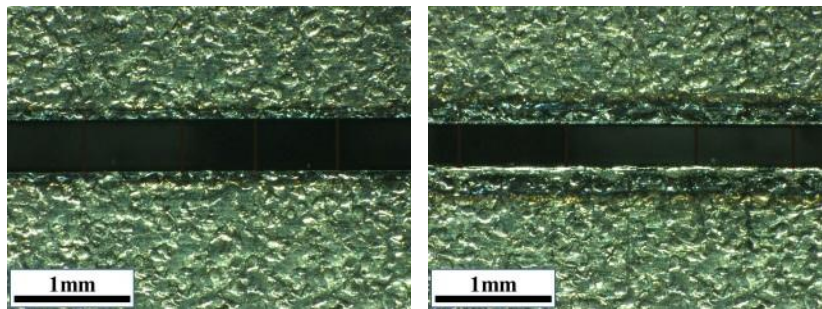


Figure 2.24- Showing typical kerf. Left: upper kerf, Right: lower kerf (focused beam diameter of 0.2 mm on the top surface, 1000 W, 6000 mm/min, 2 bar oxygen, 1.6 mm thick mild steel).

The volume of kerf across the cut represents the volume of removed material. The kerf width depends on the focused spot size, laser power, cutting speed, assist gas and pressure and, to some extent, the laser wavelength [2, 6]. A combination of laser cutting parameters will produce a uniform narrow kerf width. Uslan [49] reported that in CO₂ laser cutting, the kerf width significantly increases with increasing power but decreases with increasing cutting speed. Steen [50] explained that, overall, the upper and lower kerf width decreases with cutting speed and the upper kerf width is smaller than lower kerf width at low cutting speed range (see Figure 2.25).

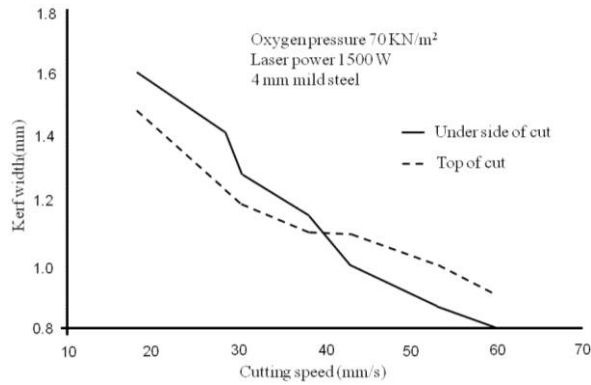


Figure 2.25- Kerf width versus cutting speed in CO₂ laser cutting [50].

Several published research reported that the kerf width in laser-oxygen cutting of mild steel is narrower than laser-nitrogen cutting [30, 51]. The main reason is that oxygen, as an active gas, reacts with the melt and releases additional energy to the melting zone, increasing the kerf width.

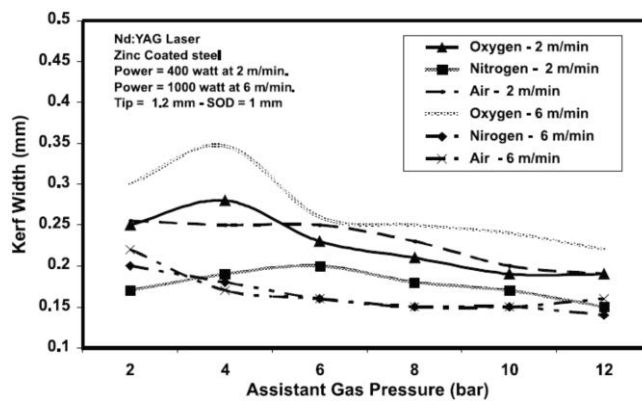


Figure 2.26- The effect of assistant gas type and pressure on the kerf width [30].

A comparison between CO₂ (10.06 μm) and fibre laser cutting (1.06 μm) of mild steel with using oxygen as an assist gas indicated that the kerf width in fibre laser cutting is wider than CO₂ laser cutting. The difference in wavelength and the waveguiding effect of the oxidised melt (Fe + FeO), for fibre laser has been concluded as one of the possible reasons [52].

2.4.2 Cut front geometry

During laser cutting, laser beam irradiates the surface of the cut front and melts the material. Simultaneously, the melted material flows on the cut front downward the cut zone. It has been confirmed that the cut front inclines and kinks during laser cutting [22, 37, 53-61].

By following Steen's arguments [50] that the beam is coupled to the plate more efficiently by less being lost through the cut kerf as the cutting speed is increased, Mahrle and Beyer [59, 60] used a model of the cut front at which the whole beam interacts with the inclined cut front as schematically shown in Figure 2.27. They calculated the cut front angle (inclination angle φ_{in}) as a function of top and bottom beam radii (r_T and r_B) and the sheet thickness (t_C).

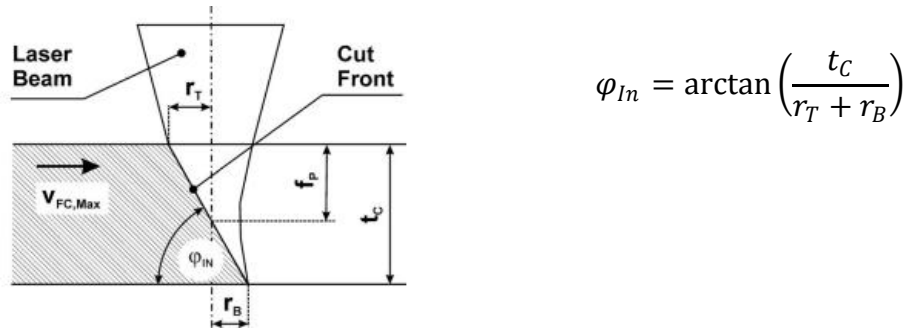


Figure 2.27- Cut front inclination as a function of beam geometry and sheet thickness [59].

Powell et al. [22] theoretically and experimentally indicated that the cut front inclination is reflected to the cut edge; hence, from the angle of striation on the cut edge, they could estimate the cut front inclination. The striation showed that the cut front inclined with increasing cutting speed as illustrated schematically in Figure 2.28. They also found that in very high cutting speed the lower part of cut front is irradiated by the reflected beam.

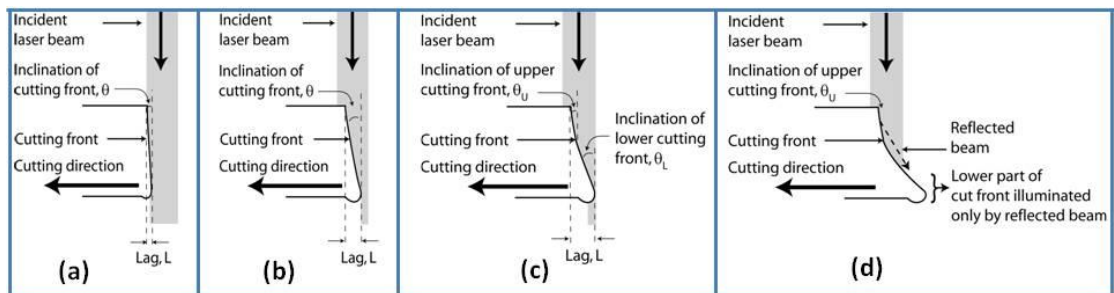


Figure 2.28- Cut front-laser beam interaction geometries at; (a) slow cutting speeds, (the cut front is and almost vertical, straight line of fluctuating position), (b) moderate cutting speeds (the cut front is straight line inclined at θ), (c) higher cutting speeds (the cut front can be approximated to upper and lower lines inclined θ_U and θ_L), and (d) very high cutting speeds (the cut front becomes extended in the direction of cutting and the reflected beam interacts more with the lower part of cut front) [22].

They also found that striation free can be obtained on the cut edge in fibre laser-oxygen cutting of thin sheet at the specific range of cutting speed. They explained that at beyond this range the roughness increases. They theoretically and

experimentally showed that in the case of striation free cut, the fine striation inclination is between 8° to 14° and the cut front inclination is 10.4° , which both are related to the Brewster angle and optimum fibre laser absorption. They also stated that there is correlation between low roughness and cut front inclination [22].

Hirano and Fabbro in an experimental observation of the hydrodynamics of melt layer and striation generation, during disk ($1.06 \mu\text{m}$) laser cutting of steel using nitrogen, found that the melt flows in the regions of kerf sides, and the kerf front exhibits instability in different velocity range [53]. They used a high speed video camera to record the changes of melt layer, striation and cut front inclination with cutting velocity. The images of typical examples were recorded as shown in Figure 2.29 and Figure 2.30. As can be seen in both figures from a-c, when the cutting speed is increased the central melt flow and side region become more stable. Moreover, the cut front inclination increases with cutting speed.

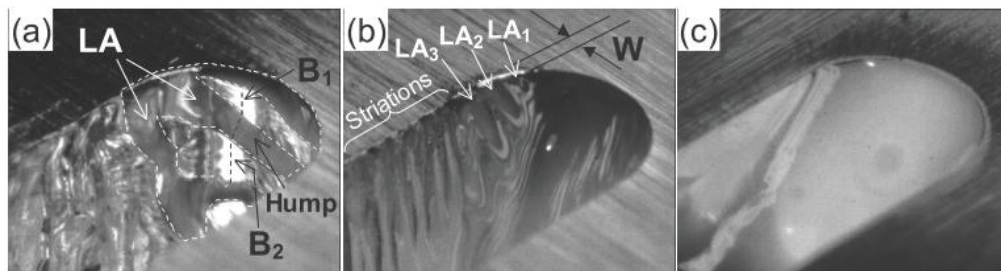


Figure 2.29- Observation result for different cutting velocities V . (a) $V=1$ m/min, (b) $V=3$ m/min, and (c) $V=6$ m/min [53].

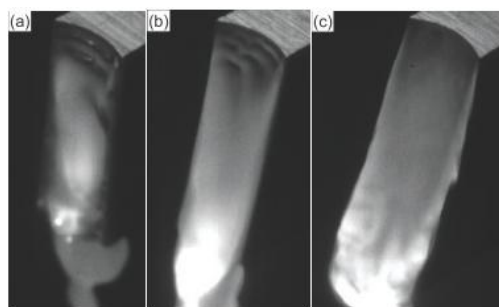


Figure 2.30- Observation results of 2D melting experiments for different velocities V . (a) $V=1$ m/min, (b) $V=2$ m/min, and (c) $V=3$ m/min [53].

Scintilla et al. [37, 61] investigated experimentally the cut front geometry in the cutting of steel with disk ($1.06 \mu\text{m}$) and CO_2 lasers ($10.6 \mu\text{m}$) using nitrogen. They found that the inclination of the cut front changes with increasing cutting speed in order to satisfy the higher energy requirement. The lower part of the cut front became curved or kinked, and extended in the cutting direction (Figure 2.31). It was reported

that the cut front, where it starts to curve, is inclined to angles close to the Brewster angle.

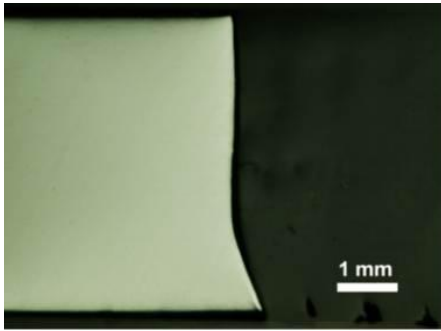


Figure 2.31- Lower part of cut front become curved (CO₂ laser, V_{max}=1.2 m/min, 5mm thickness, focal point at 33% of thickness below the upper surface) [62].

They reported that in laser cutting of a steel sheet with thickness of 5 mm when the focal position is located at 33% of thickness below the upper surface, for both laser source, with an increase in cutting velocity from 0.33 V_{max} to V_{max}, the slope of cut front slowly becomes flatter and close to 90°; however, the inclined angle of the cut front at the lower position decreases rapidly as shown in Figure 2.31. In this case, they found that the effect of focal position on the cut front geometry is not important.

On the contrary, they realised that in a thicker plate (8 mm) the focal position has greater effect on the laser fusion cutting front geometry. In thicker plate and focal position of 33% of thickness, the cut front geometry behaviour is similar to 5mm thick sheet. However, as the focal position is located at 66% of the thickness below the upper surface, for both laser sources, the cut front geometry variation has an irregular trend. They stated that this behaviour could be related to the melt flow condition and not exclusively from the laser material interaction. A comparison between CO₂ and disk showed similar cut front geometry (Figure 2.33). They stated that due to the realised similar cut front geometries of applied CO₂ and disk laser beam, the assumption of similar thermal conditions on the cut front surface for both source is acceptable.

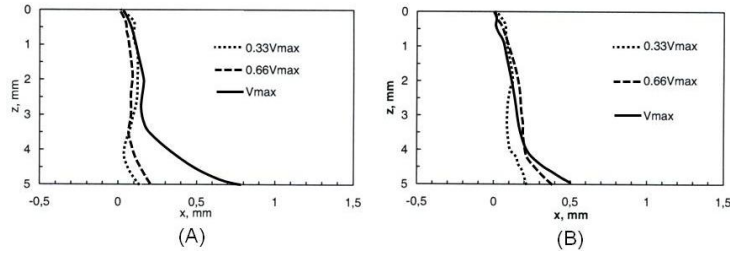


Figure 2.32- Cut front inclination as a function of cutting speed and laser source is shown for thickness of 5mm and focal position of -1.65mm. A) CO₂, B) Disk laser [37].

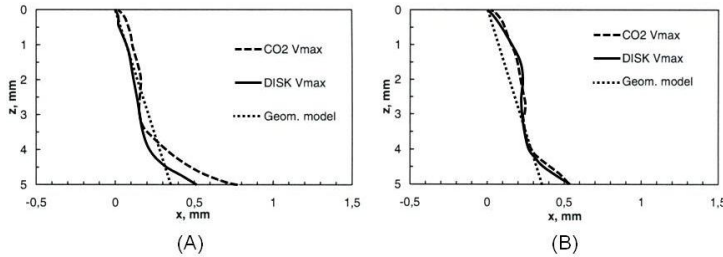


Figure 2.33- Comparison of cut front inclination between the experimental profile obtained at maximum cutting velocity and theoretical calculation as a function of focal position when thickness is 5mm. A) Focal position of -1.65mm, B) Focal position of -3.3mm [37].

2.4.3 Beam behaviour inside the cut zone

In the published research, there is an ongoing debate about the behaviour of the 1.06 μm laser beam (fibre/disk) in comparison with 10.6 μm laser (CO₂).

O'Neill et al. [6, 63] reported that due to the differences in absorption between the two wavelengths (1.06 μm and 10.6 μm), the beam with wavelength of 1.06 μm has a greater absorption than 10.6 μm laser beam. The beam with a wavelength of 1.06 μm has a better spread inside the cutting zone due to a greater waveguiding through multiple reflection effect and thereby a greater proportion of the laser power is absorbed down the cut zone.

Scintilla et al. [61] by an investigation on CO₂ and disk laser cutting has concluded that the energy absorbed by the cut front from CO₂ laser is used to increase the melt temperature causing a melt with lower viscosity. In contrast, when cutting with a disk laser, the absorbed energy is consumed to melt a larger volume of material with a lower average temperature and low viscosity. Scintilla in another research [37, 64] reported that due to multiple reflections of the CO₂ laser beam within the cut zone, the lower part of the cut front significantly interact with reflected beam.

Wandera et al. [51] reported that when cutting a thick section metal, due to multiple reflections of the incident laser beam in the cut zone, and thus increased absorption of the laser beam at lower part of cut zone, an increased erosion can be observed on the lower part of the kerf walls.

Said [52] compared CO₂ and fibre lasers in terms of kerf width when laser-oxygen cutting thin sectioned mild steel sheets. It was reported that the kerf width for fibre laser was larger than for CO₂ laser. Waveguiding effect of fibre laser in the melting zone (Fe + FeO) was concluded as one of the possible reasons for larger kerf width.

Petring et al. [58] simulated the cutting front by means of CALCut software. Using the simulation of cutting front, taking multiple reflections into account and referring to the results of other authors, they could explain some laser cutting phenomena such as wavelength influence on laser-material interaction, wavelength effect on energy redistribution within the kerf, the effect of wavelength on kerf width and why the bottom of the cut surface is rougher than the top (Figure 2.34).

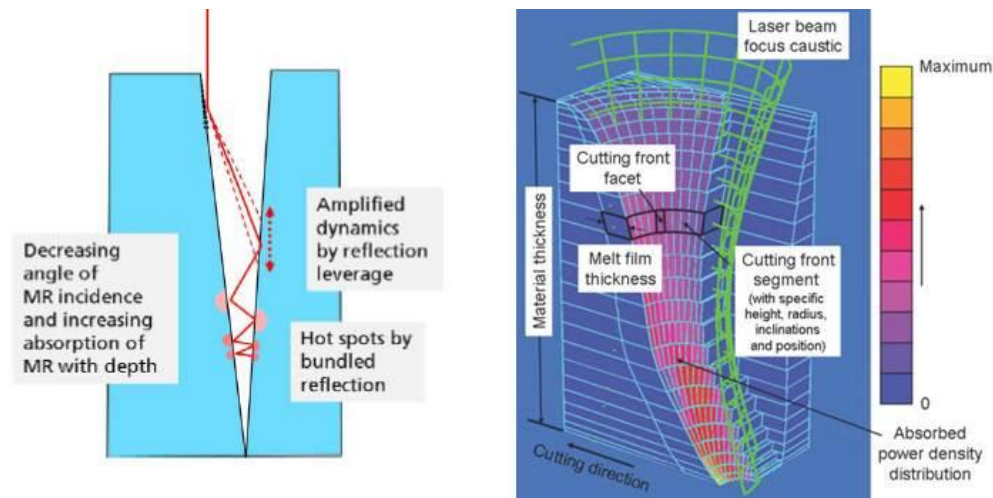


Figure 2.34- Laser cutting simulation of the cutting front with CALCut [58].

2.4.4 Depth of cut

Depth of cut in laser cutting refers to the maximum sheet thickness that can be cut with using an employed laser cutting condition. In commercial laser cutting, maximum depths of cut around 12-15 mm in mild steel with 2 kW lasers are achievable [4]. In an experimental research, a 4mm-thick aluminium was cut using 5 kW fibre laser and maximum cutting speed of 10.2 m/min. In this case, it means

that 4 mm-thick aluminium is a maximum depth of cut for laser cutting condition of 5 kW and 10.2 m/min. With the same power, a stainless steel sheet with 10mm thickness was cut at maximum cutting speed of 1.5 m/min. High pressure nitrogen was used as the assist gas [65].

It has been reported that fibre laser with 4 kW and cutting speed of about 1.2 m/min cut 20 mm-thick mild steel, while CO₂ laser cut the same thickness with 5 kW and cutting speed of about 0.7 m/min. This comparison indicates that fibre laser would be more efficient than CO₂ laser. However there was a difficulty when attempting to cut thicker mild steel plate with fibre laser and kerf width was considerably larger than CO₂ [6].

O'Neill et al. [4], from a study on the Lasox (laser-oxygen) cutting process, reported that mild steel sheets with thickness up to 50 mm can be cut, in the first instance, with power levels less than 2 kW, gas pressure of 8 bar, and 3 mm stand-off distance whilst maintaining excellent cut quality.

Ermolaev et al. [66] reported that with using specific hybrid laser-assisted oxygen cutting with assistance of CO₂ laser, they could cut mild steel sheets with thickness of 30 mm (16 bar oxygen, 1.2-2.5 kW power and a supersonic nozzle); and they concluded that it can be developed to 50 mm.

2.4.5 Cut edge quality

The characteristics of cut edge can be categorised as dross attachment, striation pattern and perpendicularity. Different combination of laser cutting parameters such as power, cutting speed, gas type and pressure will change the features of cut edge for a specified laser source, optic system and workpiece [1, 2, 45].

2.4.5.1 Dross attachment

At the lower cut edge dross can be observed. It is a part of melt that has not been completely removed from the lower cut zone by pressure of assist gas and then resolidifies and remains at the lower cut edge [2]. The formation of dross is closely related to the melt properties and geometrical shape of lower cutting front.[67]. Overall, melt with high viscosity and high surface tension is difficult to remove from

the cutting zone by assist gas resulting dross attachment. Low gas pressure also increases the possibility of adherent dross. Wandera [45] reported a dross attachment on the lower cut edge of 10 mm stainless steel when cutting with 4 kW Ytterbium fibre laser, 16 bar nitrogen, 1.0 m/min cutting speed, 254 mm focal length and focal point position at the middle of thickness. It was also reported that the volume of adherent dross when laser cutting 15 mm mild steel with 3 kW and 1 bar oxygen, increases with increasing cutting speed [45]. In fibre laser cutting of thin section mild steel sheet using 2 bar oxygen pressure and 1 kW power, there was not any dross attachment [52].

2.4.5.2 Cut edge surface roughness

Overall, on the cut edge a series of irregular/regular striation can be observed as shown in Figure 2.35.

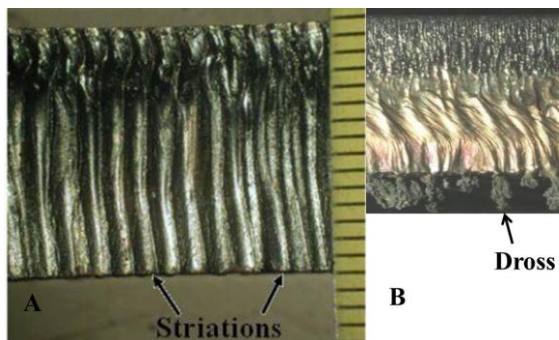


Figure 2.35- Striation pattern, A) 15mm mild steel, 4 kW power, 18 bar oxygen, 0.8 m/min cutting speed, 190.5 mm focal length, focal position 4 mm above top surface. B) 10 mm stainless steel, 4 kW power, 4bar nitrogen, 1.0 m/min cutting speed, 190.5 mm focal length, focal position 8 mm below the top surface [45].

The features of the cut surface are affected by the dynamical behaviour of the laser cutting process. The shape of the cutting front and melt flow mechanism affect the formation of striations on the cut surface [22, 67]. Wandera et al. [65] reported that a smooth cut surface ($R_z = 40 \mu\text{m}$) with a regular striation pattern on 10 mm stainless steel was achieved using 4 kW power, 1 m/min cutting speed and 20 bar nitrogen pressure while when the gas pressure decreased to 4 bar the roughness (R_z) increased to $120 \mu\text{m}$. Overall for stainless steel the cut edge was rough and drossy when cutting with lower speeds; but a cleaner cut edge was obtained with higher speeds about 20-33% below maximum cutting speed. For aluminium the overall cut surface showed a regular striation pattern but was drossy as if with using lower cutting speed the striation were more spaced but at higher speeds it was finer. They also found that

focal point position influenced the cut surface. As the thickness of the sheet decreased (e.g. 2 mm) the striation became clear and regular from top to the bottom of the cut surface [1]. In fibre laser cutting of thin section mild steel, using 2 bar oxygen, power range of 1 to 2 kW and cutting speed range of 2000-7000 mm/min, a maximum roughness of $R_a = 3 \mu\text{m}$ at lower speed has been reported. An explanation of striation free has been also reported when using a specific combination of laser cutting parameters (i.e. 2 mm-thick, 5500 mm/min, 1000 W) [22]. The surface roughness for the upper part of cut edge is less than that for lower part [45, 52].

According to SFS-EN ISO 9013:2002 [68], the surface roughness of R_z (mean height of the profile) has four levels of classification providing the standard for surface roughness of the thermal cut edge as shown in Figure 2.36. Level 1 represents the lowest R_z which gives the best cut edge surface quality (smoother surface). Further detail for R_z is given in page 81.

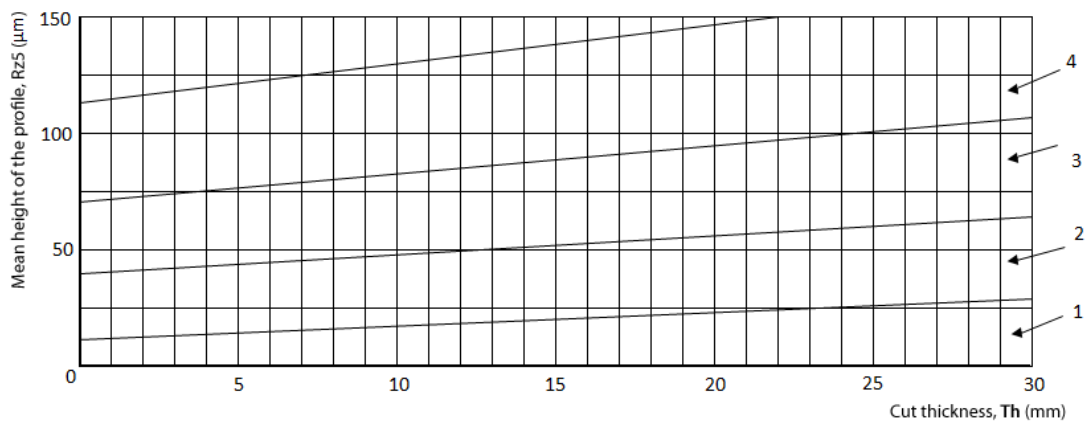


Figure 2.36- Mean height of the profile (R_z) as a function of cut thickness [68].

2.4.5.3 Cut edge perpendicularity

In laser cutting the, depending on the cutting conditions, the lower kerf width is different from the upper kerf width (§ 2.4.1) [50]. This causes that the cut edge is not perfectly perpendicular as shown in Figure 2.37. The deviation of the cut edge perpendicularity, u , is the biggest perpendicular distance between the actual cut edge and the intended surface. According to SFS-EN ISO 9013:2002 [68], the standard for perpendicularity tolerance has five levels and the smallest tolerance is presented by level 1 (Figure 2.38).

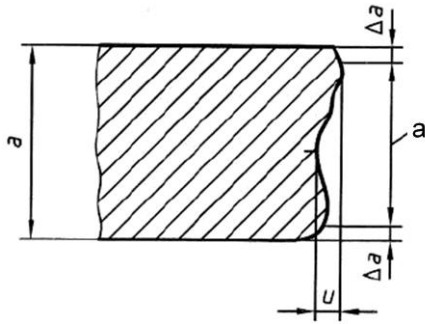


Figure 2.37- Deviation of perpendicularity (u) of a vertical cut; a is the workpiece thickness and Δa is the thickness reduction for determination of perpendicularity tolerance [68].

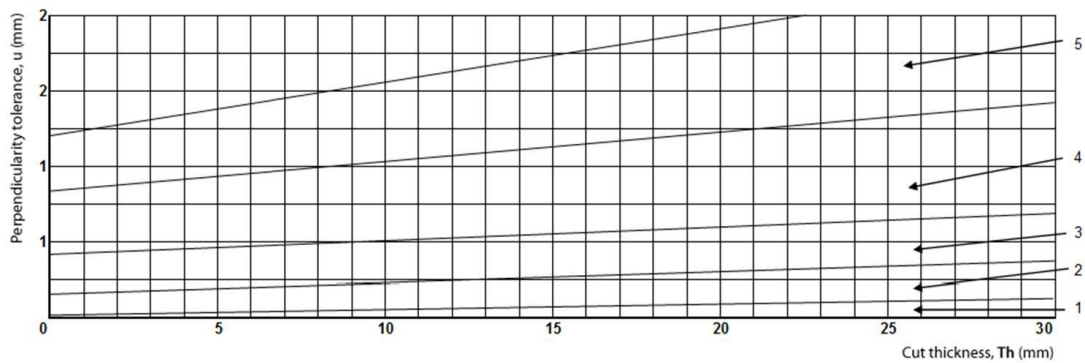


Figure 2.38- Perpendicularity tolerance (u) as a function of cut thickness [68].

2.4.6 Energy losses

In laser cutting not all incident laser power is absorbed by workpiece and always there are some laser energy losses. During laser cutting when the laser beam exposes the upper surface of workpiece, most penetrates into the workpiece through the cut kerf (or hole) while some is reflected from the unmelted surface. The primary energy losses through the cut kerf comprise of [69]:

- 1) Directly transmitted laser power
- 2) Internally and externally reflected laser beam

Evaluation of primary energy losses during cutting is of utmost significance for energy balance considerations in laser cutting. The absorption value of laser power by workpiece is dependent on the laser beam intensity distribution, the Fresnel absorption coefficient and the incidence angle of laser beam [64].

One of the well-known techniques to experimentally evaluate the transmitted and reflected energy losses during laser cutting is by collecting them within PMMA (poly methyl meth acrylate) blocks placed under the sheet being cut [1] as shown in

Figure 2.39. Experimental studies revealed that in the case of disk/fibre laser cutting, the values of primary energy losses are lower than those in the CO₂ laser cutting with respect to the same values of relative cutting speed [36].

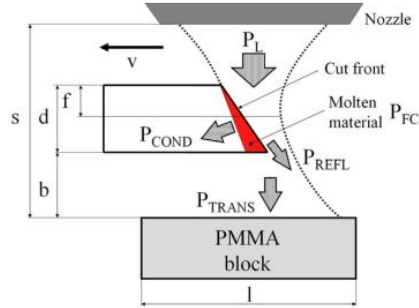


Figure 2.39- Schematic diagram of the power contributions and energy losses collecting [36].

The power balance can be written in its general form as follows:

$$P_L = P_{FC} + P_{Loss1} + P_{Loss2} \quad 2.7$$

P_L is the overall incoming laser power which is supplied to the cutting zone. P_{FC} is the power consumed by cutting process itself. P_{Loss1} and P_{Loss2} represent primary and secondary power losses respectively. The P_{FC} is the summation of three energies that is expressed as follows [70]:

$$P_{FC} = P_{TP} + P_m + P_v \quad 2.8$$

P_{TP} is the energy that is required to heat the volume of material in cutting zone. P_m is the energy that is needed to melt the volume of cutting zone material and eventually P_v is the energy consumed in vaporization of molten material. P_{Loss1} (primary energy losses) has been described as follows [64, 69, 71] :

$$P_{Loss1} = P_{TRANS} + P_{REFLE} \quad 2.9$$

$$P_{Loss2} = P_{COND} + P_{CONV} + P_{RAD} \quad 2.10$$

P_{TRANS} is that part of incoming energy to the cutting zone which directly leaves the cut zone through the bottom of kerf (hole) with no effective interaction with cut front. P_{REFLE} is the energy which is reflected internally and externally by cut front surface. Secondary energy losses (P_{Loss2}) are those energies which leave the cut front by thermal transformation mechanisms such as conduction, radiation and convection. The portion of conduction in secondary energy losses is higher than radiation and

convection [64]. Scintilla et al. [71] in an investigation on the power balance equation in laser cutting using disk (1.06 μm) and CO₂ (10.6 μm) laser, found that the maximum cutting speeds for disk laser were three times higher when cutting 1 mm-thick sheet in comparison with CO₂. However for 5 mm and 8 mm thick sheets, cutting speeds were of comparable order. Lower process temperatures were found for disk laser cuts increasing the melt viscosity. Therefore melt ejection was difficult and subsequently a worse cut quality was left behind when cutting with disk. They eventually concluded that plasma formation should be considered in the overall power balance and power loss.

2.5 Laser cutting machine parameters

2.5.1 Cutting head parameters

The cutting head delivers both laser beam and assist gas to the cutting zone; so it includes two main systems: optical and gas delivering systems. The laser beam leaves the fibre at a specified angle and it is then collimated by a collimation unit and subsequently focused on the surface of sheet using a focusing lens. Assist gas is connected from the piping system to the cutting head using gas connections. It is then led through a cone and nozzle to the cutting zone. (Figure 2.40).



Figure 2.40- YK52 cutting head components as used in this research [72].

2.5.1.1 Focusing the laser beam

The diameter of the focal point (focused beam diameter), W_0 , can directly affect the kerf width [10]. Meng et al. [73] reported that in laser cutting of 0.11 mm-thick stainless steel plate, using a fibre beam with focused spot size of 0.012 mm and power of 9 W, the kerf width was 0.026 mm. Wandera et al. [51] obtained a kerf

width of 1 mm when a fibre laser with focused spot size of 0.3 mm and power of 5 kW was used to cut stainless steel. The smallest focused beam diameter on the sheet surface is when the focal point is positioned on the sheet surface. In case of out of focus conditions, the diameter of beam projected on the surface becomes larger. The smallest beam diameter that can be obtained with a particular laser system is dependent on the optical set-up and the BPP of a laser beam. This is given by equation 2.11 [2].

$$W_0 = \frac{4F_{foc}}{D} \cdot BPP \quad 2.11$$

And equation 2.12 [35].

$$W_0 = \frac{4\lambda F_{foc}}{\pi D} \cdot M^2 \quad 2.12$$

Where the F_{foc} is focal length and D is raw beam diameter on the focusing lens (Figure 2.42). Since the kerf width is correlated with the focused beam size at the surface of the plate, and also the focused beam size on the surface is proportional to the focal position, then the kerf width is related to the focal position as shown in Figure 2.41.

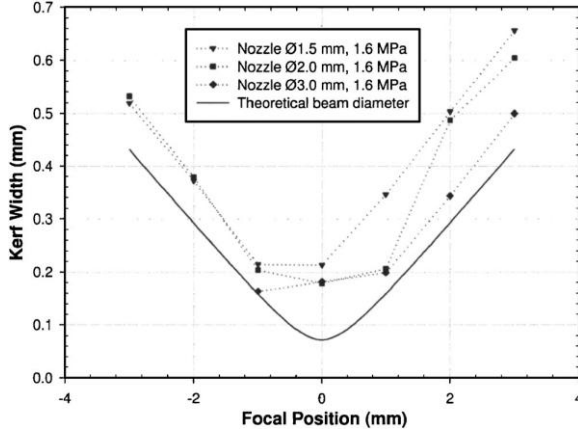


Figure 2.41- Kerf widths for varying focal positions compared to the theoretical laser beam diameter (2.2kW, fibre laser, 6mm thick stainless steel, nitrogen) [10].

The magnification of an optical system as the key parameter for describing the optical system, usually results from focusing and collimation focal lengths as given by equation 2.13 [74]:

$$Mag = \frac{F_{foc}}{F_{col}} \quad 2.13$$

In theory the focused beam diameter can be defined as a product of magnification and fibre diameter by equation 2.14:

$$W_0 = \frac{F_{foc}}{F_{col}} \cdot D_f \quad 2.14$$

The Rayleigh length is the measure of the depth of focus; it can be defined as a distance from the focal point to a point where the cross sectional area of the beam is twice that at the focal point (Figure 2.42).

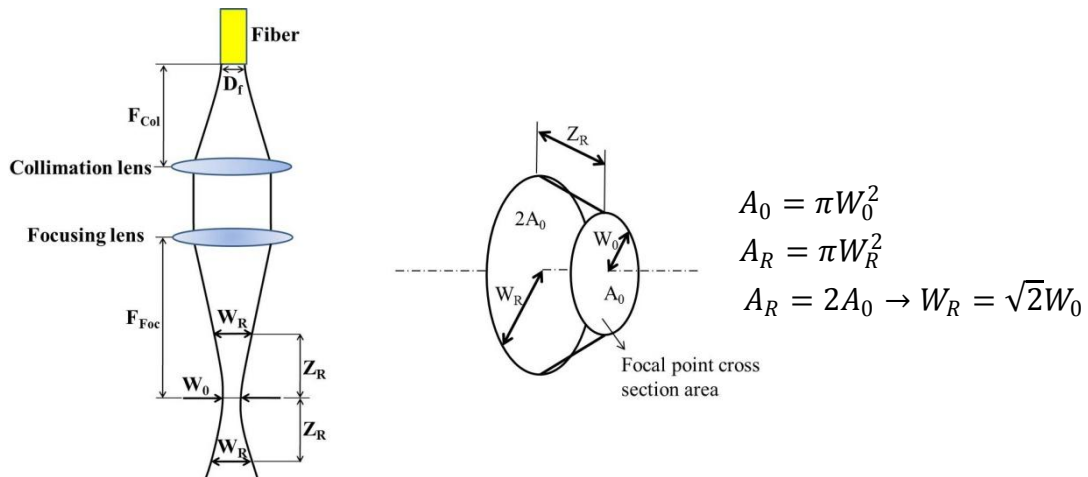


Figure 2.42- Showing a geometrical definition of focusing system. Left: focusing of laser beam. Right: geometrical definition of Rayleigh length.

As the laser beam goes through the optical system, it is absorbed in the focussing lens. This causes the optical element's temperature to increase just 3-10 degrees Kelvin. The refractive index of the lens material depends on the lens temperature. Moreover, laser beam radial distribution and additional lens deformation are considerable. As a consequence, a change in refractive index and focus point position happens. Thermal load can be induced on a small dimension optic by a high power density laser, which in some cases can lead to focus shift [75]. The focus shift strongly depends on the optical system magnification and it is proportional to the magnification squared. This means that the higher the magnification of the processing head, the smaller the fibre to be focused on the workpiece with a larger focus, the larger the focus shift [74]. To find more detail, see section 2.9.

2.5.1.2 Focal position

The maximum power intensity of the laser beam can be achieved at the focal point [76]. It means that in order to get the optimum cutting results, the focal point must be placed somewhere close to the surfaces of sheet. The focal position can be placed on the upper surface, below the upper surface (somewhere in the thickness) or at the

lower surface of workpiece, and this can affect the cut quality, cutting speed and the kerf width [2]. It has been reported that in fibre laser cutting of stainless steel, the cut surface roughness and dross attachment decrease when focal position was located inside the workpiece [77]. However, the movement of the focus inside the sheet dramatically reduces the cutting speed [78] (referred by Seefeld et al. [6]). The focal position cannot be placed too far from the upper or lower surfaces of workpiece because the interaction area increases to some point where the power intensity is not enough to melt and continue a through cut [2]. The maximum cutting speed in CO₂ laser-oxygen cutting of steel sheet was achieved when the focal position was located at the top surface for thin sheets, or about one third of the plate thickness below the upper surface for thick plates [45]. In nitrogen laser cutting of steel the focal position should be inside the sheet close to the lower surface of sheet (defocused focal position) as long as the power intensity at the upper surface of plate is sufficient to obtain complete penetration of the workpiece [77]. In this case, the kerf width becomes wider and, hence, a greater proportion of the assist gas flow can penetrate the kerf to eject the molten material through the bottom of the kerf [79]. Figure 2.43 schematically shows the effect of focus position on the cutting quality [80]. In this work, the focal position is on the surface of workpiece.

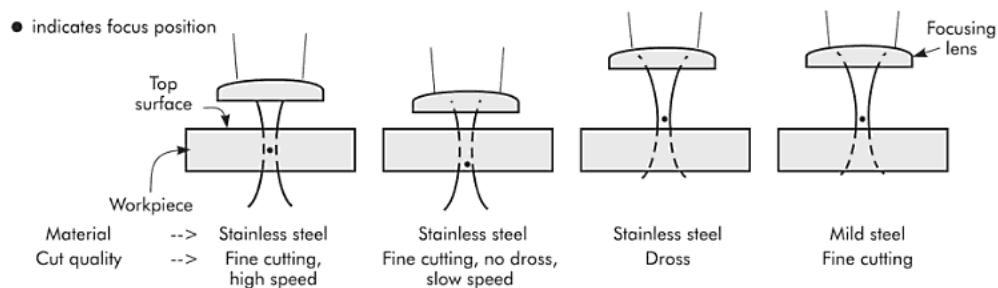


Figure 2.43- Focus position and quality of cut [80].

2.5.1.3 Nozzle diameter

The nozzle must be coaxial with the laser beam so that the beam and gas jet cut equally well in all directions. The shape of the nozzle must give optimum gas flow at the cut zone. The diameter of nozzle (Figure 2.44) is between 0.8-3 mm related to the material and thickness. A nozzle with too larger orifice will provide insufficient gas flow into the cutting zone to remove molten material. In contrast, a very small orifice will cause difficulty in beam-nozzle alignment and increase the risk of nozzle burning by defocused beam; all resulting in a rough cut edge [2]. In fibre laser

cutting of 10 mm-thick stainless steel plate, with 4 kW power and 18 bar nitrogen, the rate of melt removal from the kerf width and subsequently the cut edge quality increased with increasing nozzle diameter from 1 mm to 2.5 mm [81]. Duan et al. [82] reported that increase in pressure, nozzle orifice and overlap of the nozzle with the cut kerf, improved the gas flow field inside the kerf and enhanced efficient melt removal.

Supersonic and subsonic (conical) nozzle tips are two different nozzles that have been employed in laser cutting to achieve different gas flow behaviour in the cutting zone. Overall supersonic nozzle tip performed more uniform gas flow distribution inside the kerf than conical nozzles [83, 84]. In this work, the conical nozzle is used.

2.5.1.4 Stand-off distance

The distance between the nozzle and sheet (Figure 2.44) is the stand-off distance and can influence turbulence, cut quality and cutting speed. It is usually in the same range as the nozzle diameter between 0.5-1.5 mm [2]. A sufficient stand-off distance will stabilise the pressure on the sheet surface to minimise turbulence in the melt zone providing stable cutting condition [1]. A very short stand-off distance will increase the risk of nozzle burning from the spatter. It has been reported that in fibre laser cutting of thick stainless steel plate, with 4 kW power and high pressure nitrogen, there is no significant effect on the melt removal from the kerf with increasing stand-off distance from 0.5 to 1.2 mm [81].

Man et al. [84] studied the gas jet patterns inside the cut kerf using supersonic and subsonic (conical) nozzle tips. They reported that for the conical nozzle tip, the gas flow behaviour radically expanded and an increase in the stand-off distance worsened the behaviour of the gas jet inside the kerf. In contrast, in supersonic nozzle tip, the gas flow distribution was uniform and the behaviour of the gas jet inside the kerf was independent of the variations in stand-off distance.

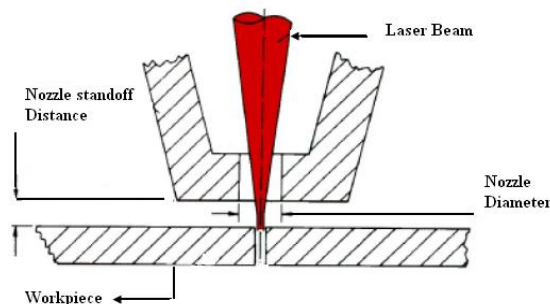


Figure 2.44- Nozzle diameter and stand-off distance [31].

2.5.1.5 Beam alignment

One of the most important considerations in order to achieve good cut quality is the alignment of laser beam with respect to the nozzle axis [1]. If the effective pressure axis of gas flow is off centre with respect to the centre of laser beam, the pressure of gas pushes the melt to the one side of the cutting zone, making a disorderly melt removal; and this can cause poor cut quality as shown in Figure 2.45 and Figure 2.46. The effect of misalignment on quality in laser-oxygen cutting of mild steel is more considerable because the viscosity of melt in oxygen laser cutting of mild steel is low [1]. More misalignment can damage the nozzle, as in the case of the author in the first laser cutting experiment (Figure 2.47).

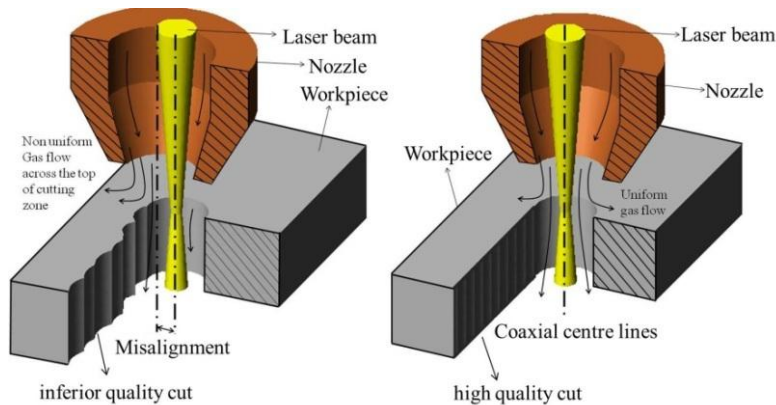


Figure 2.45- Alignment and misalignment of laser beam and nozzle (drawn by author).

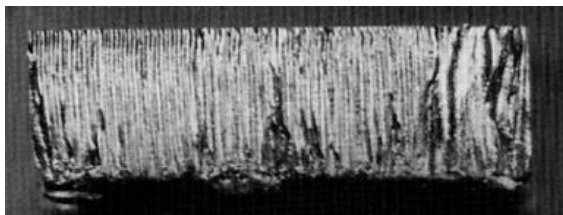


Figure 2.46- Showing a poor quality cut edge obtained when there was a nozzle-beam misalignment [1].

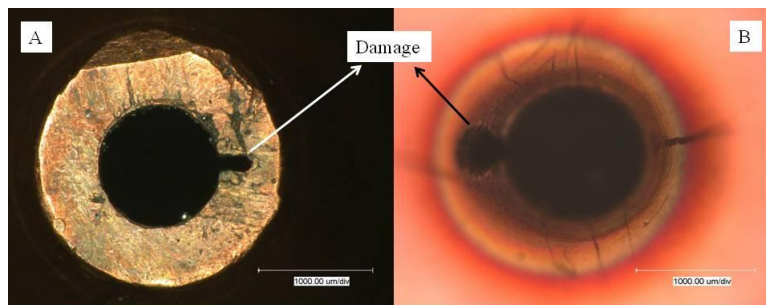


Figure 2.47- Showing 1 mm nozzle damaged by misaligned laser beam. A) Outside of the tip, B) Inside. Focused beam size was 0.2 mm.

2.5.2 Assist gas and pressure

In normal laser cutting an assist gas is employed to remove the molten material through the bottom of the kerf. Inert and active assist gases can be used based on the workpiece material. Nitrogen, argon, oxygen and air are the most well-known gases in laser cutting. Stainless steel and aluminium is often cut using an inert assist gas (e.g. nitrogen) to achieve a clean unoxidized cut edge which do not need any operation for oxidized surface removing [50]. In reactive fusion cutting, oxygen is often used as an active assist gas which is capable to react exothermically with the molten material releasing additional heat to the cutting zone [1]. It was reported that in CO₂ laser cutting of 3mm-thick mild steel the cut edge quality significantly increases by using high pressure of inert gas (12 bar). In contrast, high pressure of air and oxygen resulted in poor cut quality [85]. The cutting speed is changed when using different gas and pressure as shown in Table 2.4.

Table 2.4- The effect of gas pressure on the maximum cutting speed (mm/s) with a laser power of 1.5 kW [85].

	2 bar	4 bar	6 bar	10 bar
Oxygen	52.5 ± 2.5	57.5 ± 2.5	60.5 ± 2.5	110 ± 2.5
Nitrogen	17.5 ± 2.5	17.5 ± 2.5	17.5 ± 2.5	22.5 ± 2.5
Argon	17.5 ± 2.5	17.5 ± 2.5	17.5 ± 2.5	27.5 ± 2.5
Air	22.5 ± 2.5	27.5 ± 2.5	37.5 ± 2.5	-

Baumeister et al. [46] reported that in fibre laser micro-cutting of stainless steel sheets using 10 bar assist gas pressure, a high processing rate and lower kerf width was achieved using oxygen in comparison with nitrogen. Golnabi et al. [86] found that in CO₂ laser cutting, for an optimum condition when cutting mild steel with oxygen, a lower gas pressure is required (i.e. 1-2 bar); but for stainless steel the gas pressure increases to 4-6 bar. Ghany et al. [30] reported in Nd:YAG laser cutting of zinc-coated steel the cut surface using oxygen was rougher than nitrogen, and there was no obvious correlation between gas pressure and surface roughness.

2.5.3 Cutting speed

In order to make a successful cut with a good quality, the cutting speed must be balance with power and gas flow rate [1]. In published researches, it has been reported that many parameters influence the cutting speed: laser wavelength, focal point position, power, gas type, gas pressure, material of workpiece and thickness. A

comparison between fibre (1.06 μm) and CO₂ lasers (10.6 μm) in terms of power versus cutting speed for different material has been reported in [51] indicating that for the same cutting speeds, power will be changed when using a different laser source and different material as shown in Figure 2.48.

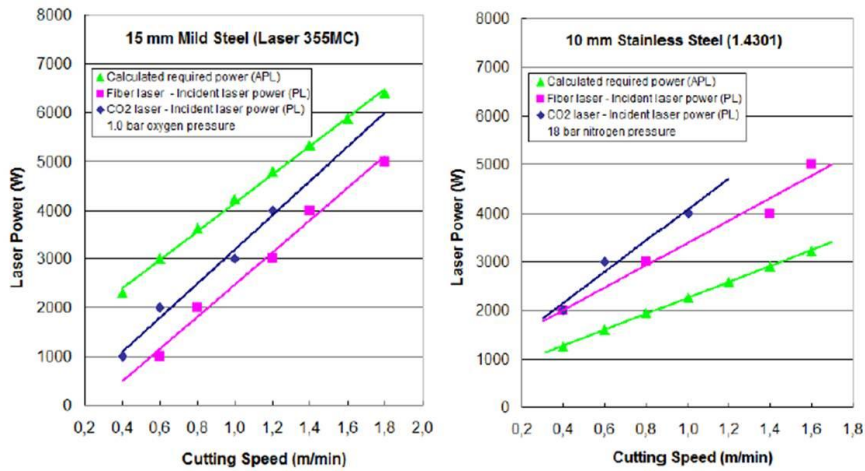


Figure 2.48- laser power versus cutting speed for different laser source and material [51].

Overall, cutting speed decreases with increasing sheet thickness [1, 2]. This is because, as the thickness is increased, the interaction time between laser and material must be increased for a complete laser penetration; so the cutting speed should be decreased. Cutting speed when using active gas (e.g. oxygen) is higher than inactive gas (e.g. nitrogen) and also it increases as the gas pressure increases (Figure 2.48) [85].

Regarding the effect of material, mild steel can be cut at higher cutting speeds range in comparison with stainless steel [86]. Figure 2.49 indicates the effect of material and thickness on the cutting speed for stainless steel and aluminium [65].

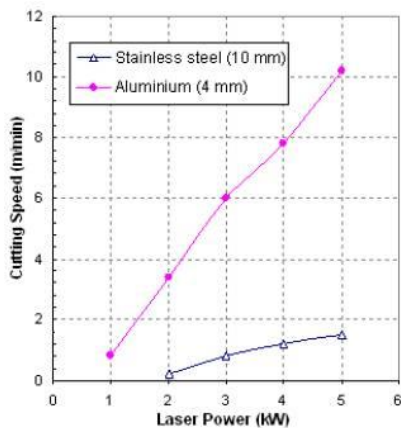


Figure 2.49- Maximum cutting speed with the corresponding required laser power (fibre laser, nitrogen, 14 bar for aluminium and 19 bar for stainless steel) [65].

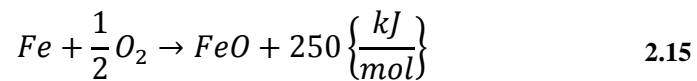
In fibre laser cutting of stainless steel, the movement of the focus point inside the plate thickness close to the lower surface of sheet, dramatically reduces the cutting speed [78].

Cutting speed can influence the surface roughness. In fibre laser-oxygen cutting of mild steel, the roughness at the top and bottom of the cut edge roughness reduces to the lowest value at moderate cutting speeds (e.g. 5500 mm/min) which is called striation free. However, from this threshold on and with increase in the cutting speed (e.g. 6500 mm/min), the roughness from the bottom of cut edge increases [22].

Ghany et al. [30] reported in Nd:YAG laser cutting of zinc-coated steel for all employed gases (i.e. oxygen, nitrogen and air) the kerf width decreased with an increase in the cutting speed.

2.6 Laser-oxygen cutting process

Due to the exothermal oxidation reaction between molten iron and oxygen in the melting zone, substantial proportion of energy is added to the cutting zone enhancing the cutting process [9].



The presence of FeO in the melting zone (Figure 2.50) has been proved [9, 87]. Studies on the oxidation dynamics of CO₂ laser cutting of mild steel showed that the oxidation reaction affects kerf width, depth of cut, cutting speed and generation of striations on the cut edge [88, 89].

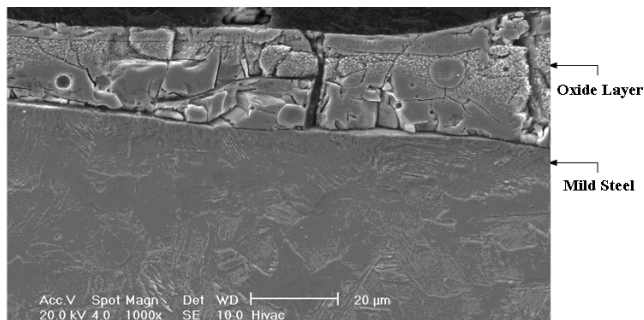


Figure 2.50- Brittle oxide layer on the cut edge [9].

Miyamoto et al. [89] found that the presence of FeO in the melt decreases the viscosity of melt as shown in Figure 2.51. Oxygen pressure, oxygen purity and any change in the viscosity of melt are the most reasonable sources of primary generation of striations [8, 88]. Ivarson et al. [8] realised that in CO₂ laser cutting of mild steel the cutting speed increases with increasing oxygen purity (Figure 2.52).

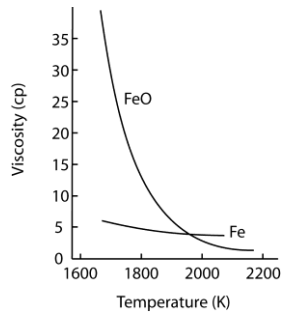


Figure 2.51- The relationship between viscosity and temperature [89].

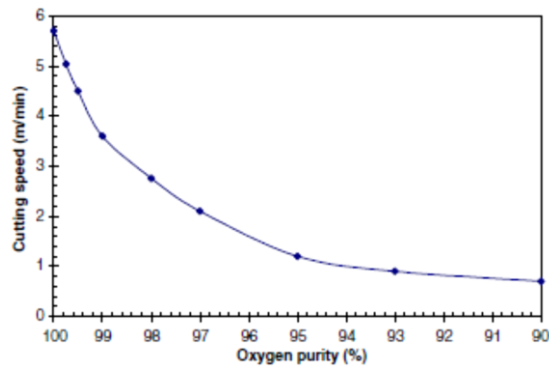


Figure 2.52- Cutting speed as a function of oxygen purity (CO₂, 400 W, 0.35 MPa, 2 mm thick mild steel) [8].

In an experimental research on the fibre laser cutting of thin section mild steel with 2 bar oxygen, it was stated that the kerf width was 1.3 to 3.25 times wider than the spot size (i.e. 0.2 mm) for different thicknesses and cutting parameters as shown in Figure 2.53. As can be seen overall, the ratio of kerf width to spot size (K/S) increases with power and cutting speed. The highest K/S was achieved when cutting 2 mm using 1500 W and 6500 mm/min. It was concluded that the waveguiding effect of FeO on the fibre laser is the reason of kerf widening as compared with CO₂ laser cutting. Regarding surface roughness, the maximum roughness was 3 μm and striation free (0.25 μm surface roughness) was achieved for 2 mm-thick at cutting speed of 5500 mm/min (Figure 2.54). All cut edges were free of dross [22, 52].

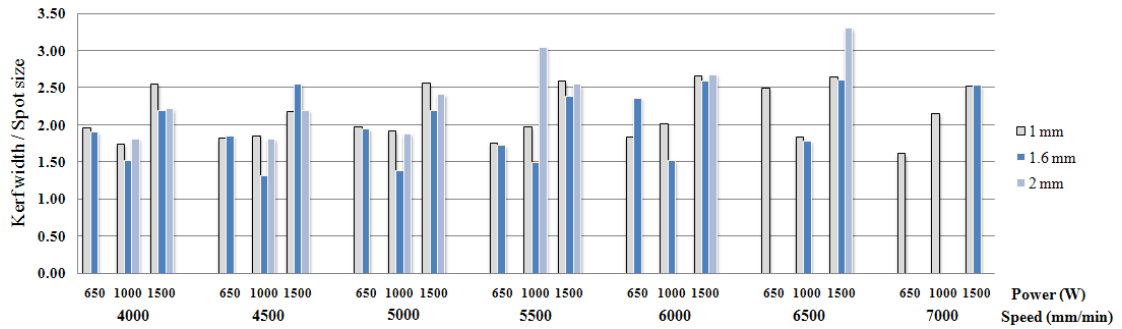


Figure 2.53- Kerf width per spot size versus different power for various thickness of mild steel sheet in fibre laser-oxygen cutting [52].

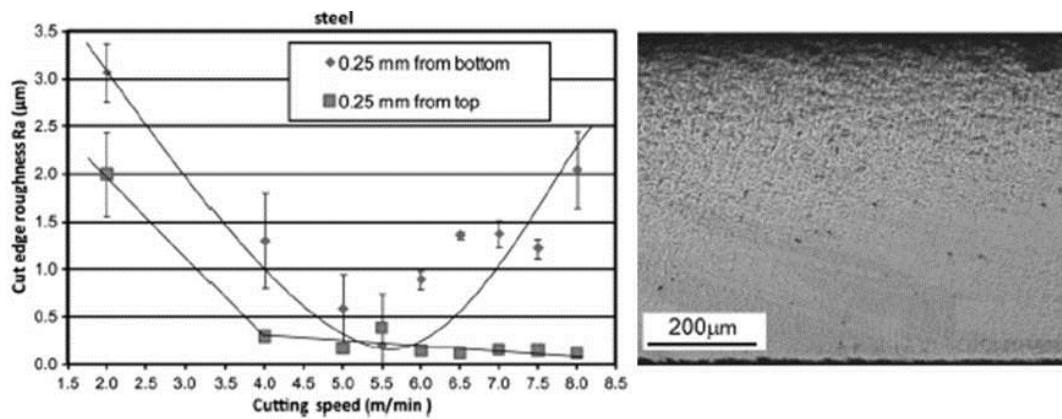


Figure 2.54- Surface roughness graph (left) and striation free on the cut edge (right), (2bar oxygen, 1000 W, 5500 mm/min) [22, 52].

In pulsed fibre laser cutting of thin section stainless steel (i.e. 0.11 mm) using 3 bar oxygen and spot size of 0.012 mm on the surface of sheet, the ratio of kerf width to spot size (K/S) was in the range of 1.5 to 2.21 for different cutting parameters as shown in Appendixes Table 10.1. As it can be seen the ratio of K/S generally increases with increasing power [73].

Baumeister et al. [46] reported that in fibre laser cutting of 0.1-0.3 mm stainless steel with 10 bar oxygen pressure, spot size of 0.02 mm, power range of 9-84 W, cutting speeds of 20 and 50 mm/sec, the ratio of kerf width to spot size was in the range of 0.9-3.25 as illustrated in Appendixes

Table 10.2. As can be seen, the ratio of K/S overall increases with power. The sheet thickness did not significantly affect the K/S, though the highest ratio of K/S (i.e. 3.25 with power of 84 W) was achieved in thickness of 0.1 mm and the lowest one (0.9 with power of 16 W) is seen in thickness of 0.3 mm.

With using a different gas type (i.e. oxygen, nitrogen and air) in the fibre laser cutting of 1 mm-thick mild steel sheet coated by zinc and with two types of wave shapes (CW and pulsed), it was found that with the same power, oxygen has the highest ratio of K/S and followed by air and nitrogen as indicated in Appendixes Table 10.3. At the constant power, the ratio of K/S decreased with increasing cutting speed. The ratio of K/S for CW generally was larger than that for pulsed laser.

Regular striation formation in laser-oxygen cutting of mild steel is independent of cutting speed. However; at low cutting speed, oxidation burning can generate large, rough striation [89]. The cut surface roughness can be due to the table vibration, fluctuations of laser power and natural striation [89]. If all cutting parameters including gas pressure, power and beam alignment are appropriate, the effect of cutting speed on the surface roughness is significant [90].

Powell et al. [22] found that at the lower cutting speeds the cut front is almost vertical and laser beam has a small interaction area with cut front. In this case, laser-cut front interaction consists of cycle burning reaction. Thus, the melt temperature is low and viscosity is high; hence, a rough cut edge will be left behind as the melt flows down the kerf. In intermediate speeds (e.g. 5500 mm/min), the cut front is curved; hence the area of laser-cut front interaction increases. The melt temperature and melt thickness increases but viscosity decreases; thus, melt flow happens with lowest turbulence. Combination of these phenomena will decrease cut edge roughness. At higher range of speeds, the melt acceleration and turbulence increases, hence the rough cut edge is produced.

Regarding the HAZ, it increases from the top to the bottom of kerf [52]. Any increase in cutting speed can decrease the HAZ in the top of kerf (with exceptions only near the maximum speed). The HAZ in the bottom increases with increase in cutting speed. While gas pressure increases, the HAZ decreases. Any increase in amount of carbon in the steel can increase the HAZ. It has been reported that the HAZ approximately remains constant with any change in the power [91]. Another reference states that any increase in power increases the HAZ and any increase in cutting speed and oxygen gas pressure decrease the HAZ [92].

Powell et al. [9] has concluded 12 guidelines in laser-oxygen cutting for future theoretical models that are quoted in this section as below:

“

Guideline 1: During the laser–oxygen cutting of mild steel the oxidation reaction of iron to FeO supplies a considerable amount of energy to the cutting process.

Guideline 2: The iron melted during cutting is not all oxidized before it leaves the cut zone. The melt leaving the cut is therefore an Fe/FeO mixture.

Guideline 3: The Fe/FeO mixture expelled from the cut zone has a considerably lower viscosity than molten iron.

Guideline 4: FeO does not boil—it does not have a gas phase. If any of the melt in the cut zone is heated to sufficiently high temperatures the FeO will dissociate into oxygen and iron or it will not form in the first place. If this happens the energy from the ‘oxidation reaction’ of the material in question will not be available as an energy input to the cut zone.

Guideline 5: The thermal energy provided to the cutting process by the oxidation reaction is approximately 250 kJ mol^{-1} .

Guideline 6: The boiling point of mild steel can be taken as being approximately 3000K and its melting point is approximately 1800 K.

Guideline 7: At very low speeds most of the laser energy does not interact with the cut front and temperatures within the cut zone will be of the order of 1900 K.

Guideline 8: For lasers cutting mild steel with oxygen assist at moderate or high speeds, the cut front temperature will rise as a function of the cutting speed.

Guideline 9: During laser–oxygen cutting of mild steel, the laser beam irradiates the whole of the cut front and the surface temperature of the melt increases towards the bottom of the cut front as a result of increased laser–melt interaction time.

Guideline 10: Standard, commercial laser–oxygen cutting of mild steel does not involve boiling or oxide dissociation.

Guideline 11: High intensity laser–oxygen cutting could involve sub-surface boiling of iron-rich melt under a layer of molten FeO (sub-surface boiling increases turbulence but does not create a recoil pressure).

Guideline 12: If the energy density of the focused laser is too high, the laser–oxygen cutting process for mild steel may become disrupted. This may result in reductions in cut quality and cutting speeds.

”

2.7 Laser-nitrogen cutting process

In laser cutting of steel using an inactive assist gas like nitrogen, a high power laser beam is applied to melt the kerf volume and a high pressure of gas is essential to remove molten material. Nitrogen, itself, does not react with melt compared to oxygen so the role of nitrogen is just to push the molten material out of the kerf [1, 2]. The features of the cut edge produced by nitrogen cutting are different from that of oxygen cutting. In laser-nitrogen cutting there is a noticeable point on the cut edge which is called Boundary Layer Separation (BLS) point. The BLS point is located on

the cutting front at which the velocity of melt decreases and thickness of melt increases [81]. This point which shown in Figure 2.55 may be located at any depth on the cut edge depending on the assist gas condition [10]. Overall, an irregular striation pattern below the BLS is indicative of an insufficient melt removal condition. The depth of the BLS point on the cut edge depends on cutting speed, focal position and nozzle diameter. In general, the location of BLS point moves down with increasing gas pressure and cutting speed [10, 81].

The nozzle has a significant effect on the BLS point location because it determines the mass flow rate of assist gas into the kerf, which influences the force to push the melt down the kerf. Wandera et al. [81] has stated that in laser cutting of 10 mm thick stainless steel (4 kW, 1.0 m/min, 18 bar nitrogen, 8 mm focal point position below top surface) the location of BLS moves down the kerf with increasing nozzle diameter, resulting in a cut edge with better quality. In contrast, Sparkes et al. [10] has reported that with a reduction of nozzle diameter from 2.5 mm to 1.5 mm, at lower range of cutting speeds (i.e. 15 mm/s) for lower pressure (i.e. 1.6 MPa), the BLS was located at the lower part of cut edge. Wandera stated that the stand-off distance did not significantly affect the BLS [81]. When the focal point is on the surface of sheet, a narrow cut kerf is produced, resulting in reduced melt removal rate; hence, BLS point occurs near the top surface of cut edge. When the focal point is located close to bottom surface of sheet, the beam spot size on the surface of sheet is defocused, then the kerf width becomes wider; which results in better melt removal and clean cut edge [10, 81]. In this case the power must be sufficient to produce complete penetration of workpiece. As the focal point position was changed away from zero (top surface of sheet) in either the positive or negative direction, the BLS location moved down on the cut edge [10].

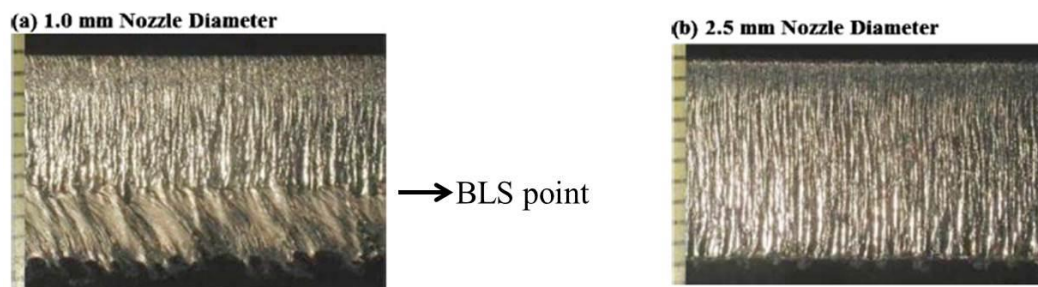


Figure 2.55- Boundary layer separation point (BLS) in 10 mm stainless steel (4 kW, 4 bar nitrogen, 1.0 mm/min cutting speed, 190.5 mm focal length, focal point position 8 mm below upper surface) [45].

Overall, kerf for nitrogen laser cutting is narrower than that for oxygen cutting. In the results from Ghany et al. [30] (Table 10.3 in Appendix), it is seen that when using nitrogen, the kerf width decreases as compared to oxygen and the percentage of reduction is 5% to 17.4% (in CW mode).

Baumeister et al. [46] reported that in fibre laser cutting of stainless steel using 10 bar nitrogen pressure, the ratio of kerf width to spot size (K/S) was in the range of 1.25-3.55 as shown in Appendix Table 10.4. As it is seen, overall, the kerf width increases with power. Comparing Table 10.2 and Table 10.4 (see Appendix), obtained from a same reference, the range of K/S for oxygen is 0.9-3.25 whilst it is 1.25-3.55 for nitrogen disregarding cutting parameters and thicknesses. This comparison shows that in this case, oxygen has produced narrower kerf width; which is in contrast with other references.

The results of Sparkes et al. [10] indicates that the kerf width showed a strong correlation with the theoretical beam diameter, while it was larger than the beam diameter. They concluded that widening of kerf beyond beam diameter was because of the increase in the melt volume as a result of heat conduction. They compared fibre laser (1.06 μm) with CO₂ laser (10.6 μm), in nitrogen cutting of 6 mm-thick stainless steel, and found that with the same power (i.e. 2.2 kW) fibre provides greater cutting speeds (e.g. 1.5 m/min for fibre 1 mm/min for CO₂) which is most likely associated with a higher absorption for the shorter wavelength.

2.8 Laser piercing

2.8.1 Definition

At the beginning of the laser cutting process, the laser beam has to pierce a hole in the workpiece in order to establish a uniform melt ejection through the bottom of the kerf. In laser-oxygen cutting process, the width of laser pierced hole is enlarged due to interaction of oxygen with the sheet [1]. In fibre laser-oxygen cutting, due to the erratic nature of the oxidation reaction and the high melting efficiency of fibre laser, a large amount of melt is generated; thus the cutting zone interacting with laser beam includes a large melt surface which in contact with oxygen generates more reaction power. The excess reaction power causes excessive melting and widening of the

kerf [51]. This behaviour at the beginning of cut is more noticeable decreasing the cut quality as shown in Figure 2.56.

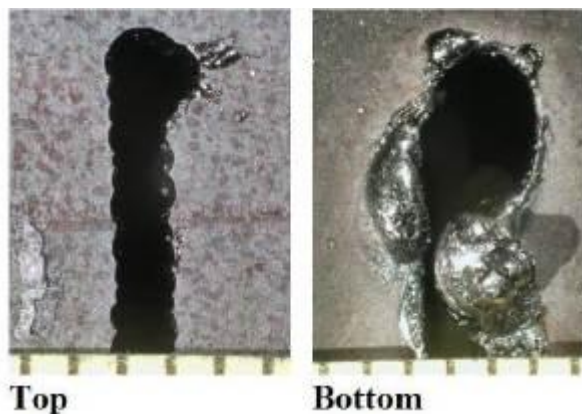


Figure 2.56- Kerf width and dross attachment with 1.0 bar oxygen pressure. Kerf width is about 1mm (15 mm mild steel, 3 kW, 0.8 mm/min, 2 mm nozzle diameter, -10 mm focal length) [51].

The laser piercing and laser cutting are two independent processes [93]. In piercing, the laser beam is stationary with respect to the sheet whilst in laser cutting, the sheet (table) or the laser beam (cutting head) moves along the required profile. The highlighted difference between piercing and cutting is that in laser piercing the majority of molten material is removed through the top of the pierced hole due to vaporisation recoil pressure, so spattering occurs; whereas in laser cutting, the majority of molten material is ejected through the bottom of the kerf.

In commercial work, two kind of piercing techniques are applied:

1. Rapid or blast piercing: during the hole piercing, a force of pressurized gas jet on the molten material, which is generated at the laser interaction area, causes an explosive ejection of the melt towards the cutting nozzle until the breakthrough happens [1].
2. Pulse piercing [1, 2]: a series of laser pulses at the same spot at a specified setting interacts with workpiece which results in melt ejection and consequently forming a hole [94]. An assist gas (active or inactive) is used to facilitate the ejection of molten material from the laser beam path in progression with the hole formation [95].

2.8.2 Laser piercing mechanism

The mechanism of metal laser piercing in simplified terms can be explained in four stages which is quoted from McNally et al. [96] as below:

“

*(i) **Surface heating:** the laser beam is focused onto the metal surface and light interacts with electrons by the mechanism of Fresnel absorption. The excited electrons collide with lattice photons and other electrons and the energy is rapidly converted to heat in a very thin surface layer a few nanometres thick.*

*(ii) **Surface melting:** if the laser intensity and interaction time are sufficient, a thin layer on the surface becomes molten. Laser beam intensities are usually so high that the timescale for surface melting is too short for significant thermal conduction into the material.*

*(iii) **Vaporisation:** at this point, the surface temperature of the irradiated zone is typically higher than the boiling temperature of the material and vaporisation begins. When the vaporised material is expelled freely into the atmosphere, the vapour pressure is considerably higher than the ambient pressure, which causes the escaping vapour to accelerate.*

*(iv) **Melt ejection:** as well as vaporisation, two types of liquid melt ejection may occur: vaporisation- induced recoil pressure ejecting the melt layer radially from the beam path; and ejection as a result of the probable existence of nucleation mechanisms that can cause violent boiling during the drilling process. Yilbas and Sami [97] reported that material below the surface can become superheated whereupon a sudden liquid-vapour phase change takes place, resulting in small vapour bubbles developing in the liquid just below the surface and expanding rapidly. The high pressure and rapid expansion cause a thermal explosion, ejecting the liquid metal in the zone of the exploded bubble from the cavity.*

“

Voisey et al. [98] have reported that melt ejection is a significant mechanism of material removal for the laser drilling conditions. They concluded that during melt ejection, the recoil pressure decreases as quoted below:

“

As the pulse progresses, the molten layer thickens, resulting in a larger average droplet size. The recoil pressure decreases, reducing the ejection velocity, but continues to remove material from the ablation front. The molten material moves along the hole walls in a relatively smooth way, breaking up into discrete droplets under the influence of surface tension on exiting the hole. Surface tension effects may also increase the angle of ejection as the molten material follows the curve of the hole entrance on exiting it.

”

The removal mechanism of molten material can also be facilitated by using an assist gas. Low et al. [95] used argon and oxygen as assist gas in laser drilling. Argon

ejected the molten material from the hole by means of chiefly bulk melt ejection and it causes a rapid cooling during the drilling process. In contrast, oxygen ejected the melt like liquid particles and vapour ejection. Moreover, due to the thermal reaction of oxygen with the melt, cooling rate decreased.

Tirumala et al. [93] used a power ramped pulse mode (PRPM) for piercing the initial hole and cutting the sheet. They used a programmable power supply to change a CW-CO₂ laser with 1 kW output power to the pulsed mode. During the piercing, the power of pulsed laser gradually increases to the maximum then cutting is started. By this method they could control the widening of start up hole as shown in Figure 2.57.

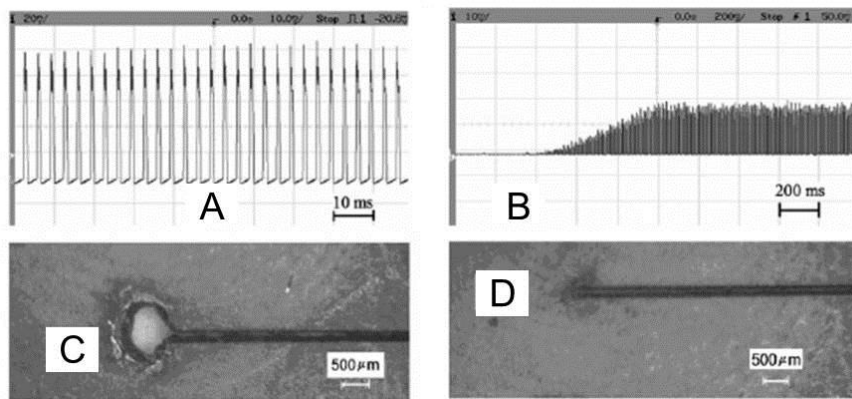


Figure 2.57- Decreases in the start-up hole by PRPM cutting. A) Normal pulsed mode, B) PRPM laser C) cutting with normal pulsed laser D) cutting with PRPM laser [93].

2.8.3 Piercing quality characteristics

The high quality of laser pierced holes has been the main subject in studies carried out on the operating parameters to pierce holes [1]. The quality characteristics of pierced holes are: accuracy in diameter, circularity, regularity, repeatability, hole taper formation and spatter formation [1, 2, 93]. It is reported that the behaviour of melt ejection can significantly affect the shape of the hole entrance [94].

2.8.4 Rapid laser piercing

Rapid laser piercing is sometimes called blast laser piercing [1]. It involves a CW laser beam to pierce a hole (Figure 2.58) so it is more appropriate to use in laser cutting.

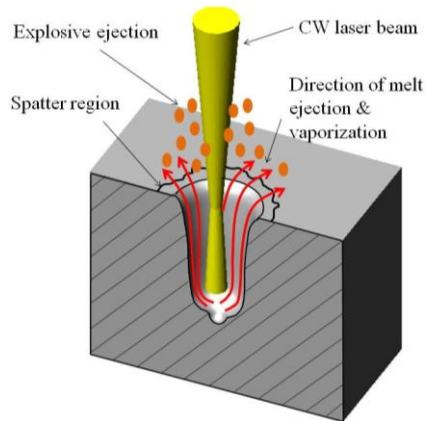


Figure 2.58 - A 3D cross section of a hole pierced by CW laser beam.

Although blast laser piercing is a fast piercing process [93], it has some detrimental effects on the pierced holes:

- 1- The hole diameter is considerably larger than spot size [1, 93].
- 2- Explosive ejection of molten material can damage the hole edge and circularity.
- 3- Spatter surrounds the hole [2, 94].
- 4- Due to explosive ejection of molten material, frequent damage of the nozzle tip occurs [1, 93].

2.9 Thermal lensing

Lens usually shows an unsteady variation in the optical parameters after incidence of high power laser beam and it takes typically 10-20 seconds until the optics reach their thermal equilibrium [99]. During thermal equilibrium, the size of lens is changed because according to the thermal coefficient of expansion of the lens material (α), the lens volume expands as the temperature of the lens increases. Moreover, the temperature coefficient of refractive index (dn/dT) of lens is changed with increasing temperature. Normally, these effects lead to a variation of the focal position, divergence angle and, subsequently, the focused beam diameter [99, 100]. The power of a lens is directly influenced by these two properties (i.e. α and dn/dT) by what is called the thermal power of a lens as shown in equation 2.16 [100]:

$$\Psi_P = \frac{dn/dT}{(n-1)} - \alpha \quad 2.16$$

The power of a lens is therefore altered as a function of temperature by the equation 2.17 [100]:

$$\Delta\Phi_P = \Phi \left[\frac{dn/dT}{(n-1)} - \alpha \right] \quad 2.17$$

Where, Φ is the power of the lens. The change in power then is the original power of the lens times the thermal power of the lens Ψ_P [100].

The typical thermal coefficient of expansion (α) for fused silica is around $0.5 \times 10^{-6}/K$ and has a dn/dT of approximately $10 \times 10^{-6}/K$. If a lens is made of fused silica and has a nominal focal length of 200 mm, then this lens will have a change in focus of more than 350 microns for a 100 °C temperature increase. Although this may not seem like a huge amount for such a long focal length lens, when used as a collimator for a fibre, it has a dramatic impact on how the light is collimated from the fibre [100]. The effect of focal shift on the cutting process has been already discussed (see 2.5.1.1 and 2.5.1.2).

The effect of thermal lensing on the relative focal shift as a function of irradiation time measured on a 6 kW laser power with 200 μm transport fibre and magnification of 1 is indicated in Figure 2.59 [101]. The focus shift is separated by the Rayleigh length (Z_R). The focal shift due to the absorbed power (ΔP_{abs}) can be estimated by equation 2.18 [101] where f is nominal focal length, R_L is the radius of fibre, K_W is the material specific thermal conductivity.

$$\Delta f = \frac{\Delta P_{abs}}{2\pi \cdot K_W} \frac{f^2}{R_L^2} \frac{dn}{dT} \quad 2.18$$

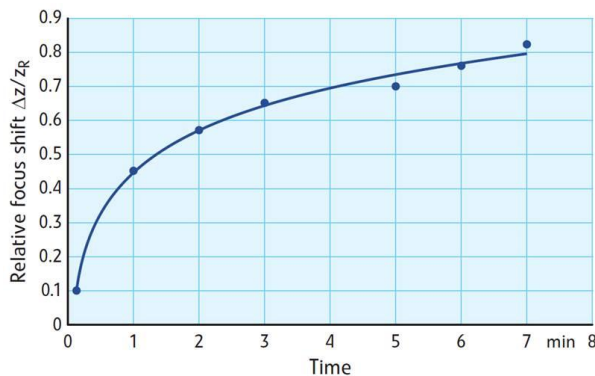


Figure 2.59- Relatively focus shift as a function of irradiation time [101].

In majority of published research, the effect of thermal lensing on the cutting process has not been considered. Said [52] has attended to the effect of power and irradiation time on the focus shift. However, it was reported that the focus shift did not affect the results of the kerf width because the maximum laser irradiation time for cut was 30 seconds which was below the threshold time for thermal lensing (i.e. 5 minutes). Also there was a waiting time between each cut that allowed the optics to cool.

2.10 Summary

This chapter briefly reviewed the literature in relation to the laser cutting of metals, in particular, the laser cutting of mild steel plates using oxygen and nitrogen as assist gases. Two sources of lasers with different wavelength (i.e. CO₂ laser with wavelength of 10.6 μm and fibre/disk/YAG with wavelength of 1.06 μm), which widely used for laser cutting, were compared. The comparison shows that the performance of fibre/disk laser in laser cutting is different from CO₂ laser. The published works in literature also indicate that the action of oxygen, in laser cutting of mild steel, is different from nitrogen. The results from the literature indicate that different optical system setups (e.g. different focal distance, different position of focal point and different focused spot size) have different effects on the laser cutting conditions. The basic laser cutting parameters, such as laser power and cutting speed, are also influenced by the parameters discussed above. This leads to the selection of optimal laser cutting parameters to cut different thicknesses being difficult (i.e. different combinations of laser cutting parameters can cut a given thickness). From the results of published works, it seems that as well as these being many different approaches to selecting laser cutting parameters, there is no quantitative way of comparing parameter sets across different laser system. Which laser cutting parameters do control the depth of cut?

In laser cutting, the laser beam has to pierce a hole in the workpiece from where the cutting proceeds. In oxygen laser cutting of mild steel, the width of start-up hole is wider than the rest of the cut, which causes the piercing to be carried out far from the final cut surface, thus leading material wastage and increased production costs. A review of the relevant literature indicates that this issue has received little attention. Better understanding of laser piercing is needed to be able to minimise the amount of

material wastage in laser cutting. How can the oxygen laser cutting of mild steel be optimised regarding material wastage?

The main topics of this thesis are to answer to the questions discussed above in fibre laser cutting of mild steel using oxygen and nitrogen.

3 Equipment and experimental procedures

3.1 Introduction

The equipment and experimental procedures used will be introduced in this chapter. The first sections concern the material, laser machine, laser power calibration and laser beam characterisation. The following sections cover the workpiece preparation, laser machine setup and laser cutting with oxygen and nitrogen. Then, the equipment which was used for the kerf width observation and surface roughness measurements will be introduced. Piercing experiments, the methods used for hole structure observation and hole geometry estimation will be discussed in the following section.

3.2 Material

The workpiece used is cold rolled mild steel and the compositions of the material are presented in Table 3.1.

Table 3.1- Composition content of mild steel sheet (% of weight) measured using spark emission (Spectrometry, Foundry Master).

	Fe	C	Si	Mn	S	Cr	Ni	Al	Co	V	Ca
1.0mm	99.5	0.0433	0.0062	0.172	0.0181	0.0557	0.0448	0.0451	0.0025	0.0021	0.002
1.6mm	99.3	0.0350	0.0056	0.173	0.0135	0.0134	0.0119	0.0422	0.0021	0.0028	0.002
2.0mm	99.5	0.0334	0.0053	0.192	0.0150	0.0231	0.0132	0.0341	0.0024	0.0025	0.0019
4.0mm	99.1	0.0632	0.0071	0.205	0.0150	0.0415	0.0325	0.0542	0.005	0.002	0.0017
6.0mm	98.7	0.145	0.0171	0.947	0.0063	0.0167	0.0248	0.0737	0.006	0.002	0.0004

It is well known that laser cutting is mainly a laser-fusion phenomenon and the laws of optics and fusion dominate the whole process. The surface quality of workpiece may affect optical-fusion-aerodynamic phenomenon. Sheets with shiny or reflective surfaces can reflect the beam out of the focused point causing a reduction in power absorption. Dirty, rusty or processed surfaces may respond unexpectedly in melting of material. Thus, the surface roughness of sheet may affect laser cutting. Hence the surface of sheet was expected off the rust and any surface damage before experimentation. The surface of the sheet was cleaned up from the oil using a methanol based cleaner before cutting. The sheet surface quality was as same as a cold rolled mild steel sheet surface and the same surface finish has been used throughout this work.

3.3 Fibre laser cutting machine

The fibre laser cutting machine used in this research is an Ytterbium fibre laser machine manufactured by IPG Laser Company. Some features are shown in Table 3.2.

Table 3.2- General characteristics of the IPG fibre laser cutting machine.

<i>Contents</i>	<i>Values</i>
Model	YLR-2000
Laser source	Ytterbium
Maximum set power	2000 W
Maximum output power	1750 W
Number of module	4 + 1 reservation
Maximum power of a module	500 W
Wavelength	1060 μm
Laser mode	CW
Beam intensity distribution	TEM00
Feeding fibre length	5 m
Cooling system	Chiller + water cooling

3.3.1 Optical system of cutting head

Two lenses with the same outer diameter of 50 mm but with different focal length were applied in this research as shown in Table 3.3.

Table 3.3- Showing the optical parameters of employed cutting heads.

Trade name	Collimation length	Focal length	Magnification
PRECITEC YK25	125 mm	120 mm	0.96
PRECITEC YK25	125 mm	80 mm	0.64

3.4 Output power measurement

On the monitor of the applied laser machine there are two power measurements of set power and displayed power. When using set power (target power), due to some technical reason the displayed power was 97.5% of the set power. However, it is important to know that how much power is available in the cutting head. The output power (actual power) from the cutting head can be measured by a power monitor. There are several different types of power monitors available on the market [102-104]. The most common power meters used for high power CW lasers are calorimetric-based devices. They measure the temperature of a cooling medium, which attains the heat from the laser beam absorbed in a highly absorbing chamber [105]. To measure the output laser power from the nozzle a Premise GmbH Power

Monitor was used as shown in Figure 3.1 and Figure 3.2 which is a calorimetric-based device.

The power meter which is made up of a parabolic mirror in entrance, a cylindrical absorber with inner surface coated by highly absorbing coating and an input and output cooling water is shown in Figure 3.1. The beam is directed to the absorber by the entrance mirror and is completely absorbed thus, heating the water around the absorber. The difference of temperature between input and output water (T_2-T_1) and its coolant flow rate are measured by a high precision sensor. The electronic data is sent to the computer and the power of the absorbed laser beam is calculated by the power monitor's software.

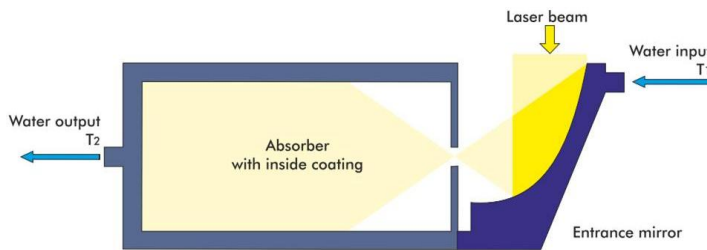


Figure 3.1- Schematic of calorimetric power meter [103].

Figure 3.2 depicts the setup of the power meter on the CNC table of the laser machine while calibrating the output power with a fixed cone on the cutting head and without the nozzle. The power meter's software monitors any increase in temperature as the time increases as per Figure 3.3. As the laser beam starts to heat the cylindrical absorbers, the temperature increases and the software calculates the power consumed and displays this on a graph. Eventually, the graph becomes steady because laser beam power is constant.

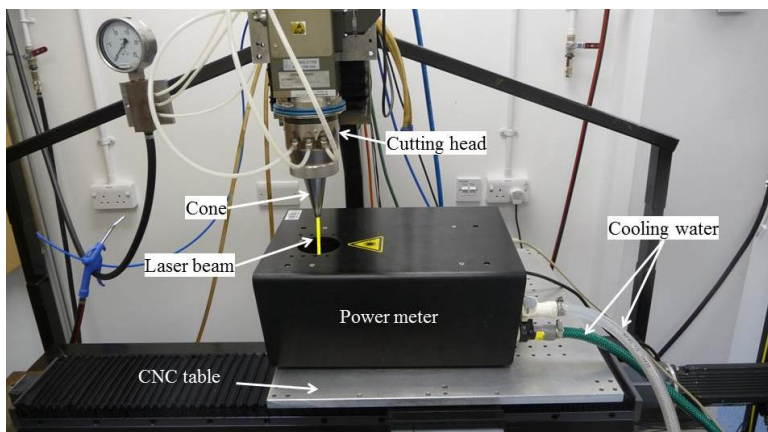


Figure 3.2- Indicating the setup for power calibration with power meter.

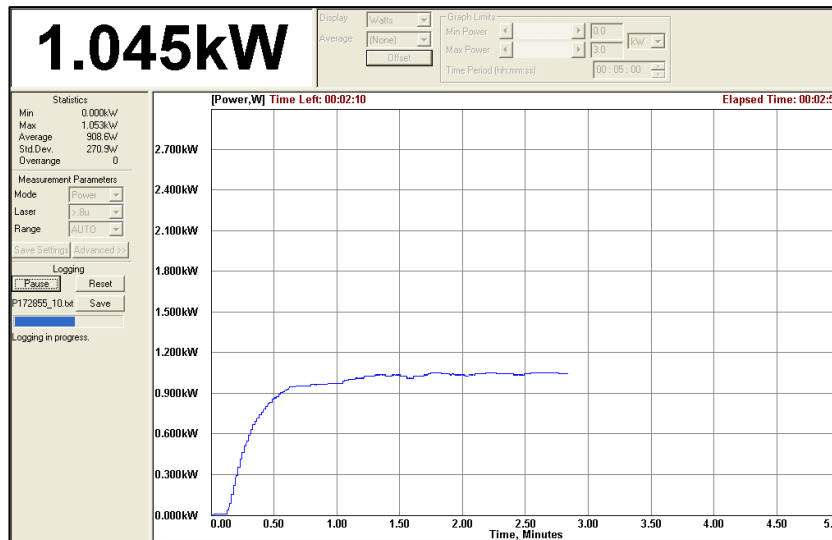


Figure 3.3- Power meter’s software window indicates the measured power for the target power of 1200 W with fibre of 200 μm and the focal length of 120 mm as the time increases.

The actual power was measured after 2.5 minutes from the beginning of laser irradiation. The power calibration was measured for both employed lenses (i.e. focal lengths of 120 mm and 80 mm) and the results were very similar. The result of the power calibration as a function of target power and actual power is shown in Figure 3.4 and Table 3.4.

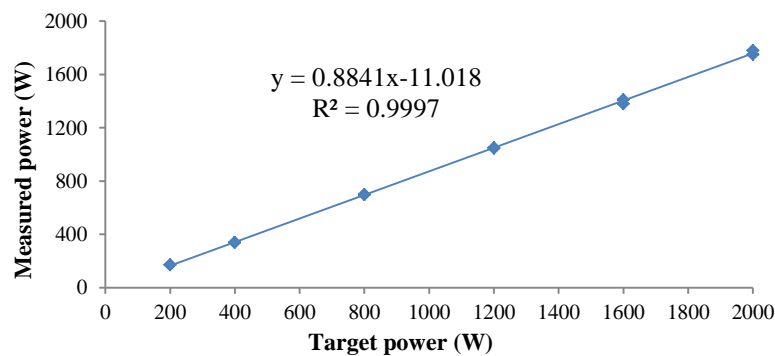


Figure 3.4- Indicating the trend of actual power versus target power using different lenses with focal length of 120 mm and 80 mm. The cone without nozzle had been set up on the cutting head.

Table 3.4- Showing the numeric values of target power and the actual power for both applied lenses with different focal length of 120 mm and 80 mm with using the output fibre of 200 μm .

<i>Target power (W)</i>	<i>200</i>	<i>400</i>	<i>800</i>	<i>1000</i>	<i>1200</i>	<i>1400</i>	<i>1600</i>	<i>1800</i>	<i>2000</i>
<i>Actual power (W) for 120 mm</i>	170	340	696	866	1045	1214	1380	1563	1750
<i>Actual power (W) for 80 mm</i>	170	340	700	877	1050	1236	1410	1595	1780

During the power calibration, the cone of cutting head was becoming hot, which potentially meant that some power was being lost by beam scattering and heat conduction. To determine the extent of this effect, the cone was disassembled and

some target powers were inspected randomly. The results indicate that approximately 1% of output power is lost when using the cone as shown in Table 3.5.

Table 3.5- Comparison of actual powers with and without cone.

Target power	Actual power with cone	Actual power without cone	Losses percentage
800 W	696 W	703 W	<1%
1200 W	1045 W	1055 W	<1%
2000 W	1750 W	1760 W	<1%

The power calibration for fibre of 600 μm was also investigated to determine the effect of output fibre diameter on the power calibration. The data in Table 3.6 confirm that the diameter of fibre does not influence the actual power.

Table 3.6- The effect of fibre diameter on the actual power.

Target power (W)	200	400	800	1200	1600	2070
Actual power for 200 μm (W)	170	340	696	1045	1380	1750
Actual power for 600 μm (W)	170	340	696	1045	1380	1750

3.5 Laser beam characterisation

The laser beam parameters such as beam diameter, focus position, power density distribution and beam divergence angle were measured by using a Primes GmbH focus monitor as shown in Figure 3.5 and Figure 3.6. The focus monitor scans the laser beam by a rotating measuring tip which includes a 20 μm pinhole located 1.5 mm from the end of the tip. The measuring tip has two movements: a rotational and a linear movement. It directs the signal target of beam to the detector using two mirrors. The detector then transfers the electrical signals to a computer where the focus position and the profile of the scanned beam can be read. The second order moment method [106-108] was used to evaluate the beam diameter and describe the laser beam propagation in accordance with the current ISO standard of 11146 [99]. To avoid the effect of focus shift, the measurement of beam diameter was carried out with a typical laser power of 600 W.

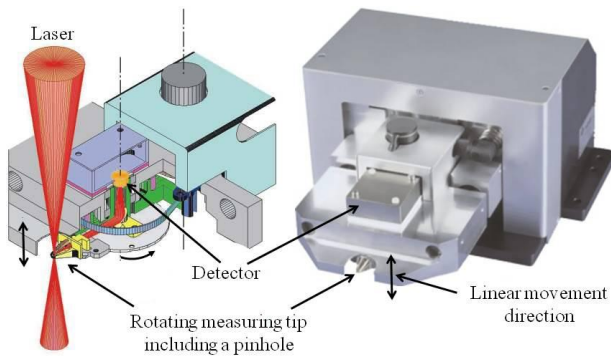


Figure 3.5- Primes GmbH focus monitor [103, 109].

The experimental setup for beam monitoring is indicated in Figure 3.6. The focus monitor is located on the CNC table below the optical lens while the rotating pinhole can touch the laser beam. The pinhole must always be located in a correct and stable position in the beam path. Easy positioning can be performed using the adjustment plate as shown in Figure 3.7. The laser beam must go through the adjustment plate's hole to show a good position of focus monitor below the laser beam. In order to test the above scenario, we used the red guide beam of the laser machine which is visible and safe to use. During the beam monitoring test, a water cooled beam dumper was applied to avoid any damage by scattered laser beam as shown in Figure 3.6.

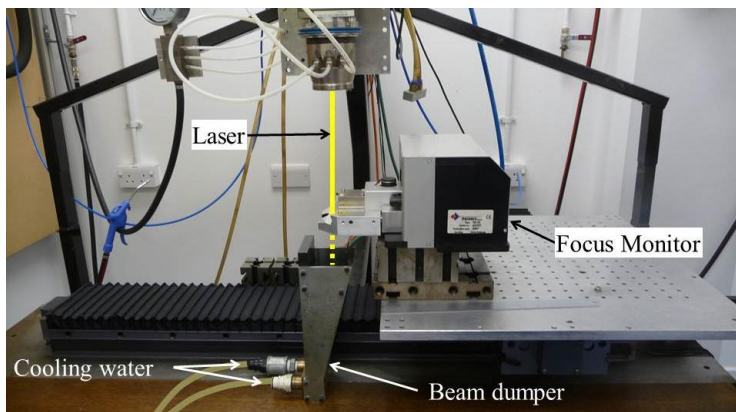


Figure 3.6- The experimental setup for monitoring the laser beam.

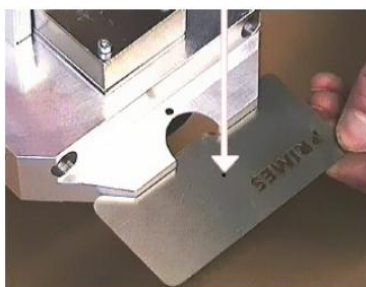


Figure 3.7- Adjustment plate on the focus monitor. Arrow shows the red guide beam path. Measuring tip has been rotated to avoid any crash with adjustment plate [99].

3.5.1 Finding the focal point by focus monitor

One of the most useful applications of the focus monitor is to find the focal point position of the laser beam since laser beam cannot be seen by eye or touched. The focus monitor was adjusted and mounted on the CNC table below the laser beam. The lens position on the outer surface of the cutting head was not identified; hence a relative measure method was used to calculate the focal point position. The distance of “A” (Figure 3.8-A) was measured by a calliper from the top surface of the beam profiler to any distinct point on the cutting head or collimator. The distance of “B” was given by the Primes company in the manual of the focus monitoring [99]. The distance of “C” is the distance from the position of the pinhole to the focal point position that the focus monitor has recognised. Considering Figure 3.8-A, the relative focal point position (F_R) can be calculated as per equation 3.1 below:

$$F_R = A + B - C \quad 3.1$$

The equation 3.1 is only usable for the lens with focal length of 120 mm. When the beam is focused by the lens with focal distance of 80 mm, due to a distance limitation in the Z axis during focus monitoring, the focus monitor was set up upside down with the inverted pinhole (Figure 3.38-B).

$$F_R = A + B + C \quad 3.2$$

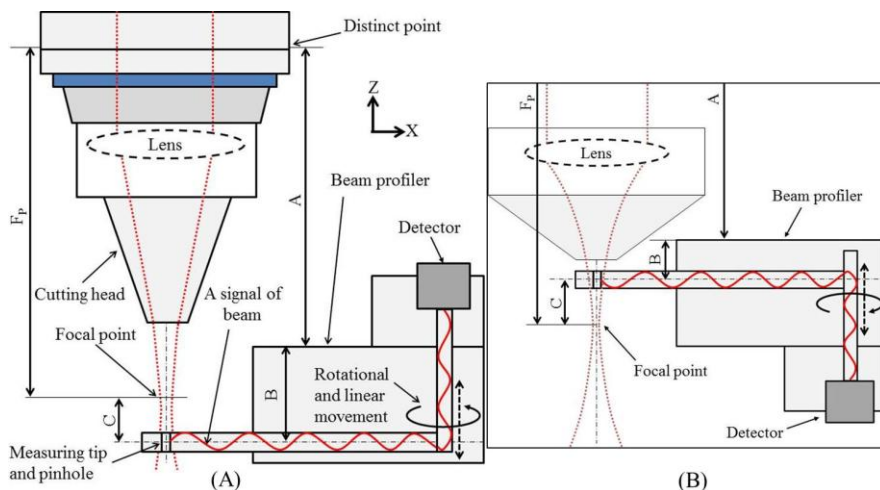


Figure 3.8- Showing the geometrical position of focus monitoring with cutting head. A) Usual setup of the focus monitor for focal length of 120 mm. B) Due to some space limitation between the focus monitor and the cutting head when monitoring the beam focussed by 80 mm-lens, the focus monitor was setup upside down with the inverted pinhole.

This set up still technically allows the focus monitor to characterise the focussed beam but the equation 3.1 must be changed to equation 3.2. The geometrical characteristics of two applied lenses in focus monitoring are shown in Table 3.7.

Table 3.7-Geometrical characteristics of two applied lenses in focus monitoring.

	Focal length (mm)		Comments
	120	80	
A (mm)	215	144.75	In this study.
B (mm)	20.5	4.5	According to the manual of Primes co [99].
C (mm)	17.5	26	Distance which was measured by the focus monitor.

In Figure 3.8, the measuring tip (pin hole) with a rotational movement records the beam geometries while moving up stepwise.

3.6 Beam monitoring results

Several useful laser beam characteristics can be ascertained by the focus monitor such as M^2 , Rayleigh length, raw beam diameter, beam parameter product (BPP), power density distribution and divergence angle as well as geometrical. Two cutting heads with different optical systems will be examined. The outcomes of laser beam characterisation are presented following.

3.6.1 Cutting head with focal distance of 120 mm

With a collimation focal of 125 mm, the magnification of the optical system in this case is 0.96 and can be calculated by equation 3.3 where M is magnification, d is the spot size and D_f is the fibre diameter:

$$M = \frac{F_{Focal}}{F_{Coll}} = \frac{d}{D_f} \quad 3.3$$

The beam profile for a fibre of 200 μm in a short interval of focal point at 18 planes is shown in Figure 3.9. The curve of beam profile realises a mathematical description of the beam propagation. It must be mentioned that for all beam profiles in this study the scale of X axis is μm while for Z axis it is mm.

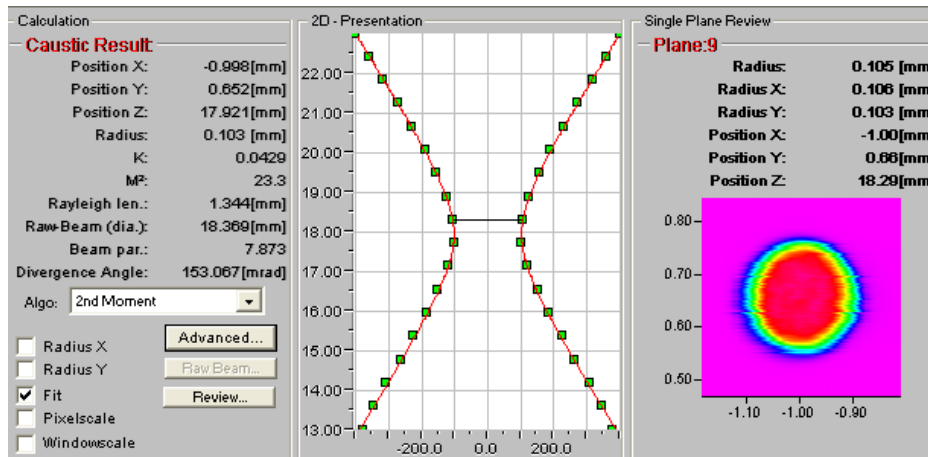


Figure 3.9- Focussed beam profile for fibre of 200 μm with focal length of 120 mm (600 W).

The focus monitor software can also generate a 3D presentation of the measured distribution of the laser power intensity (Figure 3.10). The shape of laser intensity propagation is symmetrical and quite similar to a top hat with Gaussian distribution.

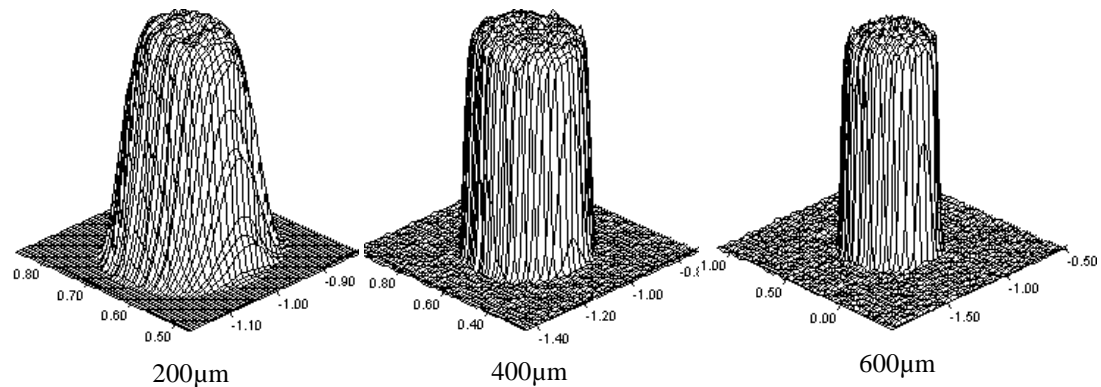


Figure 3.10- Energy distribution at the position of focus point and power of 600 W with focal length of 120 mm for different fibres.

Table 3.8 compares the results of theoretical and measured spot size for different applied fibres. Theoretical spot size was calculated by equation 3.3

Table 3.8- Indicating the theoretical and measured spot size using the lens with focal distance of 120 mm (600 W).

Fibre diameter	200 μm	400 μm	600 μm
Theoretical spot size (mm)	0.192	0.384	0.576
Measured spot size (mm)	0.201	0.374	0.605

A superposition of laser beam profile with a hole pierced by this beam allows one to envisage the geometrical situation of laser-material interaction during cutting or piercing as shown in Figure 3.11.

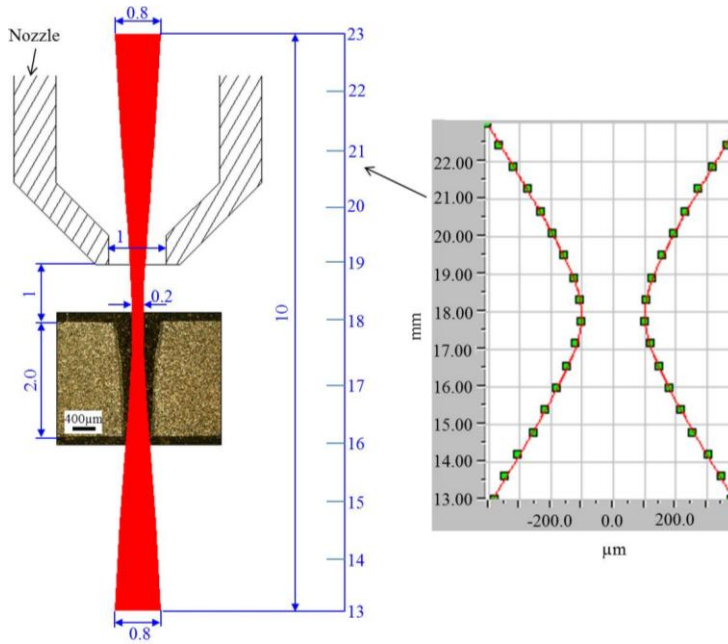


Figure 3.11- Superposition of beam profile with a pierced hole (Fibre diameter of 200 μm , focal length of 120 mm, irradiation time of 8 ms, power of 1.7 kW with 2 bar oxygen).

3.6.2 Cutting head with focal distance of 80 mm

The magnification of this optical system can be calculated from equation 3.3 previously shown:

$$M = \frac{F_{Focal}}{F_{Coll}} = \frac{80}{125} = 0.64$$

From equation 3.3, the focused beam diameter for fibre of 200 μm and for 400 μm can be determined as below:

$$\text{For } 200 \mu\text{m:} \quad d = M \cdot D = 0.64 * 200 = 128 \mu\text{m}$$

$$\text{For } 400 \mu\text{m:} \quad d = 0.64 * 400 = 256 \mu\text{m}$$

The focussed beam profile for fibre of 200 μm in a short interval of focal point at 20 planes is presented in Figure 3.12. The measured focussed beam diameter for fibre of 400 μm in four repetitions of monitoring was 260 μm however for 200 μm , it varied between 140 μm to 160 μm with an average spot size of 150 μm .

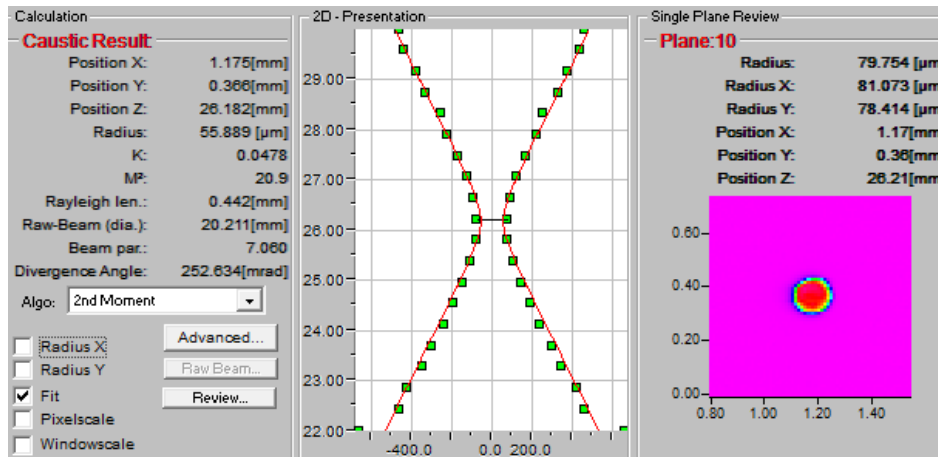


Figure 3.12- Focused beam profile for fibre of 200 μm with focal length of 80 mm (400 W).

The shape of laser intensity propagation is symmetrical and very similar to a top hat with Gaussian distribution.

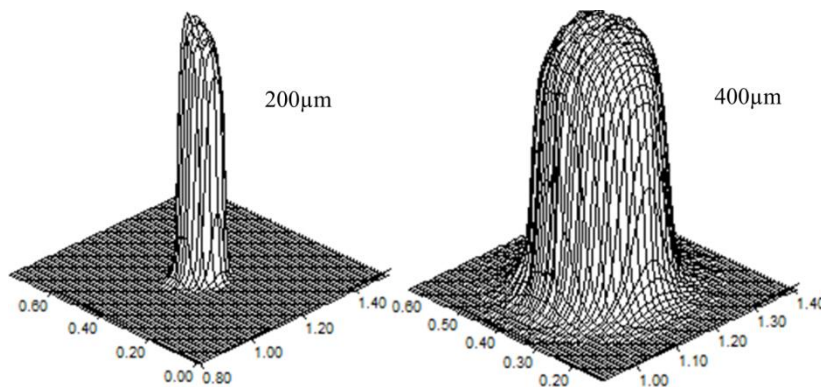


Figure 3.13- Energy distribution at the focus point with power of 400 W for different fibres with focal length of 80 mm.

3.6.3 Comparison of focussed beams with different focal length

3.6.3.1 Geometry of beams

Lenses with different focal lengths concentrate the beam at the focal point with different geometric characteristics which may affect laser cutting performance. A geometric comparison of four beams with fibres of 200 μm and 400 μm in diameter focussed by two different lenses with focal length of 120 mm and 80 mm is illustrated in Figure 3.14.

Total Rayleigh length in fibre of 200 μm for focal length of 120 mm is 2.66 mm while it is 0.882 mm for focal length of 80 mm. These values for 400 μm are 4.406 mm and 1.57 mm respectively. As can be seen, for fibre of 200 μm in 120 mm at the distance of 5 mm from the focal point (i.e. at zero) the diameter of beam is

0.8 mm while it is 1.0 mm for focal length of 80 mm at the distance of 4 mm. This means that the divergence angle in 120 mm is smaller than that is in 80 mm. More details to compare the inspected beams are indicated in Table 3.9.

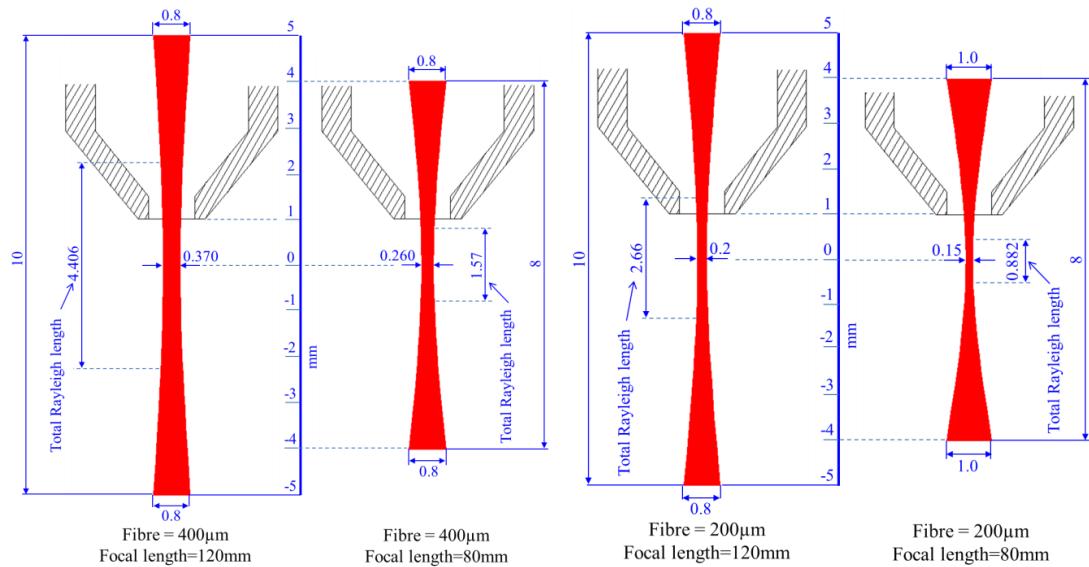


Figure 3.14- A comparison of four beams with fibres of 200 μm and 400 μm focussed by two different lenses with focal distance of 120 mm and 80 mm. This figure was carefully drawn in AutoCAD with using the geometric information which had been obtained by the focus monitoring tests.

The results of laser beam characterisation are presented in Table 3.9.

Table 3.9- Laser beam characteristics for different focal lengths and fibre diameters.

<i>Focal length</i>	<i>Mag.</i>	<i>Power (W)</i>	<i>Characteristics</i>	<i>200 μm</i>	<i>400 μm</i>	<i>600 μm</i>
120 mm	0.96	600	Focused beam dia. (mm)	0.20	0.370	0.60
			Rayleigh length (mm)	1.329	2.203	3.375
			Divergence angle (mrad)	153.6	168.27	176.76
			BPP (mm.mrad)	7.84	15.6	26.36
			M^2	23.3	46.2	78.1
80 mm	0.64	400	Focused beam dia. (mm)	0.150	0.260	-
			Rayleigh length (mm)	0.442	0.697	-
			Divergence angle (mrad)	252.6	324.96	-
			BPP (mm.mrad)	7.06	18.401	-
			M^2	20.9	54.5	-

3.6.3.2 Beam quality

Rayleigh length (RL) basically describes the depth of focus where the cross sectional area of the beam is twice that at the focal point. The results of focus monitoring indicate that the RL increases with fibre diameter but decreases with shorter focal distances (Table 3.9). With a 100% increase in the fibre diameter from 200 μm to 400 μm , there is a 66% increase in the RL. With an increase of 50% in the fibre diameter from 400 μm to 600 μm , there is 0.53% increase in the RL. When using the

fibre of 200 μm and decreasing the focal length from 120 mm to 80 mm, there is 67% reduction in the RL.

The Beam Parameter Product (BPP) describes the quality of a laser beam or more specifically, focus ability of an optical system [34]. The results show that the BPP increases with fibre diameter (Table 3.9). For the fibre of 200 μm and focal distance of 120 mm the BPP is 7.84 mm.mrad while it is 15.6 mm.mrad for 400 μm . The effect of focal length on the BPP varies. In 200 μm when the focal length is decreased from 120 mm to 80 mm, the BPP decreases from 7.84 mm.mrad to just 7.06 mm.mrad whilst for the 400 μm thick fibre, the BPP increases from 15.6 mm.mrad to 18.4 mm.mrad. The same trend is also seen for M^2 because BPP is proportion to M^2 as shown by equation 3.4 [21, 59].

$$BPP = \frac{\lambda}{\pi} M^2 \quad 3.4$$

The results of focus monitoring in Table 3.9 show that the RL increases with beam diameter. Equation 3.5 indicates that the RL is proportional to the other beam characteristics [21, 59].

$$RL = \left(\frac{d}{2}\right)^2 \cdot \frac{\pi}{\lambda \cdot M^2} = \frac{\left(\frac{d}{2}\right)^2}{BPP} \quad 3.5$$

Investigation into the laser beams characteristics indicated that for both focal lengths the divergence angle slightly increases as fibre diameter increases (Table 3.9) However when using the same fibre, the divergence angle significantly increases as focal length decreases. As far as the effect of power on the beam characteristics is concerned, an investigation on the 400 μm fibre with focal distance of 80 mm indicated that there is a very small difference in the results when the power increases from 400 W to 600 W, as presented in Table 3.10.

Table 3.10- The effect of power on the focussed beam characteristics (Fibre of 400 μm and focal distance of 80 mm).

Characteristics	400W	600W
<i>Focused beam dia. (mm)</i>	0.260	0.264
<i>Rayleigh length (mm)</i>	0.70	0.785
<i>Divergence angle (mrad)</i>	325	312
<i>BPP (mm.mrad)</i>	18.4	19.0
<i>M^2</i>	54.5	56.4

3.6.3.3 Peak power intensity

A comparison of utilised fibres in terms of peak power intensity versus focal point position is shown in Figure 3.15. With 600 W of power, the maximum power intensity reported by the focus monitor for fibre of 200 μm is 2186.7 kWcm^{-2} . For the 400 μm and 600 μm fibres, these values decrease to 592 and 236 kWcm^{-2} respectively. Hence, peak power intensity is increased with decrease in the beam diameter.

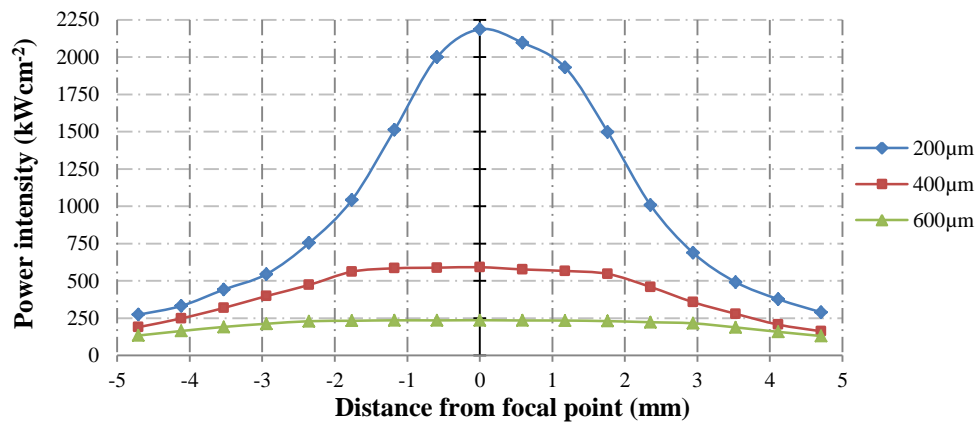


Figure 3.15- Showing a comparison of employed fibres in terms of power intensity distribution throughout the focal point position (focal length of 120 mm with power of 600 W).

Figure 3.15 indicates that with the same lens (the same focal length), the focus point position on or below the sheet surface using the fibre of 200 μm is more sensitive than 600 μm because the highest power intensity is only available at the focal point (i.e. 0). Additionally, the slope of power intensity reduction in 200 μm is steeper than that is in 600 μm . For example, by being out of focus by 1.2 mm, the power intensity reduction for 200 μm is 11% while it is less than 1% for 600 μm . However, at this point the 200 μm has still higher power intensity than 600 μm .

As the fibre diameter increases, the maximum power intensity decreases with a constant power (Figure 3.16). As can be seen, the power intensity at the point of Rayleigh length is about 80% of that is in the focal point.

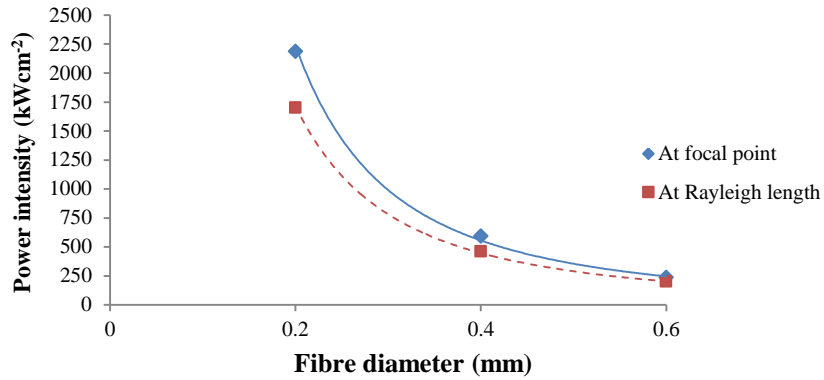


Figure 3.16- Power intensity as a function of fibre diameter at focal point and Rayleigh length for power of 600 W and focal distance of 120 mm.

Power intensity distribution throughout the focal depth for fibres of 200 μm and 400 μm with focal length of 80 mm for different powers of 400 W and 600 W are indicated Figure 3.17. As can be seen with the same power of 400 W, the peak power intensity for 200 μm is 3.5 times greater than that is for 400 μm .

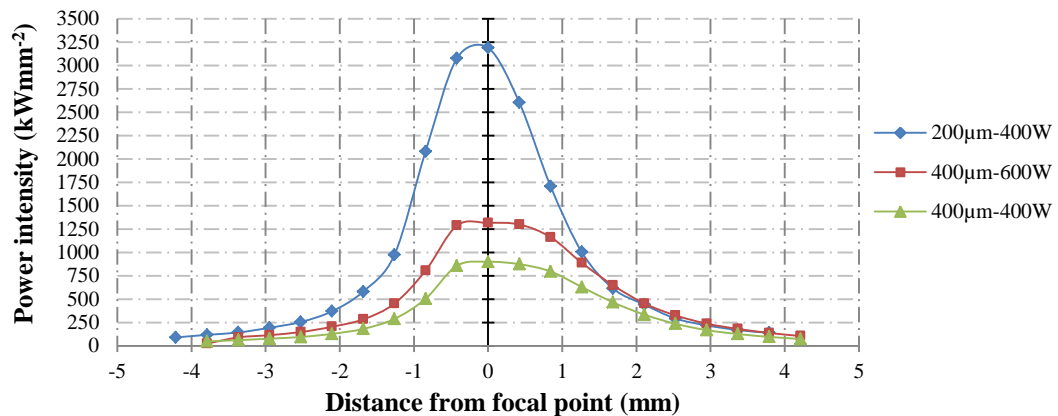


Figure 3.17- Indicating a comparison of two employed fibres in terms of power intensity distribution throughout the focal point position with different powers (focal length of 80 mm).

A comparison of power intensity distribution throughout the focal depth for different fibres, focal length and powers is shown in Figure 3.18.

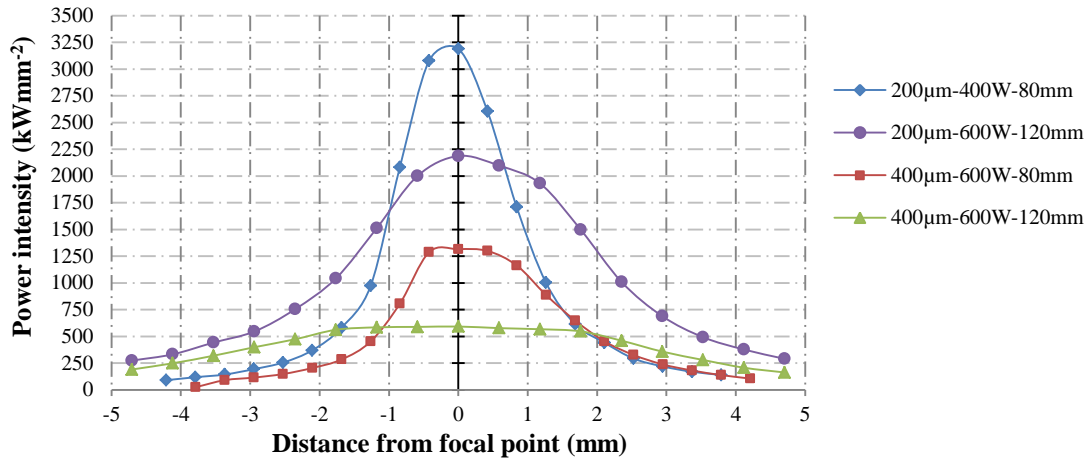


Figure 3.18- Power intensity distribution for different fibres, focal lengths and powers.

3.6.3.4 Technical analysis

During laser cutting, especially when piercing the start-up hole, lots of upward dross splashes from the melting zone. This splash can damage the cutting head. Moreover, the high temperature of melt in laser cutting of plates can heat up the cutting head. As can be seen in Figure 3.19 the height of cone for the focal distance of 120 mm is 83.9 mm while this is 41.6 mm for focal distance of 80 mm. From a technical point of view, applying a cutting head with a taller cone (focal length of 120 mm) might be advantageous as it may avoid any damage to the cutting head and optics from the dross splashes and temperature of melting zone, especially in long term laser cutting of thick material (Figure 3.20).

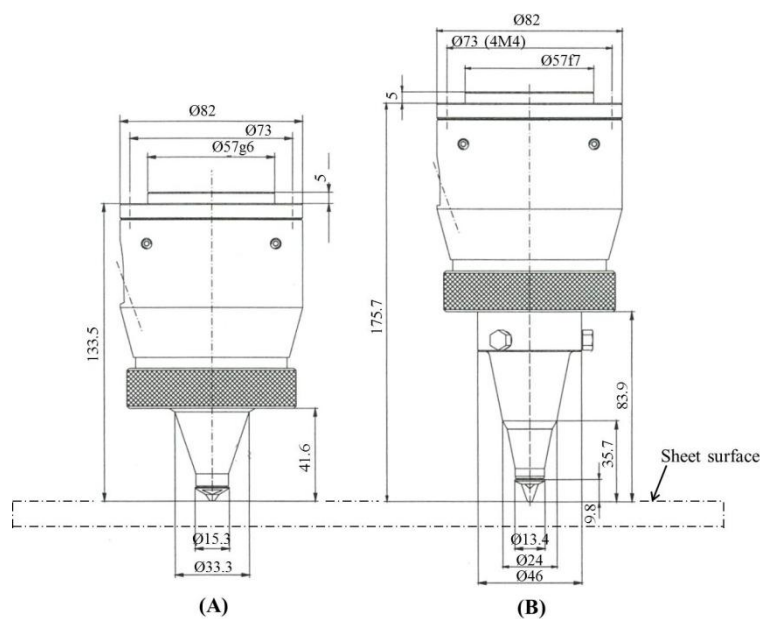
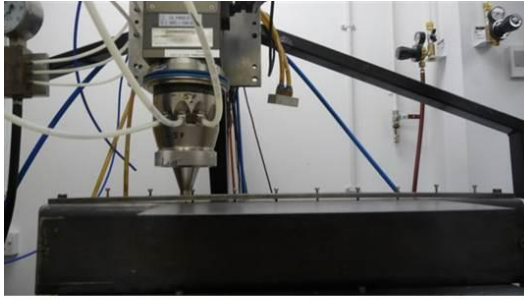
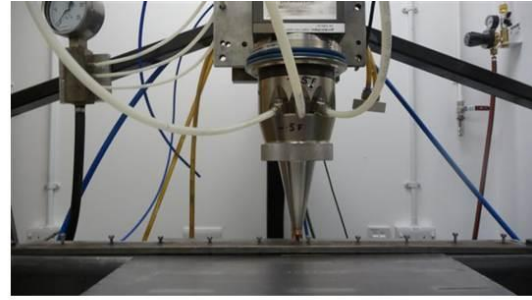


Figure 3.19- Dimensions of employed cutting heads. A) Focal length of 80 mm, B) 120 mm.



Focal length = 80mm



Focal length = 120mm

Figure 3.20- Showing two employed cutting heads are setup on the sheet ready to cut.

3.6.4 Focal point distance and focused beam diameter

The results of focus monitor for fibre of 200 μm and the lens with focal distance of 120 mm in the power range of 200 W to 800 W show that at the constant relative focal length (i.e. $F_R = 218$ mm), the diameter of focused beam slightly increases from 202 μm to 220 μm with increasing power. As is seen in Figure 3.21, in the range of applied power, the change of spot size with increasing power is insignificant; with a 400% increase in the power, there is less than 9% increase in the spot size.

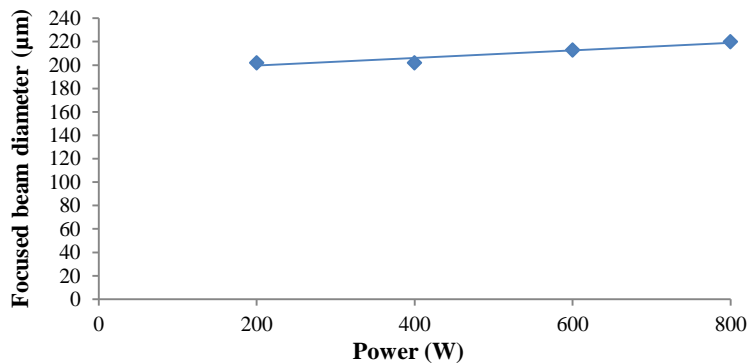


Figure 3.21- Focused beam diameter as a function of power for fibre of 200 μm at the constant relative focal length of $FR = 218$ mm.

The slight increase in the spot size is due to the focal point distance slightly decreasing as power increases as shown in Figure 3.22. It is well known that for a given optic, reduction in the focal point distance is related to the thermal expansion of the focusing lens [1, 2, 33, 70, 76, 110]. During laser cutting, when the laser beam is passing through the lens, a small portion of laser power is absorbed by the focussing lens, resulting in the lens heating and expanding in three dimensions. Absorption takes place mainly in the anti-reflective coatings (AR coatings), scratch and on dirt on the lens [111]. It should also be noted that in the power range of

200 W to 800 W, the amount of focal point shifting is insignificant; with a 0.03% decrease in focal distance as power is increased to 400%.

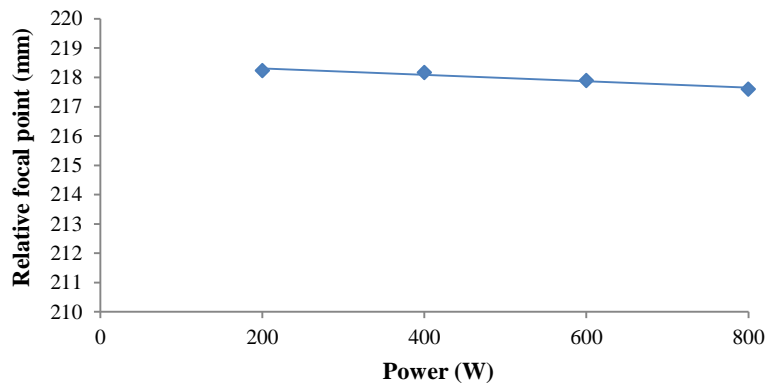


Figure 3.22- Relative focal point position (FR) as a function of power for fibre of 200 µm.

As far as the effect of irradiation time on the focal distance is concerned, previous research with the same laser showed that the focus shifting is also time dependent but the majority of the focal point shifting would happen only in the first five minutes of laser illumination [52].

3.6.5 Focal point position adjustment

Based on the laser beam monitoring results, the focal point can be adjusted in the cutting head by changing the position of lens by using the focal adjustment tool shown in Figure 3.23. The position of the lens can be read using the focal adjustment tool as it has been marked with lines from +5 to -4 mm. A complete rotation of the adjusting tool can move the lens 1 mm up or down depending on the direction of rotation. Each quarter of rotation on the tool has been marked so the accuracy of the tool is 0.25 mm. According to the beam monitoring results (Table 3.9) and by using equation 3.1 the relative focal length (F_R) for the 200 µm fibre and the focal length of 120 mm can be calculated as:

$$F_R = 215 + 20.5 - 18 = 217.5 \text{ mm.}$$



Figure 3.23- Focal point adjustment tool for YK52 cutting head.

With the distance of $F_R = 217.5$ mm, the focal point is placed on the surface of workpiece with a stand-off distance of 0.5 mm as shown in Figure 3.24-A. In order to set up cutting head with the stand-off distance of 1 mm, the lens was shifted downward by 0.5 mm and the cutting head was moved up by 0.5 mm as indicated in Figure 3.24-B. Performing this adjustment allows the focal point to be located on the upper surface of the sheet and the stand-off distance to be set at 1 mm.

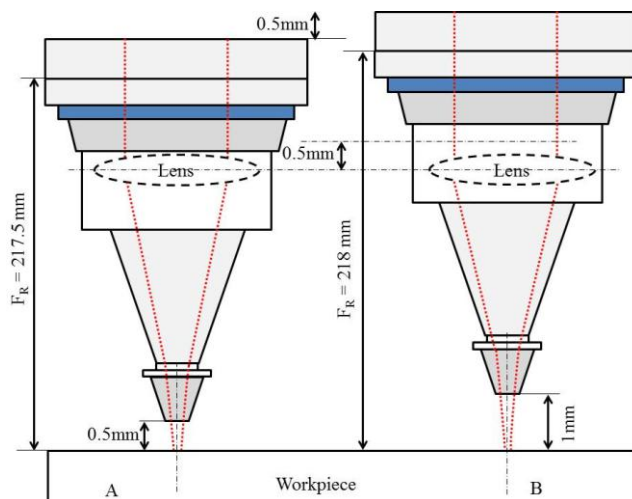


Figure 3.24- Focal point position adjustment. A) Before adjustment, B) After adjustment.

The relative focal length (F_R) and lens position for different fibres are presented in Table 3.11. The position of lens is different for different fibres and focal lengths.

Table 3.11- Relative focal length and lens position for different fibres and optical systems.

Optical system	Characteristics	200 μ m	400 μ m	600 μ m
120 mm	<i>Relative focal length</i>	218 mm	218.5 mm	218.5 mm
	<i>Lens position</i>	-0.5 mm	-1 mm	-1 mm
80 mm	<i>Relative focal length</i>	175.75 mm	175.75 mm	-
	<i>Lens position</i>	0.75 mm	0.25 mm	-

It is well known that in laser cutting, generally, the best position for the focus point is on the surface of workpiece. Literature also reports that a narrow kerf width in cutting of thin plate can be achieved when the focus point is on the surface of sheet. In order to find out the effect of lens position (focal point position) on the kerf width and also trust in the positioning of the lens, nitrogen cuts using the fibre of 200 μm , 400 μm and 600 μm were carried out on 1 mm-thick mild steel sheet. The results are presented in Figure 3.25. As can be seen, when the laser beam is focussed on the upper surface of the sheet, the kerf width becomes narrow.

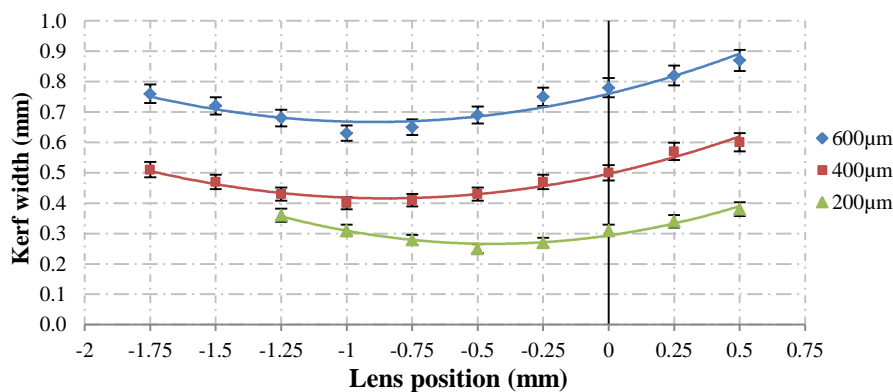


Figure 3.25- Kerf width versus lens position for different fibres (focal length of 120 mm, 1 mm thick mild steel, 12 bar nitrogen, $V = 500$ mm/min, $P = 250$ W).

A comparison of the employed fibres and optics in terms of lens position and kerf width is illustrated in Figure 3.26. The narrowest kerf width was achieved by the focal length of 80 mm and fibre of 200 μm . As can be seen, the lens position is different for different fibres.

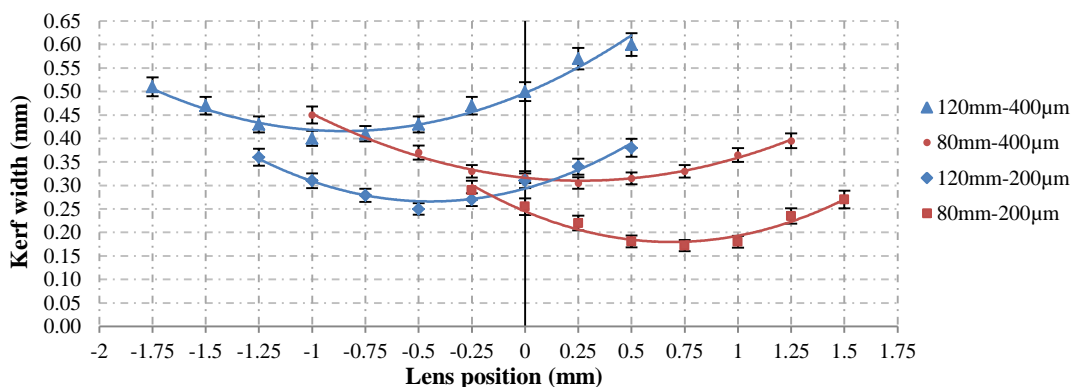


Figure 3.26- Comparison of employed fibres and optical systems in terms of lens position and kerf width (1 mm thickness, 12 bar nitrogen, $V = 500$ mm/min, $P = 250$ W).

3.6.6 Machine setup

Before performing the tests, the laser cutting machine should be checked and set up carefully in terms of:

- 1-** Optical components: These should be clean. Any dust in the way of the laser beam and on the optical components such as fibre connectors, lens, collimator and nozzle can absorb the laser beam, decreasing the laser power.
- 2-** All components should be of high quality and adhere to the safety standards according to the machine manuals and laser risk assessment booklet.
- 3-** Beam-nozzle alignment: Ensure that the laser beam is exactly in the centre of nozzle. This is possible by using the scotch tape. When the laser beam is off, a piece of scotch tape is attached to the nozzle and then, the laser beam with a power of 100 W is turned on just for a fraction of a second (e.g. 2 ms). On the surface of the scotch paper there are two features. One of them is a circular indentation which is marked by the nozzle and the second one is a hole burnt by the laser beam. If the hole has been located in the central of the circular indentation, it means the laser beam has been located in the centre of nozzle. Otherwise, by using the three lens centring screws on the cutting head, the laser beam can be aligned with the nozzle.
- 4-** The workpiece should be fixed on the table of machine by using a suitable fixture. The fixture should also allow the assist gas and melt to flow down through the cut.
- 5-** Stand-off distance is 1 mm. To adjust it, move the cutting head up and down by its motor and use a 1 mm block gauge to control the distance between the nozzle and plate.
- 6-** The focal adjustment tool is used to adjust the position of focal spot. In all experiments, the focal spot was on the top of surface.
- 7-** Select the assist gas. Check the feeding assist gas pipes to the cutting head. An accurately calibrated manometer shows the pressure of gas. The gas pressure can be adjusted by a regulator which is located in the piping system. A system of ventilation must be used to avoid any damage to respiration system.
- 8-** Set up cutting speed and power according to the experiment plan and then locate the nozzle in one side of the sheet. Use laser goggles before cutting.

3.7 Oxygen- fibre laser cutting

The first aim of this experiment is to confirm that the kerf width in oxygen-fibre laser cutting of mild steel sheet is wider than the diameter of laser beam. The second aim is to find out how the kerf width changes with changes in sheet thickness, power and cutting speed. Thirdly, to observe the striation generation and striation pattern on the cut edge. Finally, analysis of surface roughness in order to find out the effect of cutting parameters on the surface roughness will be carried out.

3.7.1 Experiment parameters

The experiment parameters are shown in Table 3.12. Each cut was repeated three times in order to increase the accuracy of results. A nozzle tip of 1 mm with 1 mm stand-off distance and 2 bar oxygen was used. The employed fibre diameter was 200 μm and the focussed beam size on the upper surface of workpiece was 0.2 mm using a lens with focal length of 120 mm. Mild steel sheet with three different thicknesses of 1, 1.6 and 2 mm were used in this experiment.

Table 3.12- Laser cutting parameters in oxygen laser cutting.

No	Target Power (W)	Cutting speed (mm/min)
1	1000	4000
2	1000	5000
3	1000	6000
4	1500	4000
5	1500	5000
6	1500	6000

3.8 Nitrogen-fibre laser cutting

3.8.1 Initial experiment

The first aim of this test is to discover experimentally how nitrogen as an assist gas affects the fibre laser cutting of mild steel. The second aim is to compare laser-oxygen and laser-nitrogen cutting in terms of kerf width, kerf width ratio and surface roughness.

3.8.1.1 Experiment parameters

The experimental plan is illustrated in Table 3.13. The nitrogen cuts were carried out using a 200 μm fibre, a 120 mm focal length lens, a 1 mm orifice nozzle with and

1 mm stand-off distance, 12 bar nitrogen pressure and 1 to 3 mm sheet thickness. The beam was focussed on the surface of workpiece with the spot size of 0.2 mm.

Table 3.13- Experiment parameters for initial laser cutting of mild steel with nitrogen.

No	Power (W)	Cutting speed (mm/min)
1	1000	400
2	1000	900
3	1000	2000
4	1500	400
5	1500	900
6	1500	2000

3.8.2 Cutting with maximum cutting speed

The purpose of this experiment is to specify the maximum cutting speed for the employed power in nitrogen laser cutting of mild steel using different fibres, focal lengths and sheet thicknesses. The results of this experiment will be used to investigate the fundamental interaction parameters such as specific point energy later in chapter 6.

3.8.2.1 Experiment methodology

The first step was to specify the minimum power and the relevant maximum cutting speed in laser cutting of different thicknesses. This initial experiment confirmed that below the employed powers there was no through cut. In other words, specified powers were the lowest powers that could penetrate and cut the applied sheet. Five different thicknesses of 1 mm to 6 mm were cut using different fibre diameters of 200 μm , 400 μm and 600 μm . Nitrogen pressure was 12 bar and the stand-off distance was 1 mm with using a 1 mm nozzle. A lens with focal length of 120 mm was applied and the focus point position for each fibre was adjusted on the surface of workpiece. The results of these cuttings are shown in Table 3.14 and were used in the next step of experiment.

Table 3.14- Minimum power at relevant maximum cutting speed to cut the applied sheets.

Fibre diameter	Parameter	1 mm	2 mm	3 mm	4 mm	6 mm
200 μm	Cutting speed	0.12 m/min	0.12 m/min	0.12 m/min	0.12 m/min	0.15 m/min
	Real Power	140 W	250 W	350 W	450 W	700 W
400 μm	Cutting speed	0.22 m/min				
	Real Power	170 W	300 W	425 W	580 W	900 W
600 μm	Cutting speed	0.36 m/min	0.36 m/min	0.36 m/min	0.36 m/min	0.45 m/min
	Real Power	250 W	375 W	550 W	680 W	1300 W

The initial results as also presented in Figure 3.27 indicate that the lowest power to cut the sheet increases with sheet thickness. The smaller the beam diameter, the lower the minimum power is. The graph becomes curved as the beam diameter increases especially when cutting thicker sheets.

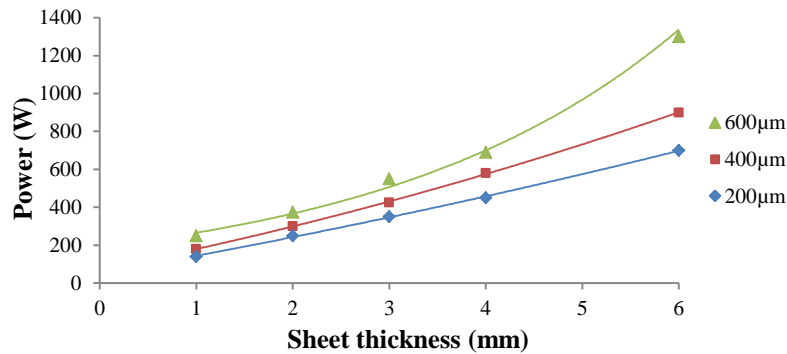


Figure 3.27- Minimum power at maximum cutting speed versus thickness for different fibres. The cutting speed range has given in Table 3.14.

The energy per unit length (E_L) can be calculated with equation 3.6. This calculates how much energy is delivered to cutting zone when a power of P is delivered to the cutting zone by a focussed beam moving with a constant cutting speed of V [46].

$$E_L = \frac{P}{V} \quad \{ Jmm^{-1} \} \quad 3.6$$

Using Table 3.14 and equation 3.6, the energy per unit length (E_L) delivered to cutting zone was calculated and the results are presented in Figure 3.38 for different thicknesses and fibres. This is the minimum energy because for each employed power the cutting speed is at the relevant maximum value. As can be seen the smaller the laser beam, the higher the E_L consumed for cutting. The E_L increases with increasing the sheet thickness.

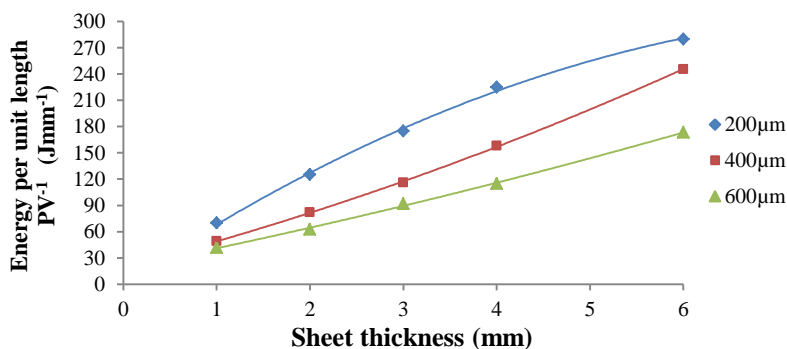


Figure 3.28- Minimum energy per unit length versus thickness for different fibres, 12 bar N2.

In the next experiments, the maximum cutting speeds were specified for different powers using the flowchart (Figure 3.29). First, the fibre and sheet thickness are selected followed by the machine being set up for the minimum power and the relevant maximum cutting speed using Table 3.14. Afterwards, cutting is carried out. This flowchart has two If-Then constructs to specify the minimum power for selected cutting speed.

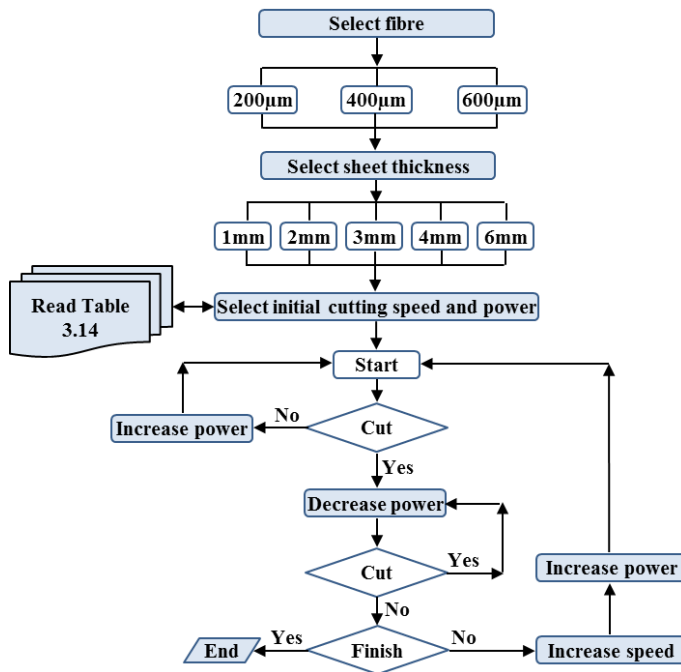


Figure 3.29- Maximum cutting speed experiment flowchart.

Cutting speed increases in accordance with the interaction time (T_i) and fibre diameter as presented in Table 3.15. Interaction time (T_i) will be discussed later in chapter 6 however here this is appropriate to state the equation of T_i as below:

$$T_i = \frac{d}{V} \quad \{sec\}$$

Where d (mm) is the spot size and V (mm/sec) is the cutting speed. Table 3.15 presents used cutting speed ranges for each employed fibre, focal length and specific interaction time (T_i).

Table 3.15- Cutting speed (mm/min) for each employed fibre, focal length and Ti.

Ti (ms)	200 μm		400 μm		600 μm	
	120 mm	80 mm	120 mm	80 mm	120 mm	80 mm
100	120	90	220	156	360	-
80	150	112	280	195	450	-
60	200	150	370	260	600	-
40	300	225	550	390	900	-
30	400	300	740	520	1200	-
20	600	450	1100	780	1800	-
10	1200	900	2200	1560	3600	-
7	1700	-	3171	-	5100	-
5	2400	1800	4550	3120	7200	-

Table 3.16 presents brief results for cutting of 4 mm-thick sheet using 200 μm fibre.

Table 3.16- Showing a concise table of cutting parameters used in maximum cutting speed experiment. Parameters were capable to cut the sheet, selected for next analysis (fibre diameter of 200 μm , spot size of 0.2 mm, focal length of 120 mm, 4 mm-thick mild steel, 12 bar N_2).

Seq.	Ti(ms)	V (mm/min)	Target power(W)	Real power(W)	Result
1	100	120	522	450	Cut
2	100	120	500	430	No cut
3	60	200	557	480	Cut
4	60	200	534	460	Cut
5	60	200	522	450	No cut
6	30	400	924	800	Cut
7	30	400	890	770	Cut
8	30	400	866	750	No cut
9	20	600	1039	900	No cut
10	20	600	1096	950	Cut
11	20	600	1062	920	No cut
12	10	1200	1200	1384	No cut
13	10	1200	1300	1458	Cut
14	10	1200	1250	1441	No cut
15	7	1700	1300	1800	No cut
16	7	1700	1620	1866	Cut
17	7	1700	1580	1820	No cut

3.9 Kerf width measurement

Due to acceleration and deceleration of machine's table at the beginning and the end of cutting process respectively, the kerf width should be measured at the middle of cut path where the cutting speed is steady. In order to increase the accuracy of measurement, the kerf width was measured in three points on each cut path as shown in Figure 3.30.

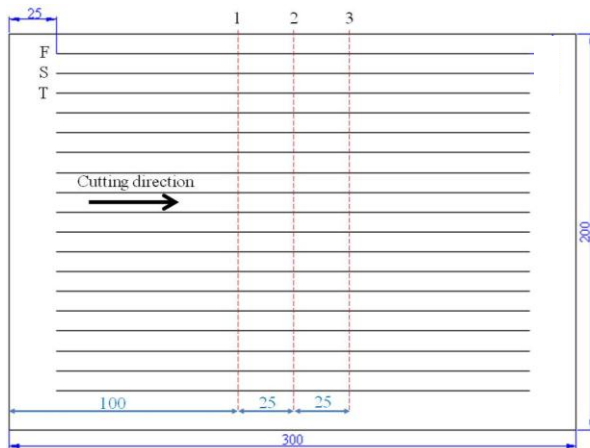


Figure 3.30- Illustrating the plan of kerf width measuring position on the cut sheet (mm).

All cuts were observed and measured under a digital microscope (Keyence VHX-100 Series Digital Microscope) and a 100x lens was used (Figure 3.31).



Figure 3.31- Keyence VHX-100 Series Digital Microscope used to measure the kerf width [52].

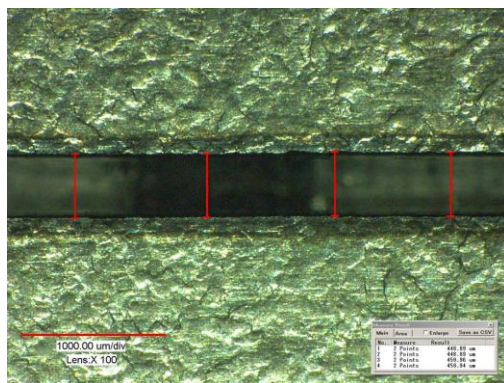


Figure 3.32- Showing the top kerf and the measurement positions.

Each position (1, 2 & 3 in Figure 3.30) was observed under a microscope and measured. In order to increase the accuracy of measurement, four points in each position (a total of 12 points in each cut path) were selected to measure as shown in Figure 3.32.

3.10 Surface roughness measurement

One of the purposes of doing this experiment was to analyse the surface roughness of cut edge. After the kerf measurements, the surface of the workpiece was engraved by a marker and needle with arrows to show the direction of cut and numbers or codes showing the parameters of cut. The engraved sheet was chopped by guillotine and from each laser cut, two samples were made.

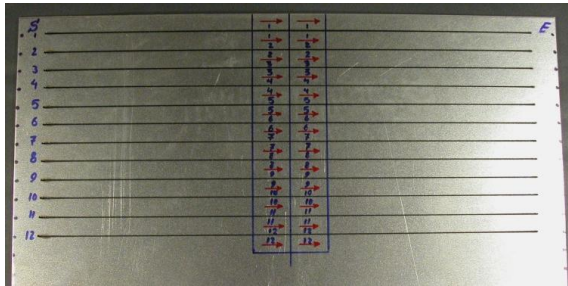


Figure 3.33- Workpiece was engraved before chopping up.

In order to study the surface roughness of the cut edge, three positions of every cut edge (upper, middle and lower surface of cut edge) were scanned by profilometer as shown in Figure 3.34.

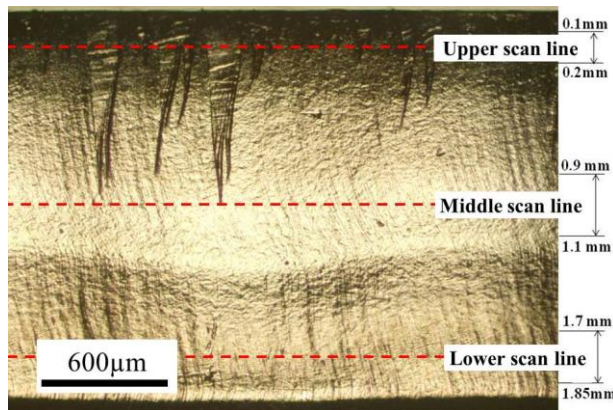


Figure 3.34- Showing the positions of surface roughness scan lines. (2 mm, 2 bar oxygen, 1000 W, 5 m/min).

Surface roughness analyses of the top, middle and bottom of the cut edge were measured by a Hobson precision CLI 100 profilometer (Figure 3.35). The sample was fixed by two magnets on the table of profilometer.

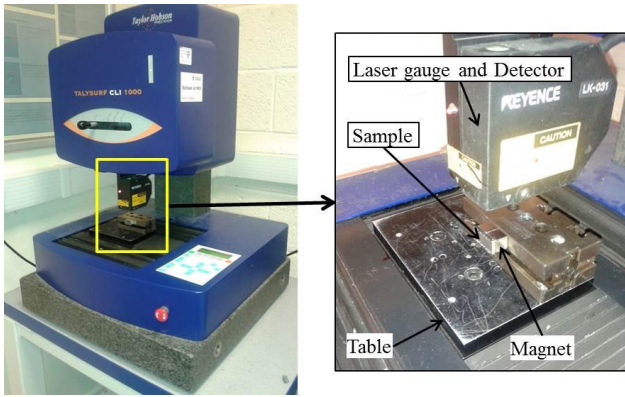
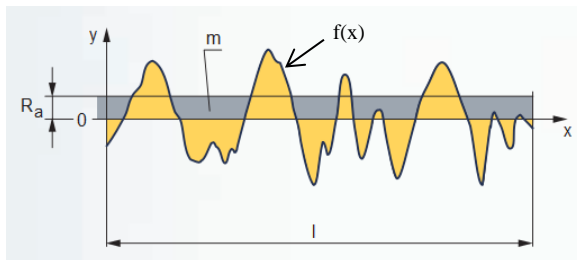


Figure 3.35- Hobson precision CLI 100 profilometer.

In surface roughness analysis, two roughness parameters are more commonly used consisting of [112]:

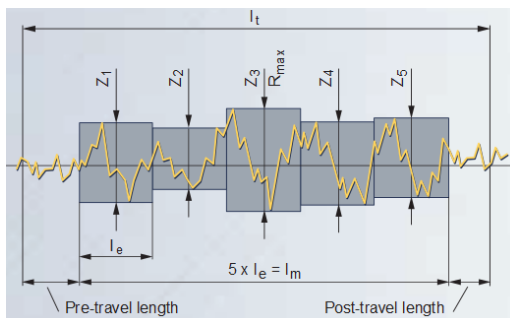
- 1- The arithmetical mean deviation of the profile, R_a , which is the mean value of the absolute value of the profile departure y within the reference length l as shown in
- 2- Figure 3.36 (according to ISO 4287 and DIN 4768).



$$R_a = \frac{1}{l} \int_0^l |f(x)| dx$$

Figure 3.36- A definition of surface roughness R_a [112].

- 3- The mean roughness depth, R_z , which is the arithmetical mean of the single roughness depths of successive sampling lengths l_e as indicated in
- 4- Figure 3.37 (according to DIN 4768).



$$R_z = \frac{1}{n} \sum_{1}^n Z_n$$

Figure 3.37- A definition of surface roughness R_z [112].

Ra is generally recognised in manufacturing engineering and it is the most employed international parameter of roughness which is why we used it in our research.

In Figure 3.38, the surface roughness + waviness profile of the middle cut edge shown in Figure 3.34 is indicated. As can be seen, a type of waviness can be observed in the results. This is due to the wobble of the laser machine's table. The waviness can be filtered out the results by the profilometer's software (Figure 3.38B). The pitch of waviness is 2.5 mm while the pitch of table's lead screw is 5 mm. The surface roughness profile can be obtained separately by the profilometer's software as illustrated in Figure 3.38C. Due to the fact that the laser cutting is a non-contact cutting process, the dynamic behaviour of the laser cutting equipment affects the surface roughness profile as indicated in Figure 3.38.

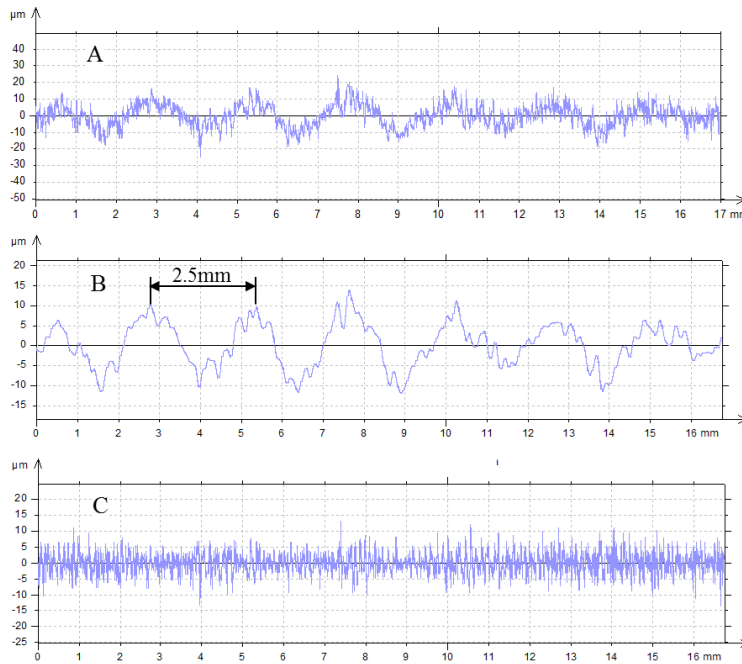


Figure 3.38- Indicating a result of surface roughness measured in the middle of cut edge shown in Figure 3.34. The length of sample is 17 mm. A) Surface roughness + waviness profile. The profile was calculated after a Gaussian filtering of 0.8 mm. B) Illustrating the waviness profile, the pitch of waviness= 2.5 mm. C) Showing the surface roughness, Ra = 2.2 μm .

3.11 Laser piercing

Every laser cutting process begins with a laser piercing process which creates a hole through the material to be used at the start of the cut. As a part of this research, the piercing process was investigated to understand how the initial hole is created and how the laser parameters affect that.

3.11.1 Experimental method

An IPG fibre laser with maximum power of 2 kW, 1.06 μm wavelength was used in the continuous wave mode. Powers in the range of 600 W to 2000 W were used. The laser beam was delivered into the cutting head by a 200 μm diameter optical fibre and focussed by a 120 mm focal length lens into a spot with a diameter of 200 μm . The focal position was on the top surface of the workpiece and the focus did not move with respect to its original position as piercing progressed. A 1 mm diameter nozzle was used to deliver the assist gas coaxially to the laser beam, the standoff distance between nozzle and sample surface was 1 mm. Table 3.17 briefly shows the parameters which were used in the piercing experiments. It should be noted that the laser was only on for the times stated, however the assist gas continued to flow for some time after the laser had been turned off. For each parameter setting, five holes were pierced and the results presented are the average values.

Table 3.17- Briefly shows the laser powers, gas type and gas pressures in piercing experiments.

<i>Assist gas</i>		<i>Laser power (W)</i>						
Gas	Pressure (bar)	600	800	1000	1200	1400	1700	2000
N ₂	0.3		•	•	•	•		
N ₂	2			•	•	•	•	•
N ₂	4					•	•	•
N ₂	8					•	•	•
N ₂	12					•	•	•
O ₂	0.3	•	•	•	•	•		
O ₂	2	•	•	•	•	•	•	•
O ₂	4					•	•	•
O ₂	8					•	•	•

3.11.2 Nitrogen laser piercing

The aim of this study is to consider the effects of nitrogen as an assist gas on hole growth, breakthrough time and hole geometry with increasing irradiation time. Every set of piercing experiments were started with a specified power and constant pressure as the irradiation time increased from 2 ms until the breakthrough time occurred (Table 3.18).

Table 3.18- Parameters for nitrogen laser piercing.

<i>Power (W)</i>	<i>Pressure (bar)</i>					<i>Increasing irradiation time (ms)</i>
800	0.3		-	-	-	2, 4, 6, 8, 10, 12, 14, ...
1000	0.3	2	-	-	-	
1200	0.3	2	-	-	-	
1400	0.3	2	4	8	12	
1700	-	2	4	8	12	
2000	-	2	4	8	12	

3.11.3 Oxygen laser piercing

The effect of oxygen on the laser piercing was examined. The experimental method, overall, was as same as the nitrogen piercing (Table 3.19). The results will compare with laser-nitrogen piercing in chapter 5.

Table 3.19- Parameters for oxygen laser piercing.

Power (W)	Pressure (bar)				Increasing irradiation time (ms)
	0.3	2	4	8	
600	0.3	2	4	8	2, 4, 6, 8, 10, 12, 14, ...
800	0.3	2	4	8	
1000	0.3	2	4	8	
1200	0.3	2	4	8	
1400	0.3	2	4	8	
1700		2	4	8	
2000		2	4	8	

3.11.4 Sample preparing

Piercing parameters were engraved below every set of the pierced holes (Figure 3.39). The workpiece was kept on a plastic zipper bag with silica gel to avoid any rust on the workpiece. All holes were observed under the optical microscope and measured the diameter of upper and lower diameter (Figure 3.40).

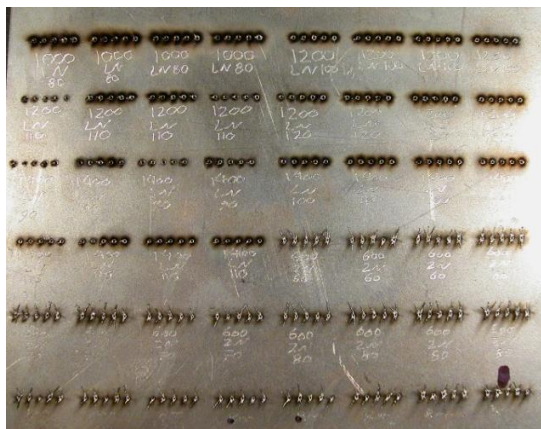


Figure 3.39- Engraving of workpiece.

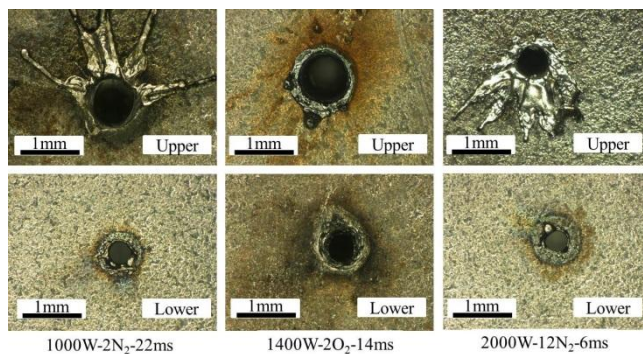


Figure 3.40- The upper and lower surface of the holes were observed and measured under an optical microscope.

In order to get an exact measure of the hole dimensions (depth, width) and also observe the heat affected zone (HAZ) and re-solidified zone (RSZ), each sample were sectioned, ground and etched in Nital 2%. After piercing experiments, the sheet was engraved and chopped to make the samples. Every sample included a set of five holes which were pierced by the same laser conditions and mounted in a conductive mounting resin. The main issue in the making of a hole cross section was working out the mid plane of the hole. The methodology is as follows:

- 1) Gentle grinding
- 2) Etch in nital 2%
- 3) Taking a photo under an optical microscope.

The taken photos were saved for future work. The procedure of sample grinding was important. Every sample was ground gently with a slight slope as is shown in Figure 3.41. To control the slight slope and also to avoid any diversion during grinding, a square tool frequently was used.

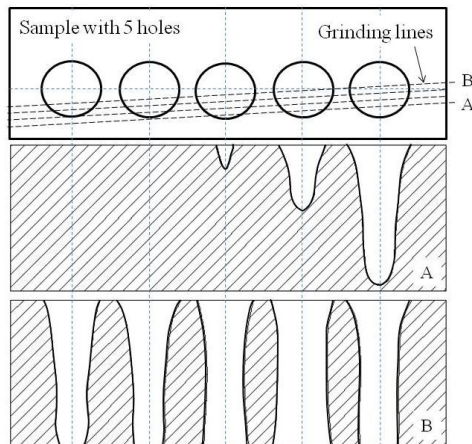


Figure 3.41- Indicating the top view of a sample with inclined grinding lines.

Two 3D view models of a ground sample are illustrated in Figure 3.42.

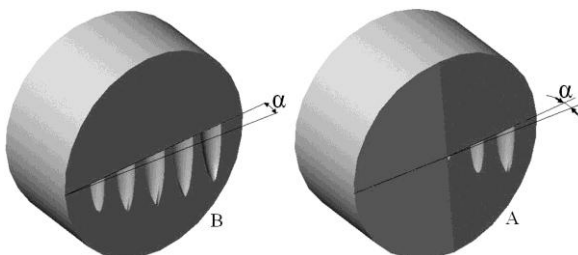


Figure 3.42- 3D view of a ground sample. A) Beginning of grinding, B) continuing of grinding.

Figure 3.43 shows the photos of a sectioned sample which was pierced with a 2 kW laser and 8 bar nitrogen pressure at an irradiation time of 8ms. This was subsequently ground and etched in Nital 2%. By observation of all photos, the mid-plane of the hole was found. In the mid-plane position, there is a photo that its previous photo and its next photo have smaller width. This photo represents the mid-plane of the hole as marked in Figure 3.43.

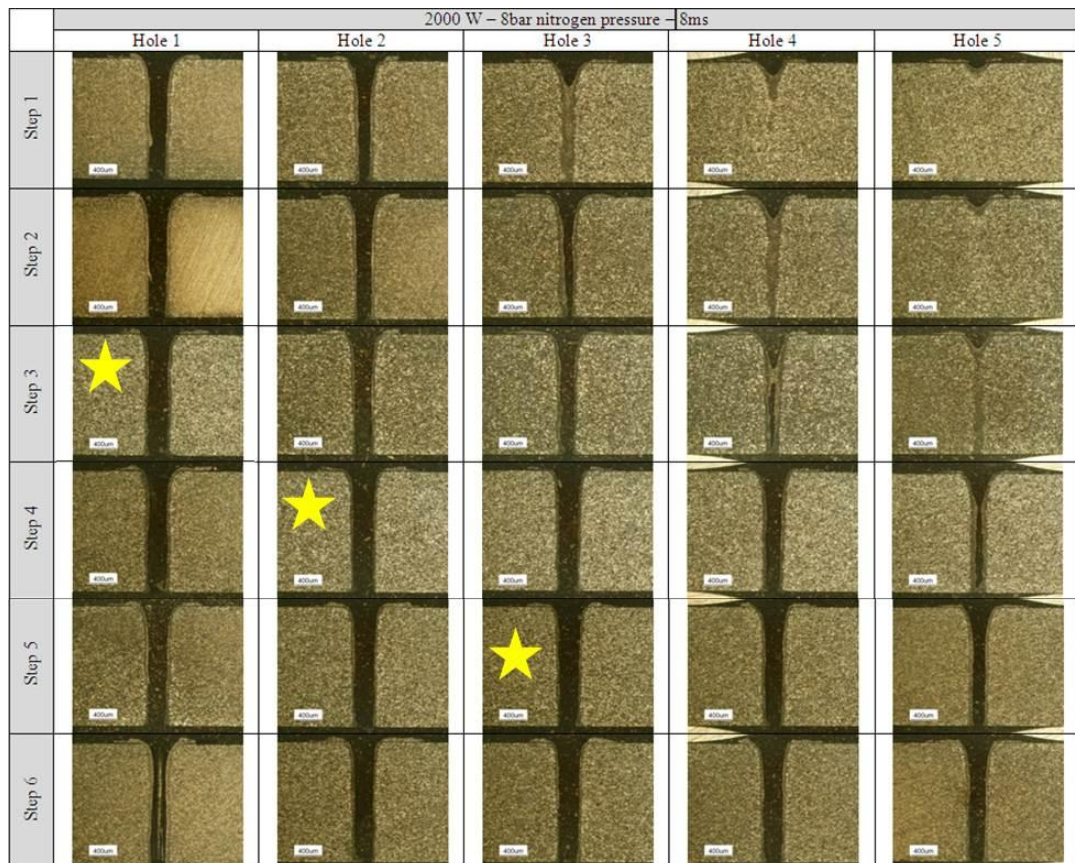


Figure 3.43- Etched cross section of holes pierced by 2000 W, 8 bar nitrogen at 8 ms irradiation time.

3.11.5 Mapping of hole growth

The photos were imported in AutoCAD using the image manager tool. Using the spline tool, a smooth curve was drawn around the hole, re-solidified zone and HAZ. With respect to the scale of photo (i.e. 400 µm) and the thickness of sheet (i.e. 2 mm) an appropriate scale was calculated. The calculated scale was then applied to the photo and curves using the scale tool of AutoCAD (Figure 3.44).

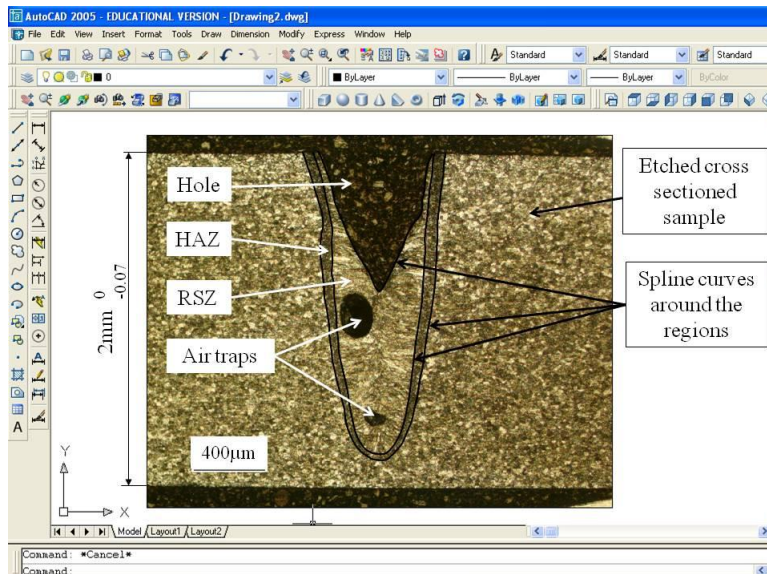


Figure 3.44- Showing a micro photo of the cross sectioned hole in AutoCAD.

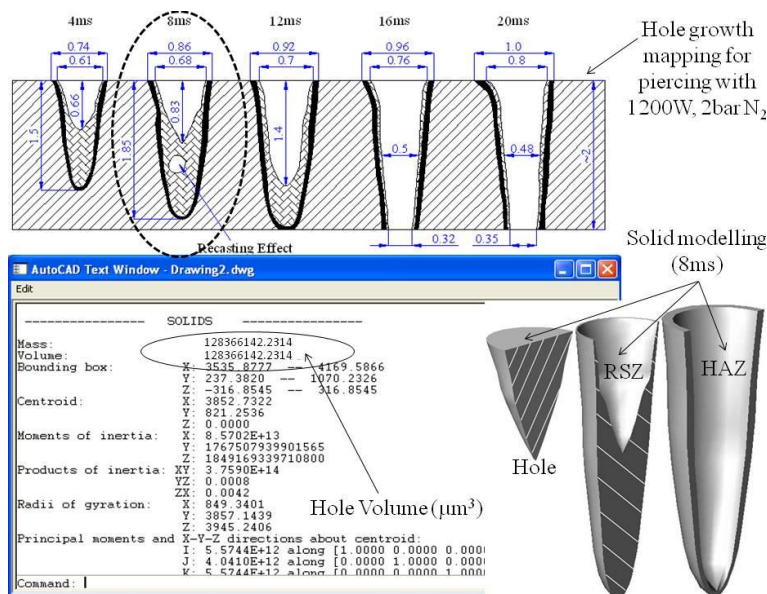


Figure 3.45- Indicating results brief from the AutoCAD.

3.11.5.1 Basic information to read the hole growth maps

All maps were drawn under the ISO drawing standards of 128 using AutoCAD [113, 114] and have the relevant information with a brief legend. In all maps, every type of hatch illustrates specific information. In this research the hatch of ANSI31 was used for base material, AR-HBONE for resolidified zone (RSZ) and SOLID for heat affected zone (HAZ) as shown in Figure 3.46.

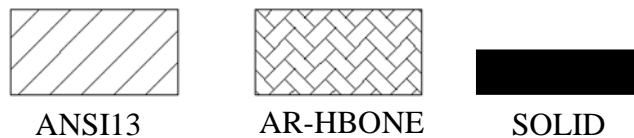


Figure 3.46- Three sorts of hatch were used in the maps.

In sporadic penetration, a continuous line was used to show the hole shape that happens very often and dash line (ISO 03100W) used to indicate the other observed shapes.

All hole growth maps were made up with appropriate dimensions according to ISO25 to show how the hole size and melt (e.g. upper and lower diameters, depth) grow with increasing irradiation time. On the top of each map, the irradiation time for each hole has been written. Additionally, in some maps there is some extra information about sporadic penetration, air traps and recast effects which are all necessary in understanding the details of the hole growth.

3.12 Piercing with nitrogen – cutting with oxygen

The aim of this experiment is to decrease the diameter of the start-up hole at the beginning of oxygen laser cutting of mild steel. This method is an innovative idea which could lead to a decrease wastage material. At the beginning of each cut, the laser beam must pierce an initial hole into the sheet. This hole usually is larger than the kerf size hence one has to locate the initial hole at the region outside the demanded profile bring about wastage material. This idea was mainly established on the basis of the piercing experiments results which will be discussed in chapter 5. In this new method the start-up hole is pierced by nitrogen then laser cutting is carried on by oxygen. A sub-nozzle, also known as a piercing nozzle, with an angle of 40° from the main nozzle supplies nitrogen pressure into the initial hole zone (Figure 3.47).

Two different views of the oxygen nozzle tip position in relation to the nitrogen nozzle are shown in Figure 3.48 which were placed on the surface of sheet with stand-off distance of 1 mm. In order to ensure that the piercing nozzle was focused on the same point with the main nozzle, it was controlled by the red guide beam through the main nozzle and a normal light irradiation through the nitrogen nozzle

towards the main nozzle tip. If the light irradiates the zone below the oxygen nozzle tip around the red beam, it means that the piercing nozzle is located at a correct position. The orifice diameter of the main nozzle was 1 mm and for the piercing nozzle it was 3 mm.

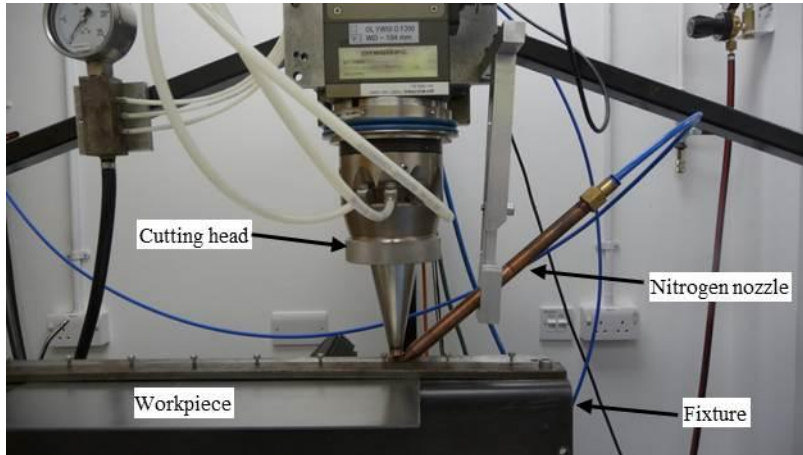


Figure 3.47- Machine setup. Piercing nozzle angle is 40° from the horizontal.

Some piercing and cuttings with different parameters were carried out to consider the feasibility study of this idea. The piercing and cutting parameters are shown in Table 3.20. The stand-off distance was 1 mm, fibre diameter 200 µm and focal point was on the surface of workpiece.

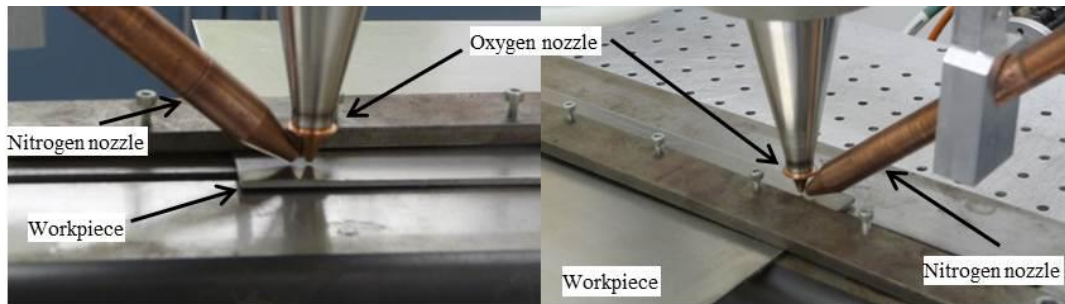


Figure 3.48- Showing the position of piercing nozzle in relation to the main nozzle in two views.

Table 3.20- Parameters of piercing and cutting experiment.

Piercing		Cutting	
<i>3 bar nitrogen pressure</i>		<i>2 bar oxygen pressure</i>	
<i>Power</i>	<i>Irradiation time</i>	<i>Power</i>	<i>Cutting speed</i>
1200 W	24 ms	1000 W	4000 mm/min
1200 W	28 ms	1000 W	4000 mm/min
1200 W	30 ms	1000 W	5000 mm/min
1200 W	32 ms	1000 W	6000 mm/min
1500 W	20 ms	1500 W	6000 mm/min
1500 W	20 ms	1500 W	5000 mm/min
1500 W	20 ms	1500 W	4000 mm/min

4 Preliminary laser cutting results

4.1 Overview

In this chapter the initial experimental results of fibre laser cutting of cold rolled mild steel sheet are presented. The purpose of this chapter is to understand the general characteristics of laser cutting in terms of kerf width, surface roughness, cut surface characterisation and striation pattern. The effect of two different gases, one active and one inert, (i.e. oxygen and nitrogen) on the cutting process will be investigated using a variety of cutting speeds and different powers. During laser cutting, a jet of assist gas exerts pressure on the melt layer to eject it through the bottom of the kerf. Interaction of melt layer with an active assist gas causes a chemical reaction which may affect the cutting process.

The first sections cover the kerf width results. The next sections then present the HAZ and dark zone around the kerf. Following sections consider the surface roughness characteristics and the striation pattern. The effect of different optics and gas pressures on the kerf width in nitrogen laser cutting will be investigated. A comparison between nitrogen and oxygen cutting and the main results of these initial experiments are summarised at the end of the chapter.

Oxygen and nitrogen have different influences on the cutting process. Hence the employed cutting parameters for each gas are different in terms of cutting speed and gas pressure. Here, it is appropriate to restate some parameters which were employed for this sequence of experiments. These are presented in Table 4.1.

Table 4.1- Showing some parameters employed in oxygen and nitrogen cutting.

<i>Descriptions</i>	<i>Values</i>
<i>Sheet thickness</i>	<i>1-3 mm</i>
<i>Laser power</i>	<i>250 – 1500 W</i>
<i>Cutting speed</i>	<i>For N₂: 400-2000 mm/min</i> <i>For O₂: 4000-6000 mm/min</i>
<i>Assist gas type and pressure</i>	<i>2 bar oxygen,</i> <i>8-12 bar nitrogen</i>
<i>Focused beam diameter</i>	<i>0.2 mm on the top surface of sheet</i>
<i>Focal length of lens</i>	<i>120 mm</i>
<i>Focal length of collimator</i>	<i>125 mm</i>

4.2 Kerf width

The following graphs present the upper and lower kerf width measurements whilst the bar charts present the ratio of kerf width to focused beam diameter in oxygen and

nitrogen laser cutting and for different laser parameters and sheet thicknesses. Error bars show the variation in measurement of the kerf width at five different points for each cut. All cuts were fulfilled using fibre of 200 μm and focal length of 120 mm.

4.2.1 Fibre laser-oxygen cutting

Throughout this section, each point in the graphs represents the results of three cuts. Figure 4.1 shows the results of upper and lower kerf width measurement when oxygen laser cutting of 2 mm thick mild steel sheet with power of 1000 W. As can be seen in the figure, there is a slight variation in upper and lower kerf width as the cutting speed increases from 4000 to 6000 mm/min. At the speed of 4000 mm/min, the top kerf width is 0.57 mm, then which decreases to 0.49 mm for 5000 mm/min before raising to 0.51 mm as the cutting speed increases to 6000 mm/min.

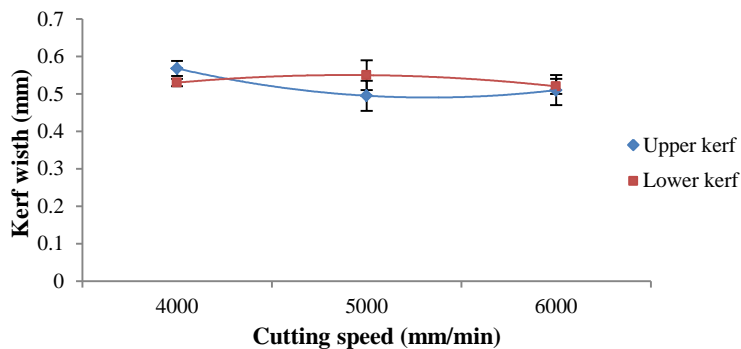


Figure 4.1- Upper and lower kerf width (2 mm, 1000 W, 2 bar oxygen).

Figure 4.2 indicates that, when using a power of 1500 W, the kerf width increases slightly with increasing cutting speed. The upper kerf width is just 0.50 mm at 4000 mm/min and then increases to 0.55 mm with an increase in cutting speed to 5000mm/min. The kerf widths are approximately the same for 5000 to 6000mm/min.

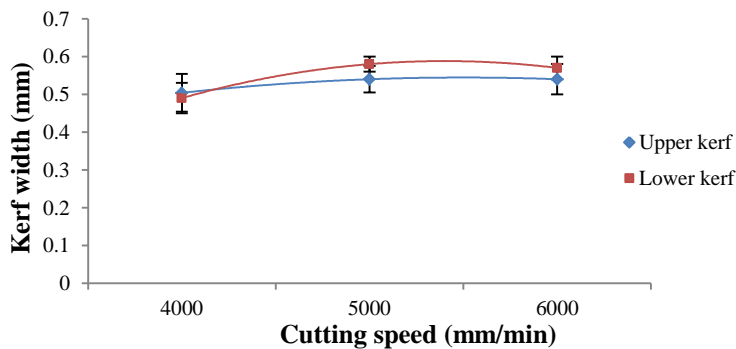


Figure 4.2- Upper and lower kerf width (2 mm, 1500 W, 2 bar oxygen).

In Figure 4.2, similar to the cutting with 1000 W (Figure 4.1), the lower kerf width becomes greater than the upper kerf as the cutting speed increases; However a 500 W increase in the power has only a slight effect on the kerf width (compare Figure 4.1 with Figure 4.2).

It must be emphasized that for both applied powers the average kerf width at the top and bottom is significantly wider than the focused beam diameter of 0.2 mm.

In order to find out the effect of sheet thickness on the kerf width, the experiments were repeated on thinner sheets with 1.6 mm (20% less than 2 mm) and 1 mm (50% less than 2 mm) thickness. The results of kerf width measurement are indicated in Figure 4.3 to Figure 4.6.

As seen in Figure 4.3 for laser cutting of 1.6 mm sheet, the kerf widths slightly decrease with increasing cutting speed which is not substantial. The upper kerf width is 0.48 mm at 4000 mm/min and then decreases to 0.45 mm as cutting speed increases to 6000 mm/min. The kerf widths are approximately the same for 4000 mm/min to 5000 mm/min. The same trend can be observed for the lower kerf width.

Figure 4.4 shows that, using a power of 1500 W the upper kerf width is almost constant with any increase in cutting speed, whilst there is a small variation in the lower kerf width. The average upper kerf width is 0.55 mm, which is 17% larger than that is obtained by 1000 W (i.e. 0.47 mm). For all employed laser conditions, the kerf width is bigger than the spot size (i.e. 0.2 mm).

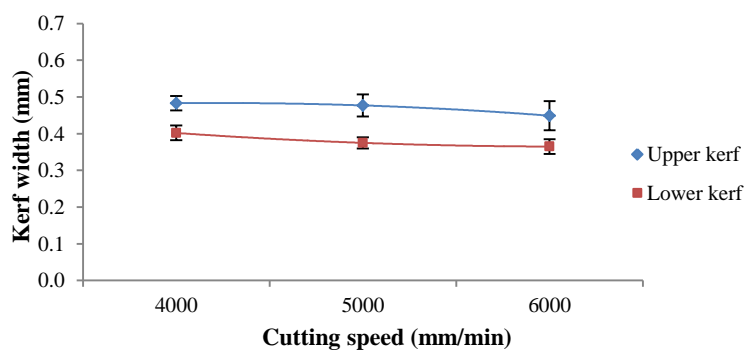


Figure 4.3- Upper and lower kerf width (1.6 mm, 1000 W, 2 bar oxygen).

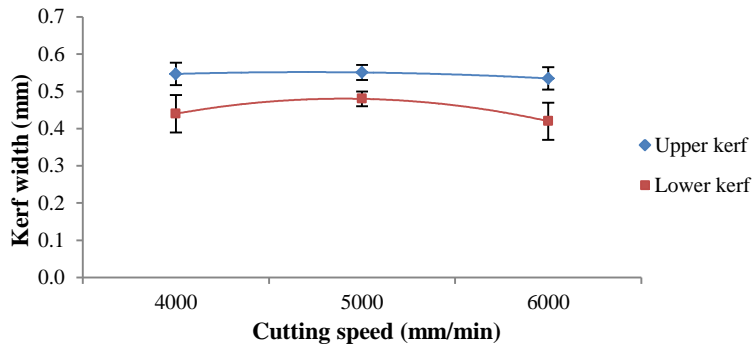


Figure 4.4- Upper and lower kerf width (1.6 mm, 1500 W, 2 bar oxygen).

Kerf width results for laser cutting of 1mm-thick plate are shown in Figure 4.5 and Figure 4.6 for different powers. As can be seen in Figure 4.5, the upper kerf width is almost constant with increasing cutting speed, and the same trend can be observed for lower kerf width. Figure 4.6 shows that the changes in the upper and lower kerf widths with increasing cutting speed are not significant and are almost constant.

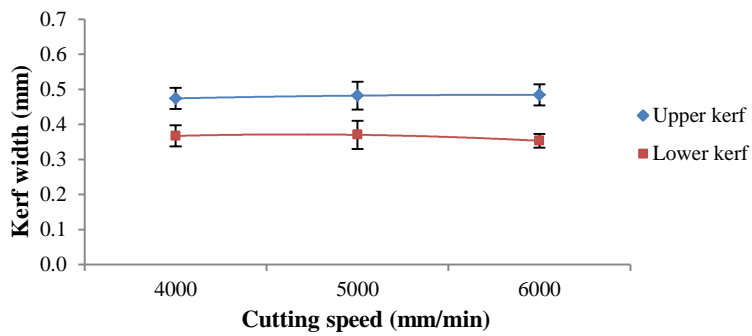


Figure 4.5- Upper and lower kerf width (1 mm, 1000 W, 2 bar oxygen).

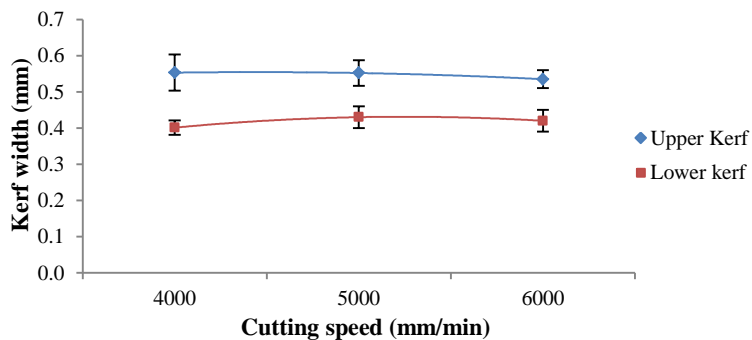


Figure 4.6- Upper and lower kerf width (1 mm, 1500 W, 2 bar oxygen).

Similar to thicknesses of 2 mm and 1.6 mm, the kerf widths for the 1 mm sheet are also wider than the focused beam diameter.

4.2.1.1 Comparison of the kerf widths

A comparison of kerf width from the 2 mm, 1.6 mm and 1 mm sheets (Figure 4.1, Figure 4.2, Figure 4.3, Figure 4.4, Figure 4.5 and Figure 4.6) indicates that, in the range of applied cutting speed, the upper kerf width is almost the same. Comparison shows that, for a given thickness, the upper and lower kerf widths increase very slightly with increasing power. For example, in this range of cutting speed when cutting 2 mm sheet with a power of 1000 W the average upper and lower kerf widths are 0.52 and 0.53 mm. These values increase to 0.53 and 0.55 mm when the power is increased to 1500 W. For a given power, the upper and lower kerf widths for 2 mm are almost the same. However, for 1.6 mm and 1 mm the upper kerf is wider than the lower kerf. It may be a key point that, in the range of employed laser parameters, there is a little effect on the kerf width. Figure 4.7 shows a comparison of upper kerf widths for different thicknesses and different powers with increasing cutting speed. As is seen, in the range of applied parameters, there is a little influence on the top kerf. The range of kerf width is between 0.4 mm to 0.6 mm. In general, the upper and lower kerf widths are constantly significantly greater than the spot size.

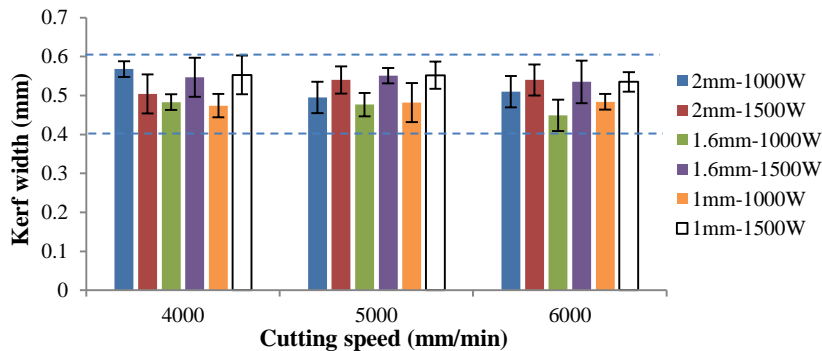


Figure 4.7- Comparison of upper kerf widths for different thicknesses and powers. The range of kerf width is shown by two lines between 0.4 mm to 0.6 mm. Focused spot size is 0.2 mm on the surface of sheet (2 bar oxygen).

Figure 4.8 illustrates the ratio of upper and lower kerf width to the laser spot size (i.e. 0.2 mm) in oxygen laser cutting of 2 mm thick mild steel. The ratio of the kerf width to the spot size clearly shows how much larger the kerf width is than the focussed beam diameter. This shows that, on average, the upper kerf widths are 2.61 and 2.67 times greater than the spot size for 1000 W and 1500 W respectively. These ratios for lower kerf are 2.67 and 2.73. For previous work done by this laser with the same

laser parameters [52], these ratios were 2.5 and 2.55. So, the present result is in agreement with the previous work's results.

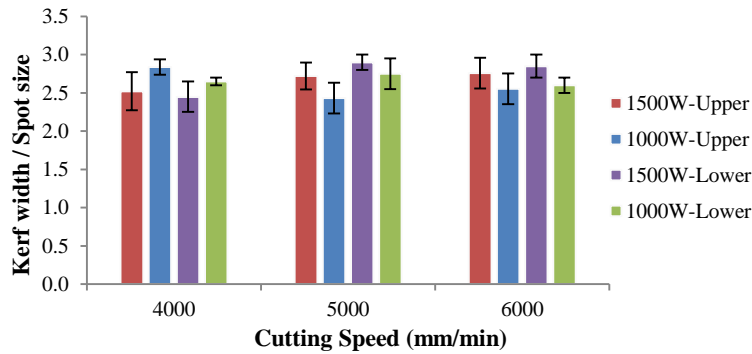


Figure 4.8- Upper and lower kerf width per spot size vs cutting speed (2 mm, 2 bar oxygen).

Figure 4.9 shows that, on average, for 1.6 mm the ratios of upper kerf width per spot size are 2.35 and 2.72 when using power of 1000 and 1500 W respectively. These ratios for lower kerf are 1.90 and 2.23. All ratios are often in agreement with the previous work done with this laser [52]. A comparison between 2 mm and 1.6 mm (Figure 4.8 and Figure 4.9) indicates that, as the thickness decreases, the ratio of upper kerf width per spot size on average decreases only from 2.64 to 2.54. The lower kerf width per spot size decreases from 2.7 to 2.1, which is considerable.

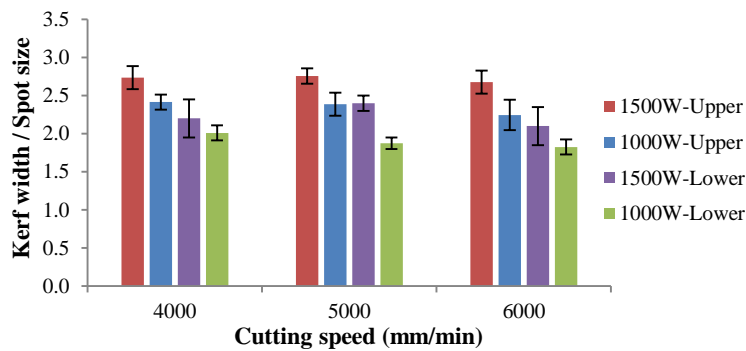


Figure 4.9- Upper and lower kerf width per spot size vs cutting speed (1.6mm, 2 bar oxygen).

The ratios of upper kerf width per spot size in laser cutting of 1 mm are 2.4 and 2.75 for powers of 1000 and 1500 W (Figure 4.10). These ratios for lower kerf are 1.82 and 2.1. In previous research [52] which was done by the same fibre, the same material and the same laser conditions, these ratios on average were 2.41 and 2.0 for upper and lower kerf respectively.

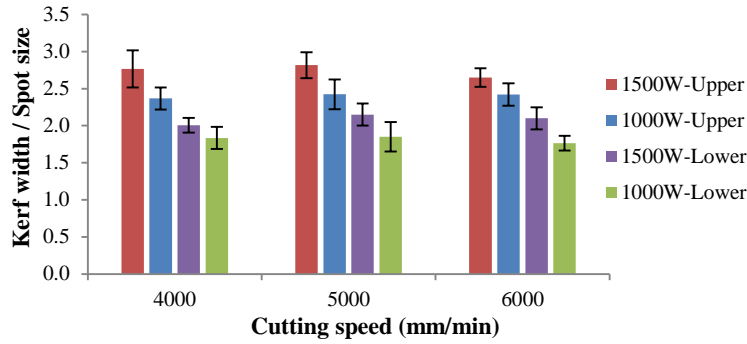


Figure 4.10- Upper and lower kerf width per spot size vs cutting speed (1 mm, 2 bar oxygen).

4.2.1.2 Discussion of kerf width

In general, the lower kerf width is narrower than the upper kerf when the laser beam is focused on the top surface of sheet [31, 52]; However, results show that the lower kerf width may become the same or slightly greater than the top (Figure 4.1 and Figure 4.2). It should be mentioned that, in the range of applied laser cutting, the lower kerf width in 1.6 mm and 1 mm, on average, was 23% to 30% less than the upper kerf width. This indicates that the thickness of sheet has an effect on the lower kerf width. Kerf width profile for sheet thickness of 1 and 2 mm is shown in Figure 4.11.

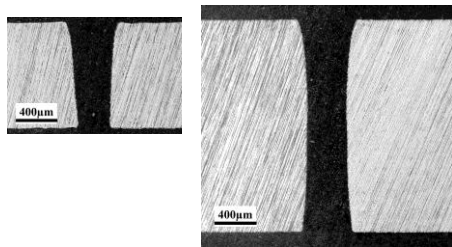


Figure 4.11- Kerf width profile when cutting 1 mm (1000 W, 6000 mm/min) and 2 mm (1000 W, 4000 mm/min) with 2 bar oxygen.

The average top kerf width, when cutting 1.6 mm with 1000 W, is 0.47 mm, which is 11% less than that is measured for cutting of 2 mm (i.e. 0.53 mm). In other words under the same laser conditions a 20% decrease in the material thickness results in 11% decrease in the kerf width (Figure 4.1 and Figure 4.3).

In the range of employed laser conditions and with the different cutting speeds and different powers, there is a little effect on the kerf width.

It is well understood that the melt flow behaviour is reflected in the patterns of solidified melt on the cut edges [22]. As the melt flows down the kerf, the lower cut edge is influenced by laser melting, and it can be said that, in addition to the absorption of the laser beam by the cut front, some other phenomena may influence the upper and lower kerf width. Turbulence in the low viscosity melt flow affects the semi-melted surface of the kerf and somehow causes a more melting on the cut edge [115]. This turbulence happens close to the bottom of the kerf where there is a thicker melt layer and the laser beam is reflected [116]. These phenomena may affect the lower kerf width to become wider temporarily.

In summary, the upper and lower kerf widths, when cutting 2 mm-thick mild steel with 2 bar oxygen, are approximately the same, whilst for the 1.6 mm and 1 mm results, the upper kerf is wider than the lower kerf. Both upper and lower kerf widths are wider than the focused spot size (i.e. 2.5 times on average), which is in agreement with other relevant published researches from the laser used in this work and works published by an entirely independent group [31, 52].

4.2.2 Fibre laser-nitrogen cutting

The results of kerf width measurements are illustrated in Figure 4.12 to Figure 4.15. Error bars indicate the variation of kerf width during measurement. Overall, the graphs show that the upper kerf width is wider than the lower kerf. The kerf width generally is wider than the focused spot size (i.e. 0.2 mm). In general and under the applied laser condition, the upper and lower kerf widths vary when the cutting speed increase from 400 mm/min to 2000 mm/min. At the cutting speed of 2000 mm/min the difference between upper and lower kerf width reduces. This indicates a low taper in the kerf profile. The upper and lower kerf width slightly increases with power (see Figure 4.12 to Figure 4.15).

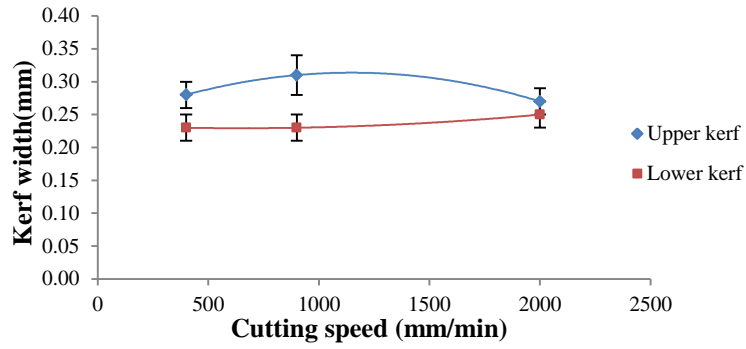


Figure 4.12- Upper and lower kerf width (2 mm, 1000 W, 12 bar nitrogen).

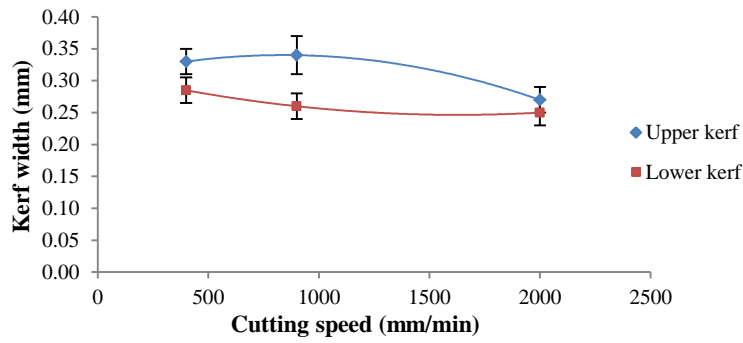


Figure 4.13- Upper and lower kerf width (2 mm, 1500 W, 12 bar nitrogen).

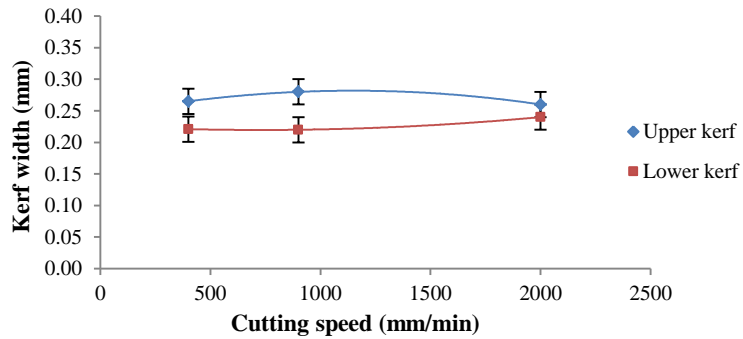


Figure 4.14- Upper and lower kerf width (1 mm, 1000 W, 12 bar nitrogen).

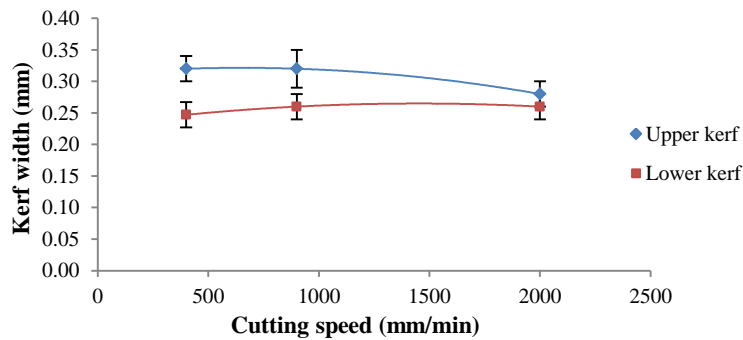


Figure 4.15- Upper and lower kerf width (1 mm, 1500 W, 12 bar nitrogen).

4.2.2.1 Comparison of the kerf widths

Considering all kerf width results, in fibre laser nitrogen cutting of thin plate mild steel (i.e. less than 2 mm) and under the employed cutting parameters the upper kerf width is in the range of 0.24 mm to 0.37 mm as presented in Figure 4.16. The spot size in this set of experiments was 200 μm , and the key point is that the kerf width is larger than the focused spot size.

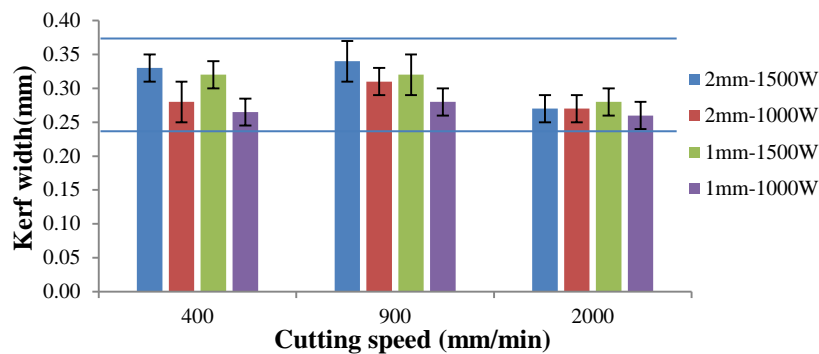


Figure 4.16- Comparison of upper kerf width for a variety of thicknesses and powers, with 12 bar N₂. The range of kerf width is shown by two lines between 0.24 mm to 0.37 mm. Focused beam size is 0.2 mm on the surface of sheet (12 bar nitrogen).

Overall, under the employed laser cutting conditions, the upper and lower kerf width increase with power. The ratio of upper and lower kerf width to the focused beam size for sheets of 2 mm and 1 mm are presented in Figure 4.17 and Figure 4.18. The upper kerf width for 2 mm with power of 1000 W is 1.43 times (on average) the focussed beam diameter (i.e. 0.2mm). This ratio increases to 1.6 as power increases to 1500 W. For the lower kerf width, these ratios are 1.2 and 1.33 for powers of 1000 W and 1500 W respectively (Figure 4.17). When cutting 1 mm thick steel, the ratio of upper kerf width to focused beam increases from 1.34 to 1.53 as powers raise from 1000 W to 1500 W. This ratio for lower kerf is 1.14 to 1.28 (Figure 4.18).

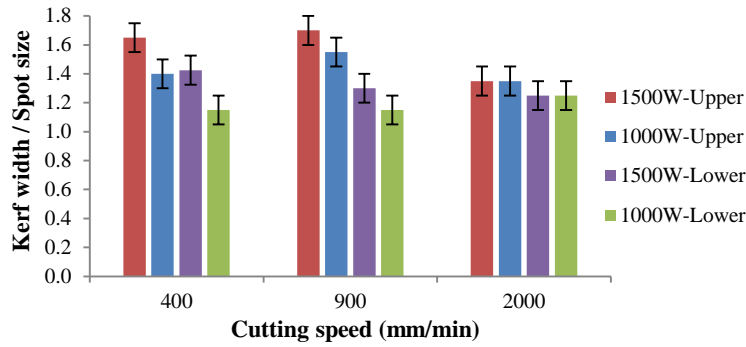


Figure 4.17- Upper and lower kerf width per spot size vs cutting speed (2 mm, 12 bar nitrogen).

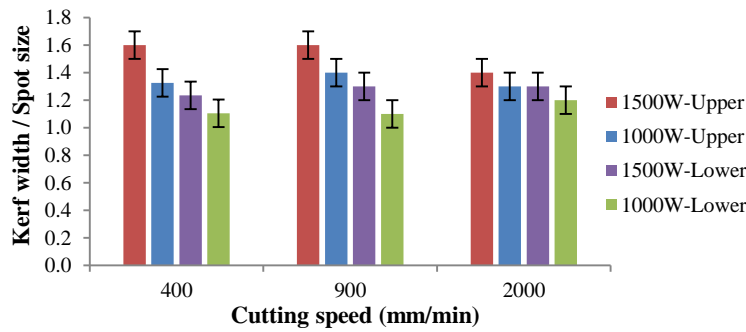


Figure 4.18- Upper and lower kerf width per spot size vs cutting speed (2 mm, 12 bar nitrogen).

4.2.2.2 Discussion of kerf width

Overall, the lower kerf width is narrower than the top. This is because, depends on the employed power and cutting speed and on the base of Brewster angle, the laser beam directly penetrates to the specify depth and lateral of the upper part of the sheet, but the lower part is just irradiated by a reflection of the beam [50, 59]. Therefore, it is reasonable to assume that the upper part of sheet receive more energy than the lower part. Hence the upper kerf is wider than lower kerf as a result of heat conduction. At higher cutting speed (e.g. 2000 mm/min), the upper kerf width decreases. This is because, as the cutting speed is increased, the interaction time between laser and workpiece decreases so there is less opportunity for the laser to penetrate laterally. Hence the upper kerf starts to decrease.

4.2.3 Comparison of kerf width in oxygen and nitrogen laser cutting

Comparison of the kerf width results in oxygen and nitrogen laser cutting reveals that in the range of applied laser cutting parameters, the kerf width in oxygen cutting is 1.5 to 2.0 times the kerf width in nitrogen assisted cutting as shown in Figure 4.19 and Figure 4.20 for two thicknesses of 1 mm and 2 mm. In laser-oxygen cutting,

oxygen reacts with melt and adds significant energy to the melting zone [9]. It can widen the melting area laterally [4]. Moreover, due to the possible waveguiding effect of the FeO in the melt, a multiple reflection of the beam happens throughout the melting zone boosting the kerf widening [52]. In contrast, nitrogen does not react with the iron melt hence the kerf width for nitrogen cutting is narrower than that for oxygen cutting.

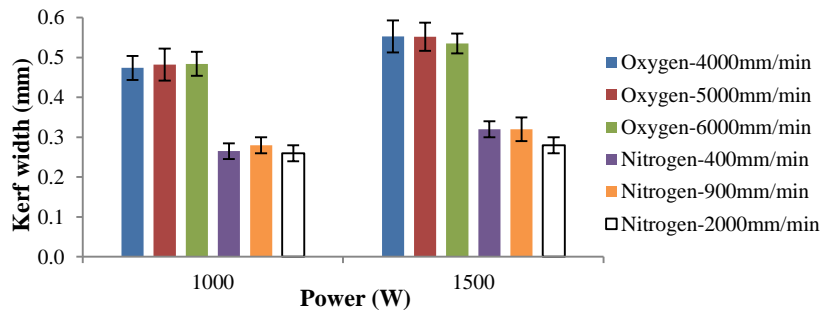


Figure 4.19- Upper kerf width versus power for different assist gas and cutting speed (1 mm, 2 bar oxygen, 12 bar nitrogen).

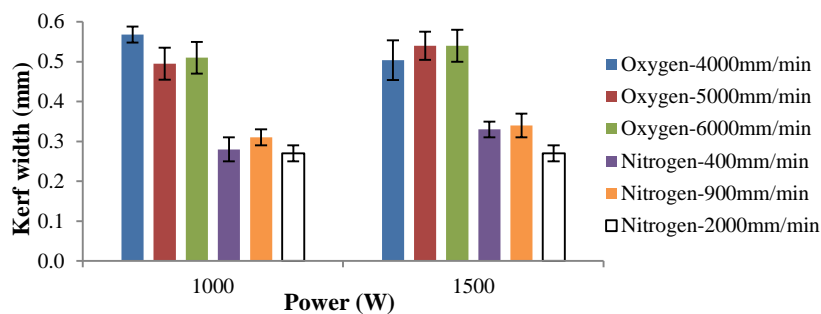


Figure 4.20- Upper kerf width versus power for different assist gas and cutting speed (1 mm, 2 bar oxygen, 12 bar nitrogen).

4.3 Heat affected zone (HAZ) and oxidation mark

4.3.1 Fibre laser oxygen cutting

4.3.1.1 Oxidation mark

On the upper and lower surface of the sheet, a dark zone can be seen in the both sides of the cut path as presented in Figure 4.21. As can be seen, the width of this dark zone on the lower surface is wider than that on the upper surface. EDS examination of the dark zone revealed the presence of oxygen. Figure 4.22 qualitatively indicates that, in the dark zone, the amount of oxygen gradually increases, with decrease in the iron, towards the cut edge, indicating that this is a product of heating and oxidation. Hence this zone is called the oxidation mark.

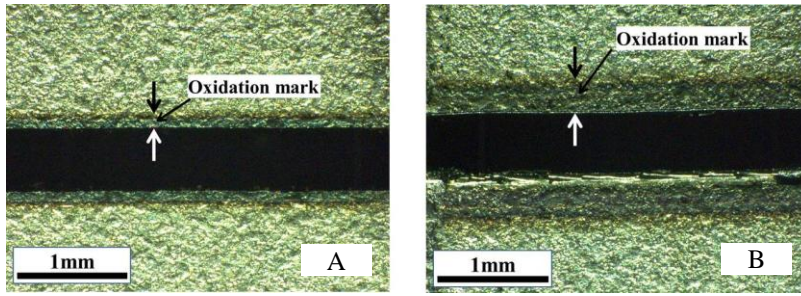


Figure 4.21- Oxidation mark. A) Upper kerf. B) Lower kerf. (2 mm-thick sheet, 1500 W, 6000 mm/min, 2bar oxygen).

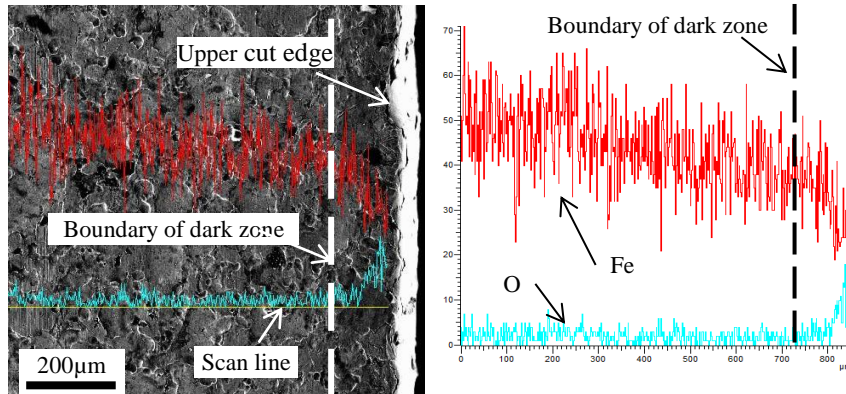


Figure 4.22- EDS examination of the dark zone on the upper surface of sheet close to the cut edge (2 mm- thick sheet, 1500 W, 4000 mm/min, 2 bar oxygen).

The EDS examination of the oxidation mark on the lower surface of the sheet is indicated in Figure 4.23. An interface of melted and unaffected surface can be observed. The dark width is started from the boundary of the dark zone to the interface line. The amount of oxygen in the dark zone increases towards the cut edge with a decrease in iron until the interface of melted/unaffected material is reached. Beyond this, the amount of oxygen rapidly decreases.

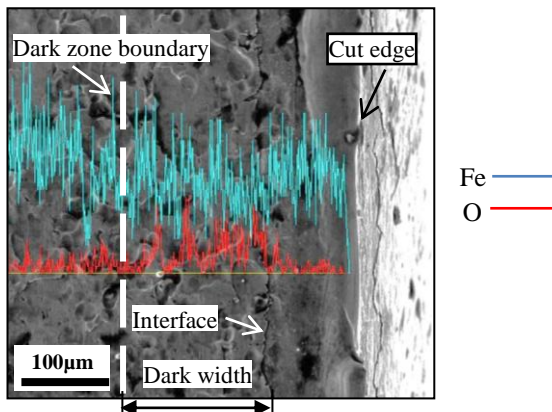


Figure 4.23- EDX examination of the dark zone on the lower surface of sheet close to the cut edge. Dark width position is shown. (2 mm-thick sheet, 1500 W, 4000 mm/min, 2 bar oxygen).

The dark width was measured from the beginning of the dark zone to the cut edge (Figure 4.24 to Figure 4.26). In the range of the applied laser cutting parameters, the oxidation mark width slightly reduces with increasing cutting speed. For both powers, the lower oxidation width is approximately 50% larger than the upper width. Larger error bars in the lower kerf are due to larger oxidation marks. The effect of power on the oxidation increases with thickness also the effect of cutting speed is more pronounced for thicker thickness.

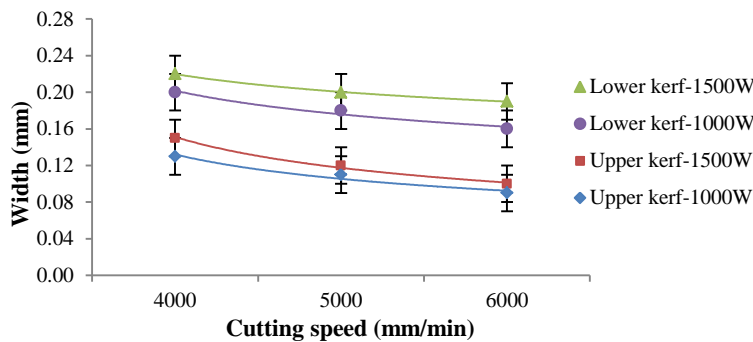


Figure 4.24- Oxidation width versus cutting speed for different powers (2 mm, 2 bar oxygen).

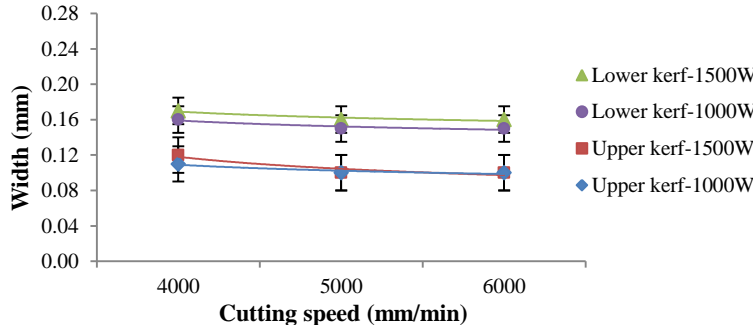


Figure 4.25- Oxidation width versus cutting speed for different powers (1.6 mm, 2 bar oxygen).

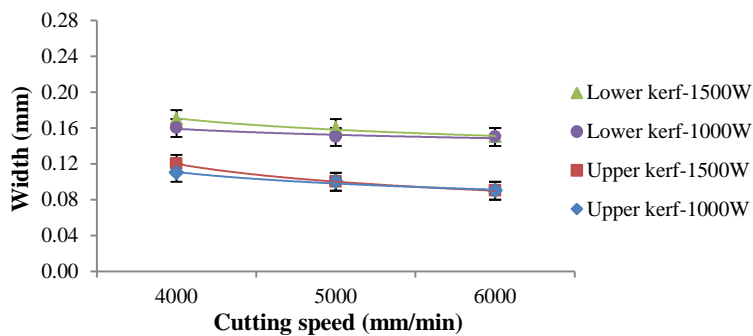


Figure 4.26- Oxidation width versus cutting speed for different powers (1 mm, 2 bar oxygen).

4.3.1.2 Heat affected zone (HAZ)

The heat affected zone inside the base material was observed by polishing and etching the cut edge as presented in Figure 4.27 for different thicknesses. As can be seen, the width of the HAZ on the lower part of the cut edge is larger than that is on the upper part.

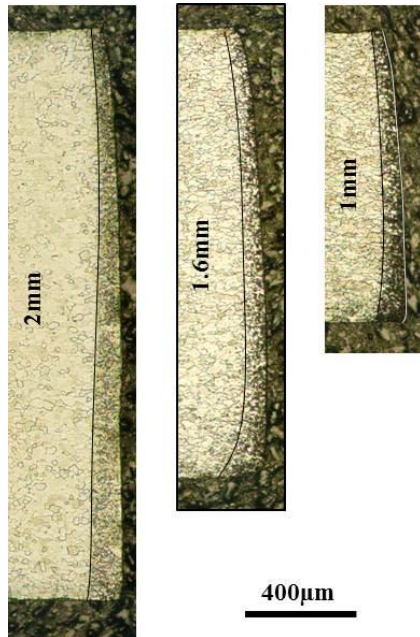


Figure 4.27- The dark thin width on the right edge of the samples indicates the HAZ. Black line added to indicate edge of the HAZ (1000 W, 4000 mm/min, 2 bar oxygen).

The results of HAZ width on the upper and lower part of the cut edge for different thicknesses, cutting speed and powers are presented in Figure 4.28 to Figure 4.30. For all thicknesses, the upper HAZ width is less than the lower HAZ width. In the range of applied cutting speed, the lower HAZ width in 2 mm and 1.6 mm (Figure 4.28 and Figure 4.29) slightly increases with cutting speed, but the upper HAZ width slightly decreases. However, this trend cannot be observed after cutting 1 mm (Figure 4.30). For the 1 mm sheet, the upper and lower widths are almost constant. For all tested thicknesses, there is no significant difference in the width of the HAZ when the power increases from 1000 W to 1500 W. In summary, the lower HAZ increases with thickness. Power and cutting speed have a little effect on the HAZ.

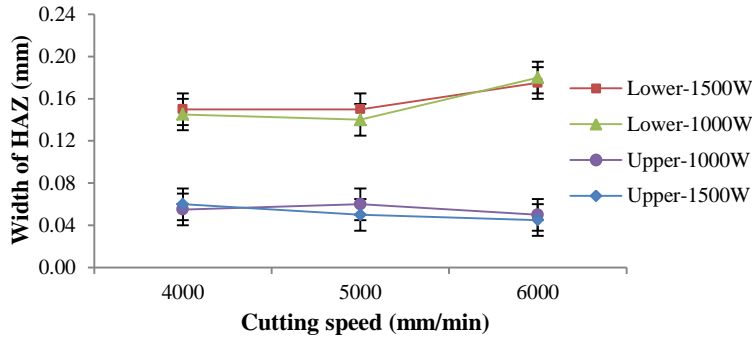


Figure 4.28- Width of HAZ versus cutting speed (2 mm, 2 bar oxygen).

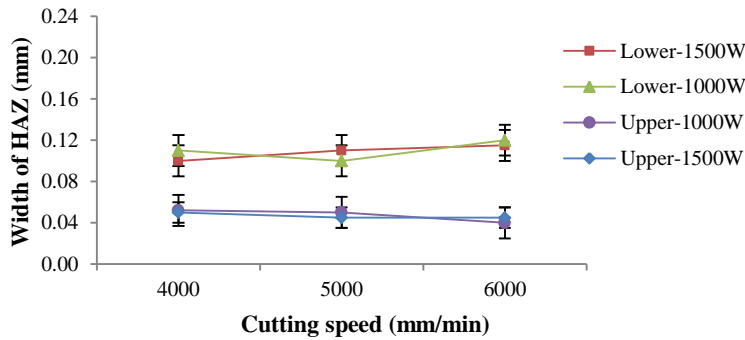


Figure 4.29- Width of HAZ versus cutting speed (1.6 mm, 2 bar oxygen).

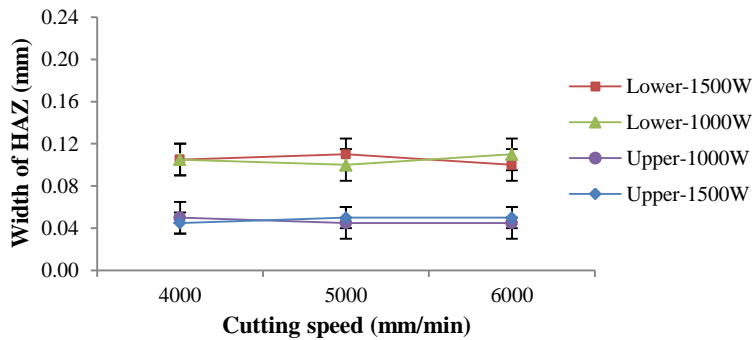


Figure 4.30- Width of HAZ versus cutting speed (1 mm, 2 bar oxygen).

4.3.1.3 Discussion of the oxidation mark and HAZ

4.3.1.3.1 Dark zone around the cut path is an oxidation mark.

EDS examination qualitatively reveals that the dark zone around the kerf has been enriched with oxygen. This is consistent with it being an oxidation zone. This oxidation zone is a product of hot metal reacting with the oxygen flow.

4.3.1.3.2 The oxidation mark width for lower surface is larger than the upper surface.

The width of oxidation zone on the lower surface is approximately twice the upper width. This difference indicates that more heat has been conducted laterally at the

bottom. Moreover, the thickness of the melt flow increases towards the bottom of the kerf as does the temperature of melt flow in the cutting zone. Also, the measured oxidation width includes the melt thickness (§ 4.3.1.1). A combination of these causes larger heat conduction, resulting in a wider oxidation zone at the bottom of kerf.

4.3.1.3.3 *The width of the oxidation zone slightly reduces with increasing cutting speed.*

This is because, as the cutting speed is increased, the interaction time between laser beam and the cutting zone decreases. Hence the heat input per cut length decreases and the extent of heat conduction decreases. On the other hand the effect of oxygen jet is moving on. A combination of these, results in a slight decrease in the width of the oxidation zone.

4.3.1.3.4 *The oxidation mark decreases slightly with a decrease in the sheet thickness.*

As the sheet thickness decreases, both the upper and lower oxidation mark decreases slightly. For sheet thickness of 1.6 mm and 1 mm, the width of the oxidation mark is less than that for the 2 mm sheet. This is because the heat conduction into the material decreases with a decrease in the sheet thickness. This was experienced directly by touching the cut sheets a few seconds after cutting. From this simple test, it was realised that the sheet was hotter when it was thicker.

4.3.1.3.5 *Overall, the width of the lower HAZ is larger than the upper HAZ.*

As the laser penetrates the sheet and moves forwards, new melt is produced from all parts of the cut front, which flows down the kerf. The melt layer thickness slightly increases as it flows down the kerf (see Figure 4.22 and Figure 4.23). Increase in the melt thickness causes the lateral heat conduction to increase. Hence, the HAZ for the lower part of cut edge is larger than that for upper cut edge as a result of heat conduction.

4.3.1.3.6 *The HAZ width increases with sheet thickness.*

When the sheet thickness is increased from 1 to 2 mm, firstly, for a given power and cutting speed, the melt mass flow rate and the melt layer thickness increase. Secondly, the length of cutting front increases thus there is more opportunity for heat

to conduct to the cut edge as the melt flows down the kerf. These two phenomena will make the HAZ deeper as a result of heat conduction.

4.3.1.3.7 *There is no relation between the width of oxidation and HAZ*

In general, the width of oxidation is larger than the HAZ, however, there is no relation between the width of HAZ and oxidation mark. This is because, the process of HAZ generation is different from oxidation mark. The heat conduction from the cutting zone and subsequent re-cooling causes the HAZ from the cut edge to the termination of the sensitizing temperature in the base metal. However, the oxidation mark is generated by a reaction between oxygen and the hot surface of the sheet.

4.3.2 Fibre laser nitrogen cutting

4.3.2.1 *Dark zone around the kerf*

Around the upper kerf in nitrogen cutting, sometimes a dark zone can be observed, as presented in Figure 4.32. However, this dark zone is always seen around the lower kerf. EDS examination indicated that this dark zone is an area enriched with a combination of oxygen. As can be seen in Figure 4.31 the amount of oxygen qualitatively increases slightly towards the cut edge. Nitrogen was not observed on the EDS examination.

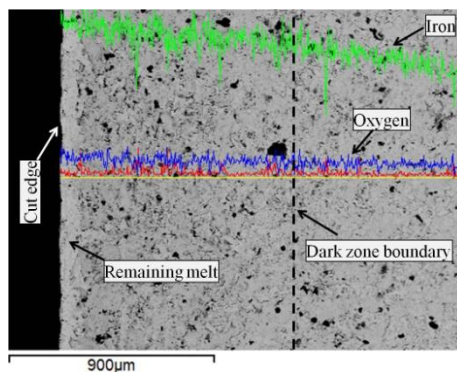


Figure 4.31- EDS examination qualitatively shows the presence of oxygen on the surface of cut sample (1500 W, 800 mm/min, 12 bar nitrogen).

From Figure 4.32 when the power and cutting speed are increased, the dark zone around the upper kerf gradually gets less dark (B). For a specific combination of cutting parameters, the dark zone disappeared (C). However, this trend was not observed for the lower kerf.

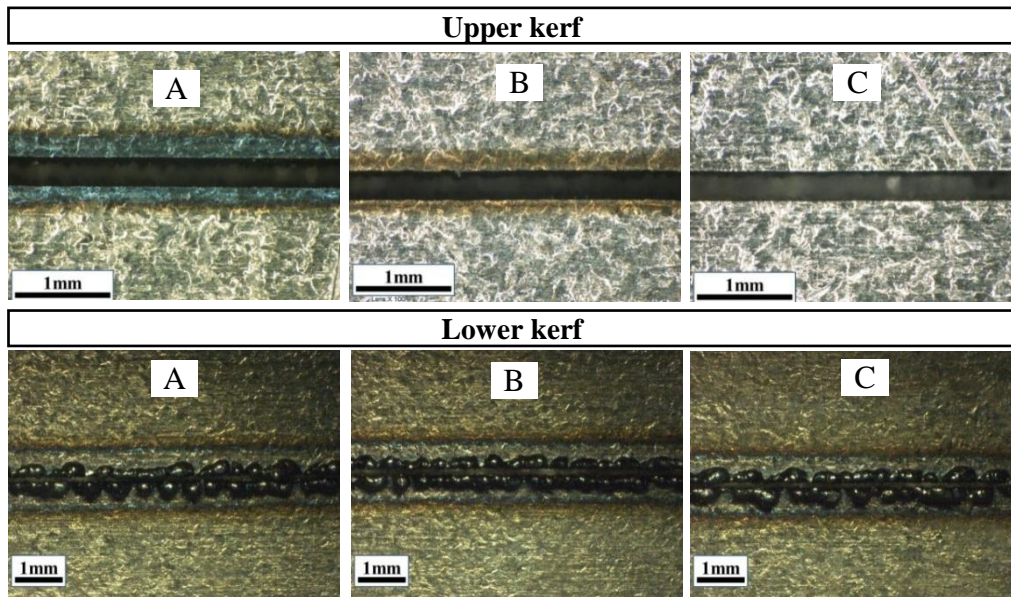


Figure 4.32- Upper and lower kerf width when laser cutting of 1mm thick mild steel sheet with 12 bar nitrogen. A) 250 W, 200 mm/min. B) 400 W, 800 mm/min. C) 600 W, 2400 mm/min.

In nitrogen laser cutting of mild steel, the HAZ width increases from the upper cut edge towards the bottom, as presented in Figure 4.33. Much more variation is seen than was seen for oxygen cutting (compare Figure 4.33 and Figure 4.27).

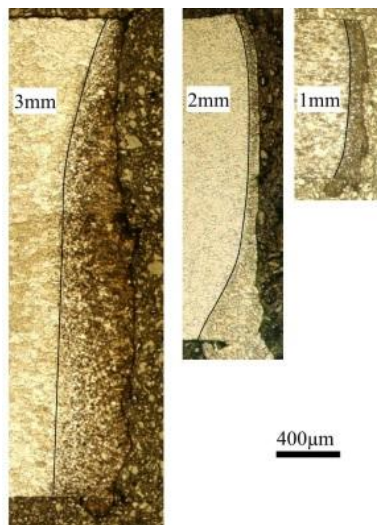


Figure 4.33- Heat affected zone in nitrogen laser cutting for three different thicknesses (1200 W, 1000 mm/min).

The upper and lower width of the HAZ versus cutting speed for different thicknesses and powers are shown in Figure 4.34 to Figure 4.36. According to the results, for the range of applied laser cutting parameters, the upper and lower HAZs decrease slightly with increasing cutting speed. In the range of employed cutting parameters, the power has had a small effect on the HAZ width. When cutting 3mm thick plate, the lower HAZ width for 800 W is larger than that for 1200 W, whilst the upper

HAZ width for 1200 W is more than that made by 800 W (Figure 4.34). Comparing cutting of 2 mm and 1 mm thicknesses, no significant change of HAZ with power was observed, but it very slightly decreases with cutting speed.

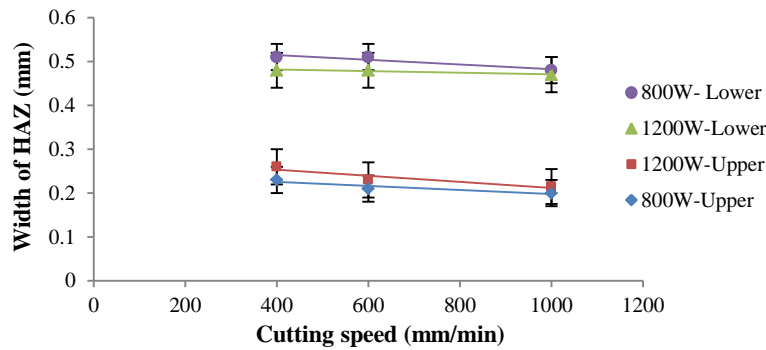


Figure 4.34- Width of HAZ when cutting 3 mm thick mild steel with 12 bar nitrogen.

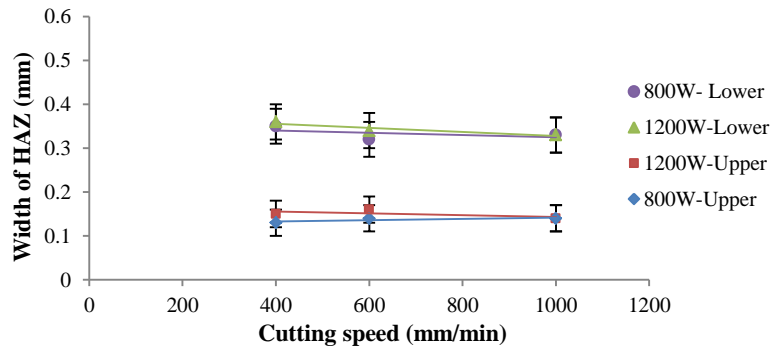


Figure 4.35- Width of HAZ when cutting 2 mm thick mild steel with 12 bar nitrogen.

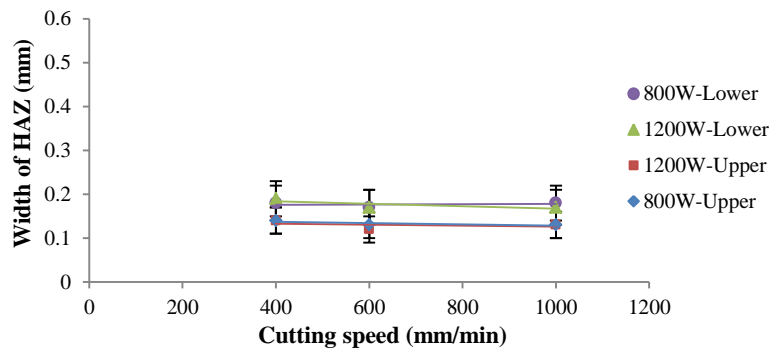


Figure 4.36- Width of HAZ when cutting 1 mm thick mild steel with 12 bar nitrogen.

A comparison of upper and lower HAZ width (Figure 4.34-Figure 4.36) indicates that for a given power and cutting speed (e.g. 1200 W, 400 mm/min) the upper and lower HAZ for 3 mm thick sheet are 0.26 mm and 0.48 mm. When power decreases to 800 W, the upper and lower HAZ are 0.23 and 0.51 mm. The upper and lower HAZ for 1 mm sheet are 0.14 mm and 0.19 mm and do not change with power. The

results show that the effect of power on the upper and lower HAZ is considerable for thicker material (e.g. 3 mm). At the same power (1200 W) as the cutting speed is increased to 1000 mm/min, the upper and lower HAZ for 3mm thick sheet are 0.2 mm and 0.47 mm. These values for 2mm are 0.14 mm and 0.33 mm. For 1 mm sheet, these are 0.13 mm and 0.18 mm. This shows that the effect of speed on the HAZ is considerable for thicker plate.

4.3.2.2 Discussion of the dark zone and HAZ

4.3.2.2.1 The dark zone around the cut after nitrogen laser cutting is a product of heat, oxygen.

During nitrogen laser cutting of mild steel, an oxidation reaction happens because the hot metal is in contact with the air containing oxygen. The oxidation reaction on the surface of mild steel sheet looks like a dark zone.

4.3.2.2.2 The dark zone around the upper kerf is dependent on the cutting speed and power and this disappears as the power and cutting speed increase.

As the cutting speed increases, the interaction time between the laser beam and the cutting front decreases. Therefore, the time for any further lateral heat conduction into the upper surface of the sheet decreases resulting in a reduction in the upper surface temperature. The reduction in the upper surface temperature of the sheet brings about a decrease in the oxidation.

4.3.2.2.3 The dark zone is always observed around the lower kerf.

In contrast with the upper kerf, the dark zone is always seen around the lower kerf. This indicates that the heat conduction in the lower kerf is higher than the upper kerf. The main reason of this is that the heat is transported by the melt movement and gas flow from the upper kerf to the lower kerf. Moreover, the thickness of the retained melt layer on the cut front rises from the top towards the bottom (Figure 4.33). Furthermore, the hot dross clung to the lower cut edge is as a source of heat (Figure 4.32). The heat from these sources (melt + dross) is conducted laterally into the base material, sustaining the temperature of the lower sheet surface. This then reacts with the oxygen existing in the air and contamination on the surface of sheet respectively.

4.3.2.2.4 The HAZ on the bottom of the cut edge is larger than that on the top.

As the melt flows down the cutting front, the heat is conducted laterally into the solid base material. From the micrographs of the HAZ (Figure 4.33) it is found that the retained melt on the cut edge increases from the top towards the bottom of the kerf. Moreover, the hot dross clings to the lower kerf. These residual melts (retained melt and dross) pass their heat into the solid base material, increasing the HAZ depth on the bottom of the cut edge.

4.3.2.2.5 The HAZ width decreases with increasing cutting speed.

The decrease in the melt temperature with increasing cutting speed (see 4.3.2.2.2) causes a reduction in the HAZ width as a result of heat conduction.

4.3.2.2.6 The HAZ width increase with sheet thickness

With the same cutting parameters, a thicker sheet has a longer cutting front in comparison with a thinner sheet, so the heat has further time to transfer to the cut edge as the melt moves down the cutting front. Furthermore, for laser cutting of a thick sheet, more material is melted in comparison with a thinner plate; and the micrographs of the HAZ (Figure 4.41) indicates that the residual melt on the cut edge for thicker plate is more than that for a thinner sheet. These phenomena will make the HAZ deeper for thick material as a result of heat conduction.

4.3.3 Comparison of the HAZ between oxygen and nitrogen laser cutting

- For both employed gases the upper dark zone decreases with cutting speed.
- Nitrogen protects the hot metal from the oxidation; therefore the relationship between HAZ and oxide marks is different from the laser-oxygen cutting.
- When cutting with oxygen the dark zone can always be observed on the top and bottom of the kerf, but when using nitrogen, the oxidation zone on the upper surface disappears with increasing cutting speed.
- For both applied gases, the width of the HAZ on the lower part of cut edge is larger than that for the upper part.
- The amount of HAZ for laser-nitrogen cutting is 2 to 2.7 times larger than that for laser-oxygen cutting. The cross sectioned, polished and etched cut edge indicates that there is a relatively thick re-solidified melt layer lining the cut edge after

nitrogen cutting. This feature is not observed for the oxygen cut edge (compare Figure 4.27 with Figure 4.33).

4.4 Surface roughness results

One of the most interesting issues in the laser cutting process is the cut surface quality. This is particularly true for commercial laser cutting, in which the highest quality is often demanded. In order to find out more about the characteristics of the cut edge, after measurement of the kerf width, the surface roughness of both sides of the kerf were investigated in three positions: top, middle and bottom of the cut edge as shown in Figure 4.37. As is seen, the striations are typical of the laser-cut surfaces and produce the Ra values. The results of this investigation are presented in this section.

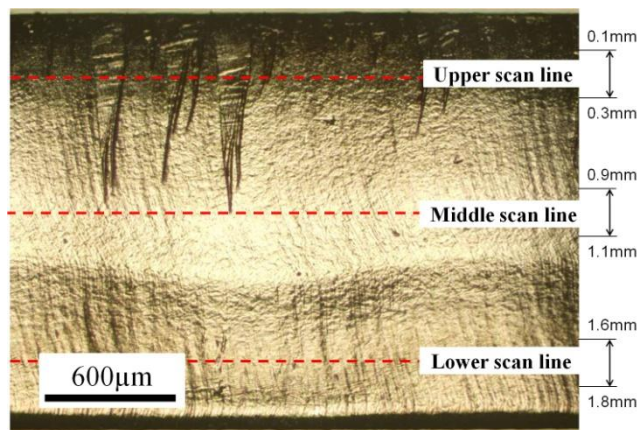


Figure 4.37- Showing the positions of surface roughness scan lines. (2 mm, 0.2 mm spot size, 2 bar oxygen, 1000 W, 5000 mm/min).

4.4.1 Fibre laser-oxygen cutting

The variations of surface roughness (Ra) versus cutting speed for three different positions of top, middle and bottom of the cut edge are presented in Figure 4.38 to Figure 4.43 for sheet thicknesses of 2 mm, 1.6 mm and 1mm using a power of 1000 W and 1500 W. As can be seen in these figures, the roughest part of the cut edge is observed at the lower part of the cut edge and the smoothest region is observed at the middle.

In laser cutting of 2 mm-thick sheet using 1500 W, as the cutting speed increases from 4000 to 6000 mm/min, the surface roughness values slightly decreases

(Figure 4.38). When using 1000 W, as the cutting speed increases from 4000 to 5000 mm/min, the surface roughness values slightly decreases before a little rising as speed is increased to 6000 mm/min (Figure 4.39).

In the range of employed cutting speeds and powers, when laser cutting of 1.6mm and 1mm sheets, the Ra values of the middle and upper cut edge are approximately the same (Figure 4.40 to Figure 4.43). In each case, the lower area of the cut has the highest Ra value.

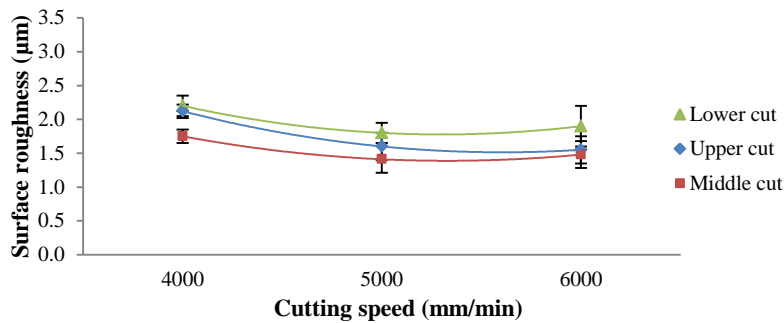


Figure 4.38- The surface roughness (Ra) versus cutting speed at different position on the cut edge (1500 W, 2 bar oxygen, 2 mm thick sheet).

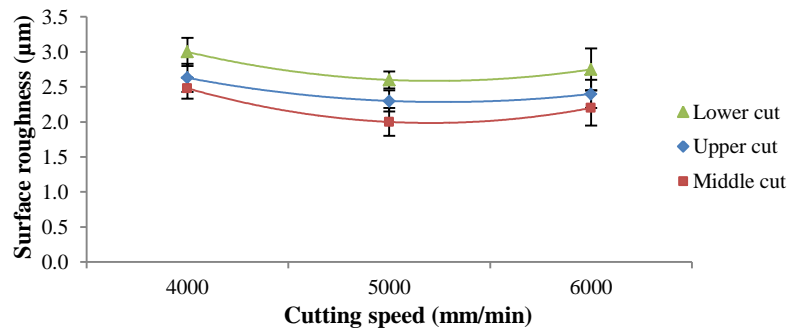


Figure 4.39- The surface roughness (Ra) versus cutting speed at different position on the cut edge (1000 W, 2 bar oxygen, 2 mm thick sheet).

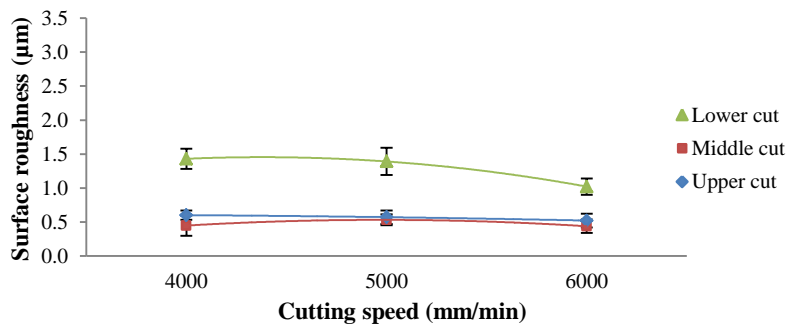


Figure 4.40- The surface roughness (Ra) versus cutting speed at different position on the cut edge (1500 W, 2 bar oxygen, 1.6 mm thick sheet).

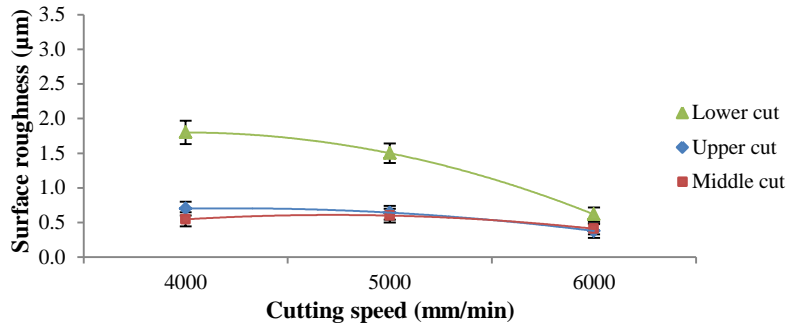


Figure 4.41- The surface roughness (Ra) versus cutting speed at different position on the cut edge (1000 W, 2 bar oxygen, 1.6 mm thick sheet).

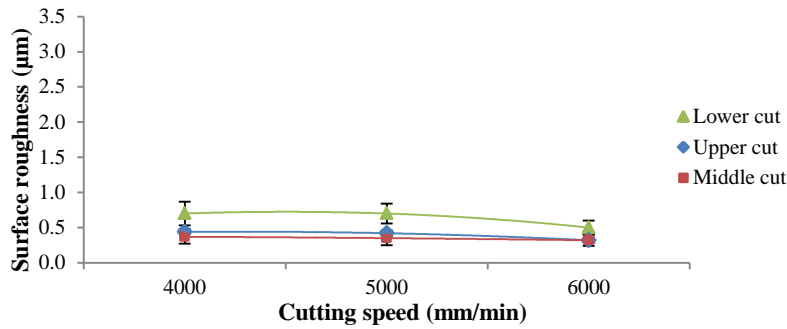


Figure 4.42- The surface roughness (Ra) versus cutting speed at different position on the cut edge (1500 W, 2 bar oxygen, 1 mm thick sheet).

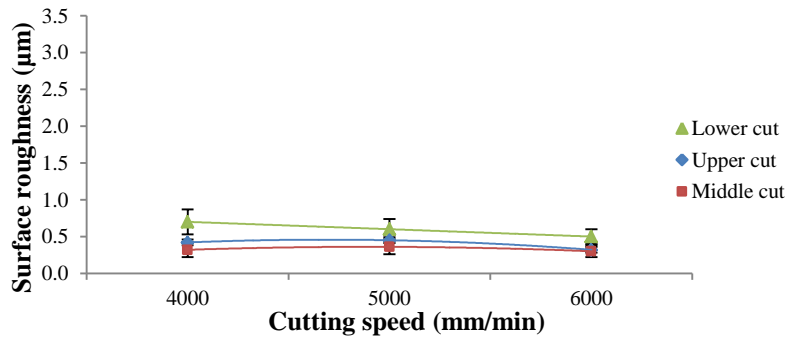


Figure 4.43- The surface roughness (Ra) versus cutting speed at different position on the cut edge (1000 W, 2 bar oxygen, 1 mm thick sheet).

A comparison of the surface roughness at each position for used thicknesses is presented in Figure 4.44 as a function of cutting speed when using power of 1000 W.

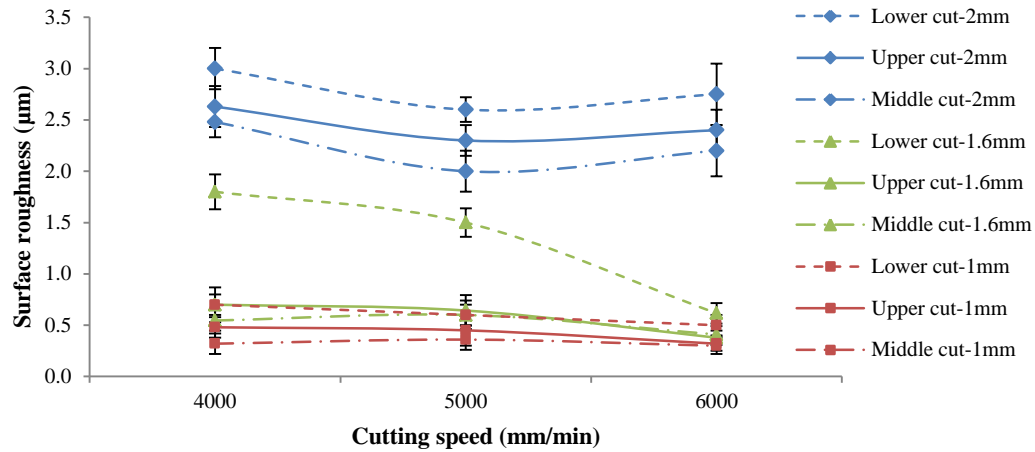


Figure 4.44- Comparison of surface roughness for different thicknesses with increasing cutting speed (1000 W, 2 bar oxygen).

As can be seen, the smoothest surface when cutting 2 mm thick sheet is obtained at a cutting speed of 5000 mm/min whilst for 1.6 mm and 1mm thicknesses, it is achieved at the cutting speed of 6000 mm/min. Overall, the surface roughness increases with sheet thickness. As is seen in Figure 4.38-Figure 4.43, for a given thickness, as the power increases the surface roughness decreases.

- Increasing power decreases surface roughness.
- Decreasing sheet thickness decreases surface roughness.

4.4.1.1 Surface roughness discussion

During laser cutting, melt flows out through the bottom of the cutting zone and this flow behaviour is reflected in the patterns of solidified melt on the cut edges [22, 58]. The micrographs of the cut edges clearly indicate that the pattern of frozen melt on the cut edge is changed by increasing cutting speed (Figure 4.45). Any turbulence in the melt flow will also be evident in the re-solidified turbulence of a rough and rippled surface [22]. This is observed in Figure 4.45, obtained for a lower cutting speed (e.g. 4000 mm/min). Alternatively, the smoothest cut edge will be created by the steadiest melt flow conditions [22, 53] which is seen in Figure 4.45 for an increased cutting speed (e.g. 5000 mm/min).

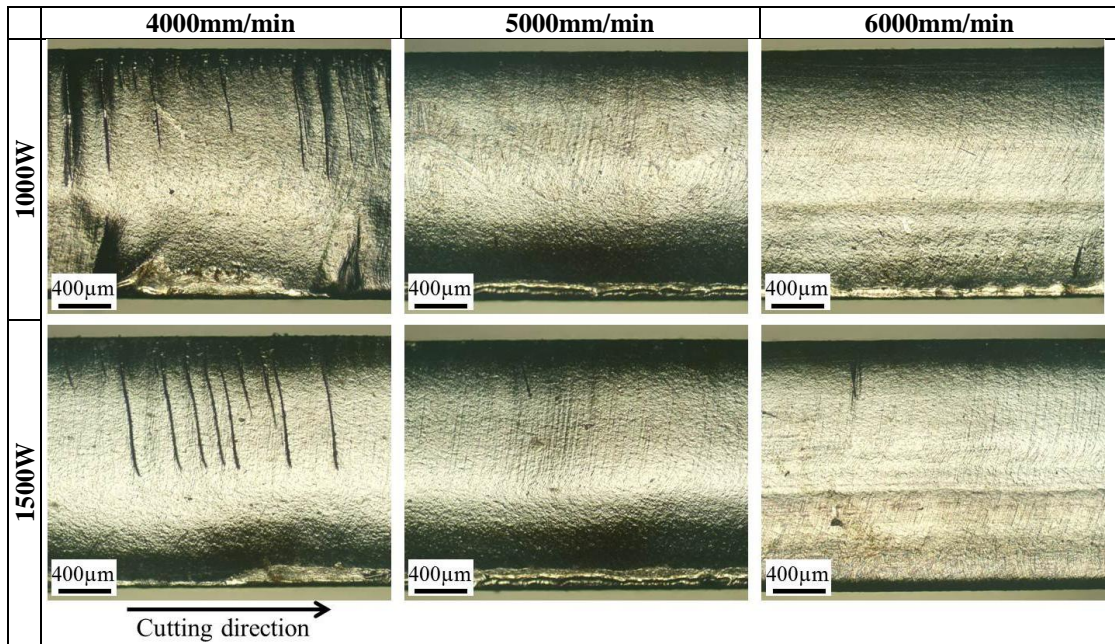


Figure 4.45- Photos of the cut edges for different powers and cutting speeds. Sheet thickness is 2 mm, 2 bar oxygen.

4.4.1.2 The effect of thickness on the surface roughness

Figure 4.46 shows that the surface roughness gets larger with an increase in the thickness. A rougher surface is observed at the bottom of the cut edge of 2 mm-thick sheet. This feature is decreased for 1.6 mm and is not seen for 1 mm. This feature is related to the melt flow behaviour. A turbulent melt flow appears at the lower part of the 2 mm cut edge whilst this influence disappears for 1mm. For 1.6mm thickness, there is a very small effect of turbulence compared with 2mm. With the same cutting parameters, as the sheet thickness decreases, the melting rate (the melt volume per interaction time) is decreased and also the residence time of the melt in the cut front is decreased. Thus, turbulence does not occur.

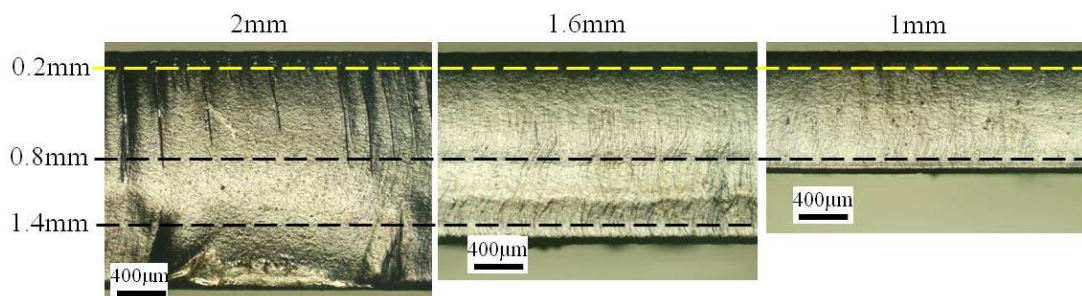


Figure 4.46- Micrographs of the cut edges from 2 mm, 1.6 mm and 1 mm thick sheet. A severe melting influence is observed on the lower surface of the 2 mm sheet. Three dash lines show the position of surface roughness examinations at distances of 0.2, 0.8 and 1.4 mm from the upper surface of the sheet (2 bar oxygen, 200 µm, 1000 W, 4000 mm/min).

Trapped gas flow in thicker sheet (e.g. 2 mm) is producing ripples on the oxide layer at the upper part of the cut edge. This feature is not observed on the thinner cut edges because there is less opportunity to trap the gas flow. This phenomenon is discussed later in 4.6.1. The surface roughness measurements of the samples shown in Figure 4.46 (at the same distances of 0.2 mm, 0.8 mm and 1.4 mm from the upper surface of the samples) are presented in Figure 4.47. The results revealed that:

- 1- In thicker cut edge (e.g. 2 mm) the surface roughness decreases at the middle position (i.e. 0.8 mm)
- 2- Turbulence happens at the same distance from the top for each sample (in this case at 1.2 mm).
- 3- The turbulence is reduced as the sheet thickness decreases.

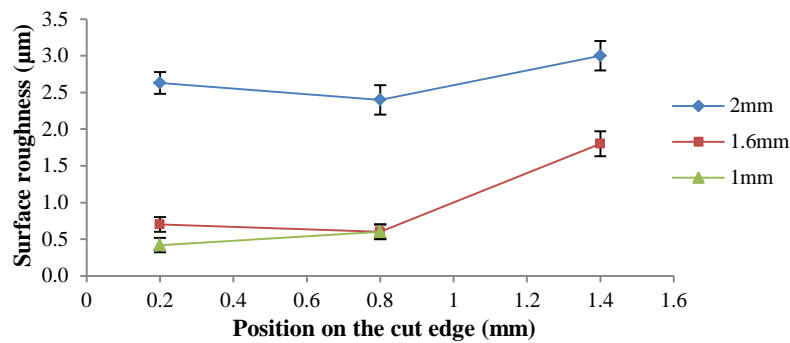


Figure 4.47- Surface roughness versus thickness as a function of distance from the upper surface of the sample (2 bar oxygen, 200 µm, 1000 W, 4000 mm/min).

4.4.1.3 The effect of laser power on the surface roughness

A comparison of the surface roughness presented in Figure 4.38 to Figure 4.43 reveals that, in the range of applied laser conditions and for a given thickness, as the power increases, the surface roughness decreases. For example, when using 1500 W for 2 mm-thick sheet, the upper surface roughness is 1.5 µm whilst for 1000 W it is 2.4 µm (Figure 4.38, Figure 4.39). This is because, at the power of 1500 W more energy is input to the melting zone compared to at 1000 W. Hence the melt temperature increases and the melt viscosity (Fe/FeO) decreases. The melt flow with a lower viscosity then produces a smoother cut edge [22]. However, for thinner sheet (e.g. 1 mm-thick sheet), the surface roughness does not change with increasing power which is related to the melt removal as discussed in 4.4.1.2.

4.4.2 Fibre laser-nitrogen cutting

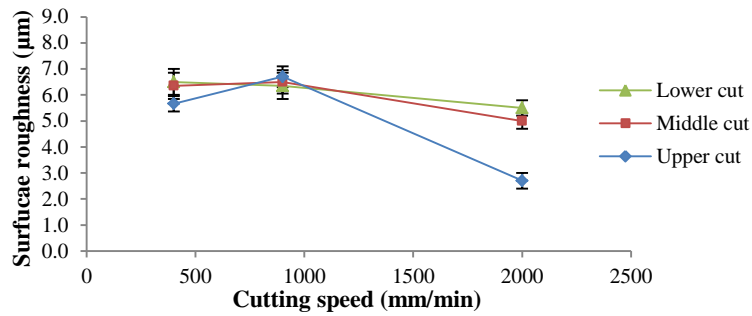


Figure 4.48- Surface roughness (Ra) versus cutting speed (2 mm, 1000 W, 12 bar nitrogen).

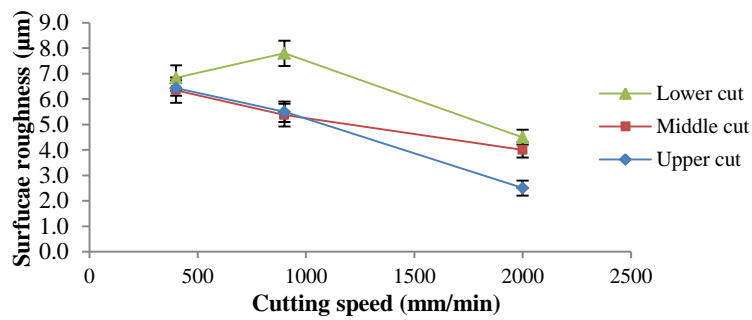


Figure 4.49- Surface roughness (Ra) versus cutting speed (2 mm, 1500 W, 12 bar nitrogen).

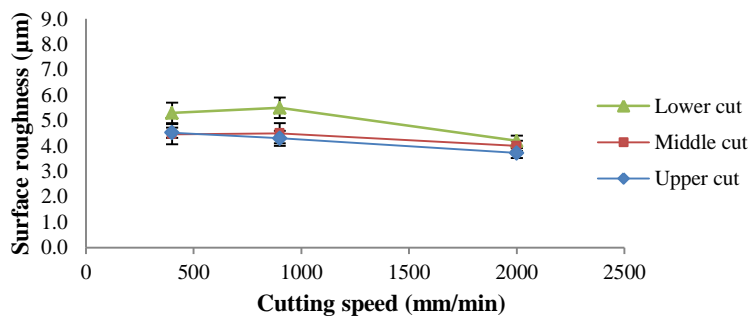


Figure 4.50- The surface roughness (Ra) versus cutting speed (1 mm, 1000 W, 12 bar nitrogen).

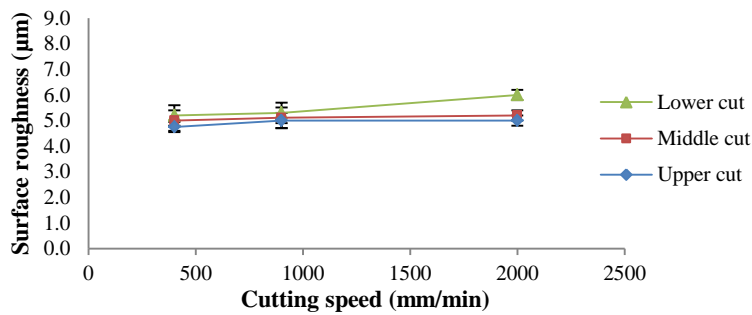


Figure 4.51- The surface roughness (Ra) versus cutting speed (1 mm, 1500 W, 12 bar nitrogen).

The results of surface roughness analyses in laser cutting of 1 and 2 mm thick mild steel sheet, using 12 bar pressure of nitrogen and different cutting speeds and powers, are presented in Figure 4.48 to Figure 4.51 (see page 118). As can be seen in the figures, there is a variation in the values of surface roughness. The smallest surface roughness is observed in the upper cut edge, and the roughest surface is seen in the lower cut edge. In the range of applied cutting speed, the lowest Ra value in the 2 mm-thick sheet is at the speed of 2000 mm/min (e.g. 2.7 μm for upper cut at a power of 1000 W). At the cutting speed of 2000 mm/min, the Ra decreases to 2.5 μm when power is increased to 1500 W.

Generally, in nitrogen laser cutting of 1mm thick mild steel in the range of employed cutting speed the Ra values are approximately constant, although a slight variation is noticeable as the cutting speed increases (Figure 4.50, Figure 4.51). The Ra for upper cut, when cutting 1 mm at cutting speed of 2000 mm/min with power of 1000 W, is 3.72 μm . When cutting with 1500 W, it increases to 5.0 μm .

Two micrographs of the nitrogen-cut edges are shown in Figure 4.52.

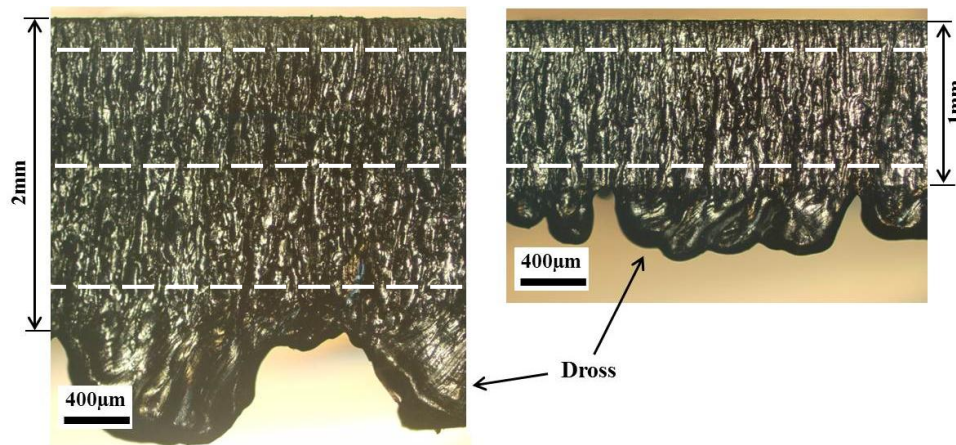


Figure 4.52- The cut surface after nitrogen laser cutting. Dross can be seen at lower cut edge. Dash lines show the position of surface roughness analysis (1000 W, 400 mm/min, 12 bar nitrogen).

It can be seen that the volume of attached dross increases with increasing sheet thickness. In general, the surface of the cut edge looks rough and is covered by resolidified scattered melt layers. The surface roughness examinations of the samples in Figure 4.52, at the same positions of 0.2 mm, 0.8 mm and 1.8 mm from the upper surface are presented in Figure 4.53. These reveal that the surface roughness for the same position on the cut edge increases with sheet thickness.

Surface roughness slightly increases from the top to the bottom of the cut edge.

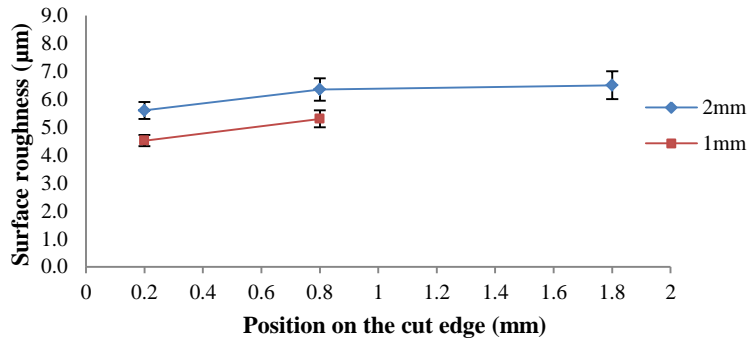


Figure 4.53- Surface roughness versus thickness as a function of distance from the upper surface of sample (12 bar nitrogen, 200 µm, 1000 W, 400 mm/min).

4.5 Cut surface characterisation

Characterisation of the laser cut edge can describe some events that occurred during laser melting and melt expulsion. As the melt layer flows out the kerf, a thin layer of the melt recast on the kerf walls. In this section the surface of cut edge is analysed for both oxygen and nitrogen laser cuttings. The X-ray diffraction (XRD) result of the oxygen-cut edge is presented in Figure 4.54 and shows qualitatively the presence of FeO and Fe₃O₄. The presence of FeO in re-solidified melt confirms that an exothermic reaction between iron and oxygen occurred during laser melting. From this reaction, a considerable amount of energy is added to the melting zone, enhancing the cutting process [9, 117, 118].

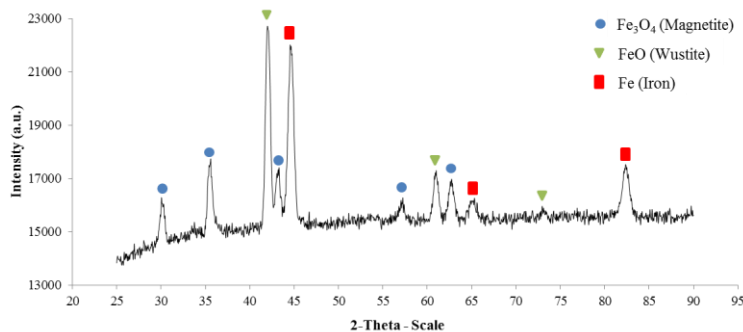


Figure 4.54- XRD of 2mm thick cut edge (fibre laser oxygen cut at 4000 mm/min and 1500 W).

EDS examination at the laser-oxygen cut edge (Figure 4.55) qualitatively shows the presence of oxygen on the surface of resolidified melt. The solid line on the SEM micrograph shows the position of EDS examination.

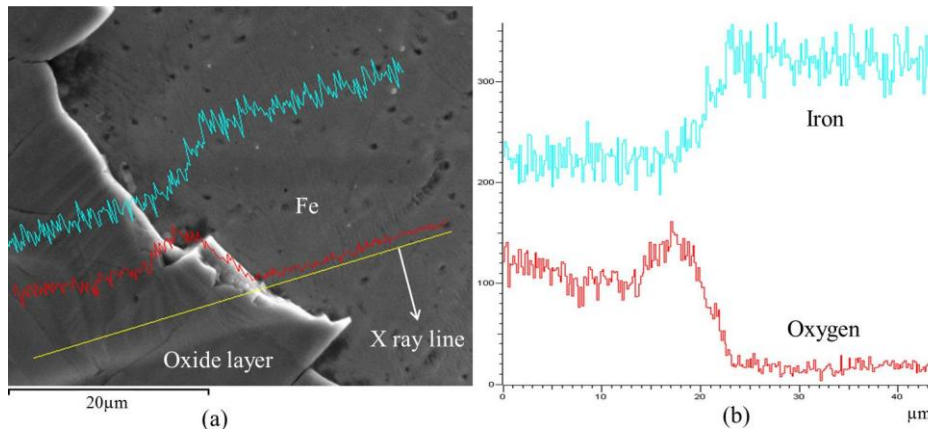


Figure 4.55- EDS line scan of a cut surface at which a piece of oxide layer was broken off the cut surface. EDS qualitatively confirms the presence of oxide on the cut edge (1500 W, 4000 mm/min, 2 bar oxygen).

The EDS line scan of a fibre laser-nitrogen cut surface (Figure 4.56) indicates that, on the cut edge, the quantity of iron is greater than that of oxygen, while the amount of oxygen increases in the dross zone. This is because, the molten dross can be affected by oxygen in the air during solidification.

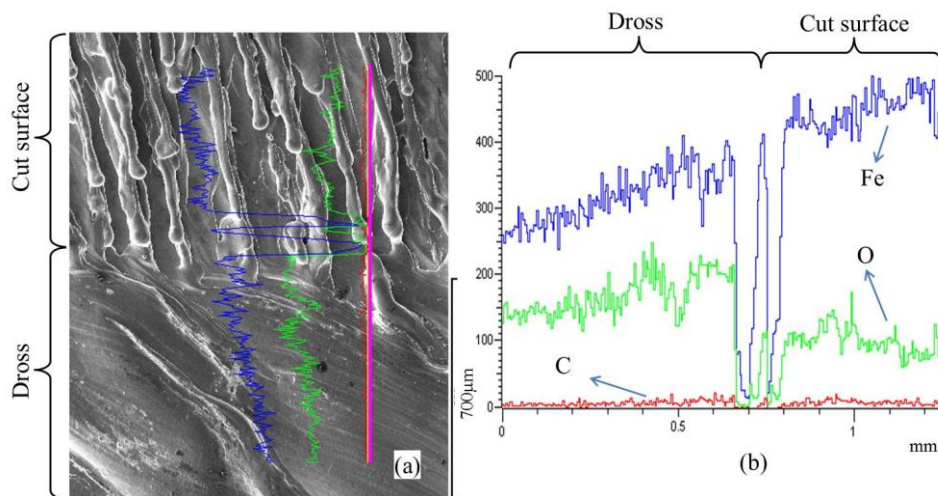


Figure 4.56- The EDS line scan of a fibre laser-nitrogen cut surface. a) The line is located on the cut surface and attached dross at the bottom of kerf. b) Iron, oxygen and carbon can qualitatively be observed. The position of cut surface and dross are shown on the top of the figure. As the EDS line-scan crosses a solidified streak, a big ripple was placed on the interface of the cut edge and dross. It is probably due to a hole formed on the streak during solidification (1500 W, 1000 mm/min, 12 bar nitrogen pressure).

As is seen in Figure 4.56-b oxygen presents on the cut surface zone. This could be for two reasons: either the nitrogen used was not pure, or it was added to the melting zone from the surroundings air during laser cutting and solidification. The first reason is unlikely because pure nitrogen of 99.95% was used. However, there was a 1mm stand-off distance between the nozzle and the cut zone. Hence oxygen from the

surroundings could have entered the melting zone by nitrogen jet. Therefore the second reason is most probably the cause. Regarding the nitrogen, EDS did not show the presence of nitrogen on the cut edge.

4.5.1 Cut edge comparison between oxygen and nitrogen laser cutting

In oxygen laser cutting FeO is produced in the melt due to exothermic reaction between melt and oxygen. The presence of this oxide in the melt decreases the melt viscosity [9, 89]. During solidification the FeO forms an oxide layer on the cut edge. This oxide layer originally covered all at the cut edge but, as it is quite fragile, some has broken off (Figure 4.57). In contrast, for nitrogen laser cutting, there is no reaction between melt and pure nitrogen [119] and such an oxide layer cannot be observed in the cut edge. However, the EDS results qualitatively show some amount of oxygen on the surface of cut edge, which may have been added from the surrounding air during laser cutting or solidification.

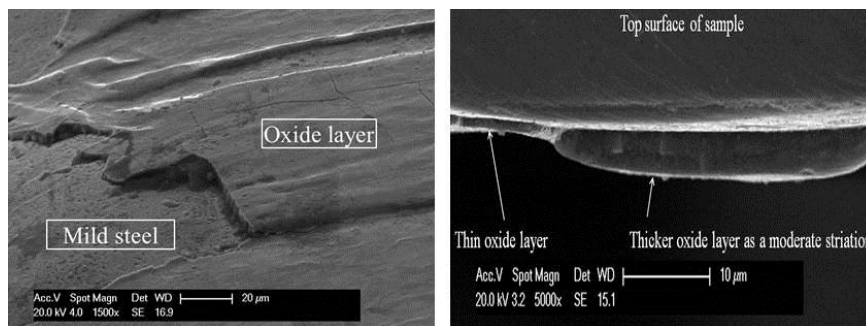


Figure 4.57- Left: presence of oxide layer on the top of the cut edge (1500 W, 6000 mm/min, 2 bar oxygen). Right: A cross section of the sample to see the thickness of oxide layer.

4.6 Striation pattern observation

The striation is a final cold state left behind by the melt flow behaviour and is not a snapshot taken during melt removal. By studying the striation pattern, we are able to find out more about the melt flow behaviour in the melting zone.

4.6.1 Fibre laser-oxygen cutting

In order to investigate the phenomenon of striation generation and its resulting pattern, a cut edge with such a pattern was observed (Figure 4.58). This cut edge was obtained by oxygen fibre laser cutting of 2 mm-thick mild steel with a power of 1000 W and a cutting speed of 4000 mm/min. The kerf wall demonstrates three

different striation types: type1 (smooth), type2 (moderate) and type3 (coarse striations) as highlighted in Figure 4.58. This cut edge can be divided to three areas as shown. Area1 includes two types of striation: type1 and type2 (i.e. smooth and moderate striation with Ra of 2.8 μm). Area2 is a connecting area with Ra of 2.5 μm ; and area 3 includes type3 and 2 of striation (i.e. coarse striation and smooth striation alternatively with Ra of 3.5 μm). Two thirds of the surface is almost striation free (with only smooth striations) whilst the other third has an intermittent coarse striation pattern. The most important issue in this selected cut surface is that the striation free zone is alternatively recreated between two areas of coarse striations. The angle of the smooth striations changes on the base of Brewster angle with cutting speed and also differs from the top to the bottom of the cut edge. At the top of the cut edge, the angle of striations is at its lowest amount of 5° to 8°. The striations are bent towards the back from the middle of the cut edge. Eventually, near the bottom, the striations are kinked towards the bottom of the cut edge. At a cutting speed of 4000 mm/min the striations are inclined between 5° - 12°, while at a cutting speed of 5000 and 6000 mm/min the range of inclination angle is between 8° - 14° and 10° - 14° respectively.

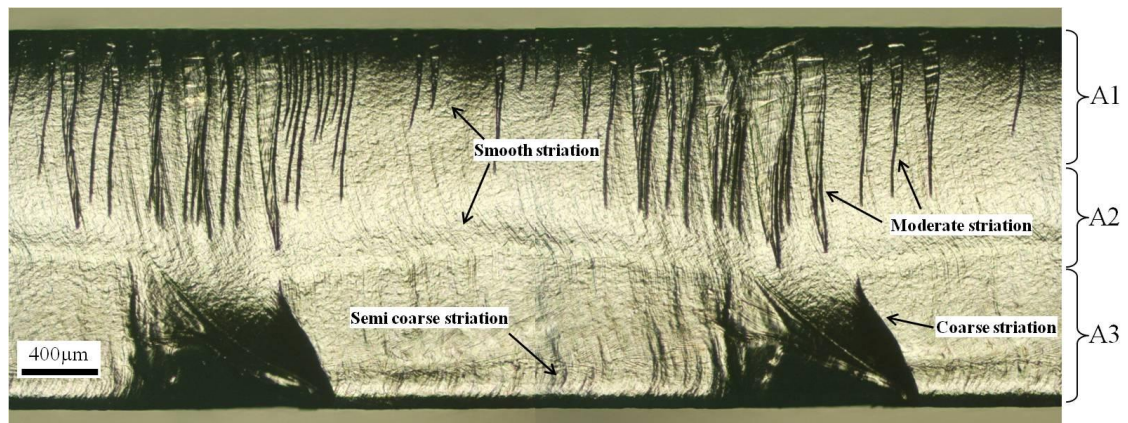


Figure 4.58- The cut surface with three kinds of striation: smooth, moderate and coarse (1000 W, 4000 mm/min, 2 bar oxygen).

It has been already identified that the cut surface is covered by an oxide layer (Figure 4.55 and Figure 4.57). From SEM observation of the kerf wall, the moderate striation at the top of the sample seems to be a wrinkle of only the oxide layer on the top of a smooth underlying resolidified sheet surface as highlighted in Figure 4.59 and Figure 4.60. This oxide layer is very fragile but stuck to the cut edge. The thickness of oxide layer varies on the cut edge.

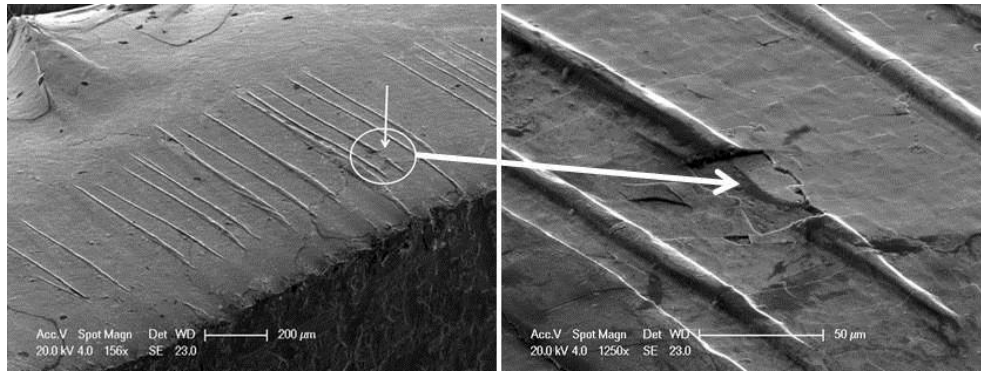


Figure 4.59- Left: some smooth striations initiated below the edge. Right: Magnified marked striation is shown (1000 W – 4000 mm/min – 2 bar oxygen).

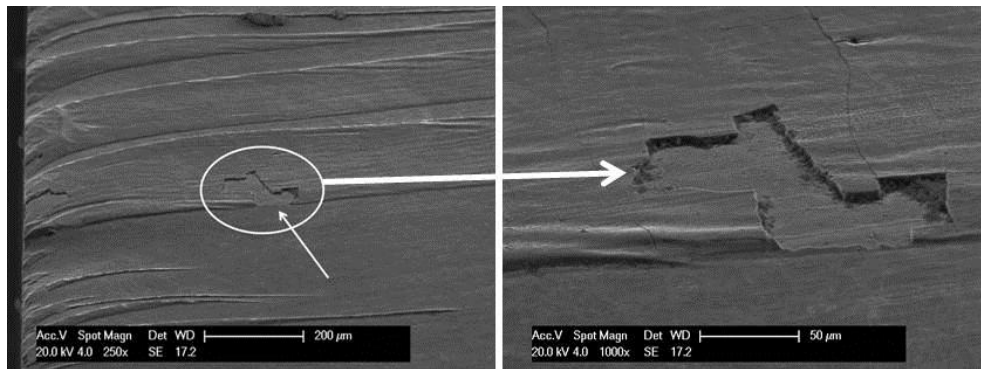


Figure 4.60- Left: some smooth and moderate striations initiated at the edge. Right: magnified marked striation is shown (1500 W – 4000 mm/min – 2 bar oxygen).

4.6.1.1 The mechanism of melting and melt removal

Figure 4.58 was re-included here as Figure 4.61 with additional information displayed (4 steps) to explain the mechanism of melting and melt removal.

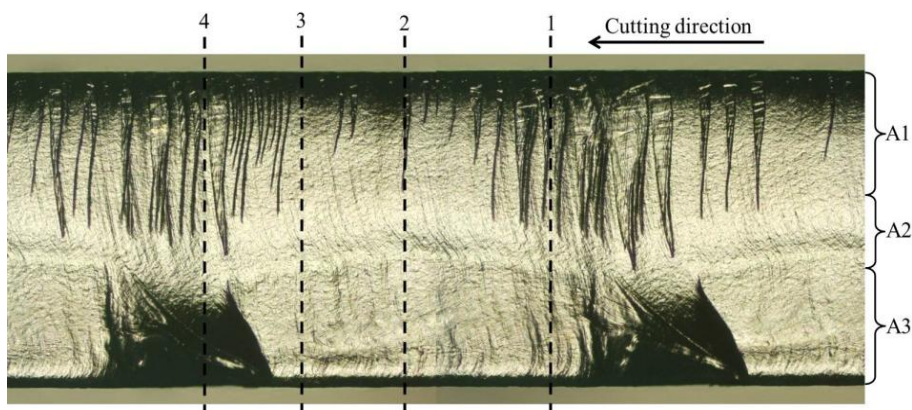


Figure 4.61- The cut surface reprinted from Figure 4.58 (1000 W, 4000 mm/min, 2 bar oxygen).

Step1: A thin melt layer is created (Figure 4.61 and Figure 4.62). From the smooth striation reflected to the upper part of cut edge, it can be inferred that, for this part of cutting process, the melt flow was primarily laminar and so a smooth/semi coarse cut surface is left behind.

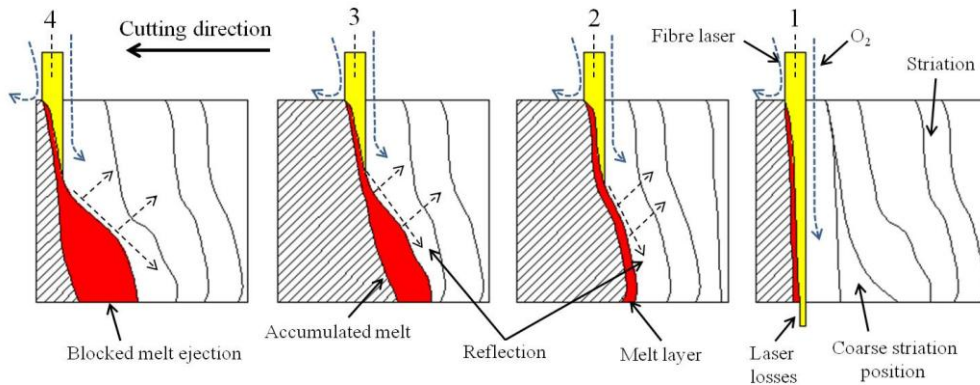


Figure 4.62- Explanation of melt build-up ejection cycle. The numbers are matched with numbers in Figure 4.61.

Step 2: As the melting proceeds, melt thickness increases and melt front kinks as a laminar flow and it starts to break down. It is seen that the striation (or cut front) kinks and bend towards the bottom of the kerf.

Step3: The entire melt cannot be pushed down to the bottom of the kerf by the oxygen pressure and some melt remains unsteadily on the cut front (accumulated melt). This phenomenon is called melt build-up [120]. Owing to the increase in the residence time of the melt flow towards the bottom of the kerf, more oxidation reaction between molten iron and oxygen occurs, increasing the melting rate.

Step4: The large build-up of melt is discharged from the cut front (Blocked melt ejection [120]), returning to striations in step 1.

Depending on power and the cutting speed laser beam can melt and penetrate into the limited depth of material (i.e. A1 in Figure 4.61) without reflection. After that, the process of melting zone generation seems to be managed by other phenomena including the beam reflections and the melting-erosion by conduction of heat from the melt above. In oxidation cutting this is all combined with oxidation heat and as the melt flows down the kerf the thickness of the melt layer increases.

At a lower cutting speed (in this case 4000 mm/min), the cut front is almost vertical and the majority of the laser energy is lost (step1 in Figure 4.61 and Figure 4.62). This type of laser-cut front interaction causes a cycle self-burning [22]. The cycle self-burning probably causes burst melting with further inclination at the upper part of the cutting front (step 2) starting the melt build-up phenomenon [120] (step 3).

4.6.1.2 Beam behaviour inside the cutting zoon

Beside the exothermic reaction, the laser beam energy may be transferred out of the laser beam irradiation area by the waveguiding effect (Figure 4.63). This was suggested by reference [52]. The re-direction of the laser beam energy from the irradiation area can be explained by two possible phenomena. The first is by external reflection and the second is by internal reflection or waveguiding. This second phenomenon is a more likely candidate in fibre laser cutting because FeO is partially transparent at the fibre laser wavelength of approximately $1.06\ \mu\text{m}$ [52].

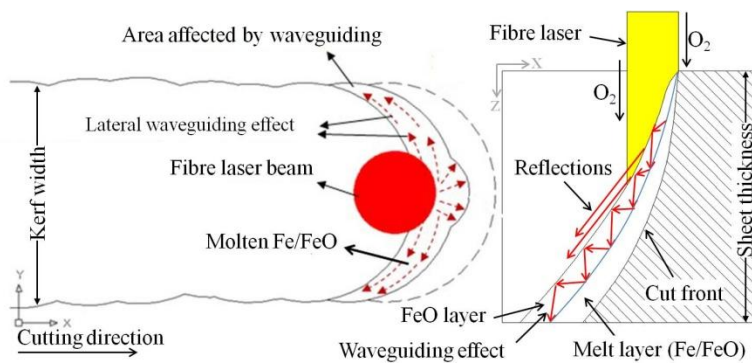


Figure 4.63- Waveguiding effect and multiple reflections explanations in the kerf and cut front.

The reflections and waveguiding effect, combined with further movement of the laser, result in the blocked melt being ejected [120] (step4 in Figure 4.61 and Figure 4.62). Further down the cut zone (close to the bottom) the thickness of the Fe/FeO melt is greater, and turbulence in the liquid flow produces a rougher cut edge.

At a constant power and cutting speed, there is a constant flow of melt from the bottom of the cut zone. For a cutting speed (in this case at 4000 mm/min), the melt periodically builds up at the bottom of the cut zone and is ejected in greater volume. Normally, for this type of melt build-up-ejection cycle, the cycle would be less periodic. The period of the cycle may be influenced by the vibration of the machine's table.

4.6.1.3 The mechanism of oxide layer generation

During oxygen laser cutting, the molten iron oxide (FeO) is created on the melt layer from the outside, where the oxygen is. As the laser beam moves forward, the melt layers in combination with gas jets, produces ripples [120] with connection lines on

the surface of the melt in the melting zone [53, 121]. The connection line is a part of a ripple that connects the ripple to the top edges (Figure 4.64). While the ripples are flowing down the kerf, connection lines expand, move to the sides and solidify on the kerf's sides resulting in striations [121].

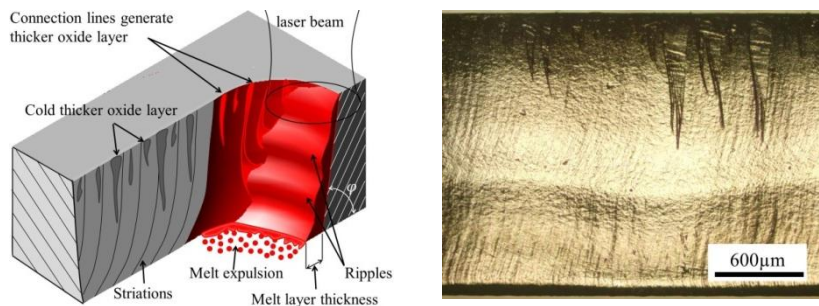


Figure 4.64- Left: Schematic showing the thicker oxidation generation. Right: Thick oxide layer on the upper cut edge (2 bar oxygen, 1000 W, 5000 mm/min).

Figure 4.65-A shows that the molten oxide layer has a chemical gradient. Powell and Ivarson [88] clearly explained that there is a fully oxidised iron on the outside surface of the melt. As the melt layer goes down the kerf, the molten FeO near the kerf walls sticks to the walls and begins solidification resulting in generation of an oxide layer on the walls. The influence of gas flow causes ripples on the oxide layer on the top surface of cut edge. The oxide layer was also observed on the cut edge that was sectioned and polished gently and presented in Figure 4.65-B. In this case, the oxide layer included resolidified iron. As can be seen, a huge oxide lumps at the bottom of the cut edge. The thickness of oxide layer in this case is 8 μm on the top and increases to 45 μm at the bottom of the cut edge.

In summary, the oxide layer is generated where the melt layer is in contact with the oxygen. The melt layer flows down the cutting front with some ripples. As the melt layer flows down the kerf, the oxide layer forms on the cut edge. Oxygen flow behaviour causes ripples on the oxide layer. The thickness of the oxide layer varies from the top towards the bottom of the cut edge. In this case, a lumped oxide was observed at the lower part of cut edge.

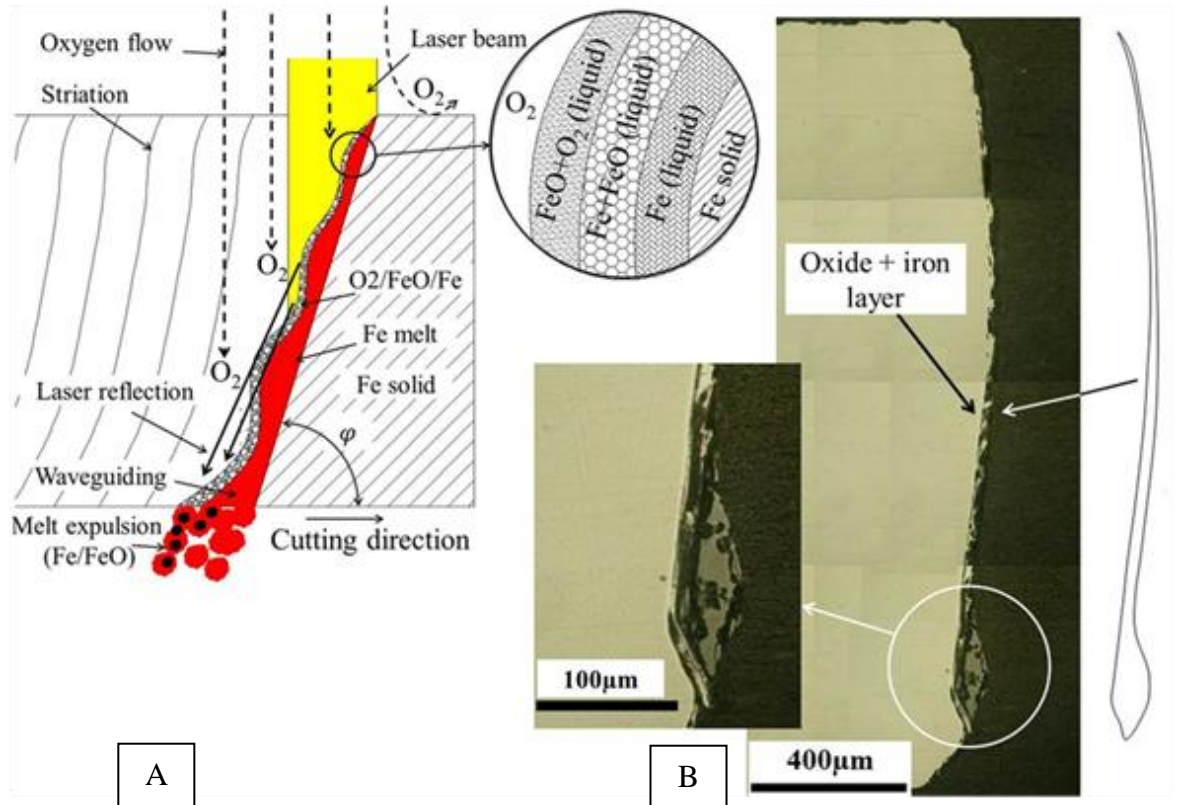


Figure 4.65- A: showing the thickness of the melt and the oxide layers with a chemical gradient in the cutting front. B: Diagram showing a gently sectioned and polished cut edge. A relatively thick porous oxide + iron layer is observed on the cut edge. Several photos with high magnification were taken with an optical microscope and then aligned together carefully. The thicker part of the oxide + iron layer is shown in a higher magnification inset in the diagram. The shape of the oxide + iron layer is also drawn for clarity (1500 W, 4000 mm/min, 2 mm).

4.6.2 Fibre laser-nitrogen cutting

After nitrogen laser cutting, relatively thick dross can be observed clinging to the lower surface of the sheet as be illustrated in Figure 4.66. The thickness of dross increases with sheet thickness and power.

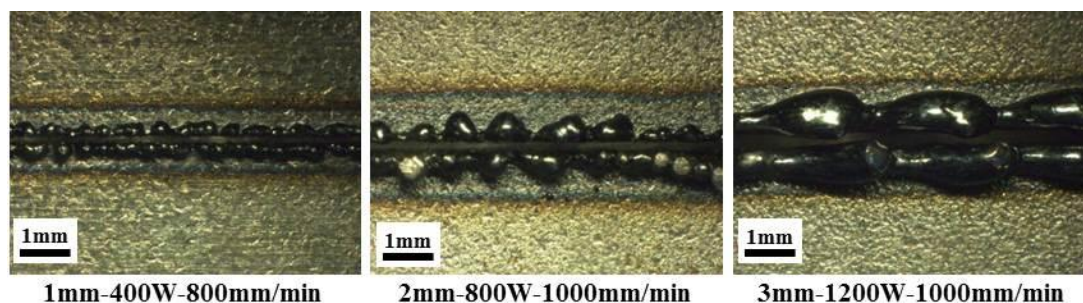


Figure 4.66- Relatively thick dross clinging to the lower surface of the sheet (12 bar nitrogen).

The cut edge is covered by lots of streaks which produced a chaotic striations pattern. Under the optical microscope, the surface of the cut looks very rough (3 to 7 μm),

and it seems that there is no significant order in the arrangement of striation pattern. Observation of the cut edge by SEM indicates that the disorder of the striation pattern increases from the top towards the bottom of the cut edge. Surface roughness examination also revealed that the surface roughness increases from the top to the bottom (Figure 4.67).

4.6.2.1 The mechanism of striations generation

The cut edge can be divided to three areas as shown in Figure 4.67.

Area 1: This area is located just below the upper edge (Figure 4.67-A1). In this area the streaks appear almost uniform.

Area 2: In this area, an integration of melt flows takes place (Figure 4.67-A2). A chaotic striations pattern is seen in this region.

Area 3: This area incorporates the dross region which has clung to the bottom surface of the sheet.

In area 1, the laser beam primarily penetrates the sheet on the base of Brewster angle and a new melt layer is produced which flows down. The high pressure of nitrogen pushes the molten material down the kerf. In area 2, the molten material then breaks up into the streaks under the influence of the surface tension and high gas pressure [65, 81, 122]. The streaks are inclined towards the back of cutting zone with angle of $5^{\circ} - 15^{\circ}$ (Figure 4.68). The inclination of striations (ϕ) increases with cutting speed which is related to the Brewster angle [122].

As the melt flows down the kerf, the temperature of melt decreases. Hence the viscosity of melt increases. The relatively thick dross clung to the bottom of the cut edge indicates that the temperature of the melt at the bottom of the kerf decreases to the lowest melt temperature before solidification (Figure 4.69).

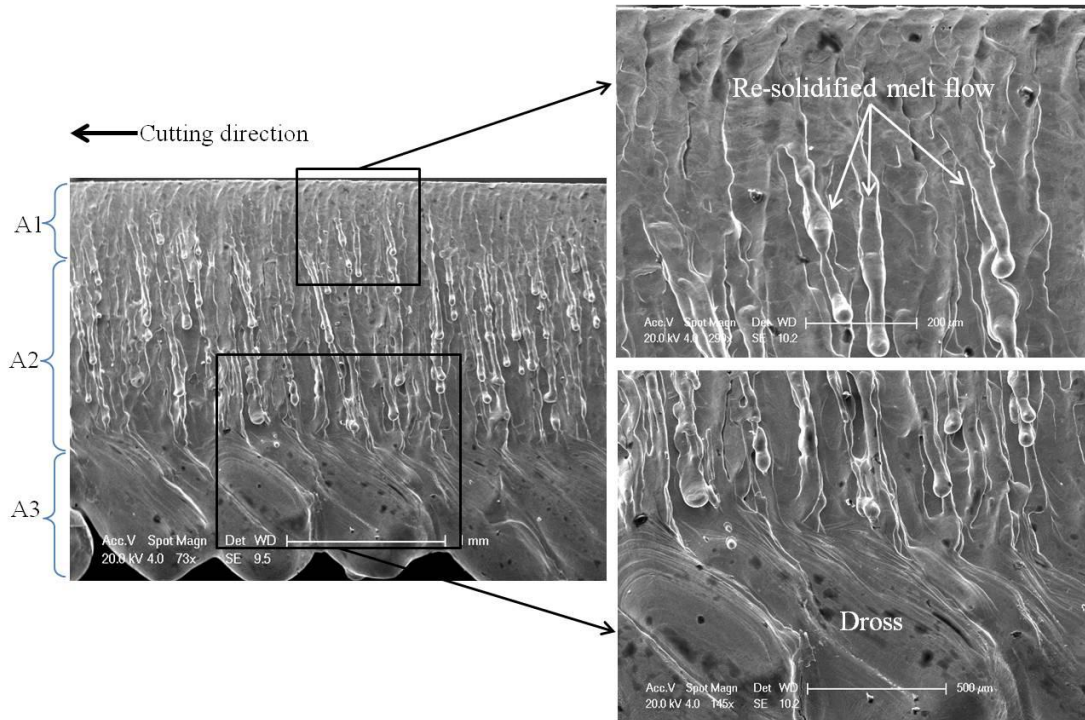


Figure 4.67- Left: a cut edge with dross clinging to the lower surface of the sample, three areas can be observed as shown with A1 to A3. Right: the boundary of areas has been presented in magnification. Re-cast melt layers and chaotic striation pattern can be seen (1000 W, 1000 mm/min, 2 mm, 8 bar nitrogen).

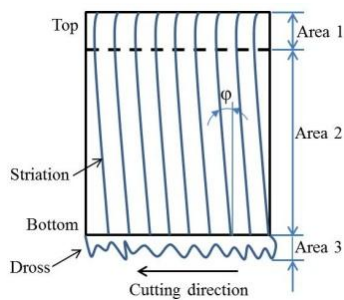


Figure 4.68- Indicating the inclination of striations in area 1 and 2.

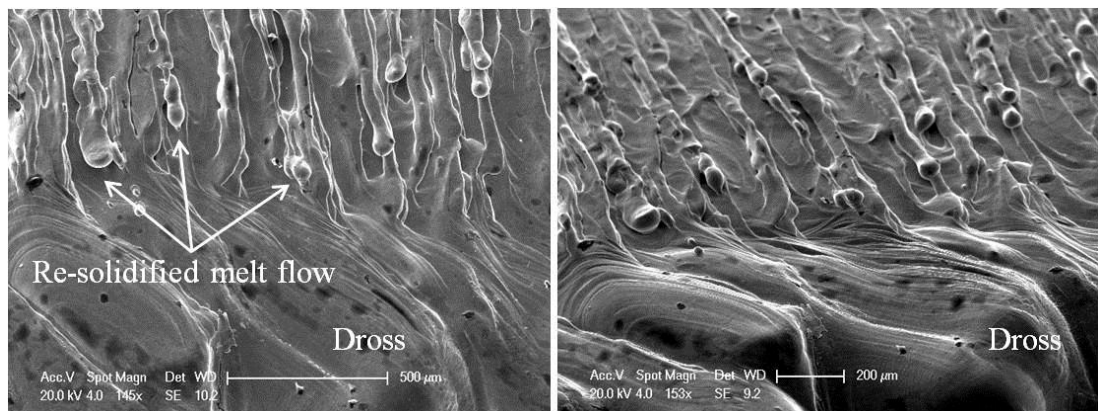


Figure 4.69- Left: Downstream region at the bottom of area 2, Re-solidified melt flow and dross generation can be seen. Right: Different view of dross attachment and integration of dross layers (1000 W, 1000 mm/min, 8 bar nitrogen).

There are some reasons for reduction of melt temperature at the lower part of the cut front:

- Nitrogen as an inert assist gas in interaction with the melt flow is capable to decrease the melt temperature as a result of heat convection.
- While the melt is flowing down the kerf, the heat absorption losses increase as a result of heat conduction from melt into the adjacent material [69].
- The influence of the laser beam to sustain the melting temperature near the bottom of the kerf decreases. During fibre laser cutting, the laser beam interacts with the upper cutting front while the lower cutting front is irradiated by the beam reflections [50, 59]. Also see Figure 4.70.

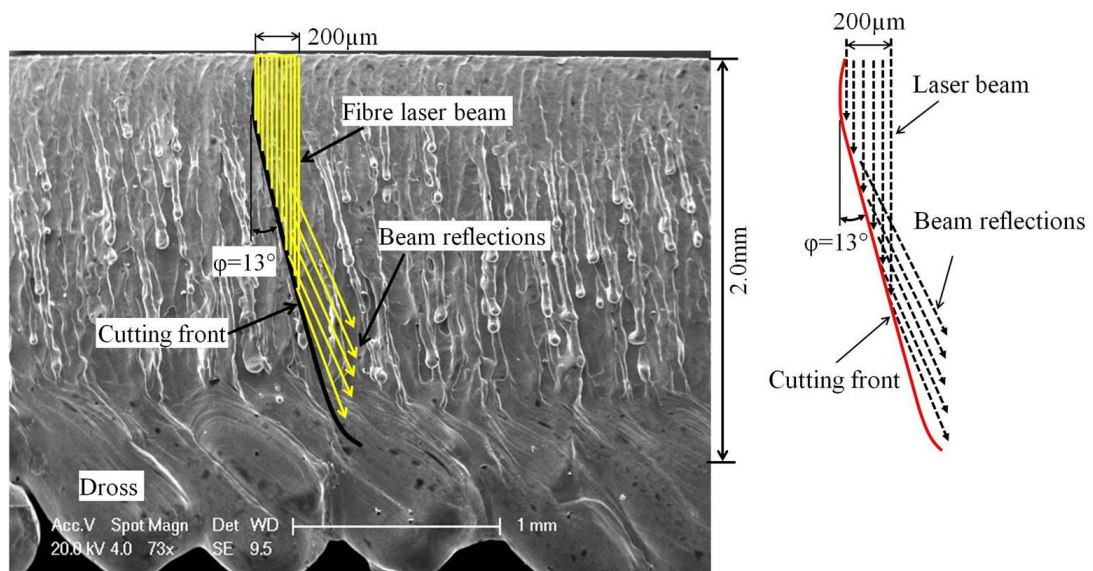


Figure 4.70- Superposition of laser beam with striation. Multiple reflections irradiate the lowest melt layers (1000 W, 1000 mm/min, 2 mm, 8 bar nitrogen).

4.6.3 Comparison between oxygen and nitrogen striations pattern

The striations pattern observed indicates that there are several significant differences between oxygen and nitrogen cut edges.

- After oxygen laser cutting, striations pattern are much smoother than those are observed in nitrogen laser cutting. This feature was identified by surface roughness analysis. The surface roughness in nitrogen cutting is 3 to 7 μm but only is 2.5 μm for oxygen cutting. This is due to the higher temperature and lower viscosity melt in laser-oxygen cutting.

- In oxygen laser cutting, some striations are simply due to oxide ripples, independent of underlying smooth resolidified metal.
- The surface of the cut edge in oxygen laser cutting is originally covered by a fragile, thin oxide layer (FeO). These features are not found in the nitrogen laser cut edge.
- For oxygen laser cutting at a certain combination of laser power, cutting speed and cut front geometry (related to the Brewster angle), a very smooth striations can be achieved. This feature is not presented for nitrogen laser cutting.
- In nitrogen fibre laser cutting, the cut edge usually includes dross attachment, while in oxygen laser cutting the cut edge generally is dross free.
- In nitrogen laser cutting, the striations are clearly due to melt flow breaking up into the streaks under the influence of the surface tension and high gas pressure.

4.7 Summary

In this chapter, oxygen and nitrogen fibre laser cutting of thin section mild steel, using variety of cutting speeds, different laser powers, the same fibre and optical system were compared together in terms of kerf width, heat affected zone surface roughness, cut edge characterization and striation pattern. The most significant results are as follows:

- For both assist gases (i.e. O₂ and N₂), the kerf width is significantly wider than the focused beam diameter. This ratio for oxygen laser cutting is 2.5 and for nitrogen is 1.4 in average. The kerf width in oxygen laser cutting is 44% wider than that is obtained in nitrogen laser cutting.
- For both applied gases, the width of the HAZ on the lower part of cut edge is larger than that for the upper part.
- The amount of HAZ for laser-nitrogen cutting is 2 to 2.7 times larger than that for laser-oxygen cutting.
- The cross sectioned, polished and etched cut edge indicates that there is a relatively thick re-solidified melt material lining the cut edge after nitrogen cutting. This feature is not observed for the oxygen cut edge.

- EDS and XRD examination of the cut edges indicate that the surface produced by oxygen laser cutting is covered by an oxide layer ($\text{FeO} + \text{Fe}_3\text{O}_4$). This feature is not seen for nitrogen laser cutting.
- In oxygen laser cutting, the striation patterns are much smoother than those observed for nitrogen laser cutting. This was evident from the results of surface roughness analysis.
- The surface roughness of the oxygen laser cut edge is less than that for the nitrogen cut edge (on average $2.5 \mu\text{m}$ and $5 \mu\text{m}$ respectively).
- Some striations in oxygen laser cutting are due to the rippled oxide on top of the smooth surface roughness.
- After nitrogen fibre laser cutting, the cut edge includes dross attachment while for oxygen laser cutting the cut edge is generally dross free.

5 Piercing process

5.1 Overview

The results of laser piercing will be presented in this chapter. The purpose of this chapter is to understand the effects of laser piercing parameters on the pierced hole geometry. First, the importance of study on the piercing in laser cutting will be discussed then the piercing results are going to be investigated. The geometrical results of the hole generation will be shown in the map which is called a hole growth map. A comparison between oxygen and nitrogen laser piercing of 2 mm-thick mild steel sheet using a variety of laser powers, gas pressures and irradiation times is going to be discussed. Finally, a new method in oxygen laser cutting of mild steel is to be introduced which can enhance the productivity in laser cutting.

More details of the piercing experiments were explained in chapter 3; however, here it is proper to rewrite some of the laser piercing parameters as presented in Table 5.1.

Table 5.1- Indicating some laser piercing parameters.

<i>Characteristics</i>	<i>Values</i>
<i>Laser power range</i>	<i>600 W to 2000 W</i>
<i>Assist gas</i>	<i>Oxygen and nitrogen</i>
<i>Gas pressure range</i>	<i>0.3 bar to 12 bar</i>
<i>Focussed beam diameter</i>	<i>0.2 mm (on the surface of sheet)</i>

5.2 The importance of study on piercing

In laser cutting process for cuts that do not start at a free edge of the material, the laser beam has to pierce a through hole at the beginning location of each cut (Figure 5.1) in order to establish an appropriate melt ejection flow from the lower side of kerf [1].

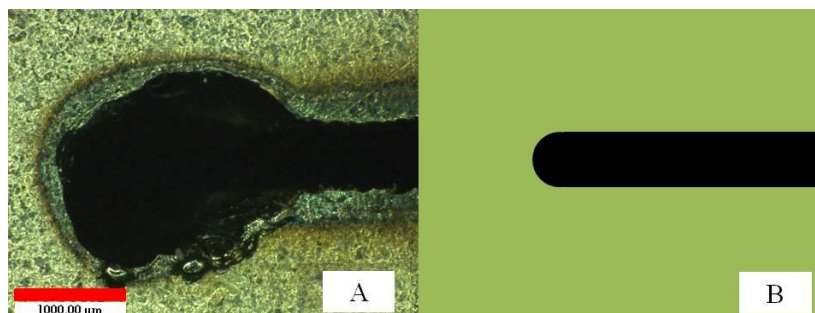


Figure 5.1- Showing how the initial hole affects the shape of cut kerf. Photo (A) shows usual initial hole shape which is seen at the beginning of a traditional laser cut (1000W, 4000 mm/min, 2 bar oxygen). Photo (B) is a schematic diagram of the ideal shape of the initial part of the kerf.

In traditional laser cutting, since the size of initial pierced hole is wider than the laser cut kerf width (Figure 5.1), the piercing is arranged at regions outside the required profile to remove the remaining marks of the pierced hole on the cut profile which results in materials wastage increment. In many applications materials wastage reduction is economically important so an attempt to pierce a fine initial hole at the beginning of the cut can directly decrease production costs. Figure 5.2 indicates an example of a traditional laser cutting plan to manufacture a single product. In order to avoid any remaining marks of the pierced hole on the required product, the cut path and initial hole are located at regions outside the required profile.

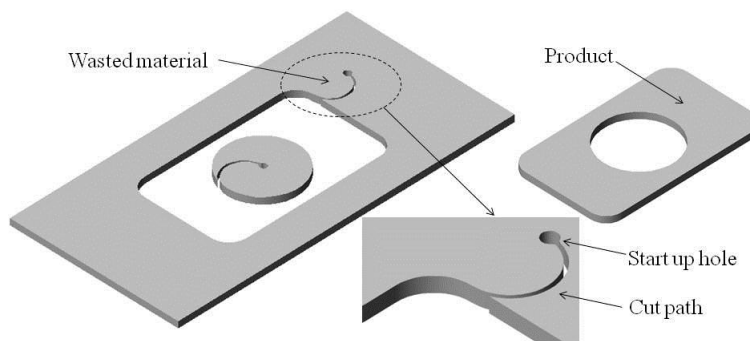


Figure 5.2- Illustrating how initial hole and cut path increase wastage of material in traditional laser cutting. Initial holes are arranged at regions outside the product area.

5.3 Basic mechanism of piercing

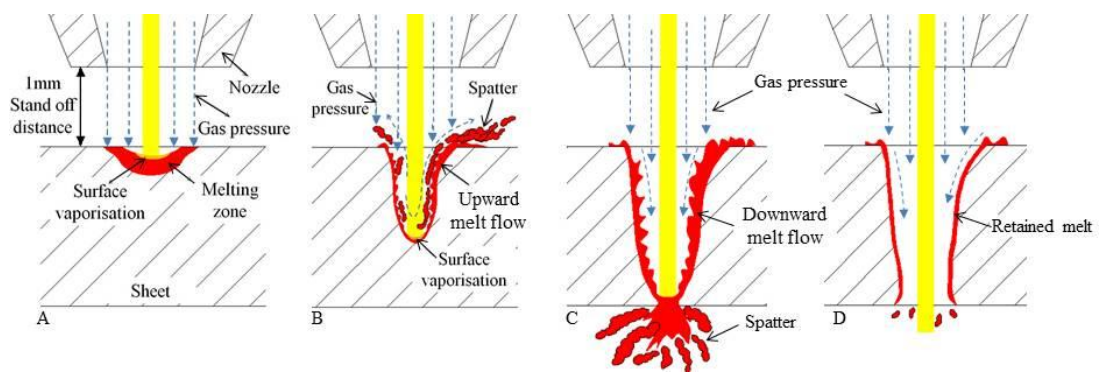


Figure 5.3- Showing the basic mechanism of piercing.

- A) The focused laser beam on the surface of sheet is absorbed by the material according to Fresnel absorption [123]. The absorption efficiency can be attributed to by the surface oxide, surface contamination, surface roughness and the presence of alloying elements [16]. The absorbed laser beam energy causes heating in a very thin surface layer of the sheet [98], and if the power intensity and irradiation time are sufficient, the temperature rapidly increases

to melting point [59]. Then the laser beam penetrates the molten material, and the volume of the melting zone rapidly grows in depth and width. The heat affected zone (HAZ) generates as the melting zone expands [124-126]. Surface vaporisation on the melt occurs during melting time [76]. The vapour pressure is considerably higher than the atmosphere pressure making a recoil pressure that acts on the melt surface [98], this brings about an ease ejecting the melt/vaporised material [29, 96, 127-129].

B) As the laser irradiation continues and the laser melts and penetrates the material, the melt layer begins to flow upward along the hole wall [98]. The upward melt flow is due to the pressure gradient inside the hole. This pressure gradient is produced by:

- 1- Surface vaporisation across the melt surface [29, 96, 98].
- 2- The pressure of assist gas [95].

C) Since the laser beam melts the lower surface of the sheet, due to the gas pressure the direction of melt flow is changed to downward, and melt ejection occurs through the bottom of the sheet resulting in breakthrough.

D) After breakthrough, with further irradiation time, the laser beam passes the sheet through the pierced hole with no effective melting.

5.4 Piercing in comparison with cutting

Although laser piercing is seemed to be similar to cutting in terms of melting process, the mechanism of melt ejection in laser piercing is completely different from cutting.

- 1- In laser piercing, the workpiece is stationary whereas in laser cutting the workpiece or cutting head moves with a defined velocity. [115].
- 2- At the beginning of piercing the direction of melt flow is upward until the laser beam melts the lower surface of the sheet, the melt is then removed through the bottom so the direction of melt flow changes to the downward direction [98, 127]. In contrast, in laser cutting the melt flow is always downward and melt is removed through the bottom of the kerf [1].

- 3- Melt removal in laser cutting is solely due to assist gas pressure [1, 2, 76, 130] while in laser piercing in addition to the assist gas pressure there is also a recoil pressure resulting from surface vaporisation [29, 96, 127-129].

5.5 Kerf width results

The graphs below summarise the typical kerf width results of laser cutting of 2 mm thick mild steel from chapter 4 in order to aid comparison with the pierced hole diameters presented in this chapter (Figure 5.4 and Figure 5.5).

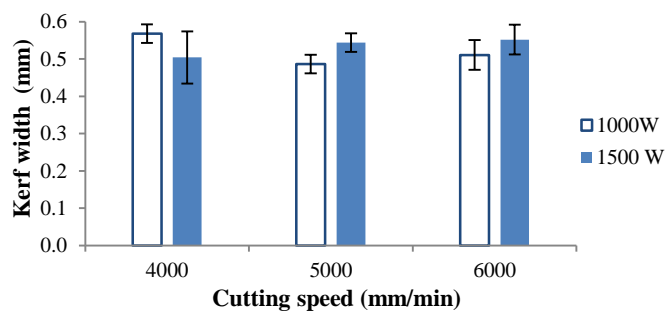


Figure 5.4- Upper kerf width versus cutting speed for different powers (2 mm thick mild steel, 2 bar oxygen, spot size of 0.2 mm on the upper surface of sheet, focal length of 120 mm).

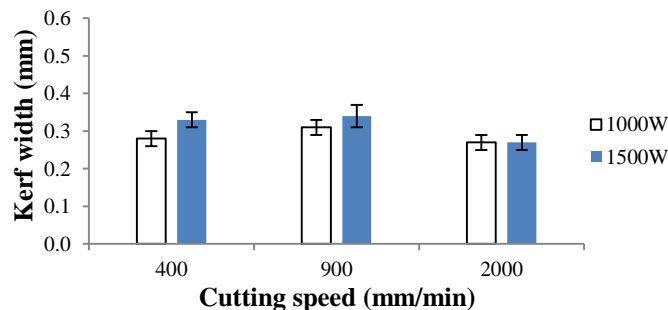


Figure 5.5- Upper kerf width versus cutting speed for different powers (2 mm thick mild steel, 12 bar nitrogen, spot size of 0.2 mm on the upper surface of sheet, focal length of 120 mm).

5.6 Definition of hole structure

The hole structure definition is shown in Figure 5.6.

Although the HAZ in mild steel is very small and is usually unimportant, it is still a part of laser- material interaction. Hole + NEM + Air trap indicates the total volume of material that has melted. Ejected melt consists of Hole + Air trap.

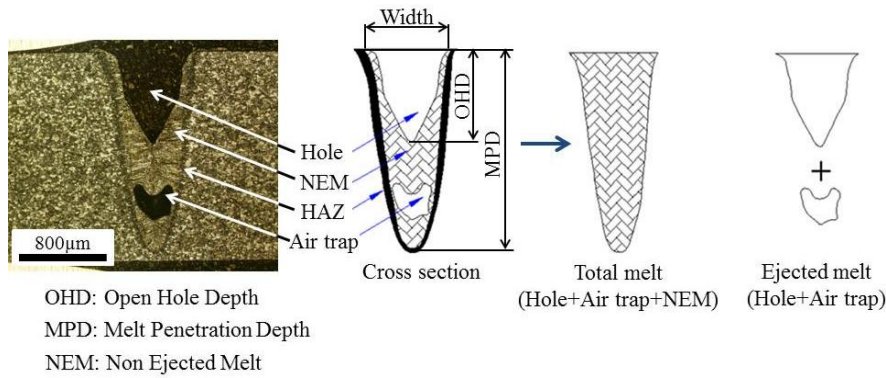


Figure 5.6- Indicating hole structure terms (1000 W, 2 bar nitrogen, irradiation time of 12 ms).

5.7 Quality requirement in laser piercing

In laser piercing, from an engineering point of view, only the hole diameter and the time of penetration are practically interested. In laser cutting, engineers are interested to pierce the start-up hole on the cut line of the finished product matching the kerf width. Moreover, they would like to pierce the start-up hole at the shortest time with reasonable cost.

5.8 Mapping of hole growth

One of the aims in this chapter is to produce the map which demonstrates how a hole grows when the irradiation time increases. Figure 5.7 shows the photos of the holes which were sectioned, ground and etched in nital 2%. These photos generally show how a hole grows with increasing irradiation time, however, it must be highlighted that each photo indicates the hole shape after solidification which is not the same as the condition of the hole in the middle of a larger irradiation time. For example in Figure 5.7, 12 ms result does not give a true image of the state of the hole of 12 ms into a 24 ms interaction. This is because, once the laser is turned off after 12 ms the heat from the melt is conducted away to produce more melt. Also, if oxygen is used with mild steel, the oxidation process will continue for a few milliseconds after the laser is turned off. As a result of these effects, the interrupted piercing will be slightly different from the state of the hole at that point in a larger interaction.

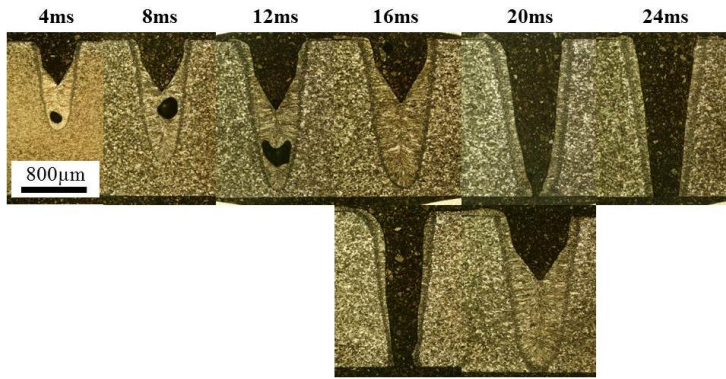


Figure 5.7- Showing hole growth with increasing irradiation time. The first row was often observed; the second one was rarely seen (1000 W, 2 bar nitrogen).

In addition, it is realised that sometimes with the same irradiation time, a sporadic penetration may happen at which two different hole shapes can be produced: blind and through hole. The first row (Figure 5.7) indicates the hole shape that is often observed, and the photos below show the other observed holes shape. For instance, at the irradiation time of 16 ms and 20 ms, we came across a sporadic penetration situation at which some holes were blind and others were through holes. In this example, at 16 ms, 40% of holes were through holes and this increases to 80% at 20ms. At 24 ms all holes were through holes. In the hole growth exhibition, in order to take everything into consideration, it seems that the best way is that we map the hole growth. Figure 5.8 indicates the hole growth map of the laser piercing in Figure 5.7. Because there is some variation in breakthrough time, the hole growth map at/or near breakthrough can vary widely (Figure 5.7 & Figure 5.8). As can be seen, much information in terms of hole shape, hole structure and dimensions can be illustrated on the hole growth map. Moreover, the volume of hole and melt total can be estimated by the hole dimensions.

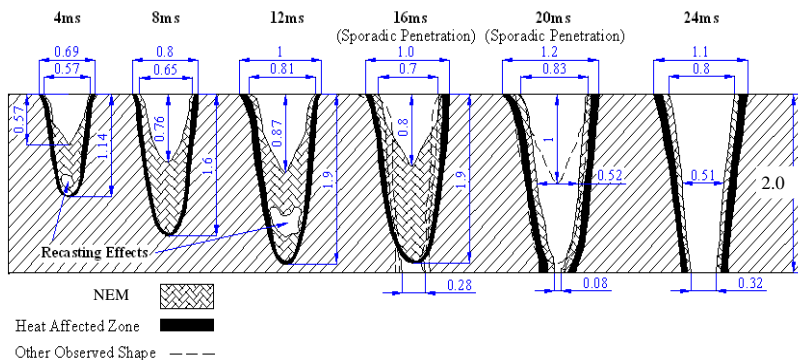


Figure 5.8- Indicating the hole growth map of Figure 5.7. Much information can be shown in the map.

5.9 Piercing with low and moderate nitrogen pressure

5.9.1 2 bar pressure of nitrogen

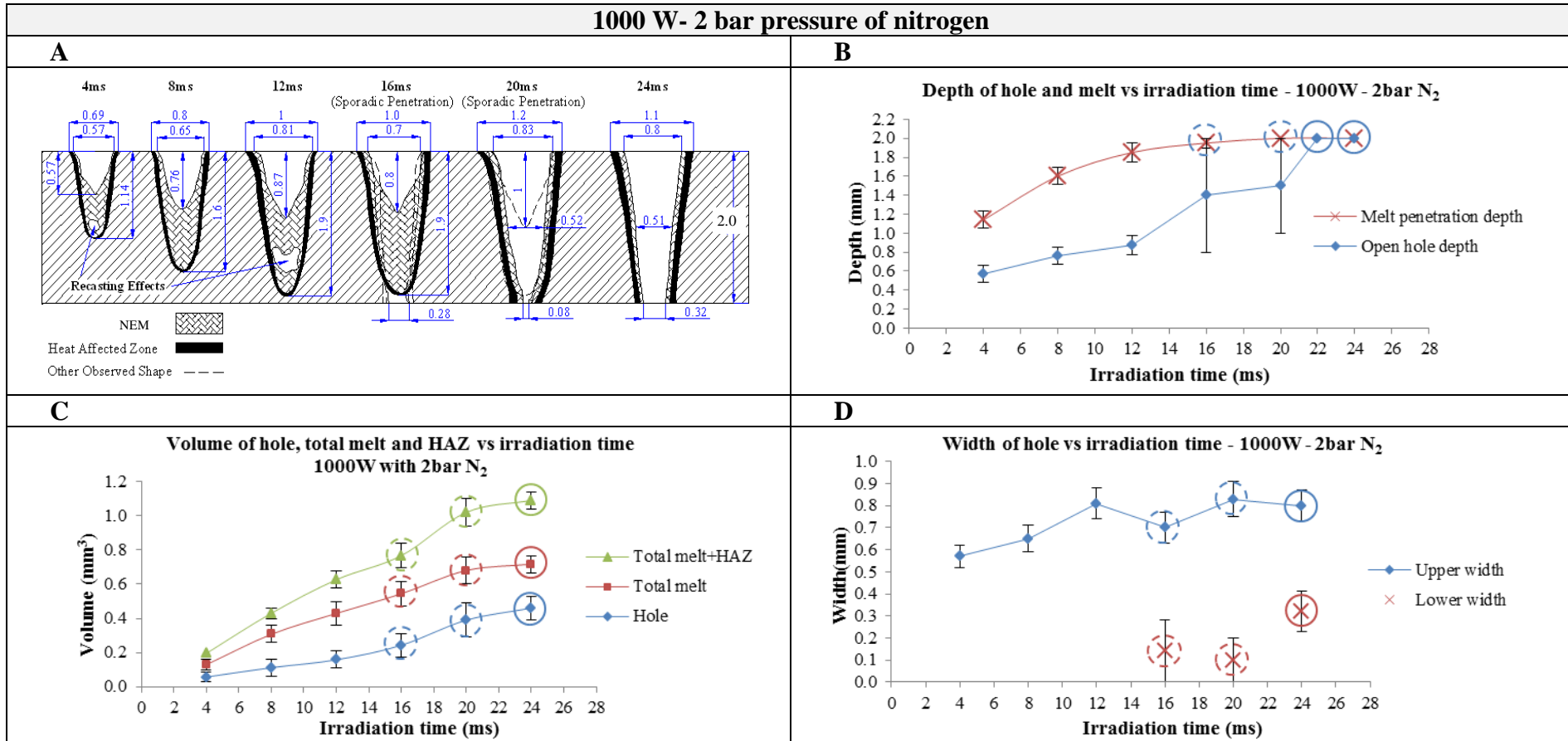


Figure 5.9- Piercing results for 1000 W with 2 bar nitrogen. A) Map of hole growth. B) Depth of hole and melt versus irradiation time. C) Volume of hole, melt total and HAZ versus irradiation time. D) Width of hole versus irradiation time. Solid circles indicate the through holes. Dash circles indicate the sporadic through holes.

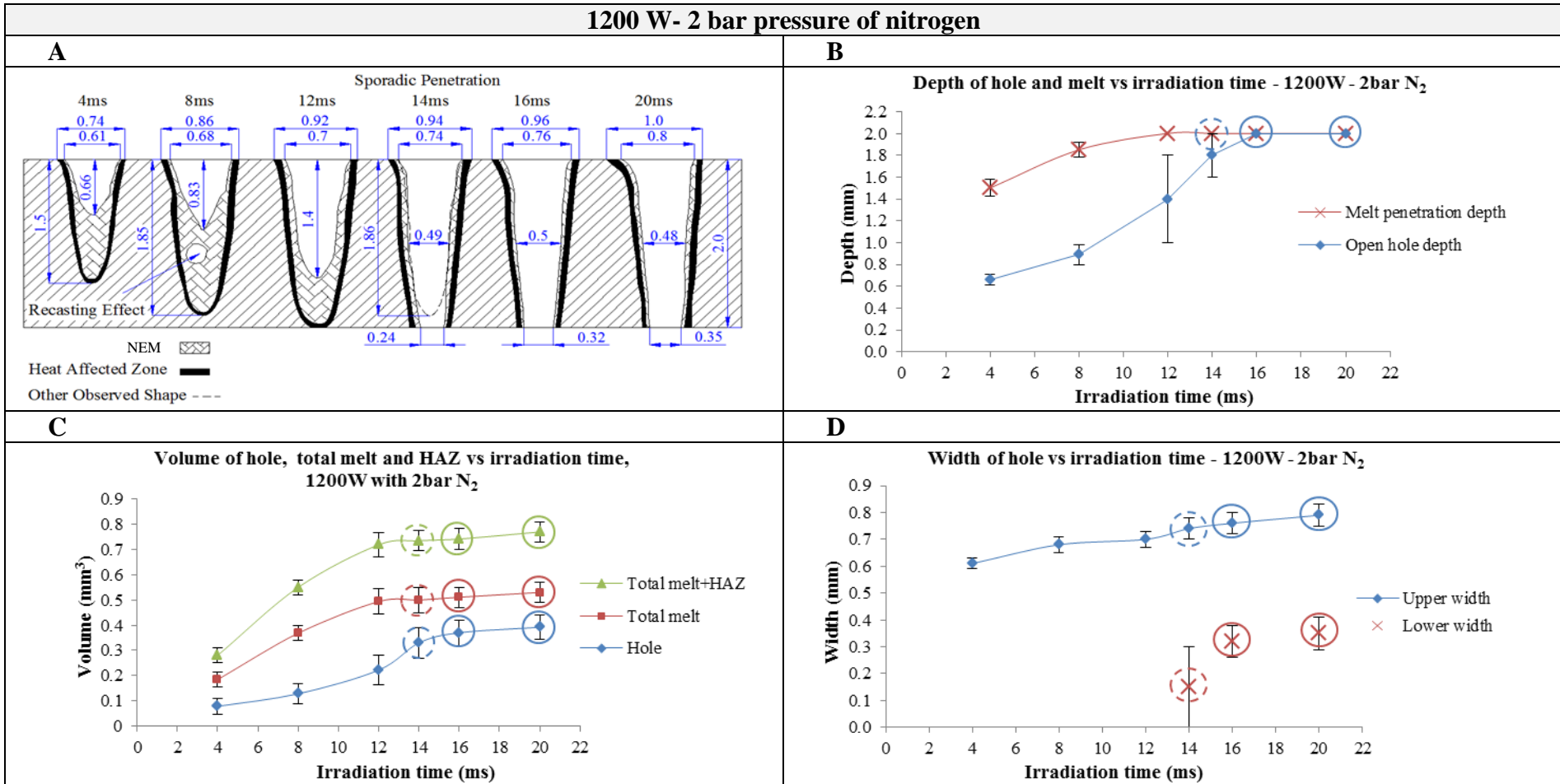


Figure 5.10- Piercing results for 1200 W with 2 bar nitrogen. A) Map of hole growth. B) Depth of hole and melt versus irradiation time. C) Volume of hole, melt total and HAZ vs irradiation time. D) Width of hole vs irradiation time. Solid circles indicate the through holes. Dash circles indicate the sporadic through holes.

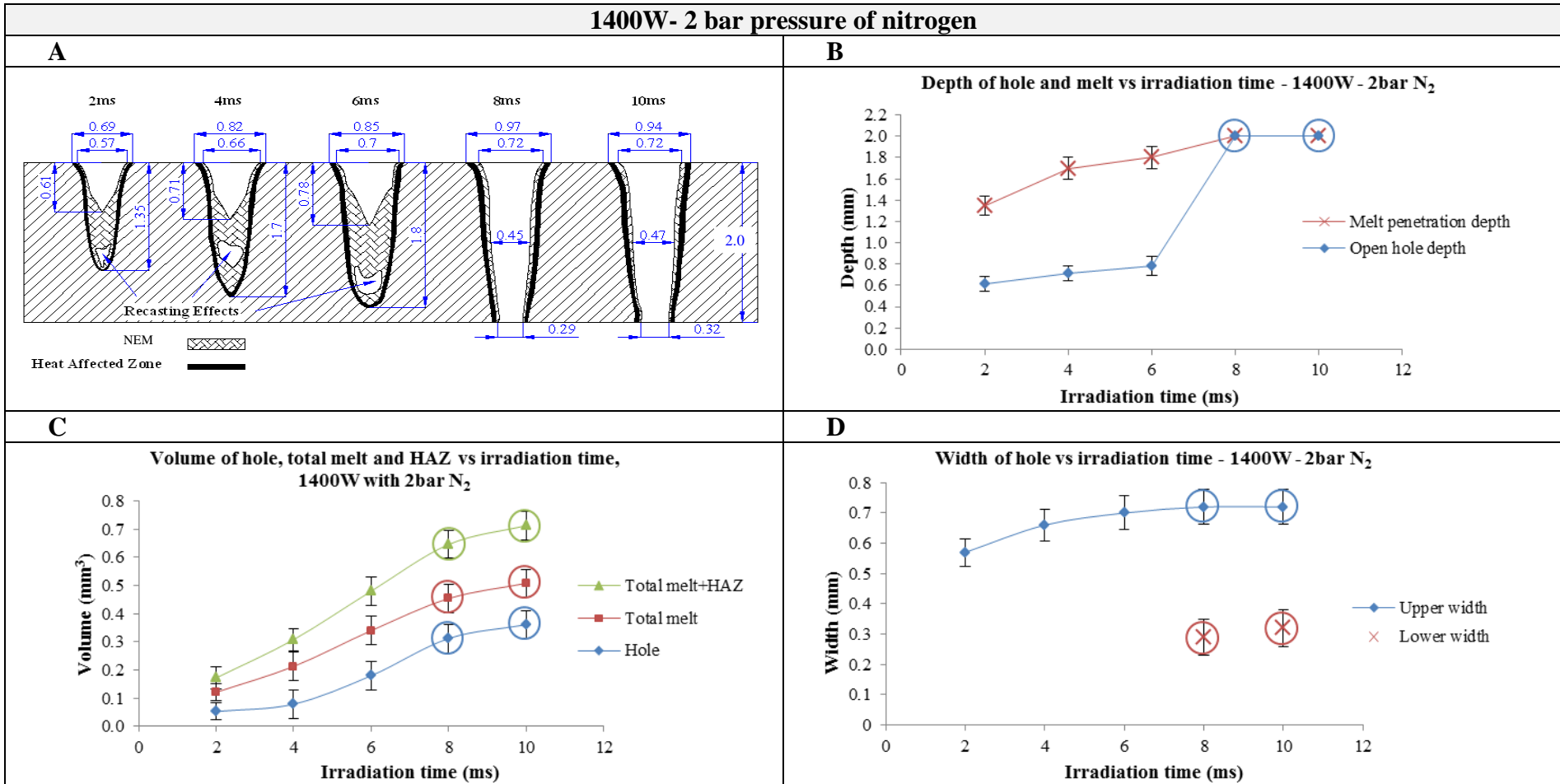


Figure 5.11- Piercing results for 1400 W with 2 bar nitrogen. A) Map of hole growth. B) Depth of hole and melt versus irradiation time. C) Volume of hole, melt total and HAZ versus irradiation time. D) Width of hole versus irradiation time. Solid circles indicate the through holes.

5.9.2 0.3 bar pressure of nitrogen

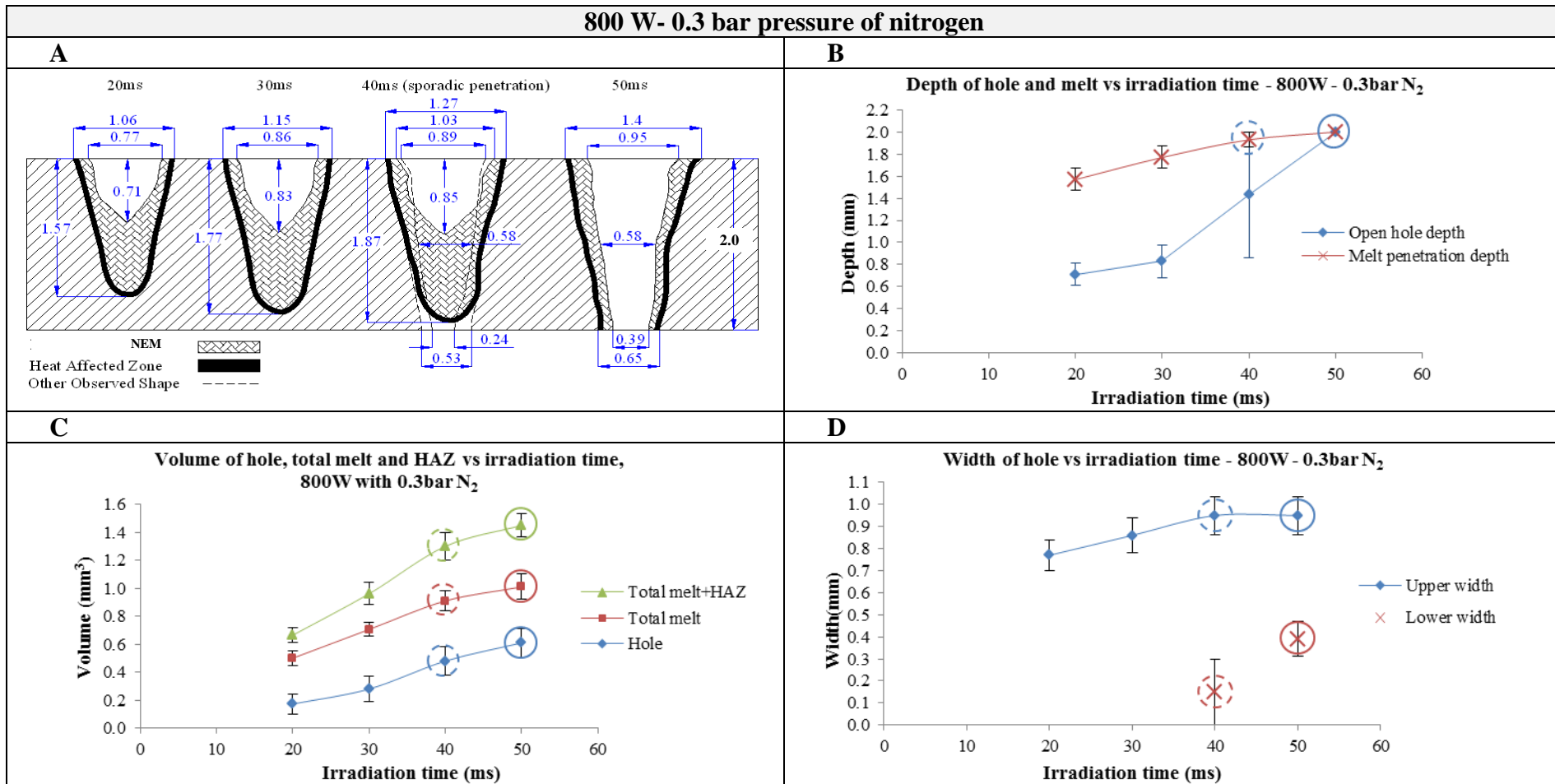


Figure 5.12- Piercing results for 800 W with 0.3 bar nitrogen. A) Map of hole growth. B) Depth of hole and melt vs irradiation time. C) Volume of hole, melt total and HAZ vs irradiation time. D) Width of hole vs irradiation time. Solid circles indicate the through holes. Dash circles indicate the sporadic through holes.

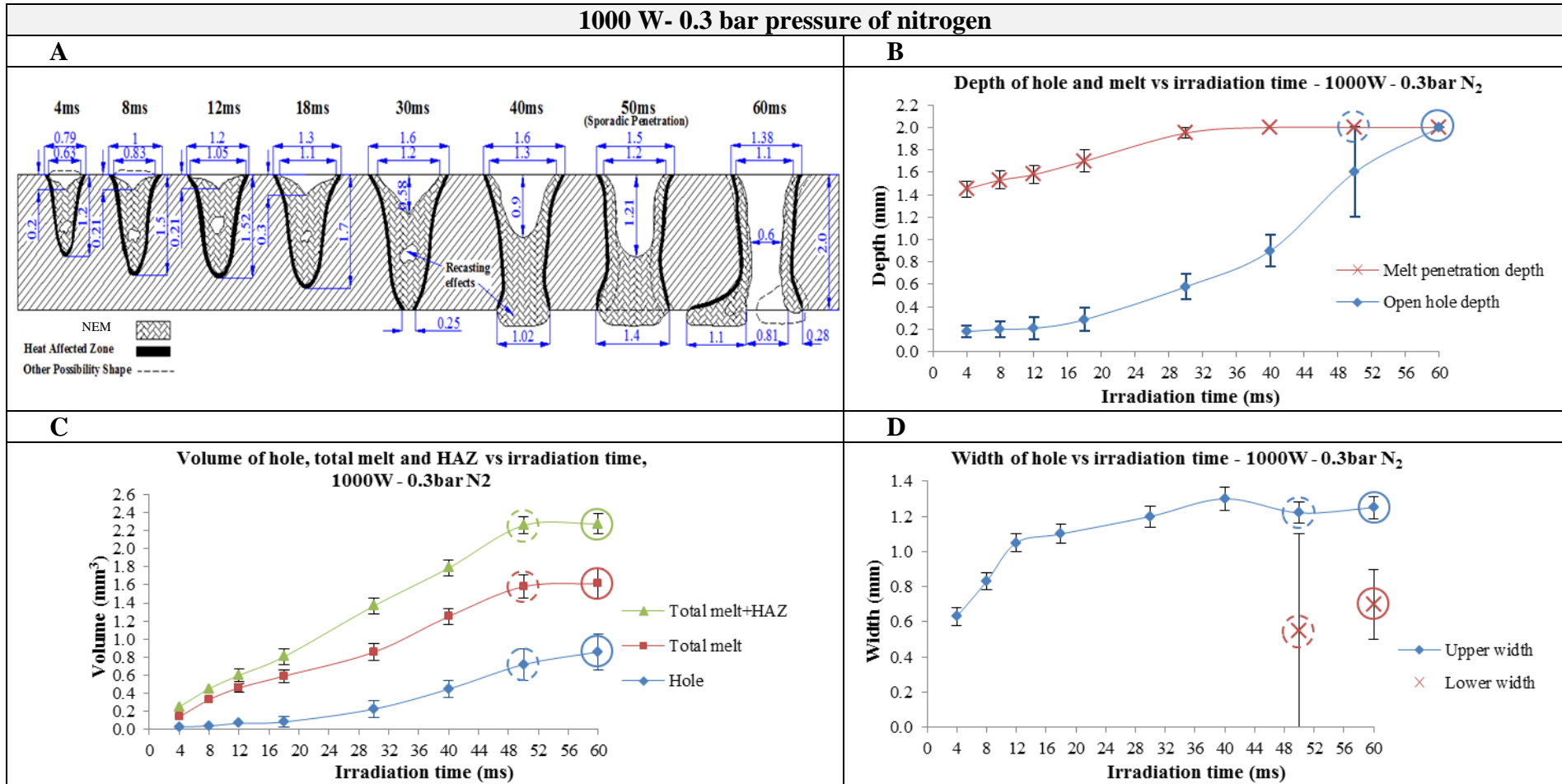


Figure 5.13- Piercing results for 1000 W with 0.3 bar nitrogen. A) Map of hole growth. B) Depth of hole and melt vs irradiation time. C) Volume of hole, melt total and HAZ vs irradiation time. D) Width of hole vs irradiation time. Solid circles indicate the through holes. Dash circles indicate the sporadic through holes.

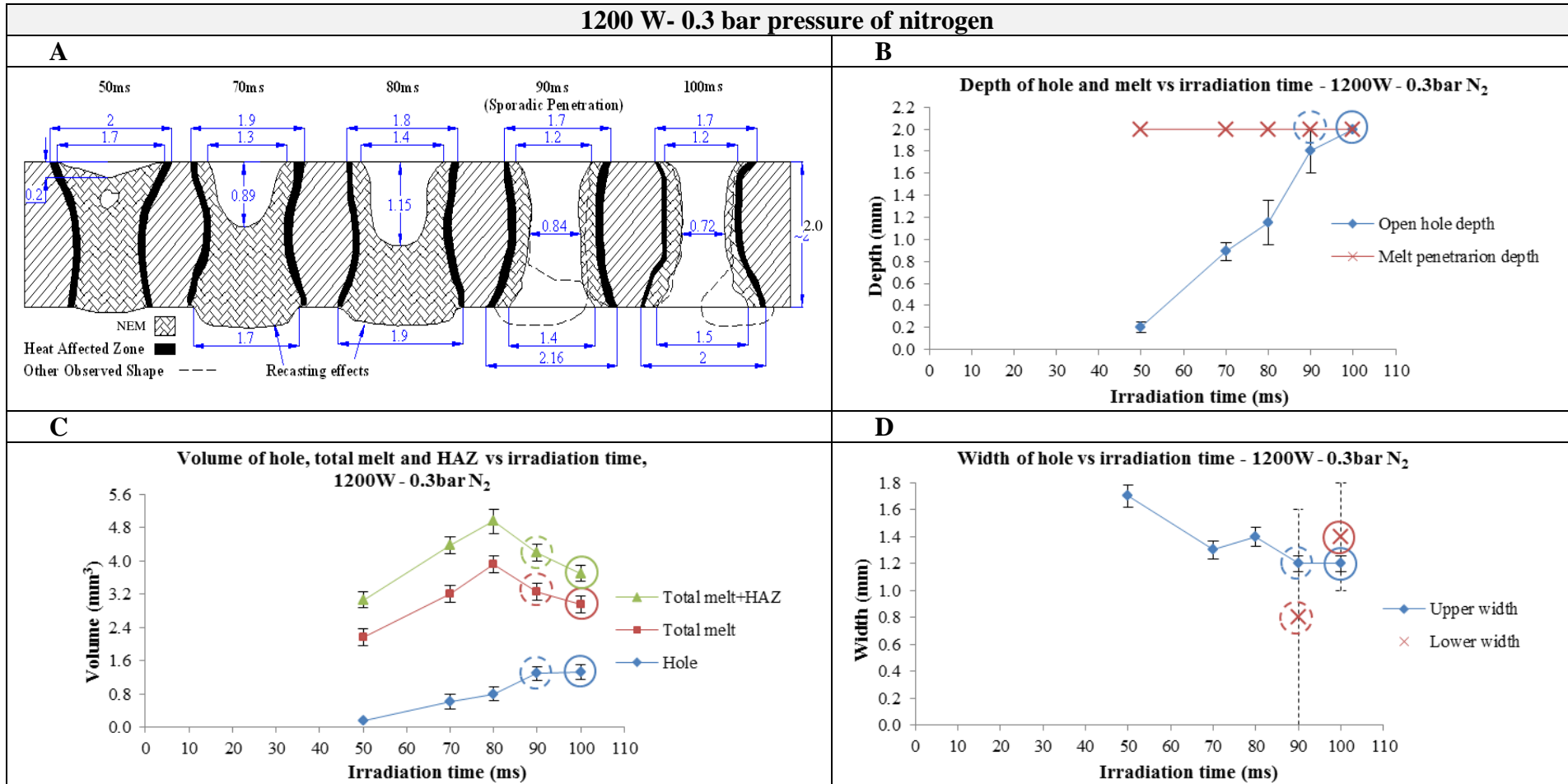


Figure 5.14- Piercing results for 1200 W with 0.3 bar nitrogen. A) Map of hole growth. B) Depth of hole and melt vs irradiation time. C) Volume of hole, melt total and HAZ vs irradiation time. D) Width of hole vs irradiation time. Solid circles indicate the through holes. Dash circles indicate the sporadic through holes.

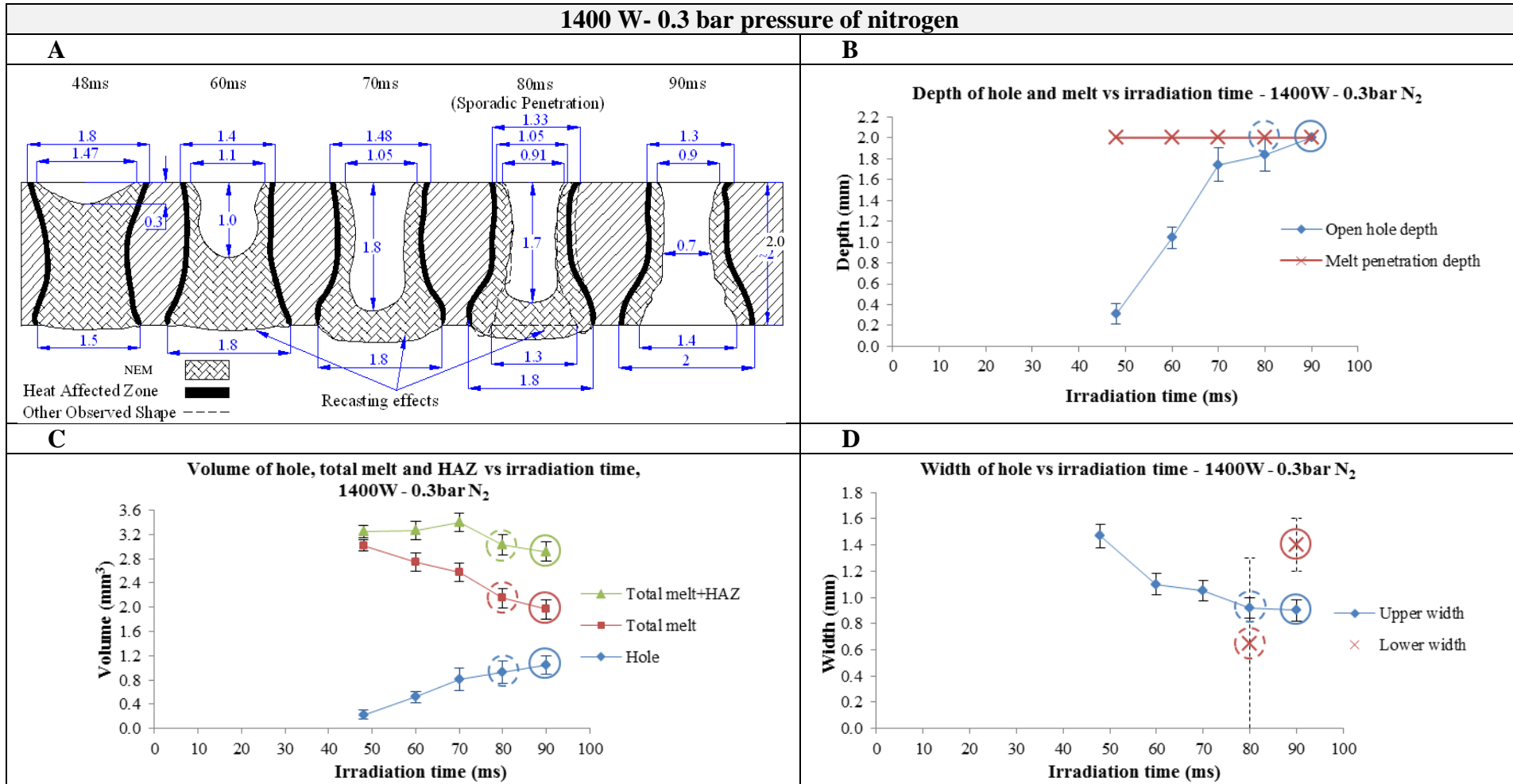


Figure 5.15- Piercing results for 1400 W with 0.3 bar nitrogen. A) Map of hole growth. B) Depth of hole and melt vs irradiation time. C) Volume of hole, melt total and HAZ vs irradiation time. D) Width of hole vs irradiation time. Solid circles indicate the through holes. Dash circles indicate the sporadic through holes.

The hole and melt growth maps in laser piercing using 2 bar and 0.3 bar nitrogen pressure have been presented in part A of Figure 5.9 to Figure 5.15 for powers of 800 W to 1400 W. As the irradiation time increases, the OHD and MPD increase until breakthrough happens (part B of Figure 5.9 to Figure 5.15). Before all holes become through, there is sporadic penetration. The breakthrough time and the percentage of through hole appearance for different powers is shown in Table 5.2. A large variation in melt removal at sporadic penetration time is observed.

Table 5.2- Breakthrough time and the percentage of hole through, 2 bar nitrogen.

	800 W		1000 W			1200 W		1400 W	
2 bar	-		16 ms	20 ms	24 ms	14 ms	16 ms	8 ms	
	-		40%	80%	100%	80%	100%	100%	
0.3 bar	40 ms	50 ms	50ms		60 ms	90 ms	100 ms	80 ms	90 ms
	40%	100%	40%		100%	60%	100%	40%	100%

The volumes of the open hole, total melt (Hole + NEM) and total melt + HAZ, overall, increase as the irradiation time is increased until breakthrough happens, then they almost become constant just with a slight variation (part C of Figure 5.9 to Figure 5.15). This trend is a little different for 1200 W and 1400 W with 0.3 bar (Figure 5.14-C and Figure 5.15-C), at which the melt volume increases to a peak until breakthrough occurs then begins to decrease and with further irradiation time it almost becomes constant. In power of 1200 W and 1400 W the melt volume is considerable in comparison with the hole volume. Overall, at breakthrough, the gap between open hole and total melt volumes decreases (part C of Figure 5.9 to Figure 5.15).

In general, the upper hole width gradually increases with irradiation until breakthrough happens, then it is almost kept constant just with some variation (part D of Figure 5.9 to Figure 5.15). When piercing with 1200 W and 1400 W with 0.3 bar and in the range of time observed, the upper width decreases with increasing irradiation time until breakthrough occurs (Figure 5.14-D and Figure 5.15-D). In the range of applied irradiation time, the lower width gradually increases with irradiation time. With further irradiation time, it tends to become constant (Figure 5.10-D and Figure 5.11-D).

5.9.3 Comparison of results

- The depths of open hole and melt gradually increase with irradiation time until breakthrough occurs (Figure 5.9-B to Figure 5.15-B).
- Breakthrough time decreases with increasing power when piercing with 2 bar while it increases with power when piercing with 0.3 bar (Table 5.3).

Table 5.3- Breakthrough time for different powers and pressures in nitrogen piercing.

	800 W	1000 W	1200 W	1400 W
2 bar	-	24 ms	16 ms	8 ms
0.3 bar	40-50 ms	50-60 ms	90-100 ms	80-90 ms

- With the same power, the breakthrough time decreases when the pressure increases from 0.3 to 2 bar (Table 5.3).
- Overall, the melt and hole volumes increase with irradiation time until breakthrough occurs, then they become almost constant just with a variation (Figure 5.9-C to Figure 5.15-C).
- When piercing with 2 bar, the hole and melt volumes at breakthrough decrease with increase in the power while in piercing with 0.3 bar the volumes of hole and melt at breakthrough overall increase with power as presented in Table 5.4.

Table 5.4- The hole and total melt volumes at breakthrough for different powers and pressures in nitrogen piercing.

		800 W	1000 W	1200 W	1400 W
2 bar	Melt volume	-	0.7 mm ³	0.54 mm ³	0.47 mm ³
	Hole volume	-	0.46 mm ³	0.40 mm ³	0.32 mm ³
0.3 bar	Melt volume	1.1 mm ³	1.6 mm ³	2.8 mm ³	2.2 mm ³
	Hole volume	0.64 mm ³	0.85 mm ³	1.15 mm ³	1.15 mm ³

- The hole and melt volumes decrease when the pressure increases from 0.3 bar to 2 bar as presented in Table 5.4.
- The HAZ is observed around the NEM. The graph of HAZ volume follows the melt (Figure 5.9-C to Figure 5.15-C).
- In general, the upper hole width widens with irradiation time until breakthrough occurs then it almost becomes constant just with a slight variation.
- The hole width variation decreases with increase in the power and pressure. When piercing with 2 bar, the upper hole width at breakthrough slightly decreases as the power increases but in 0.3 bar there is a variation as presented in Table 5.5.

Table 5.5- Upper hole width at breakthrough for different powers and pressures in nitrogen piercing.

	800 W	1000 W	1200 W	1400 W
2 bar	-	0.83 mm	0.77 mm	0.7 mm
0.3 bar	0.9-0.95 mm	1.1-1.2 mm	1.2 mm	0.9 mm

- At breakthrough time the gap between hole and total melt volumes decreases. This gap indicates the NEM volume. Using the same power, as the gas pressure increases, the NEM lining the hole surface decreases. Furthermore, when using 2 bar the NEM decreases with increasing power while with using 0.3 bar, overall, it increases as presented Table 5.6.

Table 5.6- The volume of NEM lining the hole surface for different powers and pressures in nitrogen piercing.

	<i>800 W</i>	<i>1000 W</i>	<i>1200 W</i>	<i>1400 W</i>
2 bar	-	0.24 mm ³	0.14 mm ³	0.15 mm ³
0.3 bar	0.46 mm ³	0.75 mm ³	1.65 mm ³	1.05 mm ³

5.9.4 Discussion of results

5.9.4.1 The depths of hole and melt gradually increase with irradiation time.

As the irradiation time increases, the MPD increases as a result of laser penetration and heat conduction. Regarding the OHD, the pressure inside the hole is more than the ambient pressure thus the melt is removed as the laser is melting the material, resulting in an increase in the OHD. Melt surface vaporisation can also help the melt ejection resulting in further increase in the OHD (Figure 5.9-B - Figure 5.15-B).

5.9.4.2 When piercing with 2 bar, the breakthrough time decreases with increasing power but it increases with power when piercing with 0.3 bar.

When piercing with 2 bar, the gas pressure is able to eject the molten material from the hole faster than 0.3 bar does resulting in decrease in the breakthrough time. Whereas, the pressure of 0.3 bar is not sufficient to remove the yielded melt and so the enormous volume of the melt retains in the melting zone (compared to 2 bar) resulting in delay in the breakthrough.

5.9.4.3 With the same power, the breakthrough time decreases when the pressure increases from 0.3 bar to 2 bar.

With the same power (the same melting rate), the melt removal ability increases when the gas pressure is increased from 0.3 bar to 2 bar, thus the breakthrough occurs more quickly. However, it is expected to have a limit when the melt is ejected at the same rate at which it is formed i.e. there will be a maximum gas pressure beyond which no further benefit would be seen.

5.9.4.4 Overall, the melt and hole volumes increase with irradiation time until breakthrough occurs then they almost become constant just with a variation.

As the irradiation time increases, the time taken for the laser to melt and penetrate the material laterally increases, resulting in an increase in the melt and hole volumes. When the breakthrough occurs, the laser beam crosses the sheet through the pierced hole with no further significant absorption into the material; hence there is no further increase in the volumes of the melt and hole. However, the hole maps indicate that after breakthrough, the lower hole width increases and the hole taper decreases with further increase in the irradiation time generating a cylindrical hole. This change in the hole shape is the main reason for the slight increase in the volumes. Moreover, hole development does not stop as soon as the energy input from the laser stops. On-going melt flow and heat input from the melt continues to affect the hole shape and dimensions.

5.9.4.5 When piercing with 2 bar, the hole and melt volumes at breakthrough decrease with increasing power while in piercing with 0.3 bar the volumes at breakthrough overall increase with power.

When piercing with 0.3 bar, because of insufficient gas pressure, there is inadequate melt removal therefore as the power increases the melt grows laterally making the volumes of hole and melt larger. When the pressure is increased to a sufficient pressure (e.g. 2 bar), the rate of melt ejection increases and the melt is not allowed to grow laterally. Thus, with more laser power the melt grows vertically, and penetration happens faster, resulting in a decrease in the volumes. Figure 5.16 shows that when piercing with sufficient gas pressure, the laser penetrates the material vertically (A) but with inadequate pressure, the laser beam penetrates laterally as a result of heat conduction. C and D present two piercings with the same power, but with different gas pressure.

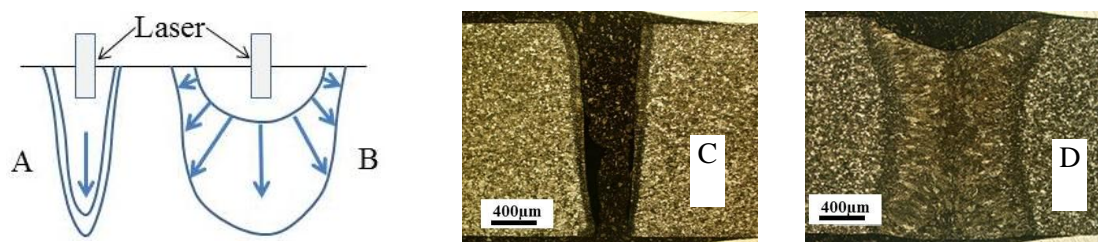


Figure 5.16- The effect of nitrogen pressure on the hole and melt volumes. A) Sufficient gas pressure. B) Inadequate gas pressure. C) 1400 W, 2 bar, 10 ms. D) 1400 W- 0.3 bar , 48 ms.

5.9.4.6 Overall, the hole and melt volumes decrease when the pressure increases from 0.3 bar to 2 bar.

As the gas pressure increases, the effectiveness of melt removal increases. This then increases the hole penetration rate, and so, the breakthrough time decreases thereby decreasing total energy input, and hence decreasing total melt volume.

5.9.4.7 The hole width becomes almost constant at breakthrough.

At breakthrough time, any further upper edge erosion is stopped by changing the upward melt ejection to the downward melt removal.

5.9.4.8 The hole width variation decreases with increase in the power.

Upward melt ejection causes erosion on the upper edge of the hole and also upward melt ejection is a fluctuating process; hence, it gives rise to variations in the hole width. When the power is increased, the breakthrough happens quickly, hence, there is less melt flow through the entrance of the hole, decreasing the variation of the hole width.

5.9.4.9 When piercing with 2 bar, the upper hole width at breakthrough slightly decreases as the power increases while in 0.3 bar there is a variation.

This is because, with using 2 bar, when the power is increased the breakthrough time decreases, so there is less time for the hole to grow laterally as a result of heat conduction and erosion from upward melt ejection.

5.9.4.10 HAZ follows the melt.

HAZ is observed surrounding the NEM. The heat conduction from the melting zone causes the HAZ from the melt interface towards the end of the sensitizing temperature in the unaffected metal. As more heat is input, there will be a larger HAZ.

5.10 Piercing with low and moderate oxygen pressure

5.10.1 With 2 bar pressure of oxygen

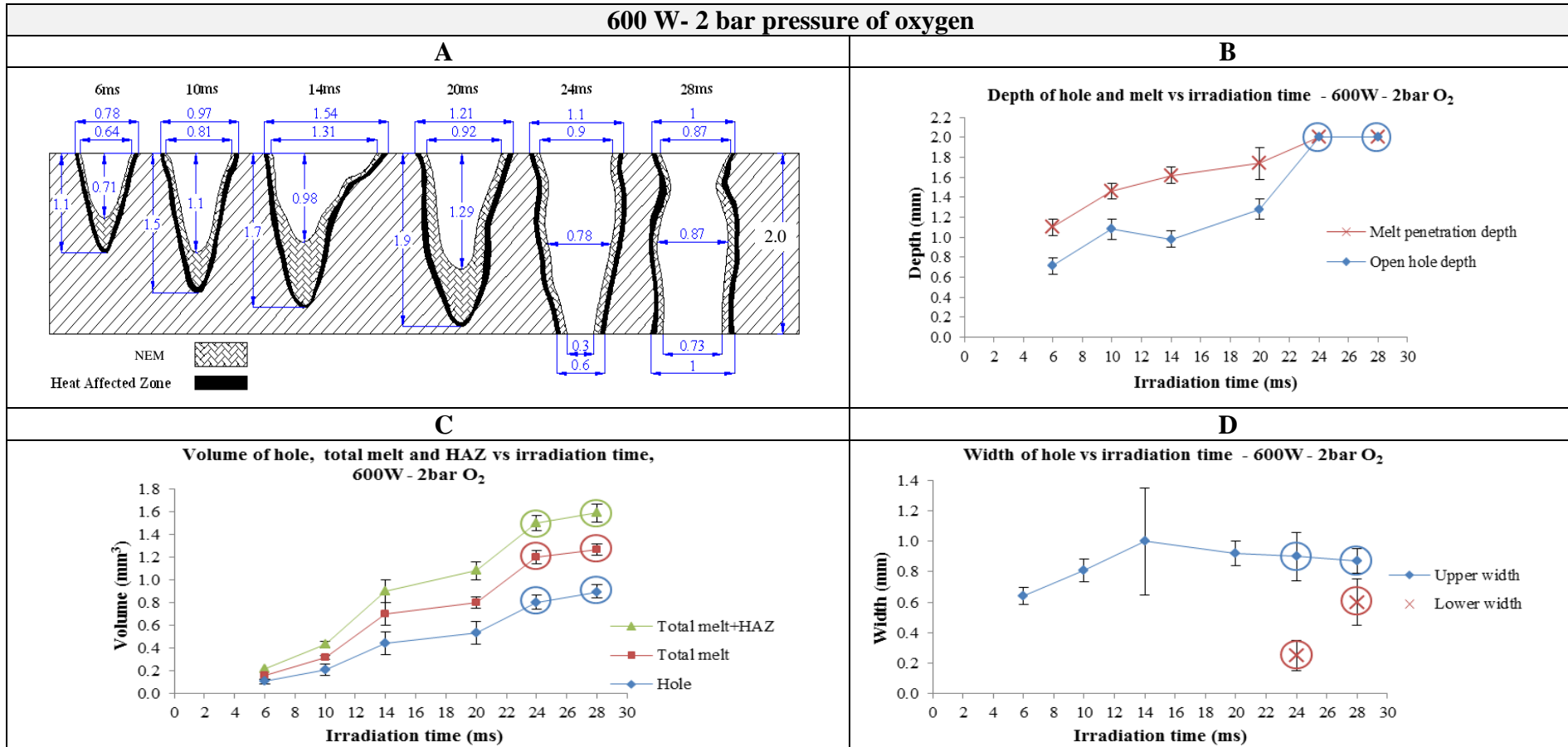


Figure 5.17- Piercing results for 600 W with 2 bar oxygen. A) Map of hole growth. B) Depth of hole and melt versus irradiation time. C) Volume of hole, melt total and HAZ versus irradiation time. D) Width of hole versus irradiation time. Solid circles indicate the through holes.

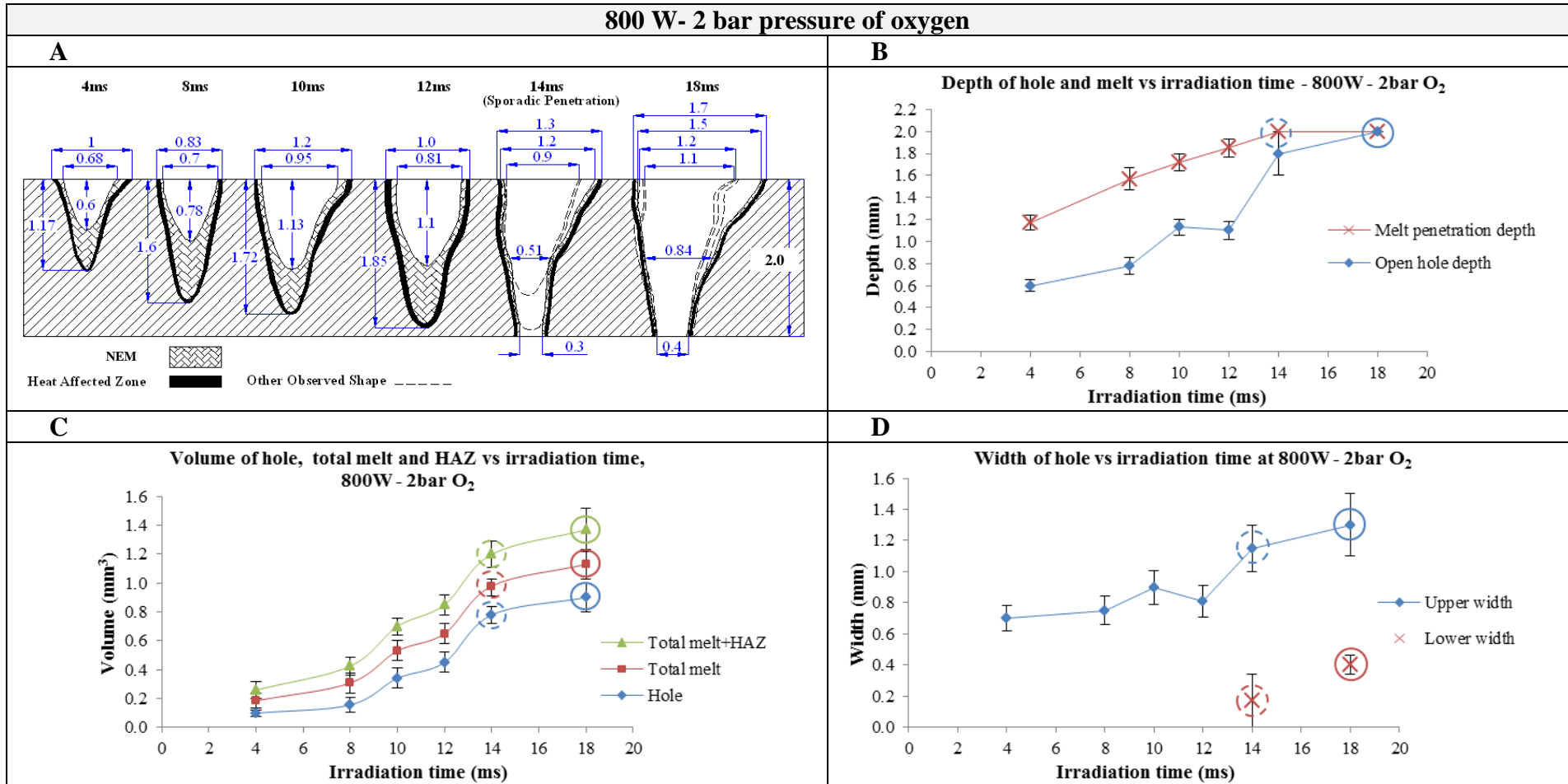


Figure 5.18- Piercing results for 800 W with 2 bar oxygen. A) Map of hole growth. B) Depth of hole and melt vs irradiation time. C) Volume of hole, melt total and HAZ vs irradiation time. D) Width of hole vs irradiation time. Solid circles indicate the through holes. Dash circles indicate the sporadic through holes.

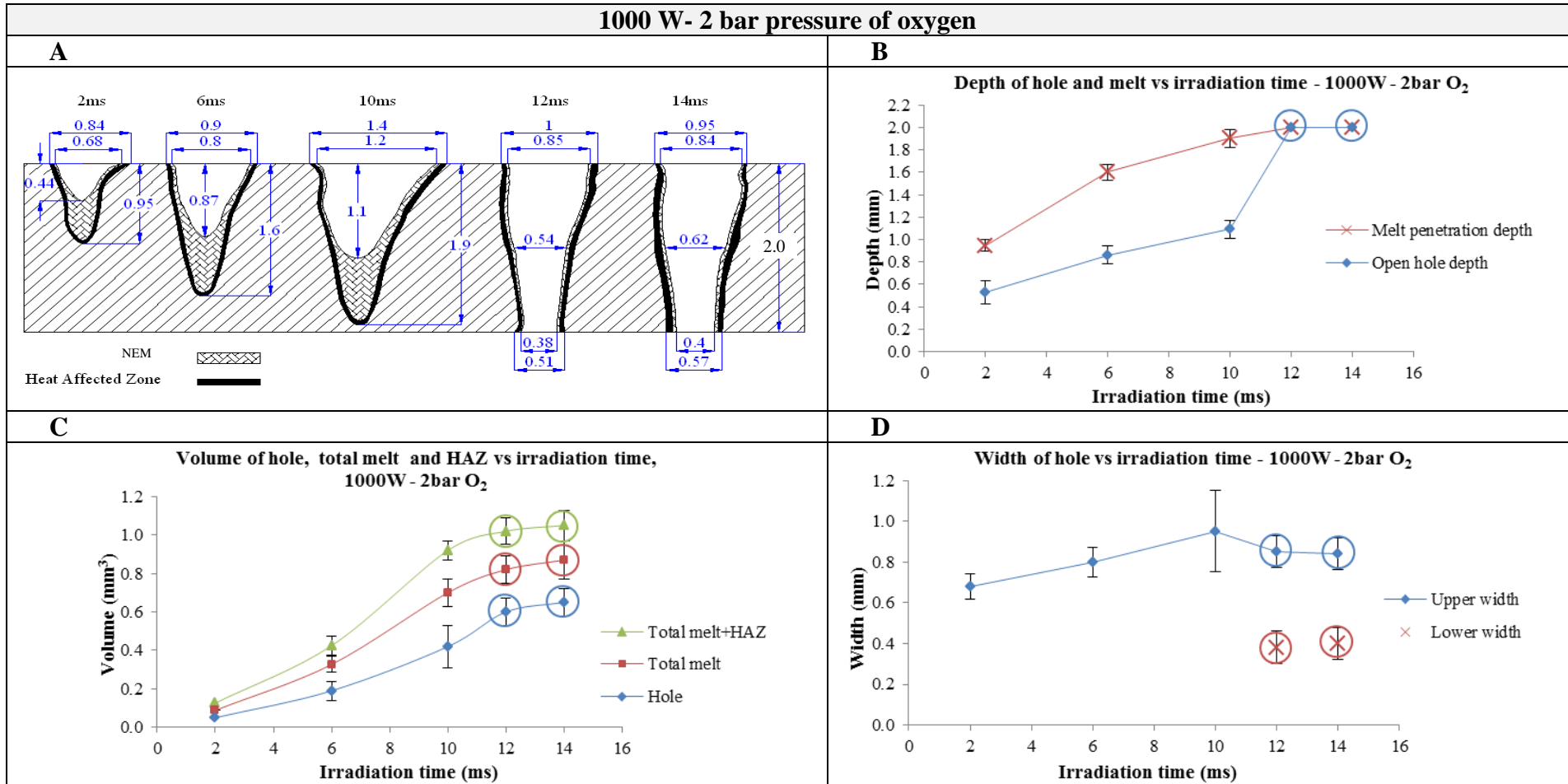


Figure 5.19- Piercing results for 1000 W with 2 bar oxygen. A) Map of hole growth. B) Depth of hole and melt versus irradiation time. C) Volume of hole, melt total and HAZ versus irradiation time. D) Width of hole versus irradiation time. Solid circles indicate the through holes.

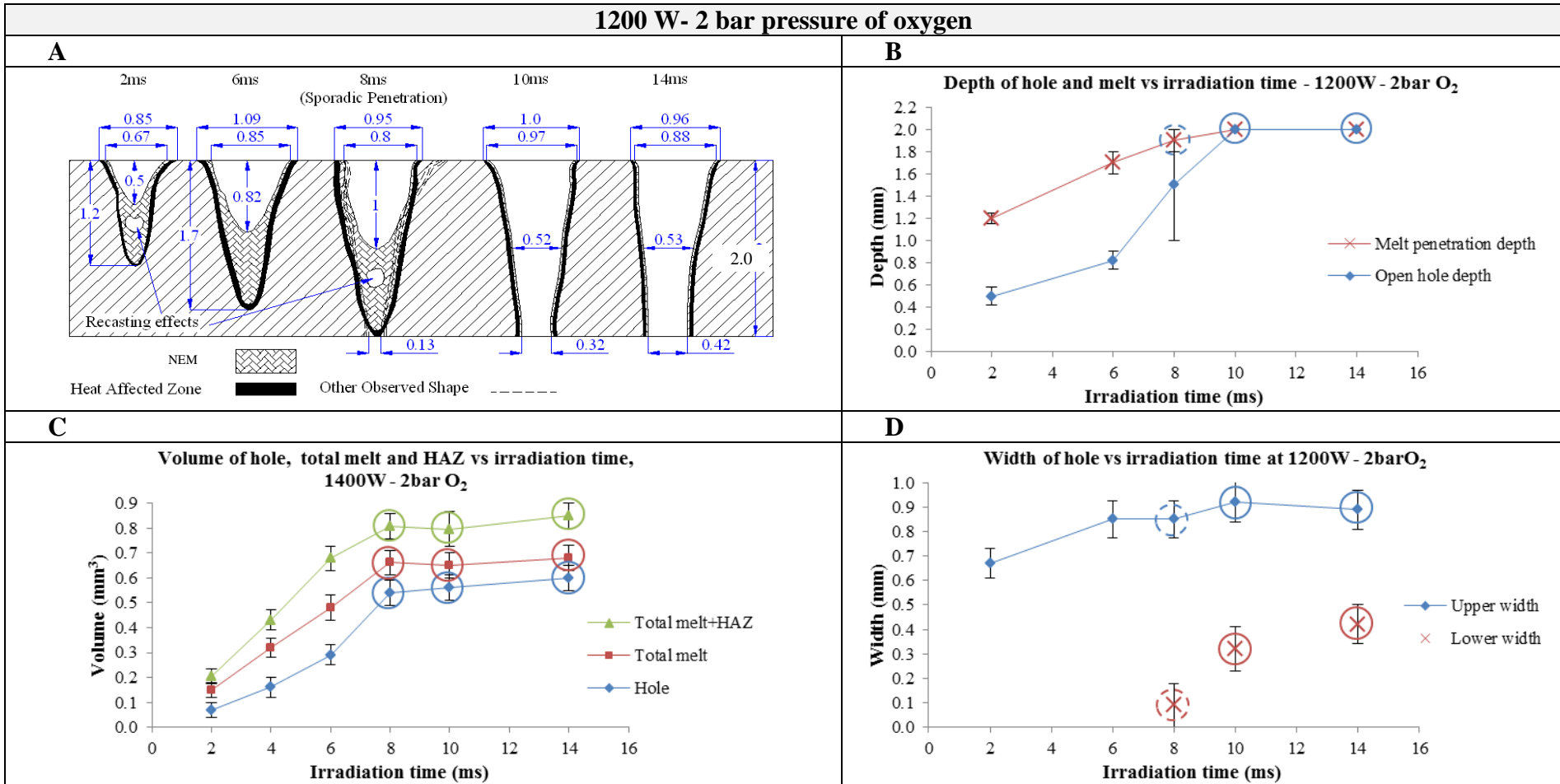


Figure 5.20- Piercing results for 1200 W with 2 bar oxygen. A) Map of hole growth. B) Depth of hole and melt versus irradiation time. C) Volume of hole, melt total and HAZ versus irradiation time. D) Width of hole versus irradiation time. Solid circles indicate the through holes. Dash circles indicate the sporadic through holes.

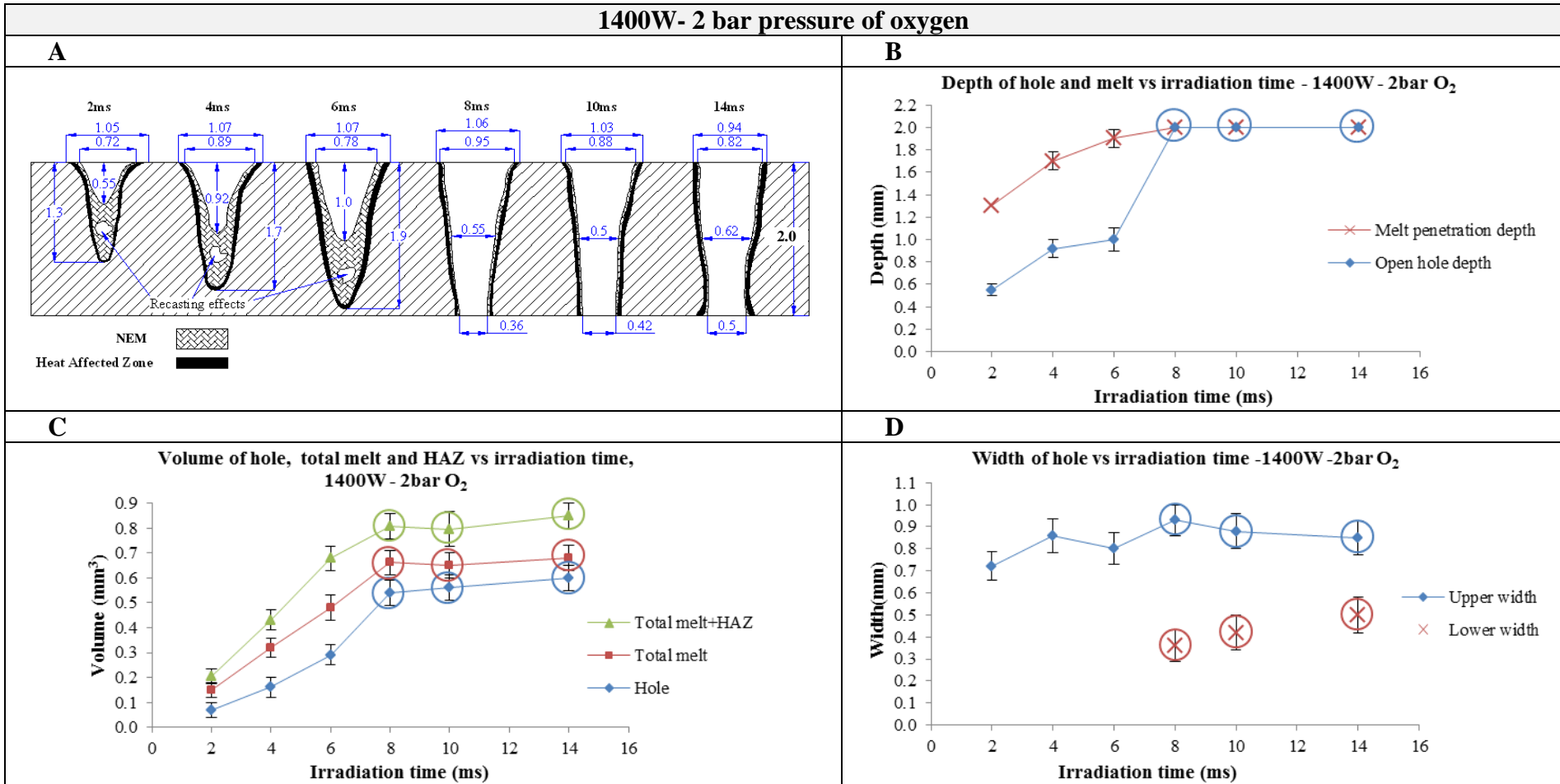


Figure 5.21- Piercing results for 1400 W with 2 bar oxygen. A) Map of hole growth. B) Depth of hole and melt versus irradiation time. C) Volume of hole, melt total and HAZ versus irradiation time. D) Width of hole versus irradiation time. Solid circles indicate the through holes.

5.10.2 With 0.3 bar pressure of oxygen

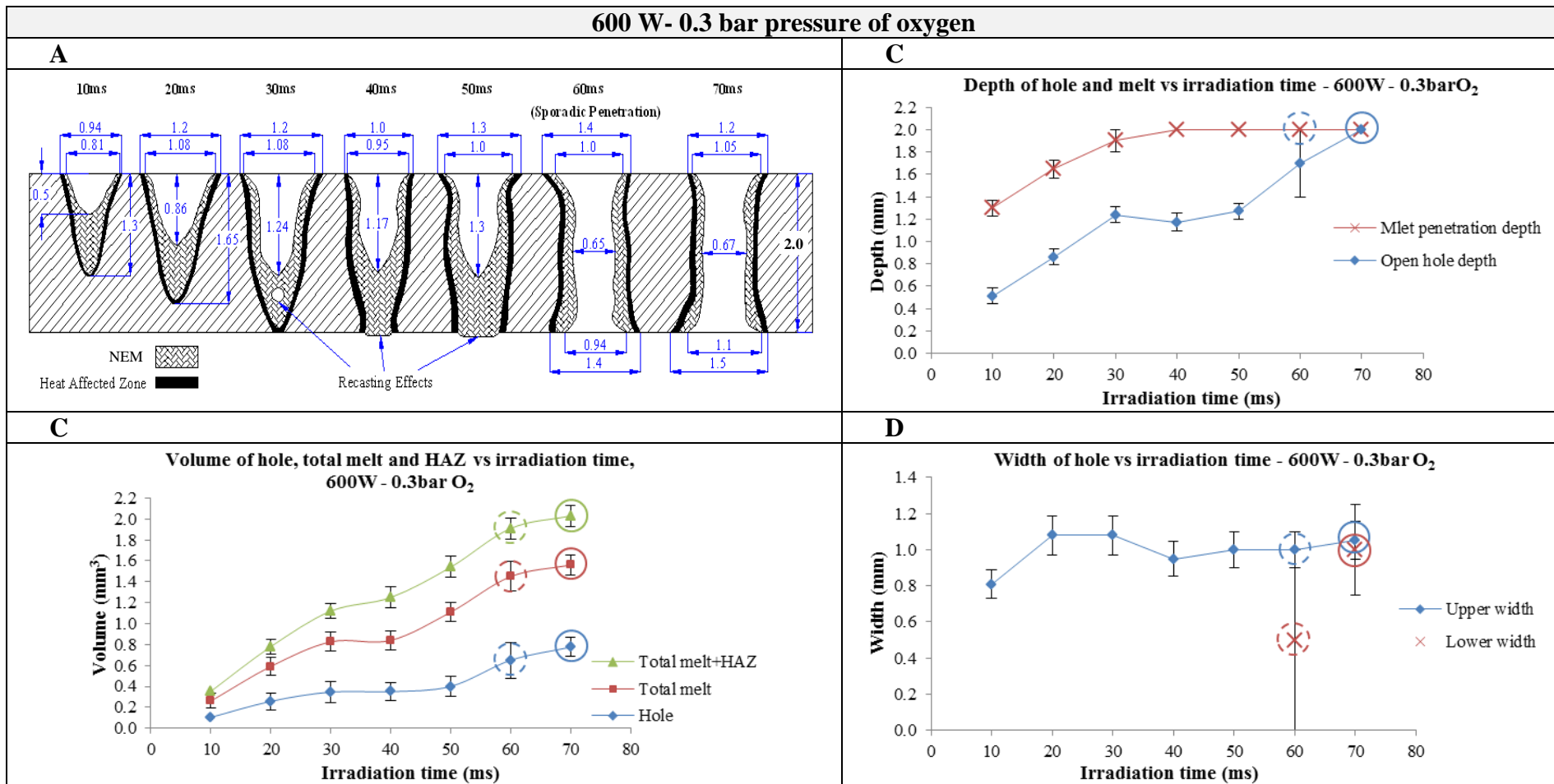


Figure 5.22- Piercing results for 600 W with 0.3 bar oxygen. A) Map of hole growth. B) Depth of hole and melt versus irradiation time. C) Volume of hole, melt total and HAZ versus irradiation time. D) Width of hole versus irradiation time. Solid circles indicate the through holes. Dash circles indicate the sporadic through holes.

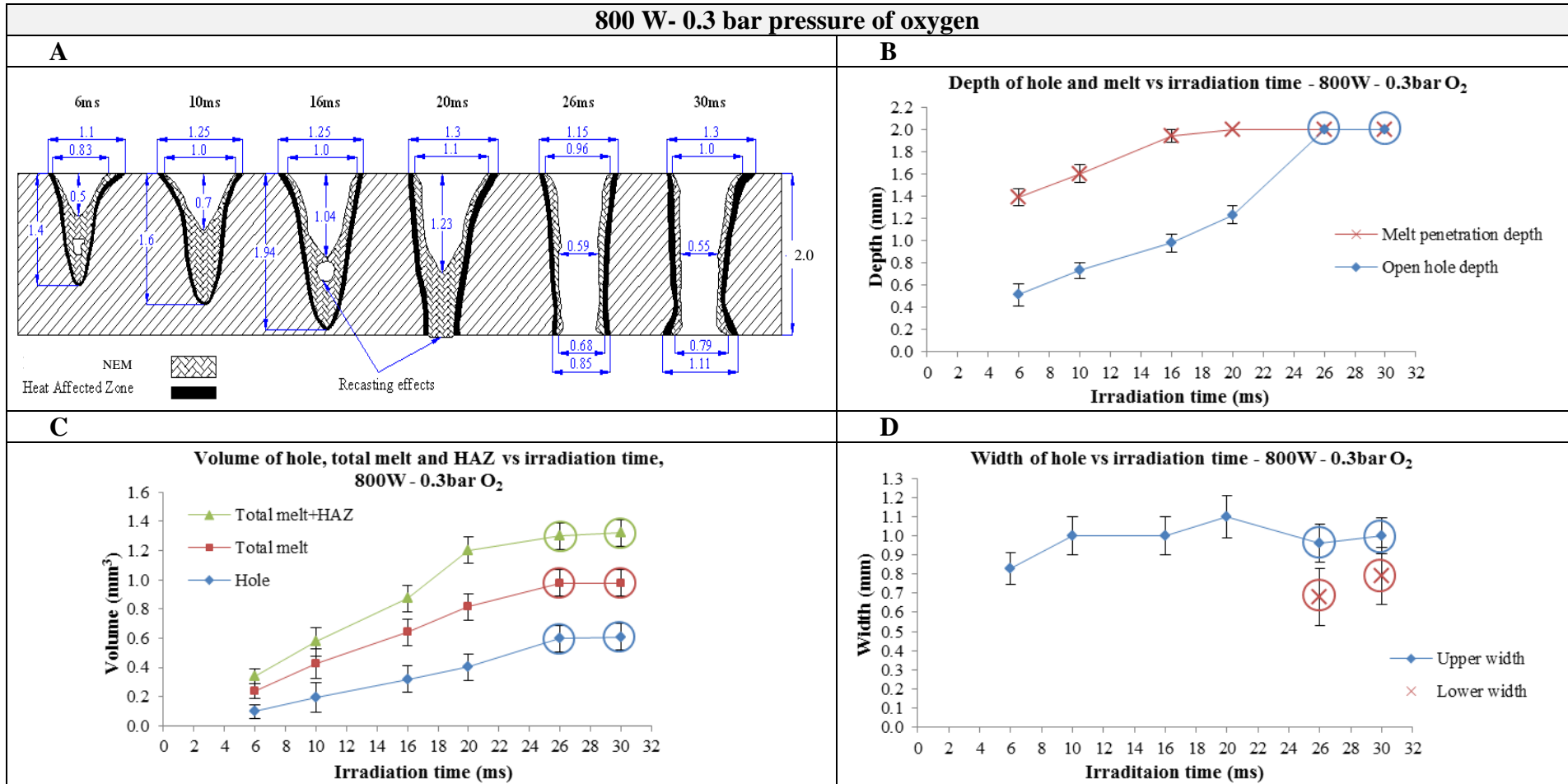


Figure 5.23- Piercing results for 800 W with 0.3 bar oxygen. A) Map of hole growth. B) Depth of hole and melt versus irradiation time. C) Volume of hole, melt total and HAZ versus irradiation time. D) Width of hole versus irradiation time. Solid circles indicate the through holes.

1000 W- 0.3 bar pressure of oxygen

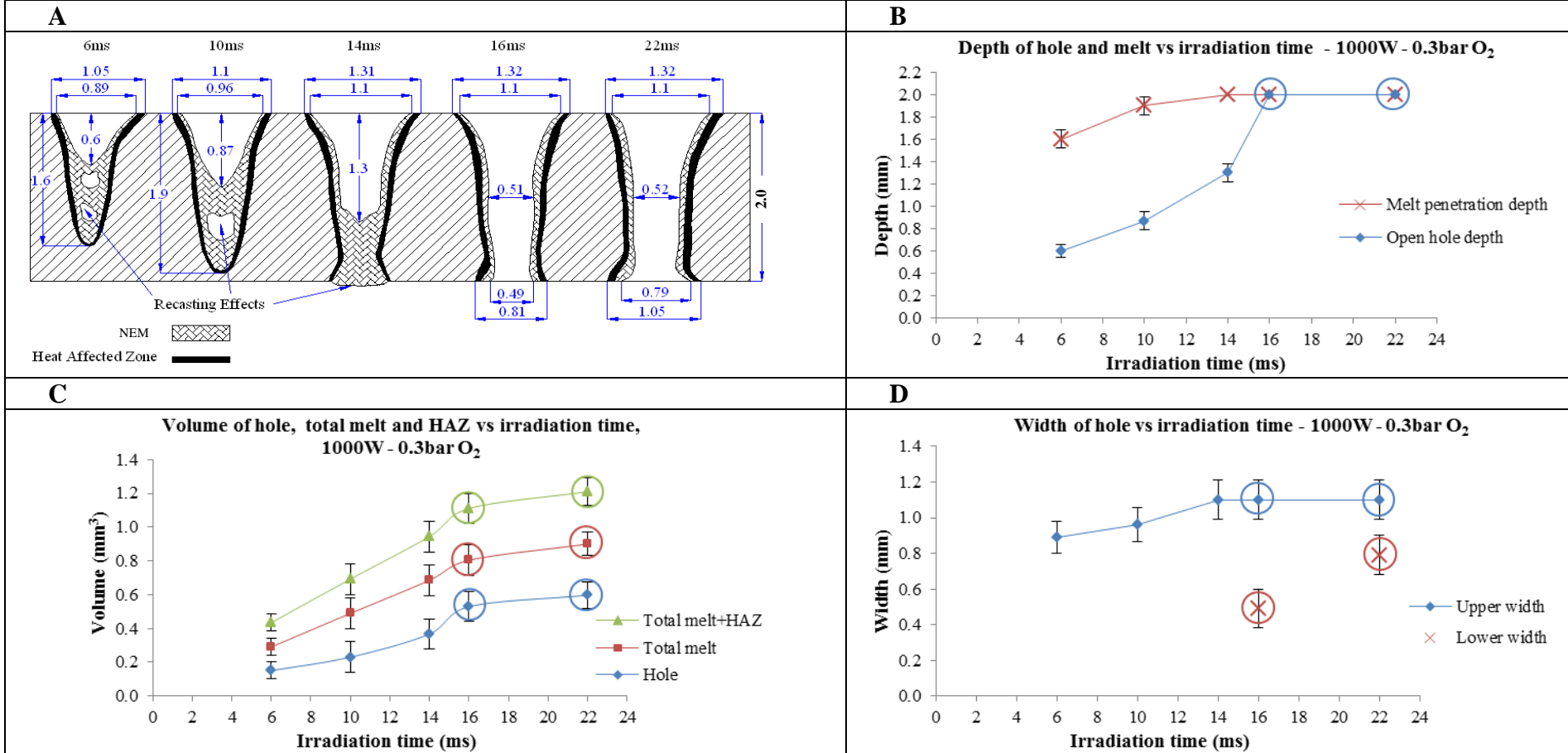


Figure 5.24- Piercing results for 1000 W with 0.3 bar oxygen. A) Map of hole growth. B) Depth of hole and melt versus irradiation time. C) Volume of hole, melt total and HAZ versus irradiation time. D) Width of hole versus irradiation time. Solid circles indicate the through holes.

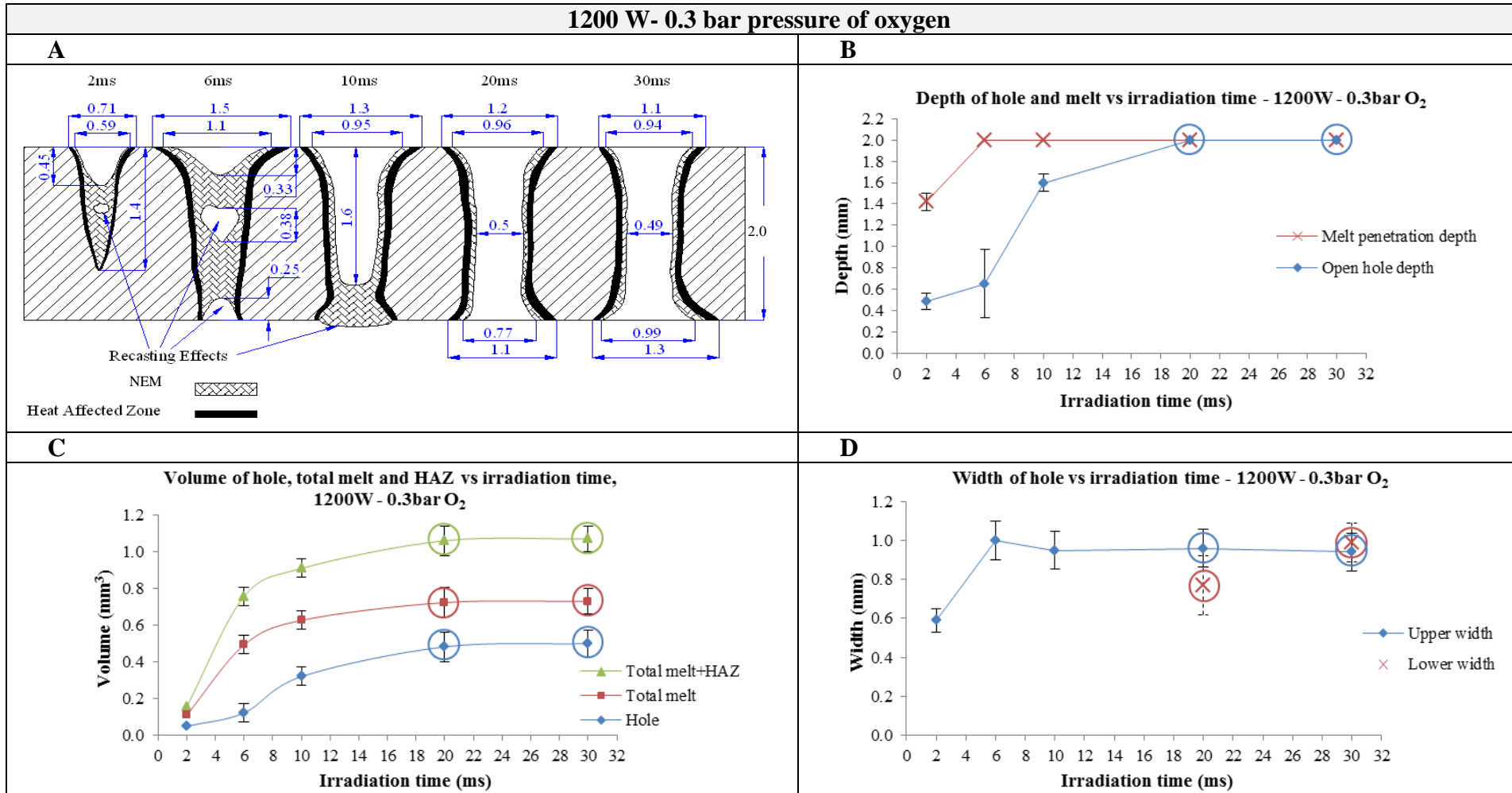
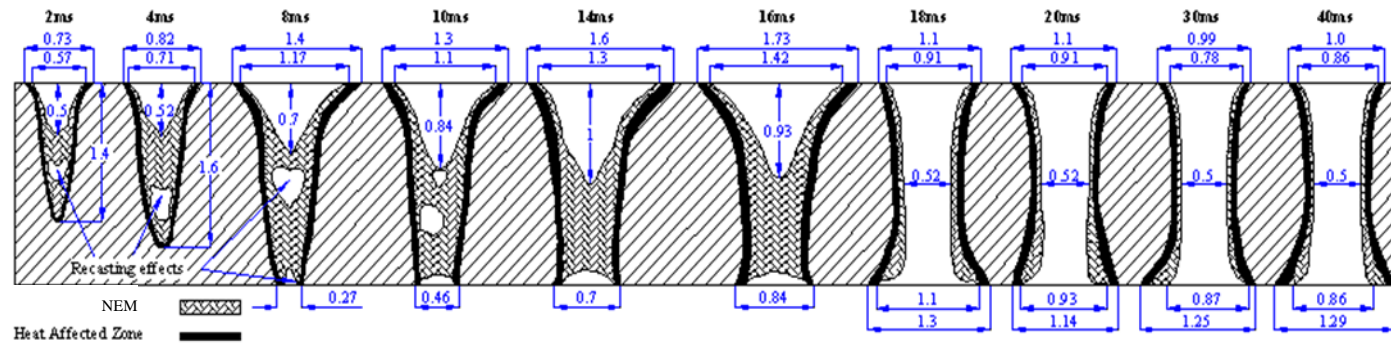


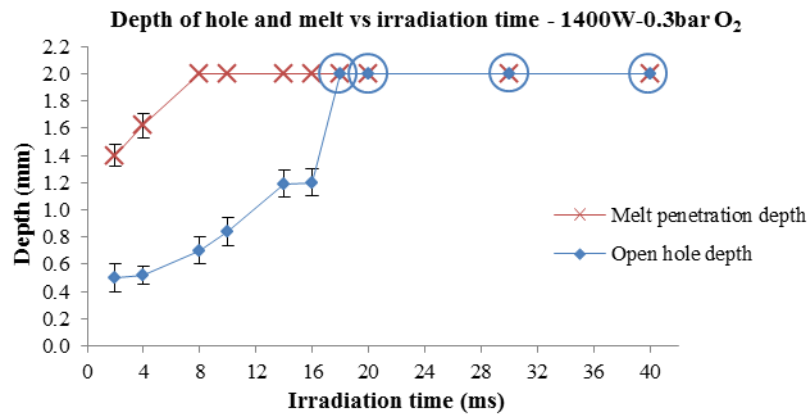
Figure 5.25- Piercing results for 1200 W with 0.3 bar oxygen. A) Map of hole growth. B) Depth of hole and melt versus irradiation time. C) Volume of hole, melt total and HAZ versus irradiation time. D) Width of hole versus irradiation time. Solid circles indicate the through holes.

1400 W- 0.3 bar pressure of oxygen

A



B



C

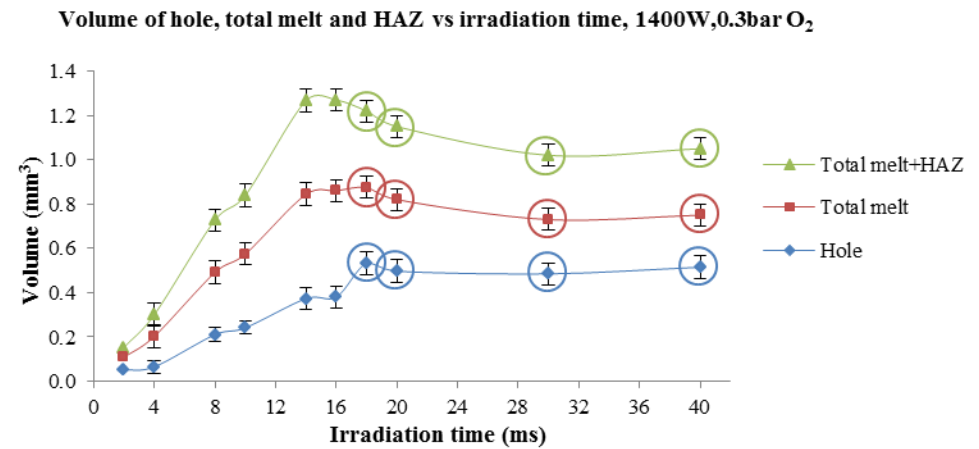
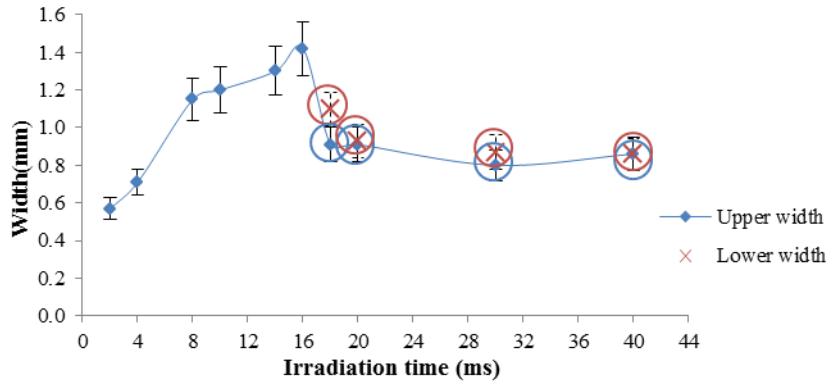


Figure 5.26- Piercing results for 1400 W with 0.3 bar oxygen. A) Map of hole growth. B) Depth of hole and melt versus irradiation time. C) Volume of hole, melt total and HAZ versus irradiation time. D) Width of hole versus irradiation time (printed in the next page). Solid circles indicate the through holes.



In continuation of Figure 5.26: D) Width of hole versus irradiation time at power of 1400 W with 0.3 bar pressure of oxygen. Circles show through holes.

The results of hole growth and melt penetration with increasing irradiation time in piercing with 2 bar and 0.3 bar pressure of oxygen for powers of 600 W to 1400 W have been shown in Figure 5.17 to Figure 5.26. Overall, the same trend with nitrogen can be seen in oxygen laser piercing in terms of depth and volume of the open hole and melt i.e. they increase with irradiation time until breakthrough happens then they almost become constant just with a slight variation (Figure 5.17 to Figure 5.26). However, at some irradiation times before breakthrough, the depth of hole either decreases or stays constant (B in Figure 5.17, Figure 5.18, Figure 5.22 and Figure 5.26). There is also a jump in the hole depth graph as breakthrough happens. Generally, in terms of hole width, the same trend is seen with nitrogen laser piercing i.e. the upper hole width gradually increases with irradiation until breakthrough happens then it is almost kept constant just with some variation (Figure 5.17-D to Figure 5.26-D). However in piercing with 0.3 bar, when the power is increased to 1200 W and 1400 W the lower hole width is almost equal to the upper hole width (D in Figure 5.25 and Figure 5.26).

5.10.3 Comparison of results

- Usually, the OHD and MPD increase as the irradiation time increases until breakthrough occurs.
- Generally, there is variation in the graph of OHD.
- There is a jump in the OHD graph at breakthrough happens.
- The open hole and total melt volumes increase with irradiation time until breakthrough occurs then the volumes are generally maintained steady just with a slight increase.

- In most case, the breakthrough time decreases with increasing power as presented in Table 5.7.

Table 5.7- Breakthrough time for different powers and pressures in piercing with oxygen.

	600 W	800 W	1000 W	1200 W	1400 W
2 bar	24 ms	14-18 ms	12 ms	8-10 ms	8 ms
0.3 bar	60-70 ms	26 ms	16 ms	18-20 ms	18 ms

- The breakthrough time decreases with increasing gas pressure as presented in Table 5.7.
- Overall, the volumes of hole, total melt and NEM decrease with increasing power as presented in Table 5.8.

Table 5.8- The volumes of hole, melt and the NEM at breakthrough for different powers and pressures in piercing with oxygen.

		600 W	800 W	1000 W	1200 W	1400 W
2 bar	Melt volume	1.25 mm ³	1-1.1 mm ³	0.8 mm ³	0.62 mm ³	0.62 mm ³
	Hole volume	0.85 mm ³	0.8 mm ³	0.6 mm ³	0.53 mm ³	0.54 mm ³
	NEM volume	0.4 mm ³	0.25 mm ³	0.2 mm ³	0.09 mm ³	0.08 mm ³
0.3 bar	Melt volume	1.5 mm ³	1.05 mm ³	0.8 mm ³	0.75 mm ³	0.85 mm ³
	Hole volume	0.7 mm ³	0.6 mm ³	0.56 mm ³	0.5 mm ³	0.53 mm ³
	NEM volume	0.8 mm ³	0.45 mm ³	0.24 mm ³	0.25 mm ³	0.32 mm ³

- In general, the volumes of total melt, hole and NEM decrease with increasing gas pressure as presented in Table 5.8.
- The upper hole width increases as the irradiation time increases until breakthrough occurs then it becomes almost constant.
- The upper hole width at breakthrough slightly decreases just with a variation with increasing power as presented in Table 5.9.

Table 5.9- Upper hole width at breakthrough for different powers and pressures in piercing with oxygen.

	600 W	800 W	1000 W	1200 W	1400 W
2 bar	0.85-0.9 mm	0.9-1.5 mm	0.85-0.9 mm	0.8-0.9 mm	0.8-0.9 mm
0.3 bar	1.05 mm	0.96 mm	1.1 mm	0.96 mm	0.91 mm

5.10.4 Discussion of results

5.10.4.1 Overall, the OHD and MPD increase as the irradiation time increases.

As the irradiation time increases, more energy is exerted onto the material. Moreover, the time for exothermic oxidation reaction between oxygen and melt increases. Thus, the MPD increases as a result of laser irradiation and exothermic oxidation reaction. The OHD increases as the yielded melt (with a relatively low viscosity [9]) is removed from the hole due to the pressure gradient. The pressure

inside the hole is higher than the ambient pressure thus the melt is expelled from the hole.

5.10.4.2 There is a variation in the hole depth graph

The melt with relatively low viscosity (Fe/FeO [9]) lining the hole wall may collapse in the hole during piercing [98] and this brings about a variation in the OHD graph.

5.10.4.3 There is a jump in the hole depth graph at breakthrough.

When the breakthrough happens, a large volume of the melt is suddenly removed through the rear of the hole resulting in a jump in the OHD graph.

5.10.4.4 The hole and melt volumes increase with irradiation time until breakthrough occurs then the volumes are generally maintained steady just with a slight increase.

The same explanation with 5.9.4.4 (see page 150) i.e. as the laser irradiation time increases, the opportunity for laser to melt and penetrate the material laterally increases, enlarging the melt and hole volumes. At breakthrough, the laser beam passes the sheet through the pierced hole with no further increase in the volumes of the melt and hole. However after breakthrough, the lower hole width increases and the hole taper decreases with further increase in the irradiation time, increasing the volumes slightly. Moreover, hole development does not stop as soon as the energy input from the laser stops. On-going melt flow and heat input from the melt continues to affect the hole shape and dimensions.

5.10.4.5 The breakthrough time decreases with increasing power.

This is because, the energy exerted to the melting zone increases with increase in the power thus the laser penetrates the sheet thickness more quickly as a result of heat conduction and laser penetration so the breakthrough happens in a shorter irradiation.

5.10.4.6 The breakthrough time decreases with increasing gas pressure.

When the pressure of gas is increased, the pressure gradient inside the hole increases thus the melt is removed more quickly resulting in decrease in the breakthrough time.

Since the gas pressure is increased from 0.3 bar to 2 bar, the pressure inside the hole increases and as a result of more effective melt ejection the breakthrough time decreases. This indicates that a sufficient pressure of oxygen (e.g. 2 bar compared with 0.3 bar) in laser piercing can improve the effectiveness of melt ejection to decrease the breakthrough time.

It has been confirmed that in oxygen laser cutting of mild steel there is no vaporisation [9] hence the mechanism of melt ejection when piercing with 0.3 bar may not be based on the surface vaporisation. In this case, it is to say that due to the relatively low viscosity of the melt (Fe/FeO), even a 0.3 bar pressure of oxygen is a sufficient pressure to eject the melt. A brief comparison between 0.3 bar O₂ with 0.3 bar N₂ clarifies the effect of low viscosity of the melt on the melt ejection and breakthrough time (Table 5.10).

Table 5.10- Breakthrough time for 0.3 bar pressure of nitrogen and oxygen.

	600 W	800 W	1000 W	1200 W	1400 W
0.3 bar N ₂	-	40-50 ms	50-60 ms	90-100 ms	80-90 ms
0.3 bar O ₂	60-70 ms	26 ms	16 ms	18-20 ms	18 ms

In another point of view, the melt inside the piercing zone undergoes the longer irradiation in contrast with cutting. For example, in a typical laser cutting of 2 mm-thick mild steel sheet with a moderate speed of 5000 mm/min, power of 1400 W and with a spot size of 0.2 mm the maximum irradiation time to cut the sheet for a length of the beam diameter (disregarding the cutting front angle) will be:

$$Ti = \frac{0.2}{5000} * 60 * 10^3 = 2.4 \text{ {ms}}$$

However, the minimum irradiation time to pierce a sheet with the same thickness and power is 18 ms. Thus, there is a possibility that due to the longer irradiation time in piercing, the melt may become hotter (i.e. 3000K) to generate a surface vaporisation.

5.10.4.7 The volumes of hole, melt and the NEM decrease at breakthrough with increasing power.

When the power is increased, the breakthrough happens more quickly. When the breakthrough occurs, the laser beam passes through the pierced hole without significant further melting so the melt and hole volumes overall decrease

(Figure 5.27). As can be seen, the NEM (difference between hole and melt) also decreases with increasing power.

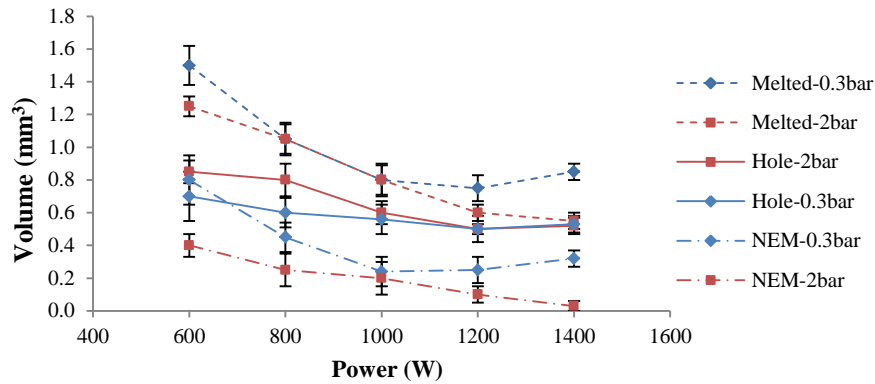


Figure 5.27- Volumes of melt, hole and the NEM versus power at breakthrough for different oxygen pressure.

5.10.4.8 In general, the volumes of melt, hole and the NEM at breakthrough decrease with increasing gas pressure.

When the gas pressure is increased, the breakthrough time decreases. When the breakthrough happens, the laser beam crosses the sheet through the pierced hole. Thus, when the pressure is increased, the breakthrough time decreases, and there is less time for the hole and melt to grow laterally as an effect of exothermic reaction and heat conduction, this results in decrease in the volumes. Regarding the NEM, 2 bar oxygen removes the melt from the hole more efficiently in comparison with 0.3 bar (Figure 5.27).

5.10.4.9 Overall, the upper hole width increases as the irradiation time increases until the breakthrough occurs then it becomes almost constant.

An upward melt ejection causes erosion at the upper edge of the hole before breakthrough. Once the breakthrough occurs, the melt flow is changed to downward; hence, there is no further erosion of the upper hole width, so the width is almost kept steady. Moreover, at breakthrough the laser crosses the sheet through the pierced hole without further melting to widen the hole entrance.

5.10.4.10 Usually, the upper hole width at breakthrough slightly decreases just with a variation with increasing power.

The same explanation with 5.9.4.8 (see page 151) i.e. the upward melt ejection causes erosion on the upper edge of the hole and upward melt ejection is a

fluctuating process and hence boosts variations in the hole width. When the power is increased, the breakthrough happens quickly, hence there is less melt flow through the entrance of the hole, decreasing the variation of the hole width.

5.11 Comparison of O₂ and N₂ piercing in low and moderate pressure

Considering the same irradiation time, the depth of melt for 2 bar oxygen is the same with 0.3 bar oxygen (Figure 5.28). In most case, when using oxygen, the melt penetrates the sheet thickness quicker than nitrogen. For the same irradiation and before breakthrough, the OHD in 2 bar oxygen is deeper than that for all other employed conditions. This indicates that the melt in 2 bar oxygen piercing is expelled easier, and so the breakthrough happens quicker (Figure 5.28).

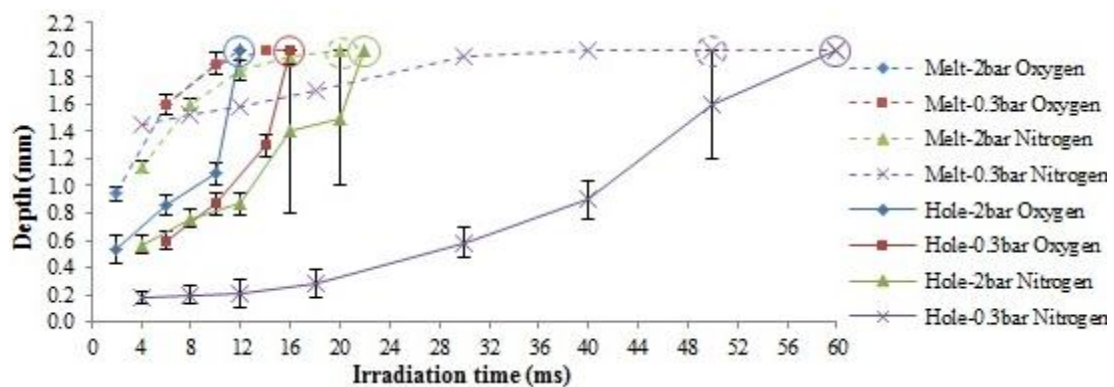


Figure 5.28- Hole and melt depth versus irradiation time at 1000 W for different gases and pressures. Circles show through holes. Dash circles indicate sporadic through holes.

Regarding the melt volume, Figure 5.29 indicates that considering the same irradiation time, the melt volume for oxygen is larger than that produced by nitrogen. This is due to the contribution of additional energy input from the oxidation reaction to the melting zone. As can be seen, in nitrogen piercing for both employed pressures, the melt volume grows with the same slope whereas in oxygen piercing, with an increase in the pressure, the melting rate becomes steeper. It must be mentioned that the amount of heat produced by the oxidation reaction per mole is not affected by the oxygen pressure; and, the thermal energy contributed by the oxidation reaction is about 250 kJmol⁻¹ [9]. 2 bar pressure has greater melt ejection effectiveness and thus the laser can penetrate further into the material, increasing melting rate. Faster penetration with 2 bar confirms this reason (Figure 5.29).

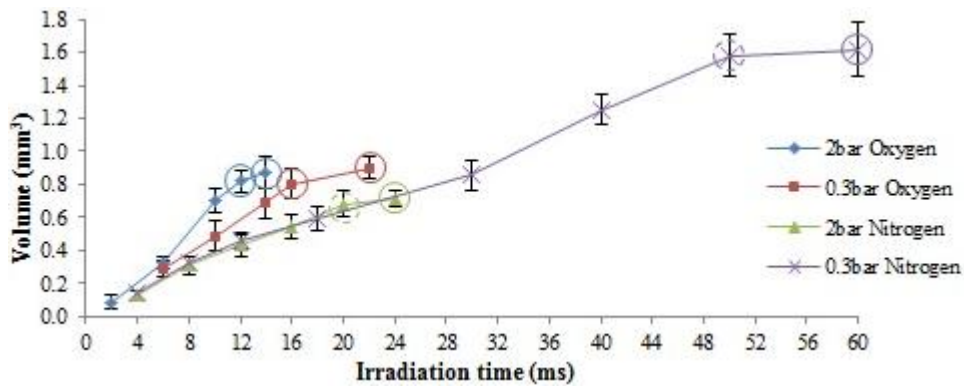


Figure 5.29- Melt total volume versus irradiation time at power of 1000 W for different gases and pressures. Through holes are shown by circles. Dash circles show sporadic through holes.

Overall for all conditions, the hole volume increases with irradiation time until breakthrough happens, then it almost becomes constant (Figure 5.30). As it is seen, the through hole volume in 2 bar oxygen pressure is larger than that for other conditions. 2 bar O₂ and 2 bar N₂ have the same pressure, thus the larger hole volume in oxygen is related to the difference in the melting rate, melt properties and melt removal efficiency.

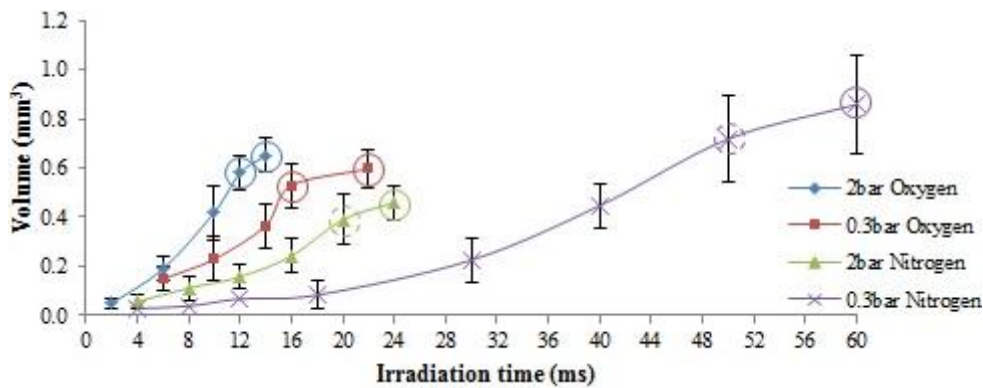


Figure 5.30- Hole volume versus irradiation time at power of 1000 W for different gases and pressures. Circles indicate through holes. Dash circles show sporadic through holes.

The melt and hole volumes for oxygen piercing are larger than those are with nitrogen (Figure 5.31). This indicates that at the same laser power and same gas pressure, oxygen enhances melting and ejects more melt than nitrogen does. The molten oxidised iron generates heat as it oxidises and therefore melts more of its surrounding material [89]. This exothermic reaction continues for a short time even after the laser is turned off. The partially oxidised melt produced has a lower viscosity than the unoxidised melt produced when nitrogen is employed [88]. This lower viscosity melt can be more easily ejected, resulting in greater hole volume. So

there are two things going on here due to the oxidation: 1- More melt is generated.
 2- The viscosity of melt is less. Both of these contribute to increase the volumes.

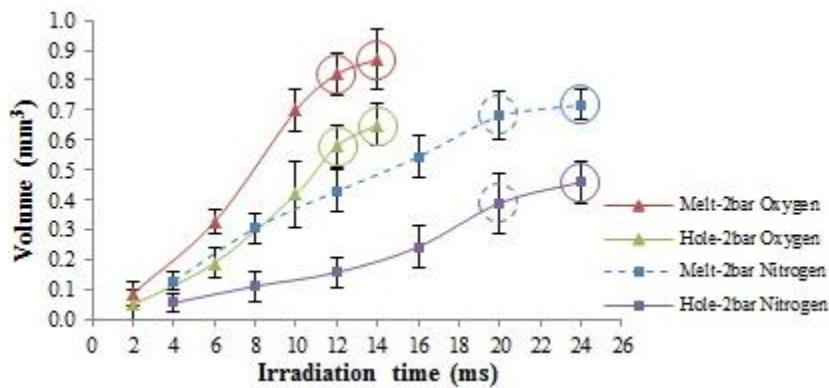


Figure 5.31- A comparison of oxygen and nitrogen in terms of melt total and hole volumes when piercing with 1000W and 2 bar pressure. Circles indicate through holes. Dash circles show sporadic through holes.

The rate of material ejection from the melting zone increases dramatically as the gas pressure is increased from 0.3 bar to 2 bar (Figure 5.32). Moreover, if the gas pressure is too low to remove the melt at the same rate at which it is generated, then hot melt is retained in the hole. This hot melt then conducts heat laterally, which causes an additional melting and broadening of the penetration hole.

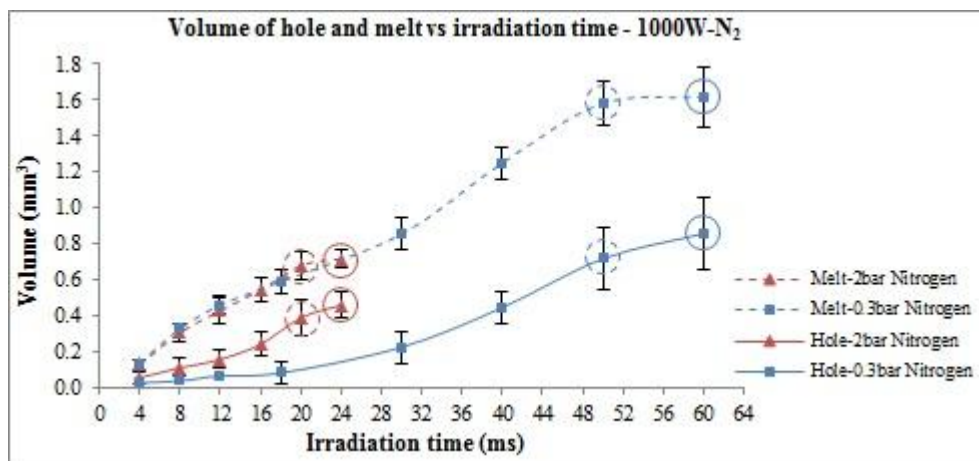


Figure 5.32- A comparison between 2 bar and 0.3 bar nitrogen pressure in terms of melt and hole volumes versus irradiation time. Circles indicate through holes. Dash circles show sporadic through holes.

For both employed gases, with the same pressure and the same irradiation time, the MPD increases with power (Figure 5.33). As can be seen, in oxygen when using 1000 W and 1200 W, the melt reaches the sheet thickness (2 mm) quicker than nitrogen, however, when the power increases to 1400 W, both gases show the same penetration time.

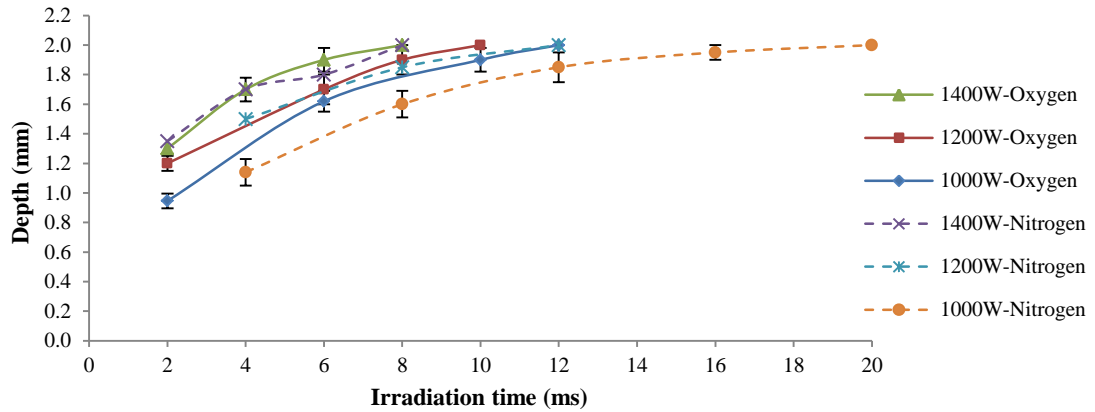


Figure 5.33- Depth of melt versus irradiation time for different powers in 2 bar oxygen and nitrogen.

As can be seen in Figure 5.34, for both assist gases overall, the breakthrough time decreases with increasing power. For the same irradiation times, the OHD increases with power. With the same power, the breakthrough time in oxygen happens quicker than nitrogen. For all conditions, the OHD increases with irradiation time.

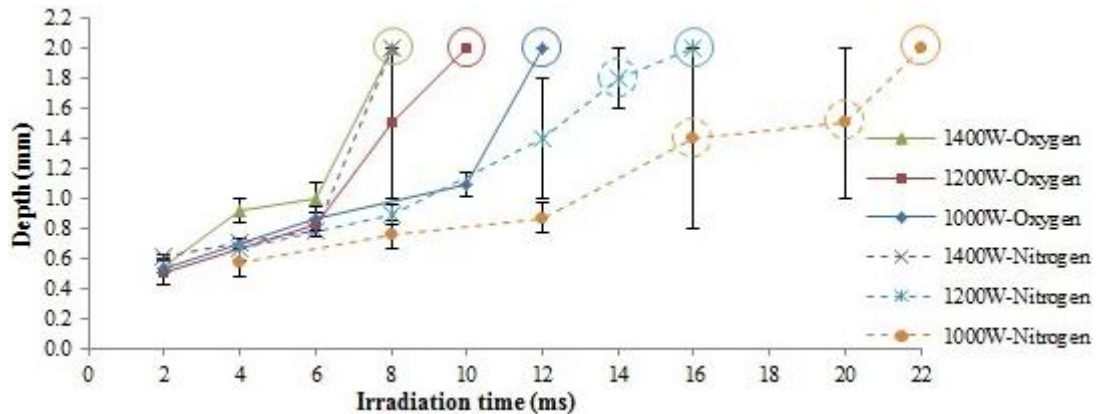


Figure 5.34- Depth of hole versus irradiation time for different powers and gases with 2 bar pressure.

Overall, for both assist gases the volumes of melt and hole at breakthrough decrease when the power increases from 1000 W to 1400 W. However, as presented in Figure 5.35, for oxygen there is slight increase in the volumes when the power increases from 1200 W to 1400 W. In most case, the amount of NEM lining the hole (the gap between melt and hole volume) for oxygen is less than that for nitrogen.

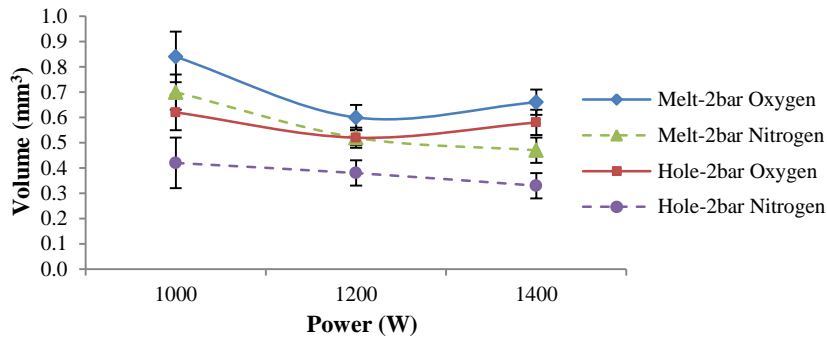


Figure 5.35- The melt and hole volumes versus power for different gases and pressures.

As is seen in Figure 5.36, the hole diameter at breakthrough decreases with increasing power except for 0.3 bar N₂. For 2 bar N₂, it is in the range of 0.7 mm to 0.8 mm and for oxygen it is between 0.8 mm to 1.3 mm.

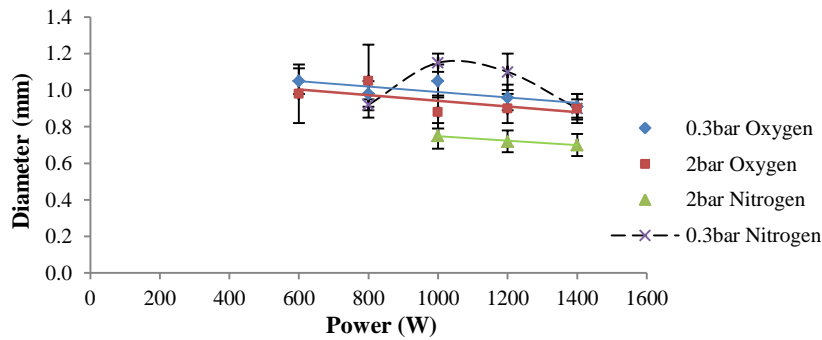


Figure 5.36- Showing hole diameter versus power for different employed gases.

In general, the time of breakthrough decreases as the power increases except for 0.3 bar pressure of nitrogen (Figure 5.37).

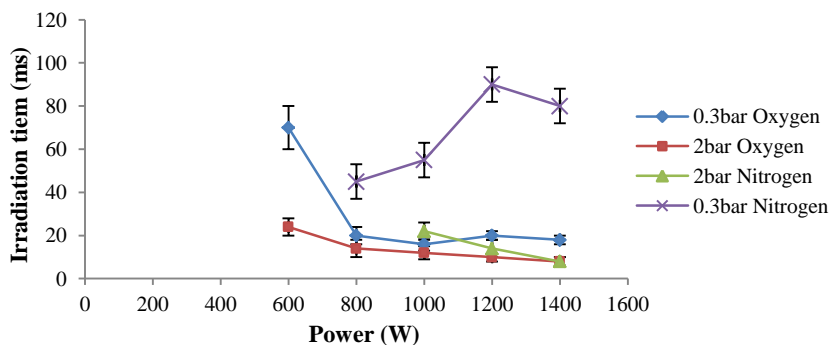


Figure 5.37- Showing the time when through hole appears at each power intensity.

5.12 High power piercing with moderate and high pressure of nitrogen

5.12.1 With 2 bar nitrogen pressure

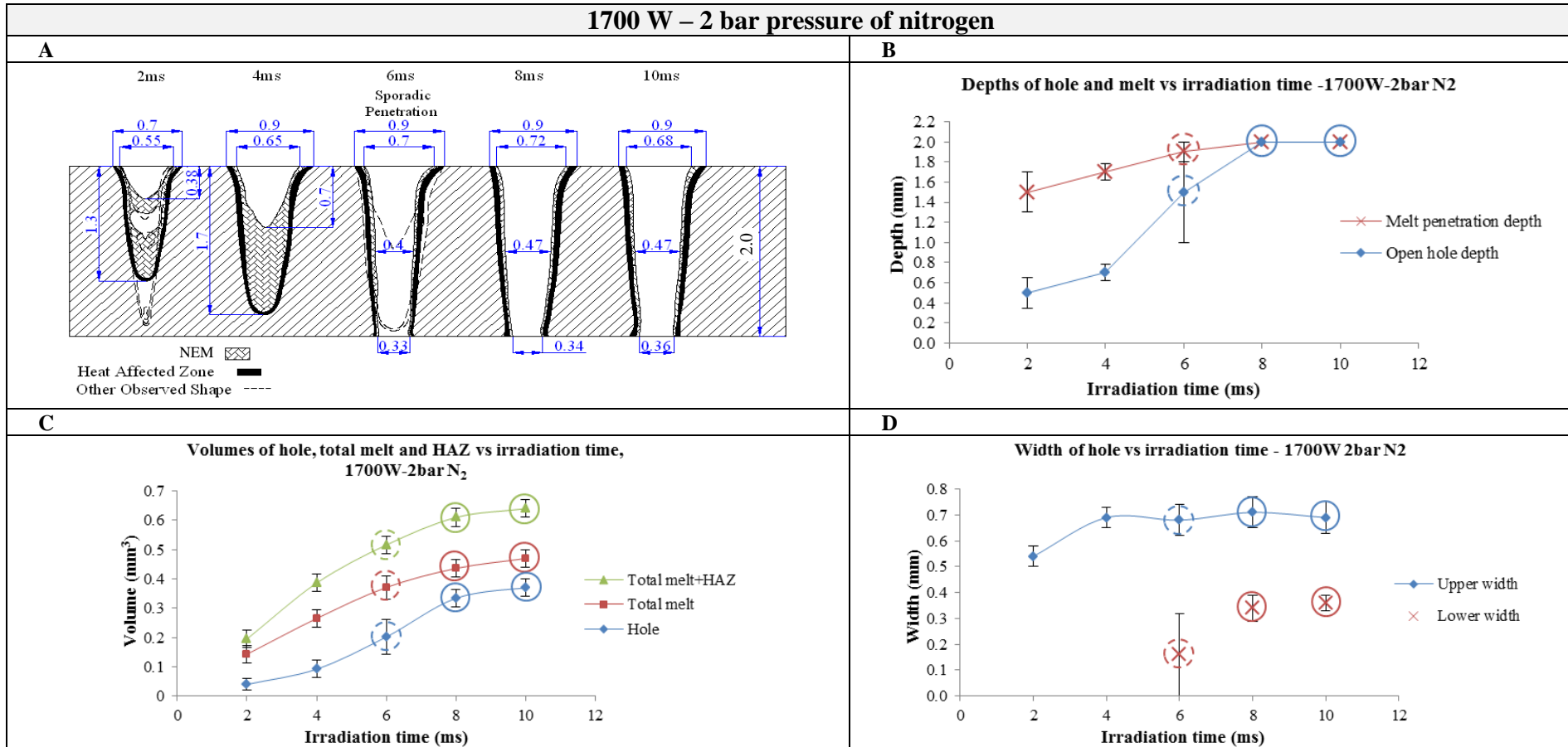


Figure 5.38- Piercing results for 1700 W with 2 bar nitrogen. A) Map of hole growth. B) Depth of hole and melt vs irradiation time. C) Volume of hole, melt total and HAZ vs irradiation time. D) Width of hole vs irradiation time. Solid circles indicate the through holes. Dash circles indicate the sporadic through holes.

2000 W – 2 bar pressure of nitrogen

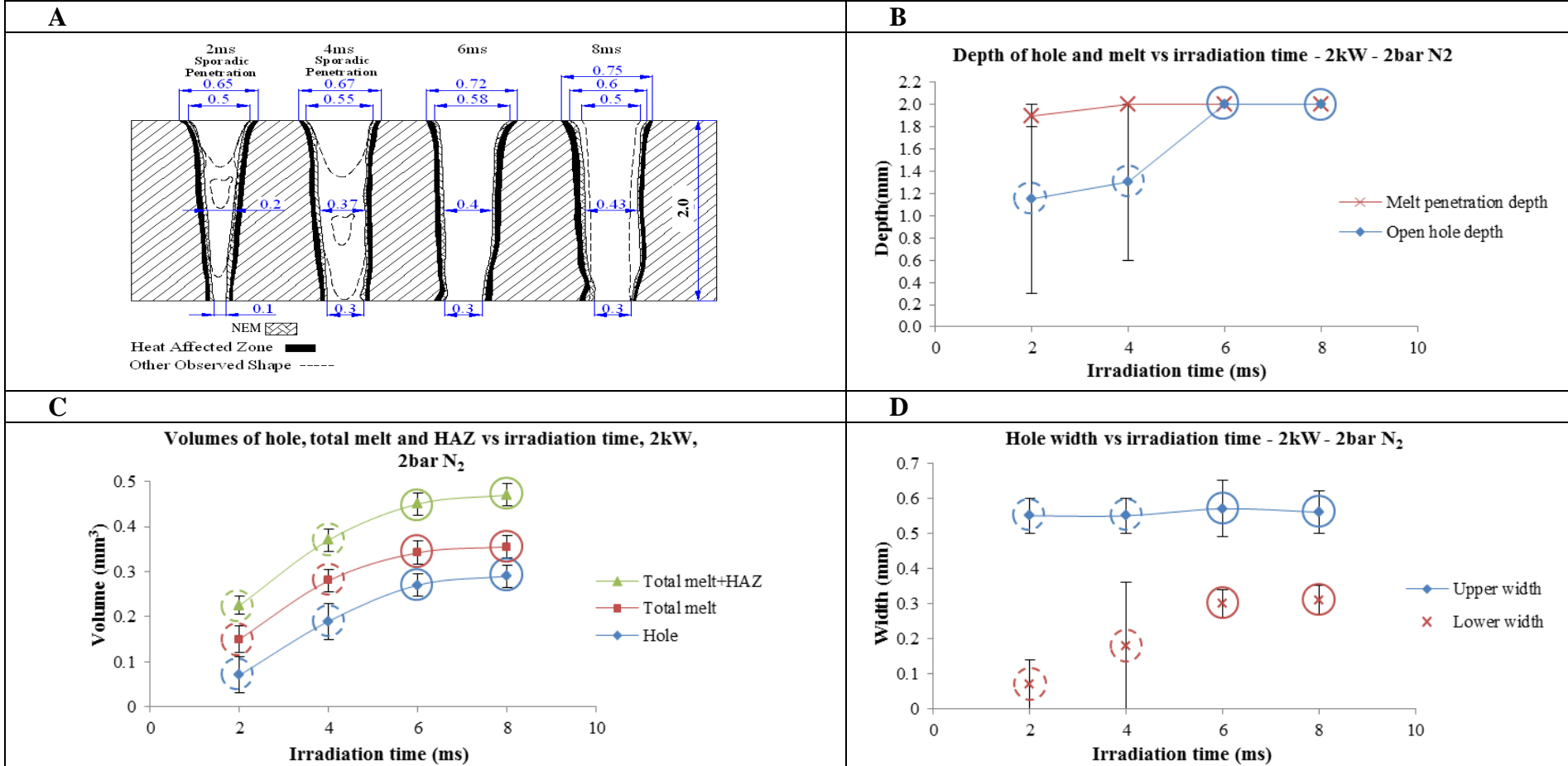


Figure 5.39- Piercing results for 2000 W with 2 bar nitrogen. A) Map of hole growth. B) Depth of hole and melt versus irradiation time. C) Volume of hole, melt total and HAZ vs irradiation time. D) Width of hole vs irradiation time. Solid circles indicate the through holes. Dash circles indicate the sporadic through holes.

5.12.2 With 4 bar nitrogen pressure

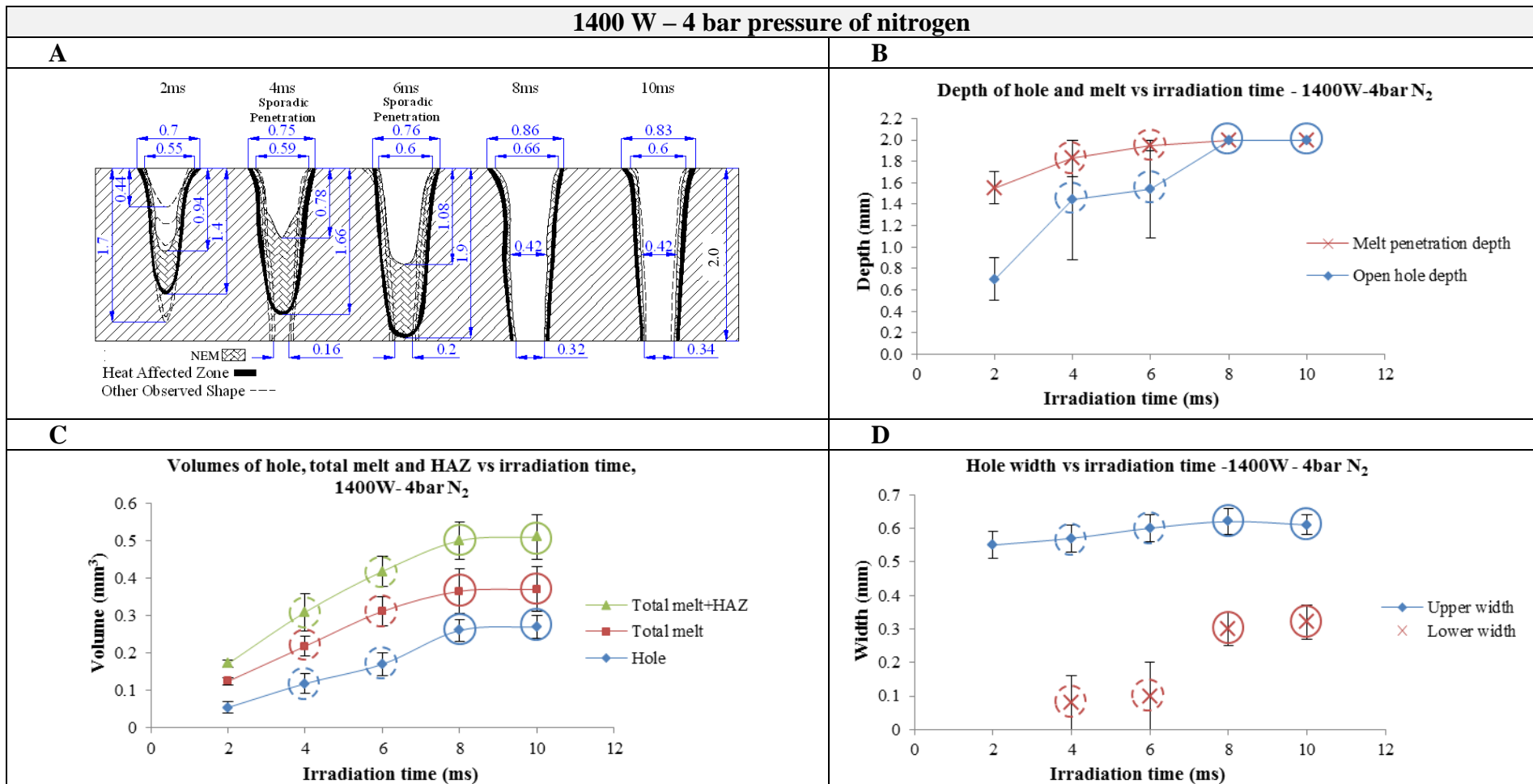


Figure 5.40- Piercing results for 1400 W with 4 bar nitrogen. A) Map of hole growth. B) Depth of hole and melt vs irradiation time. C) Volume of hole, melt total and HAZ vs irradiation time. D) Width of hole vs irradiation time. Solid circles indicate the through holes. Dash circles indicate the sporadic through holes.

1700 W – 4 bar pressure of nitrogen

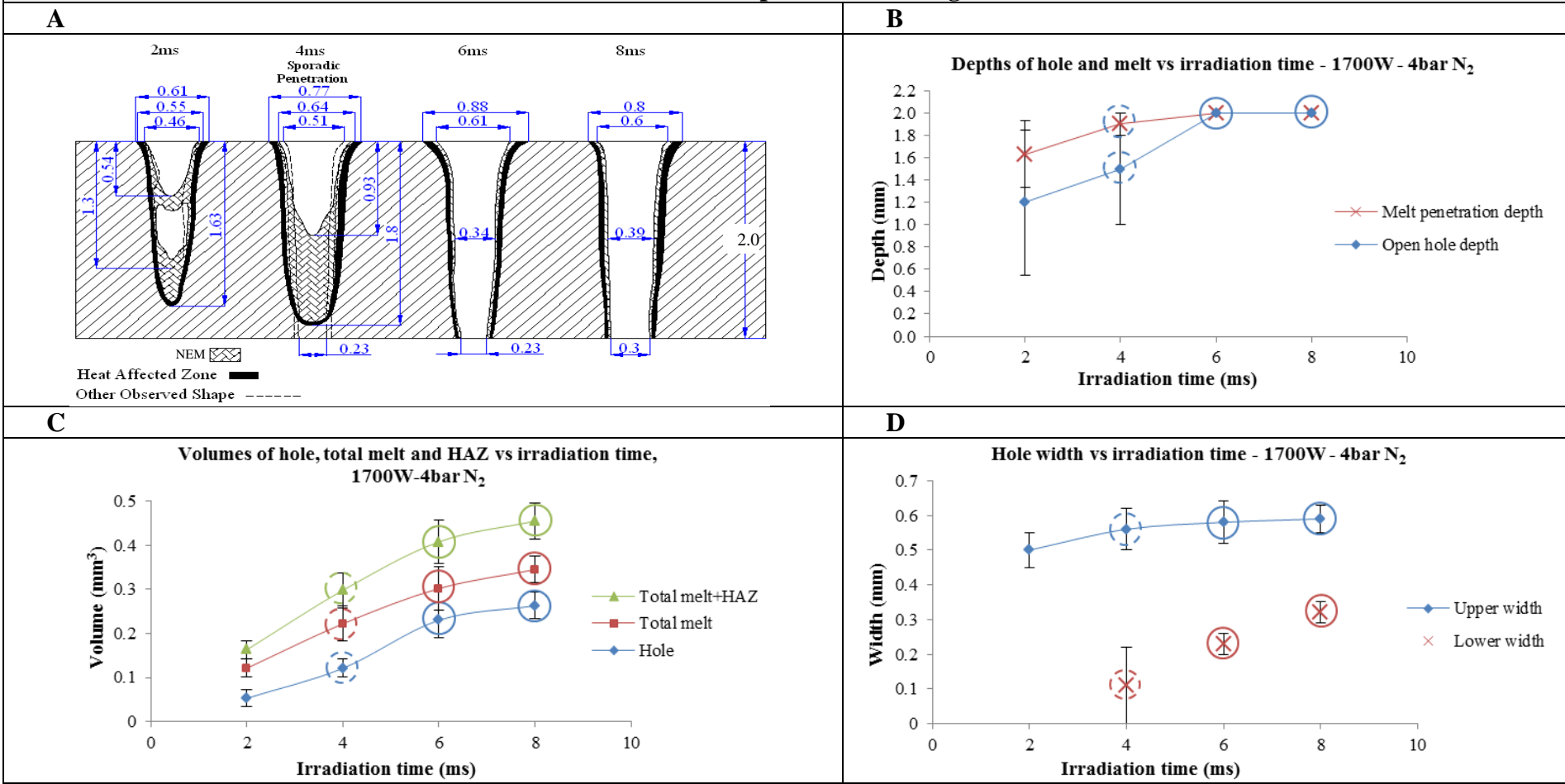


Figure 5.41- Piercing results for 1700 W with 4 bar nitrogen. A) Map of hole growth. B) Depth of hole and melt vs irradiation time. C) Volume of hole, melt total and HAZ vs irradiation time. D) Width of hole vs irradiation time. Solid circles indicate the through holes. Dash circles indicate the sporadic through holes.

2000 W – 4 bar pressure of nitrogen

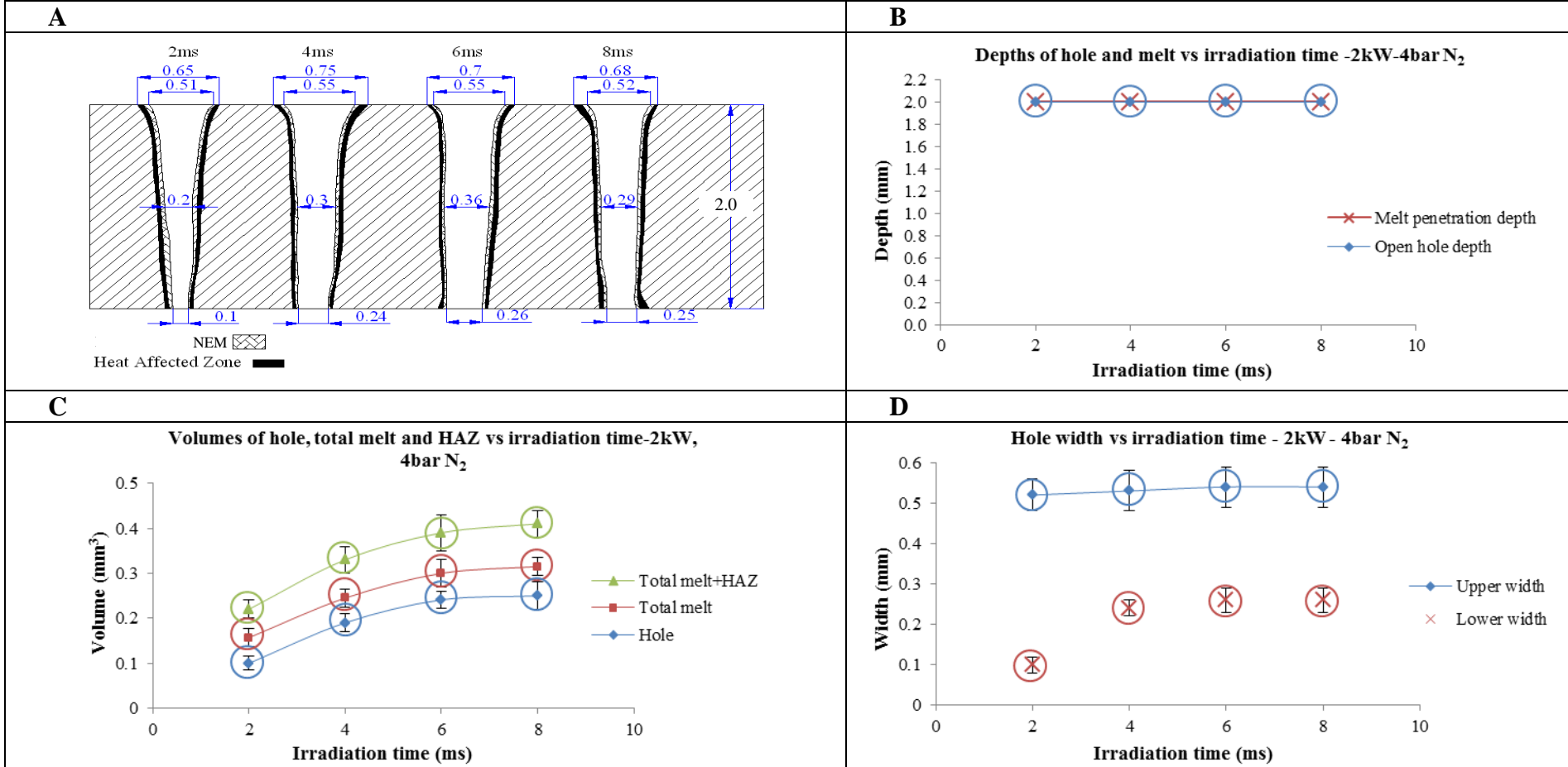


Figure 5.42- Piercing results for 2000 W with 4 bar nitrogen. A) Map of hole growth. B) Depth of hole and melt vs irradiation time. C) Volume of hole, melt total and HAZ vs irradiation time. D) Width of hole vs irradiation time. Solid circles indicate the through holes. Dash circles indicate the sporadic through holes.

5.12.3 With 8 bar nitrogen pressure

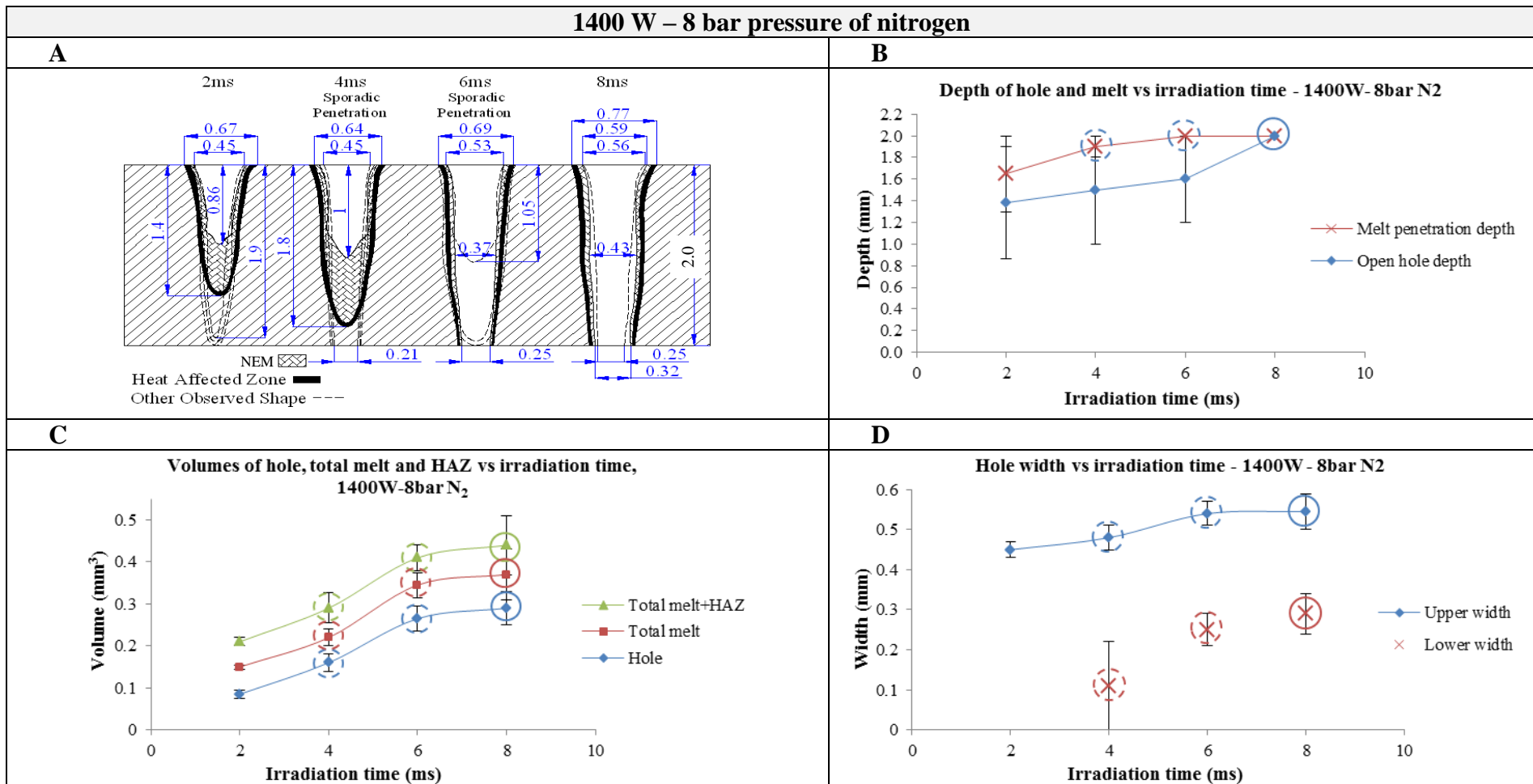


Figure 5.43- Piercing results for 1400 W with 8 bar nitrogen. A) Map of hole growth. B) Depth of hole and melt vs irradiation time. C) Volume of hole, melt total and HAZ vs irradiation time. D) Width of hole vs irradiation time. Solid circles indicate the through holes. Dash circles indicate the sporadic through holes.

1700 W – 8 bar pressure of nitrogen

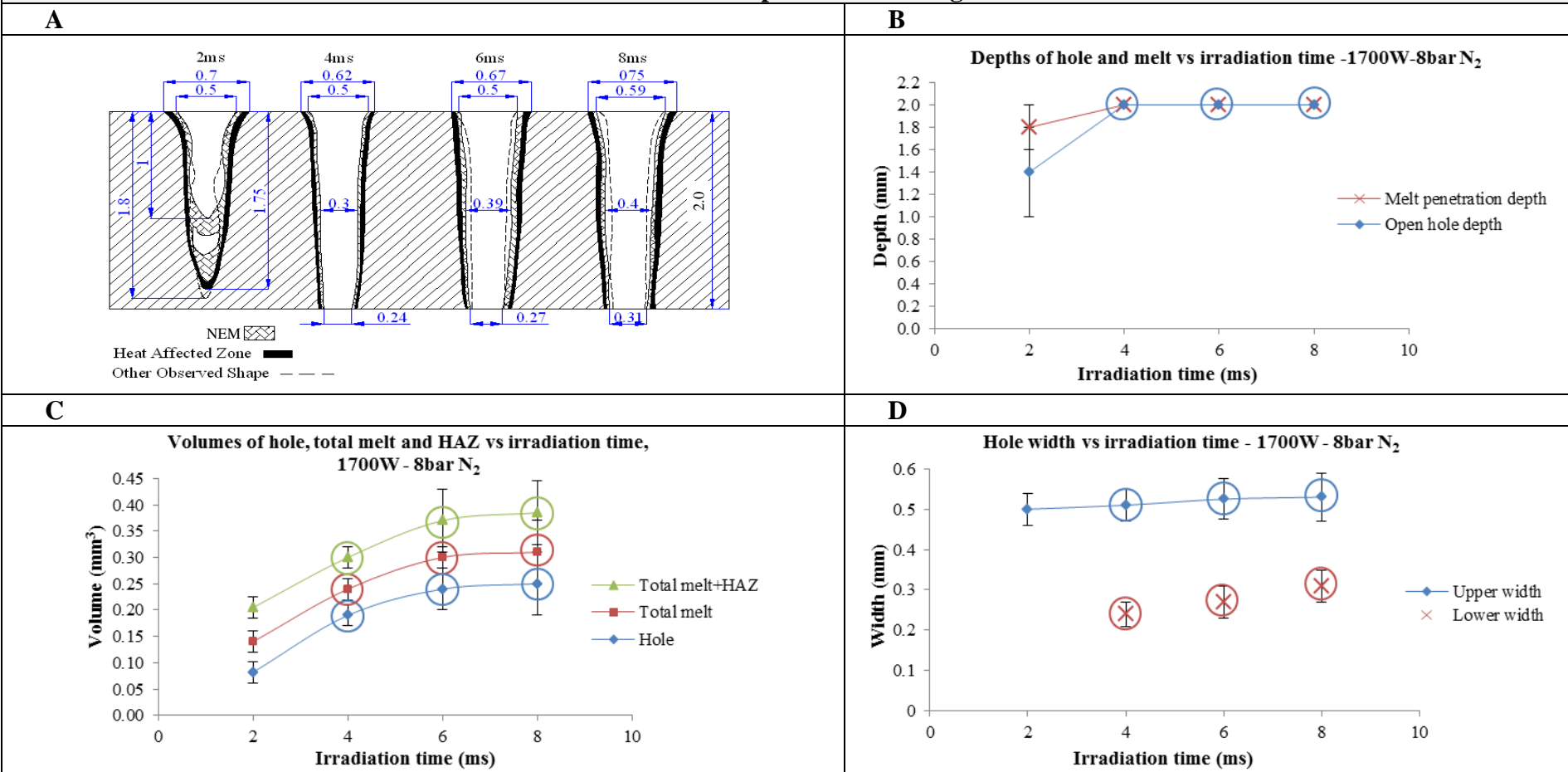


Figure 5.44- Piercing results for 1700 W with 8 bar nitrogen. A) Map of hole growth. B) Depth of hole and melt vs irradiation time. C) Volume of hole, melt total and HAZ vs irradiation time. D) Width of hole versus irradiation time. Solid circles indicate the through holes. Dash circles indicate the sporadic through holes.

2000 W – 8 bar pressure of nitrogen

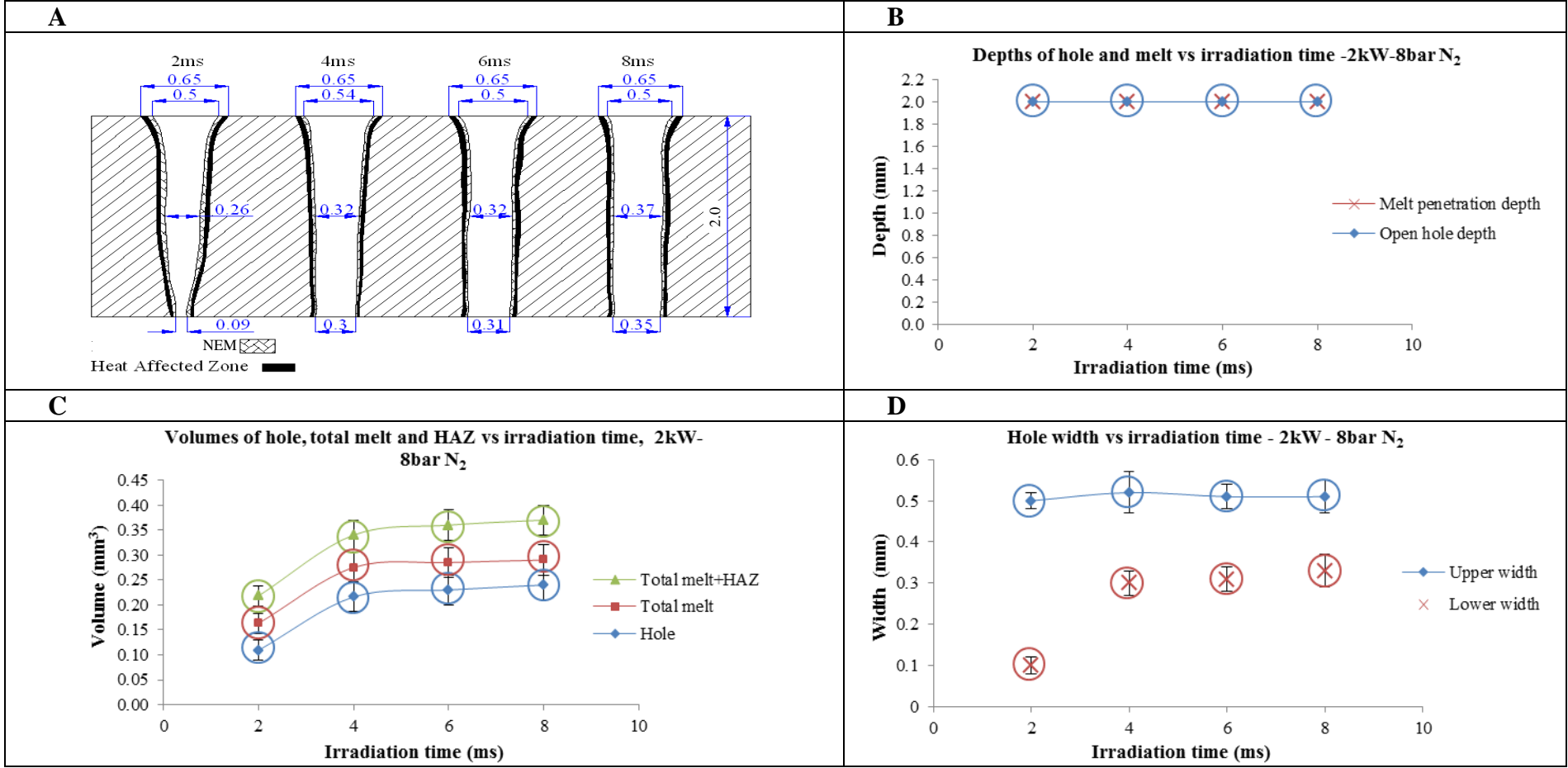


Figure 5.45- Piercing results for 2000 W with 8 bar nitrogen. A) Map of hole growth. B) Depth of hole and melt vs irradiation time. C) Volume of hole, melt total and HAZ vs irradiation time. D) Width of hole vs irradiation time. Solid circles indicate the through holes. Dash circles indicate the sporadic through holes.

5.12.4 With 12 bar nitrogen pressure

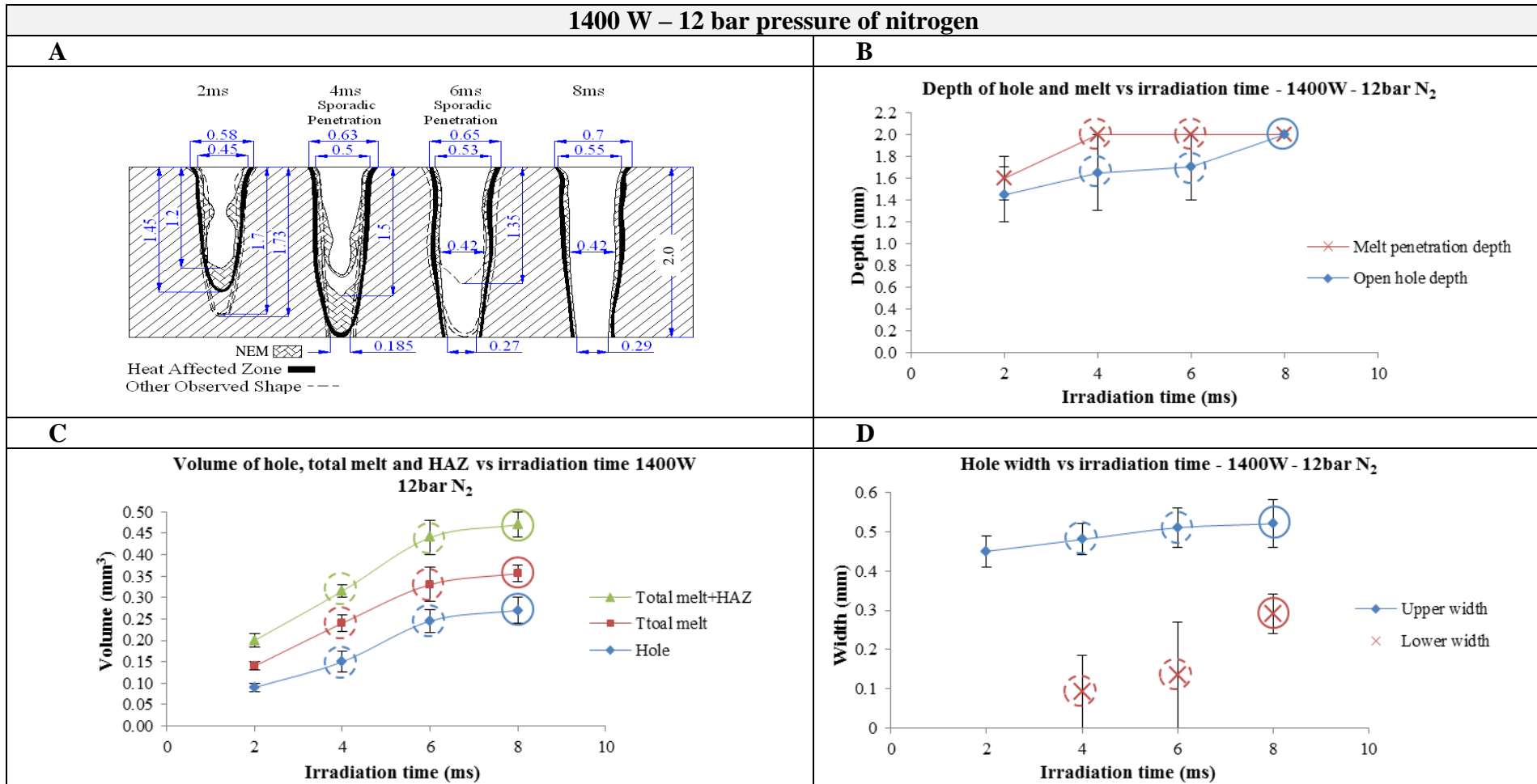


Figure 5.46- Piercing results for 1400 W with 12 bar nitrogen. A) Map of hole growth. B) Depth of hole and melt vs irradiation time. C) Volume of hole, melt total and HAZ vs irradiation time. D) Width of hole vs irradiation time. Solid circles indicate the through holes. Dash circles indicate the sporadic through holes.

1700 W – 12 bar pressure of nitrogen

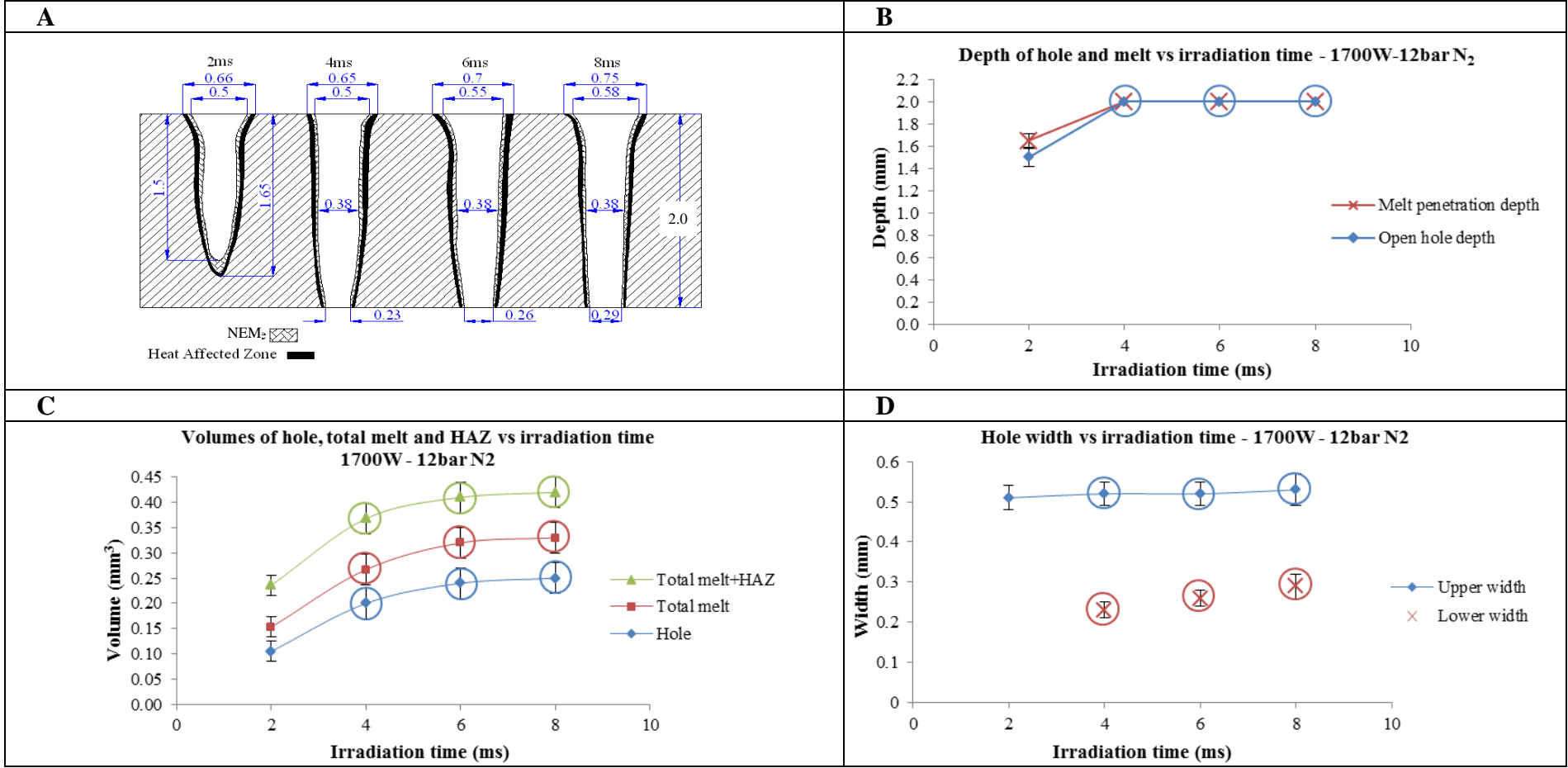


Figure 5.47- Piercing results for 1700 W with 12 bar nitrogen. A) Map of hole growth. B) Depth of hole and melt vs irradiation time. C) Volume of hole, melt total and HAZ vs irradiation time. D) Width of hole vs irradiation time. Solid circles indicate the through holes.

2000 W – 12 bar pressure of nitrogen

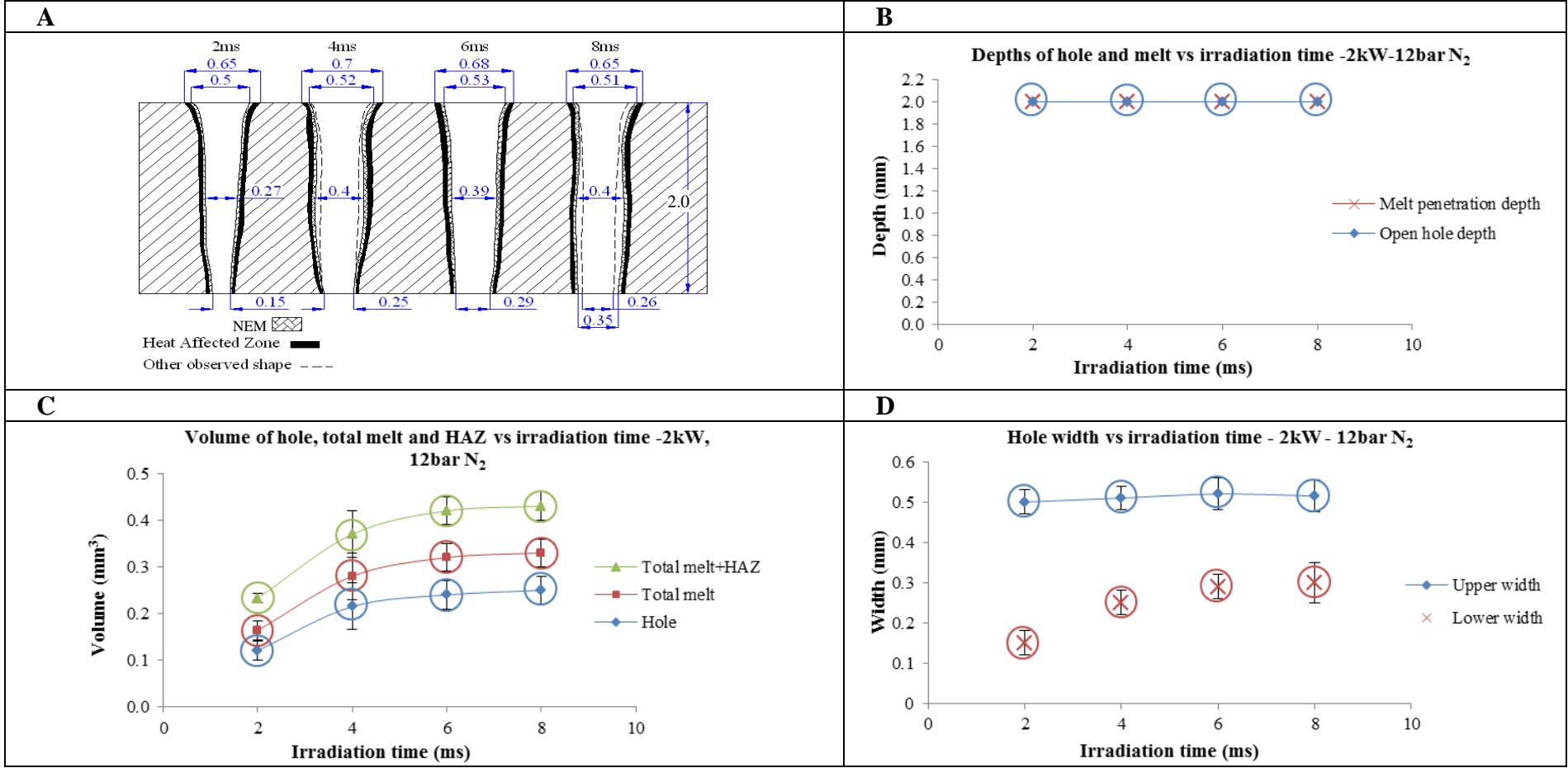


Figure 5.48- Piercing results for 2000 W with 12 bar nitrogen. A) Map of hole growth. B) Depth of hole and melt versus irradiation time. C) Volume of hole, melt total and HAZ versus irradiation time. D) Width of hole versus irradiation time. Solid circles indicate the through holes.

The results of hole and melt growth in piercing with different powers of 1400 W to 2000 W and a variety of nitrogen pressure from 2 bar to 12 bar, are illustrated in Figure 5.38 to Figure 5.48 as the irradiation time increases. Qualitatively, the hole shape has been changed with decrease in the hole taper and becomes cylindrical as the irradiation time increases (Figure 5.38-A to Figure 5.48-A). Overall, the OHD and MPD are enlarged with increasing irradiation time until they reach the thickness of sheet (Figure 5.38-B to Figure 5.48-B). Penetration is sporadic before it becomes established except when piercing with a combination of sufficient power and pressure e.g. 2000 W- 4 bar. Table 5.11 presents the percentage of through hole appearance at breakthrough time.

Table 5.11- Percentage of through hole appearance for variety of nitrogen pressure at different irradiation times and powers.

Pressure	1400 W			1700 W		2000 W		
2 bar	-			6 ms	8 ms	2 ms	4 ms	6 ms
	-			60%	100%	60%	80%	100%
4 bar	4 ms	6 ms	8 ms	4 ms	6 ms	2 ms		
	40%	60%	100%	60%	100%	100%		
8 bar	4 ms	6 ms	8 ms	4 ms		2 ms		
	40%	80%	100%	100%		100%		
12 bar	4 ms	6 ms	8 ms	4 ms		2 ms		
	40%	80%	100%	100%		100%		

In general, the volumes of hole and melt total increase with irradiation time until breakthrough occurs then they become constant just with a slight increase (Figure 5.38-C to Figure 5.48-C). Regarding the hole diameter, overall, the upper hole diameter initially increases with irradiation time until breakthrough happens then it becomes almost constant just with a slight variation (Figure 5.38-D to Figure 5.48-D). The lower width gradually increases with irradiation time and then just with a slight increase it becomes constant.

5.12.5 Comparison of results

- Breakthrough time decreases with increasing power and pressure as presented in Table 5.12.

Table 5.12- Breakthrough time for different nitrogen pressure with different powers.

Pressure	1400 W	1700 W	2000 W
2 bar	-	6-8 ms	4-6 ms
4 bar	6-8 ms	4-6 ms	< 2 ms
8 bar	4-6 ms	4 ms	< 2 ms
12 bar	4-6 ms	4 ms	< 2 ms

- In general, the hole and melt volumes at breakthrough slightly decrease with increasing power as indicated in Table 5.13.
- The hole and melt volumes at breakthrough slightly decrease with increasing pressure as presented in Table 5.13.

Table 5.13- The melt and hole volumes at breakthrough time for different powers and nitrogen pressures.

Pressure		1400 W	1700 W	2000 W
2 bar	Melt	-	0.46 mm ³	0.35 mm ³
	Hole	-	0.36 mm ³	0.28 mm ³
4 bar	Melt	0.37 mm ³	0.33 mm ³	0.3 mm ³
	Hole	0.26 mm ³	0.25 mm ³	0.24 mm ³
8 bar	Melt	0.36 mm ³	0.31 mm ³	0.29 mm ³
	Hole	0.28 mm ³	0.25 mm ³	0.23 mm ³
12 bar	Melt	0.34 mm ³	0.33 mm ³	0.3 mm ³
	Hole	0.27 mm ³	0.25 mm ³	0.24 mm ³

- The upper hole width at breakthrough decreases with increasing power as presented in Table 5.14.
- The upper hole width at breakthrough slightly decreases with increasing pressure as shown in Table 5.14.

Table 5.14- Upper hole width at breakthrough time for different powers.

Pressure	1400 W	1700 W	2000 W
2 bar		0.7 mm	0.56 mm
4 bar	0.62 mm	0.58 mm	0.53 mm
8 bar	0.56 mm	0.53 mm	0.51 mm
12 bar	0.53 mm	0.53 mm	0.51 mm

5.12.6 Discussion of results

5.12.6.1 Breakthrough time decreases as the power and pressure increase:

In Table 5.12, Figure 5.49 and Figure 5.50, the difference in breakthrough between 2 bar and other pressures at the similar power range of 1400 W to 2000 W is meaningful. As the power increases, more energy is input to the melting zone increasing the melt temperature, decreasing the melt viscosity and easing the melt ejection, resulting in increase in penetration and a decreasing breakthrough time. As the pressure is increased, the melt removal effectiveness is increased; hence the laser penetration increases, resulting in quick breakthrough. Although breakthrough time can be decreased by increasing power or pressure or both, diminishing returns can be observed which is related to the sheet thickness. This means that for a specific thickness, there is a certain limit (highest power and pressure) where beyond that certain limit there is no further effect on the breakthrough time.

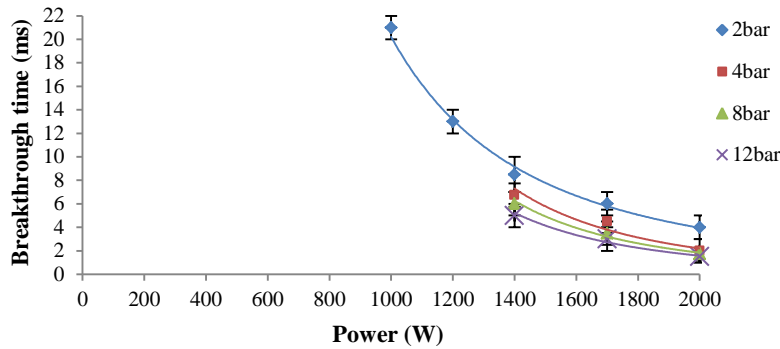


Figure 5.49- Breakthrough time as a function of power and nitrogen pressure.

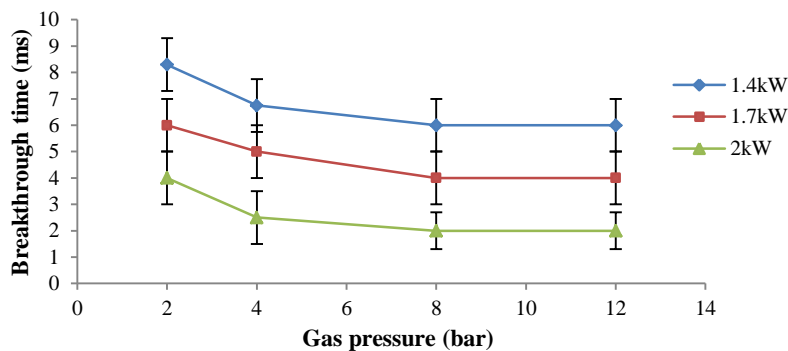


Figure 5.50- Breakthrough time versus nitrogen pressure for different powers.

5.12.6.2 The hole diameter decreases with increasing power and gas pressure:

As the power increases, the breakthrough time decreases. Therefore, there is less time for hole width to widen laterally as a result of heat conduction. Moreover, there is less time for the upward melt ejection to erode the upper hole edge. Thus, the through hole width decreases with increasing power and pressure as presented in Figure 5.51. Although the hole entrance decreases with increasing power or pressure or both, a diminishing returns can be seen at which there is more effective increasing pressure from 2 to 4 bar than from 8 to 12 bar.

5.12.6.3 The hole and melt volumes at breakthrough decrease with increasing power and pressure.

This is because, when the power increases, more energy is input into the piercing zone, so the melt temperature increases, the melt viscosity decreases, the melt ejection effectiveness increases and the breakthrough time decreases as a result of vertical penetration, thus there is less time for melt and hole to grow laterally as a result of laser absorption and heat conduction. As is seen in both graphs, the volumes decrease with increasing pressure. Moreover, the volume of NEM lining the hole

(difference between melt and hole volumes) meaningfully decreases with increasing power and pressure. This is because, with increase in the power the temperature of melt increases and it is more likely that the viscosity of melt decreases. Lower viscosity will also enhance melt ejection efficiency. Figure 5.52 and Figure 5.53 show how the volumes at breakthrough decrease with power and pressure.

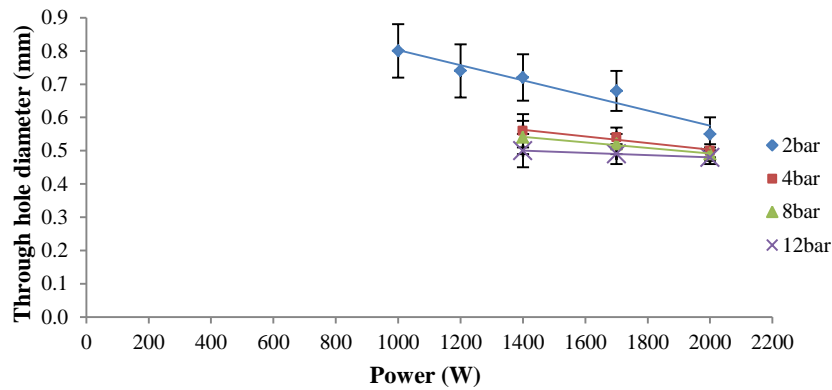


Figure 5.51- Showing the upper diameter of the through hole versus power intensity for variety of nitrogen pressure.

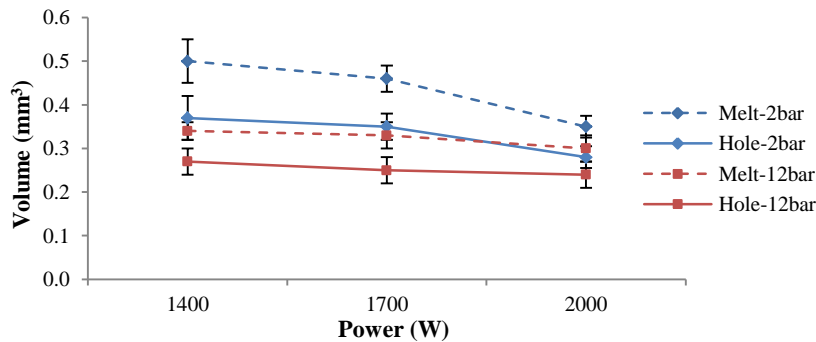


Figure 5.52- The volumes of melt and hole (at breakthrough) vs power for nitrogen pressures.

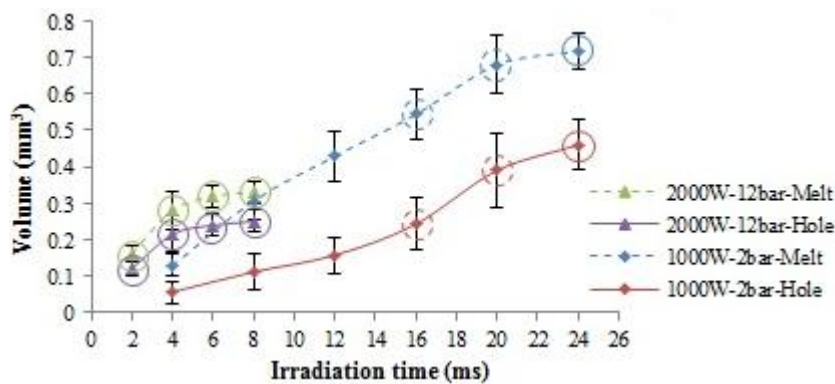


Figure 5.53- The melt and hole volumes versus irradiation time for a moderate power-pressure (1000 W, 2 bar nitrogen) and a relatively high power-pressure nitrogen piercing (2000 W, 12 bar). Circles show through holes. Dash circles show sporadic penetration.

5.13 High power piercing with moderate and high pressure of oxygen

5.13.1 With 2 bar pressure of oxygen

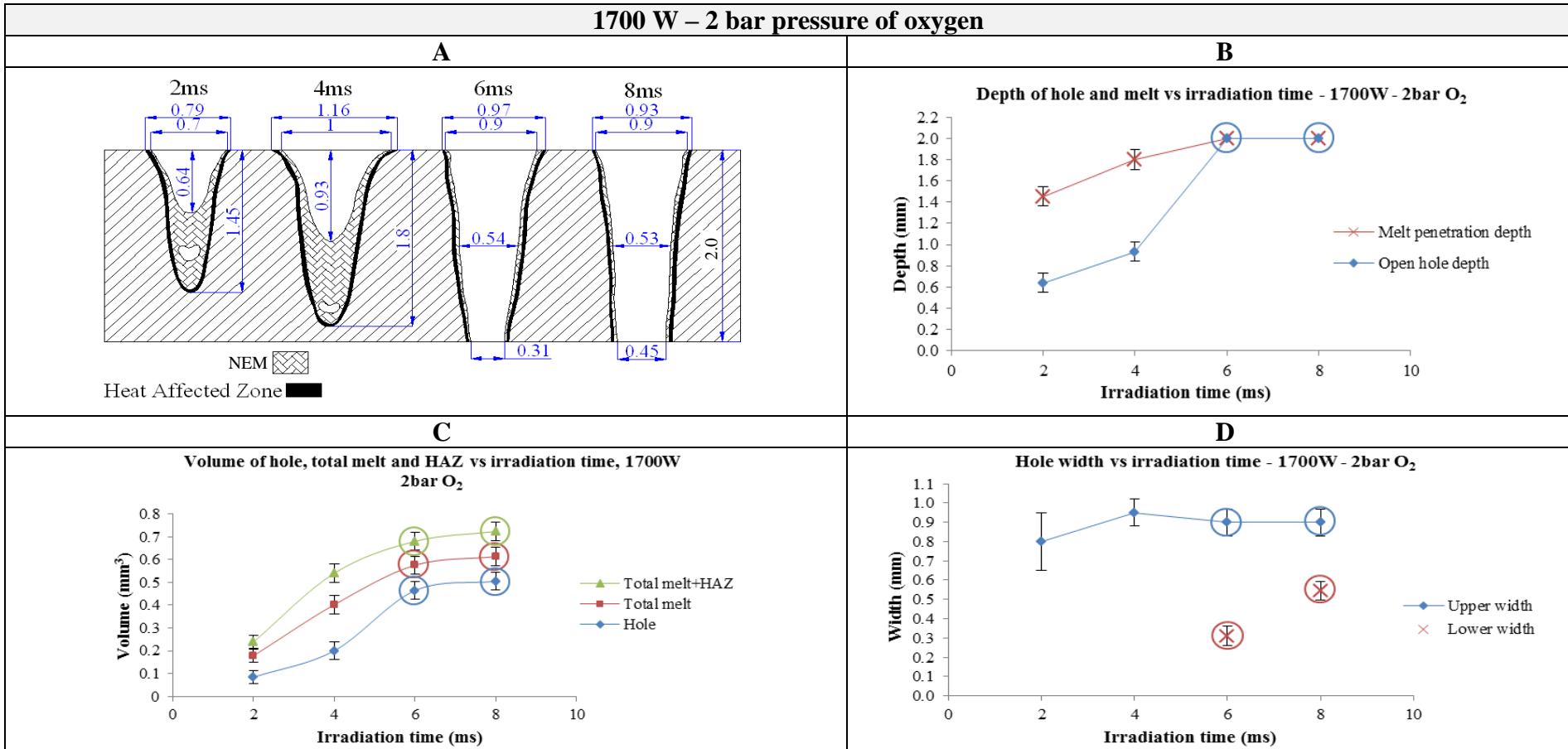


Figure 5.54- Piercing results for 1700 W with 2 bar oxygen. A) Map of hole growth. B) Depth of hole and melt versus irradiation time. C) Volume of hole, melt total and HAZ versus irradiation time. D) Width of hole versus irradiation time. Solid circles indicate the through holes.

2000 W – 2 bar pressure of oxygen

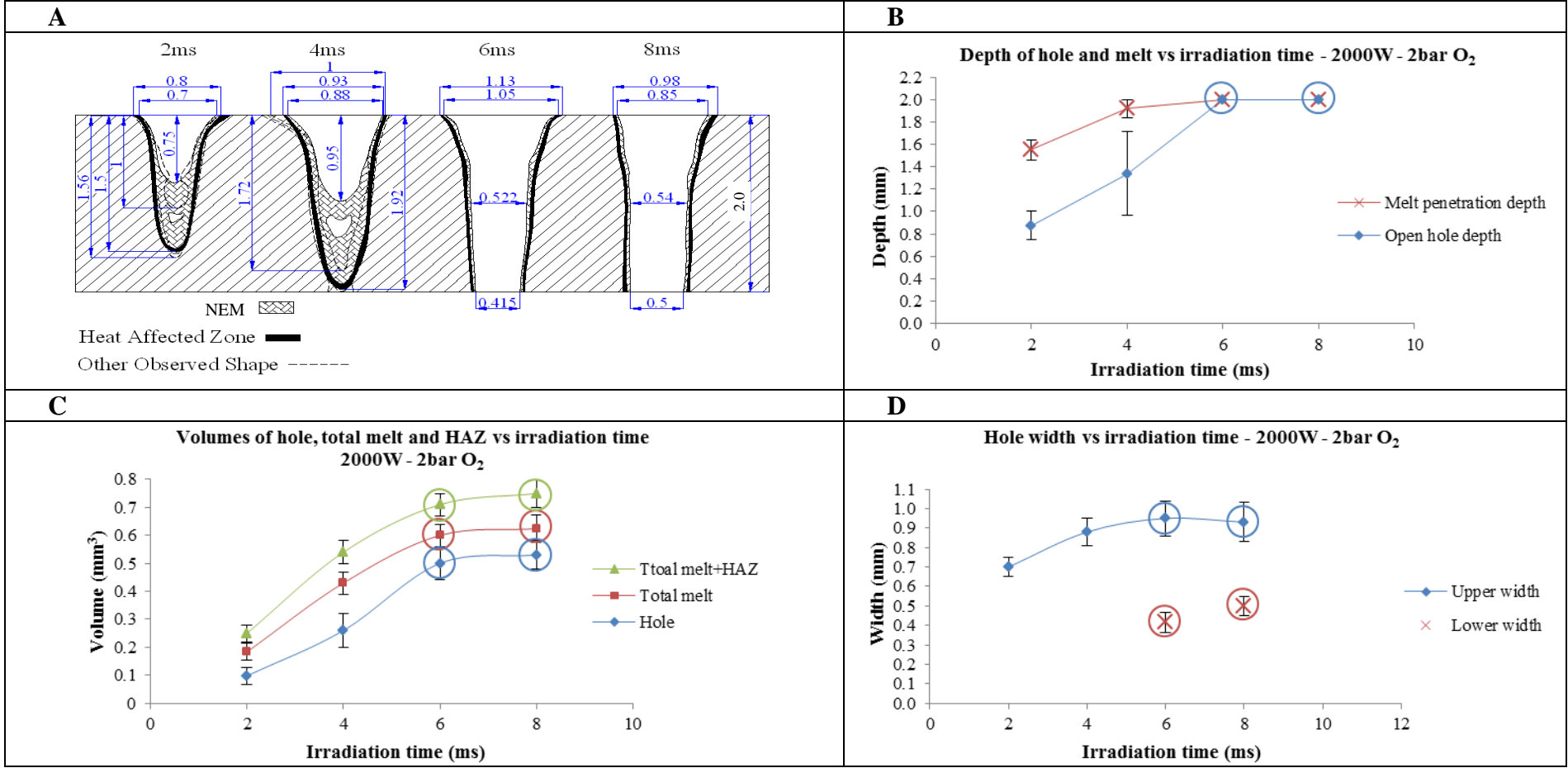


Figure 5.55- Piercing results for 2000 W with 2 bar oxygen. A) Map of hole growth. B) Depth of hole and melt versus irradiation time. C) Volume of hole, melt total and HAZ versus irradiation time. D) Width of hole versus irradiation time. Solid circles indicate the through holes.

5.13.2 With 4 bar oxygen pressure

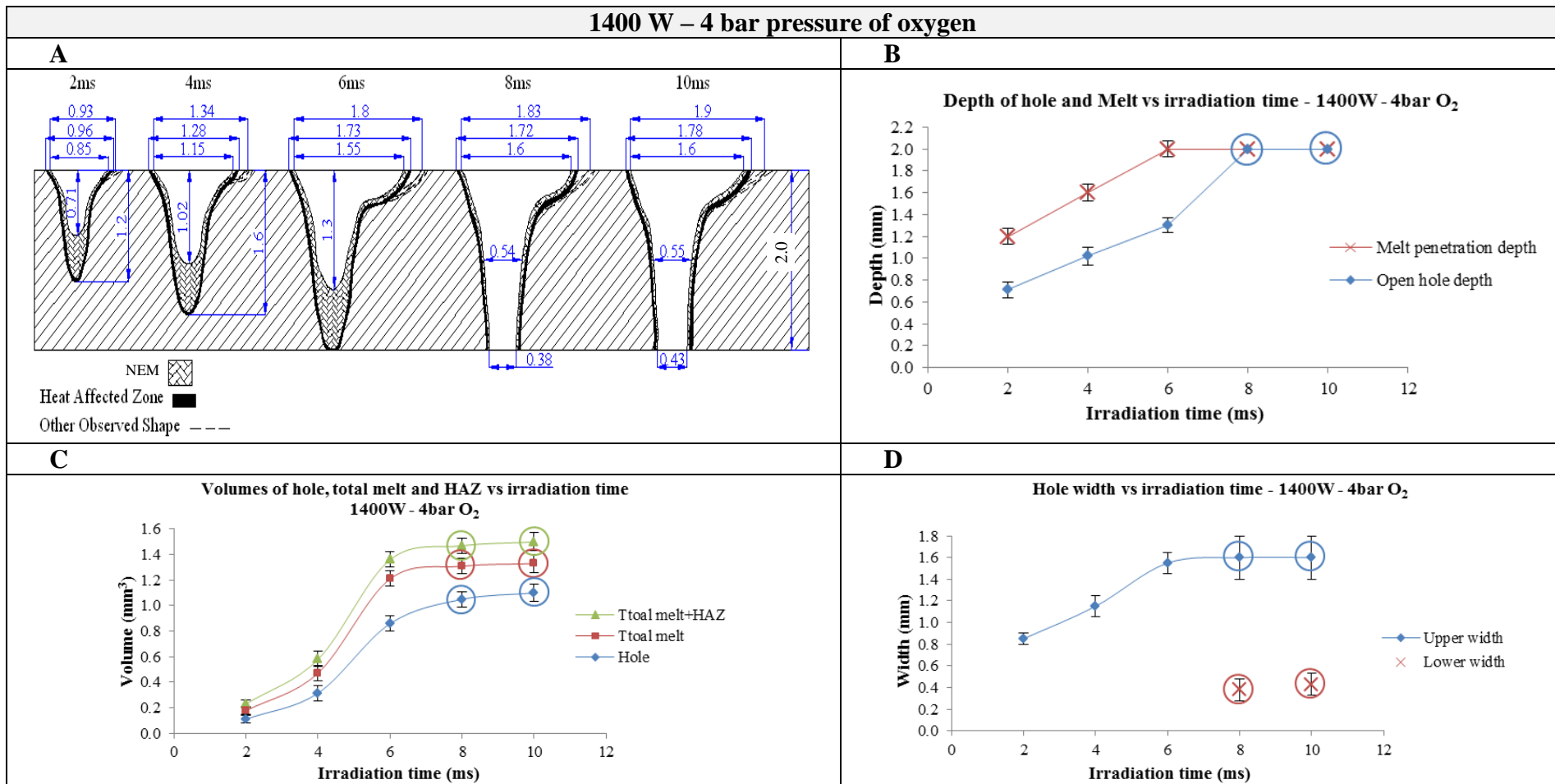


Figure 5.56- Piercing results for 1400 W with 4 bar oxygen. A) Map of hole growth. B) Depth of hole and melt versus irradiation time. C) Volume of hole, melt total and HAZ versus irradiation time. D) Width of hole versus irradiation time. Solid circles indicate the through holes.

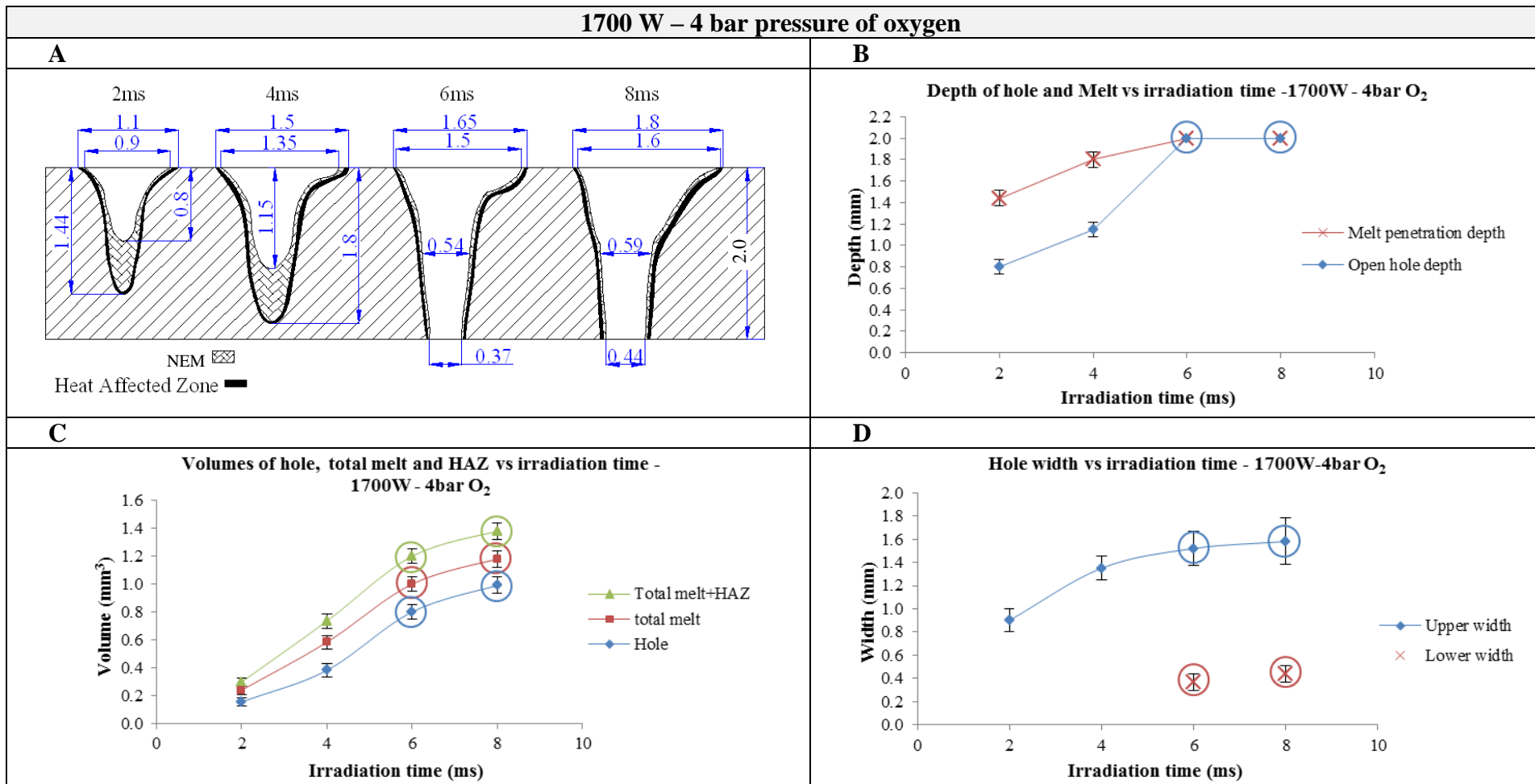


Figure 5.57- Piercing results for 1700 W with 4 bar oxygen. A) Map of hole growth. B) Depth of hole and melt versus irradiation time. C) Volume of hole, melt total and HAZ versus irradiation time. D) Width of hole versus irradiation time. Solid circles indicate the through holes.

2000W – 4 bar pressure of oxygen

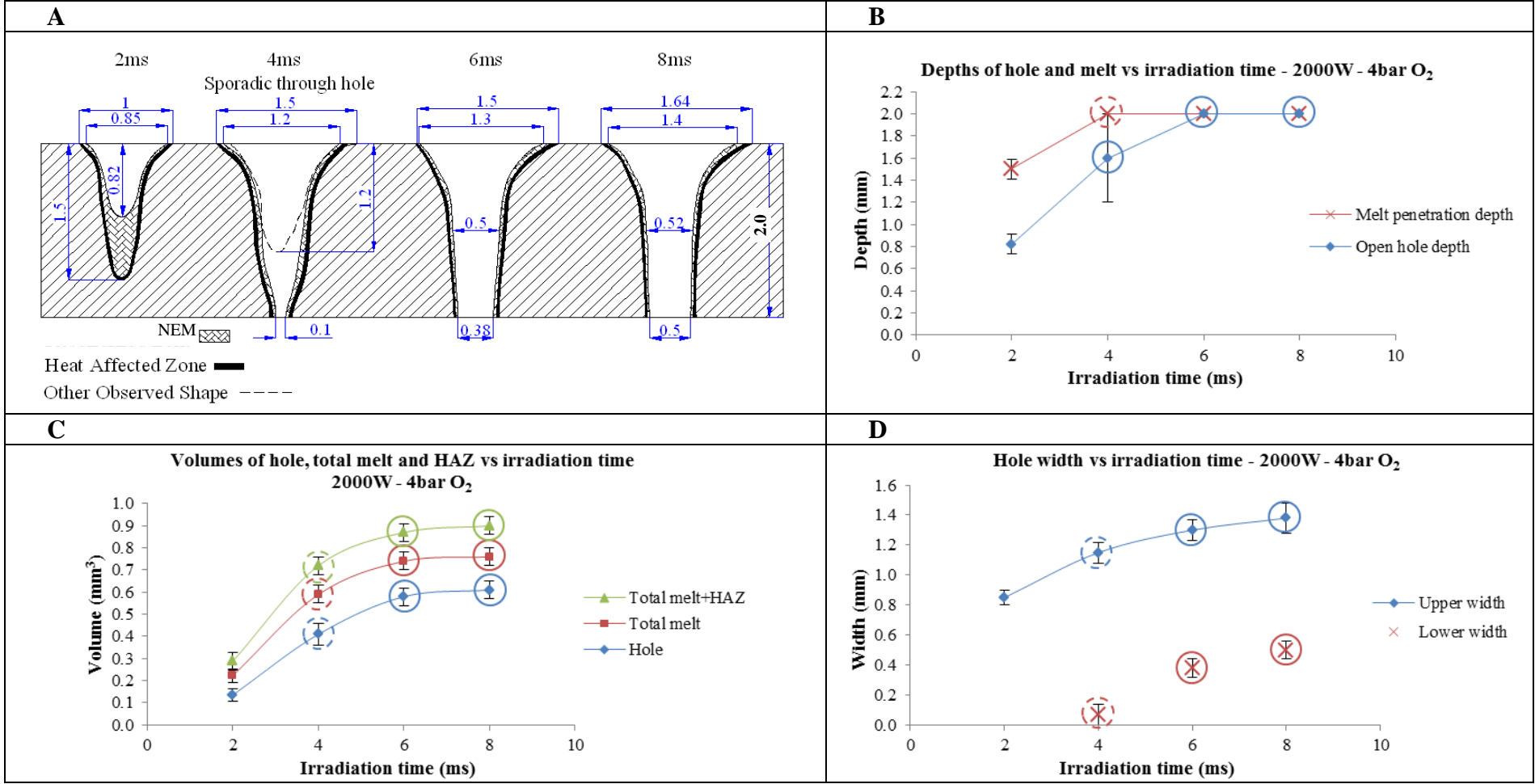


Figure 5.58- Piercing results for 2000 W with 4 bar oxygen. A) Map of hole growth. B) Depth of hole and melt versus irradiation time. C) Volume of hole, melt total and HAZ versus irradiation time. D) Width of hole versus irradiation time. Solid circles indicate the through holes. Dash circles indicate the sporadic through holes.

5.13.3 With 8 bar oxygen pressure

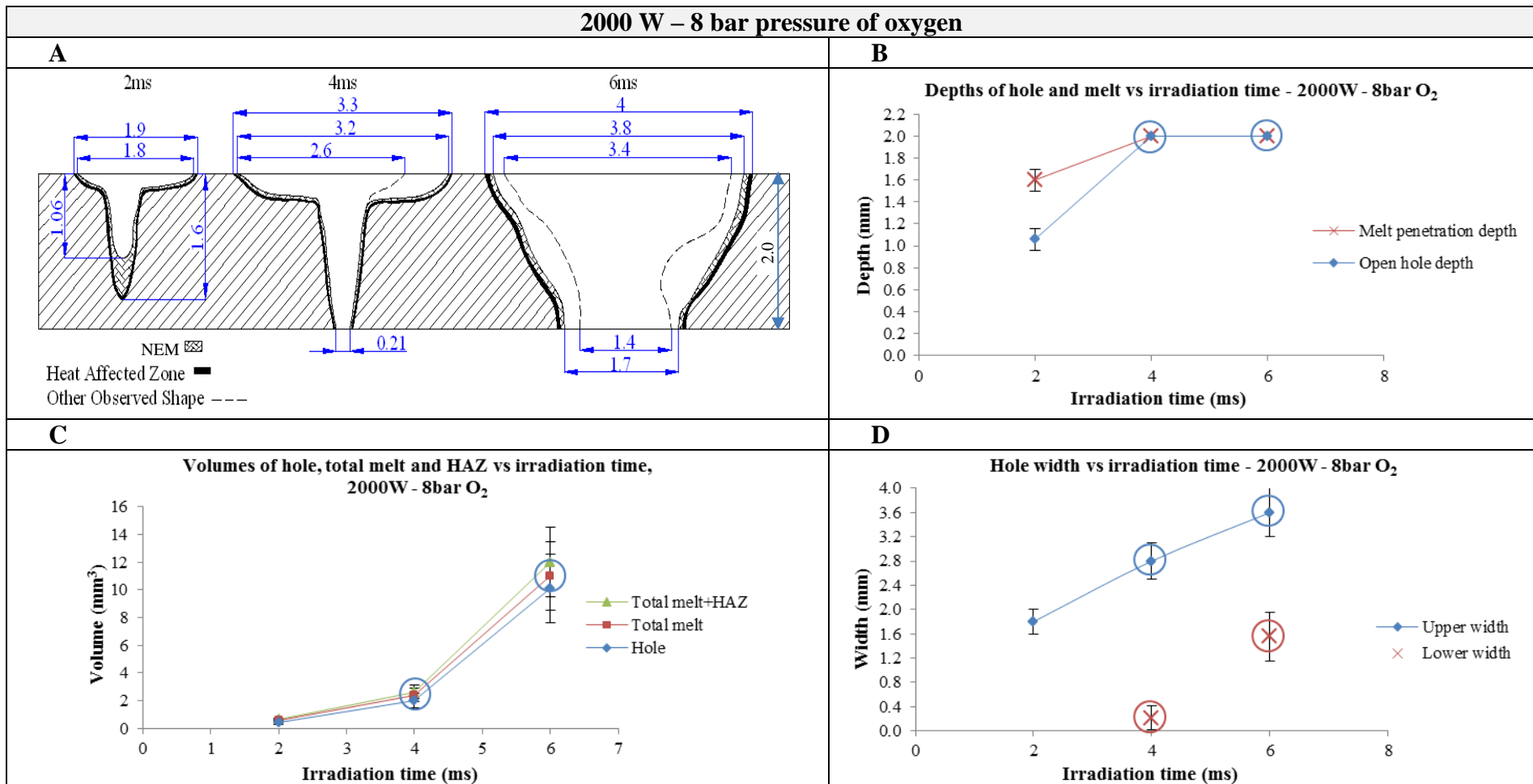


Figure 5.59- Piercing results for 2000 W with 8 bar oxygen. A) Map of hole growth. B) Depth of hole and melt versus irradiation time. C) Volume of hole, melt total and HAZ versus irradiation time. D) Width of hole versus irradiation time. Solid circles indicate the through holes.

The results of piercing for different powers of 1400 W to 2000 W using a variety of oxygen pressures from 2 bar to 8 bar with increasing irradiation time have been presented in Figure 5.54 to Figure 5.59. In most case, the depths of melt and hole extend with irradiation time until breakthrough happens (Figure 5.54-B to Figure 5.59-B). In general, the volumes of melt total and hole enlarge with irradiation time until breakthrough occurs, then they remain steady (Figure 5.54-C to Figure 5.59-C). Generally, upper width slightly widens as the irradiation time increases, with a variation, however at breakthrough it tends to become constant (Figure 5.54-D to Figure 5.59-D). At breakthrough, the lower diameter increases with further irradiation time decreasing the hole taper. Here, it must be mentioned that during piercing with 8 bar of oxygen pressure it was observed that due to a huge oxidation burning, fiery particles were thrown out of the piercing zone in all directions with a risk of burning which could destroy the nozzle. Piercing with 8 bar pressure of oxygen made a hole with a coarse shape and very large hole diameter.

5.13.4 Comparison of the results

In order to better compare the effect of power on 2 bar oxygen piercing, the results of piercing with 1400W have been added to this section.

- The breakthrough time decreases with increasing power as presented in Table 5.15.

Table 5.15- Breakthrough time for different powers and oxygen pressures.

Pressure	1400 W	1700 W	2000 W
2 bar	8 ms	6 ms	6 ms
4 bar	8 ms	6 ms	4-6 ms
8 bar	6-8 ms	4-6 ms	4 ms

- The hole and melt volumes at breakthrough decrease with increasing power as presented in Table 5.16.
- The volumes enlarge with increase in the gas pressure as indicated in Table 5.16.

Table 5.16- Melt and hole volumes at breakthrough and afterwards for different powers and oxygen pressures.

Pressure		1400 W	1700 W	2000 W
2 bar	Melt	0.62 mm ³	0.6mm ³	0.58mm ³
	Hole	0.54mm ³	0.49mm ³	0.51mm ³
4 bar	Melt	1.3mm ³	1.2 mm ³	0.78mm ³
	Hole	1.1mm ³	1.0mm ³	0.60mm ³
8 bar	Melt	-	-	2-15 mm ³
	Hole	-	-	2-15 mm ³

- Overall, the hole width at breakthrough slightly decreases with increasing power as presented in Table 5.17.
- With the same power the hole width widens with increase in the oxygen pressure.

Table 5.17- Upper hole width at breakthrough time for different powers and oxygen pressures

Pressure	1400 W	1700 W	2000 W
2 bar	0.8-0.9 mm	0.9 mm	0.85-1 mm
4 bar	1.6 mm	1.55 mm	1.35 mm
8 bar	3-4.5 mm	2.8-4 mm	2.5-3.8 mm

5.13.5 Discussion of results

5.13.5.1 Breakthrough time decreases with increasing power.

When the power is increased, the applied heat to the melting zone is increased. As a result of heat conduction, the melt vertically penetrates the thickness of sheet more quickly thus the breakthrough time decreases (Figure 5.60).

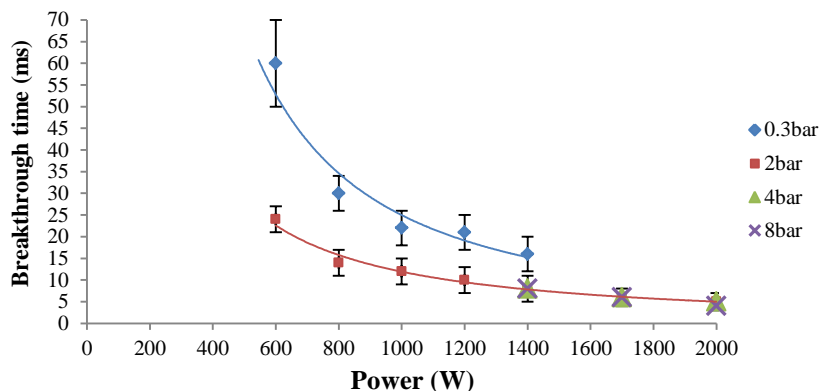


Figure 5.60- Breakthrough time as a function of power for variety of oxygen pressures.

5.13.5.2 Breakthrough time decreases with increasing oxygen pressure.

When the gas pressure is increased from 0.3 bar to 2 bar, the melt is removed more efficiently and hence the breakthrough time significantly decreases (Figure 5.60). In high power piercing (e.g. from 1400 W forwards), the breakthrough time slightly decreases with increasing oxygen pressure (Figure 5.61). A comparison between Figure 5.60 and Figure 5.61 implies that there is no further benefit in breakthrough time beyond 2 bar showing that 2 bar oxygen can eject melt as fast as it is generated. Moreover, power is more effective at decreasing breakthrough time.

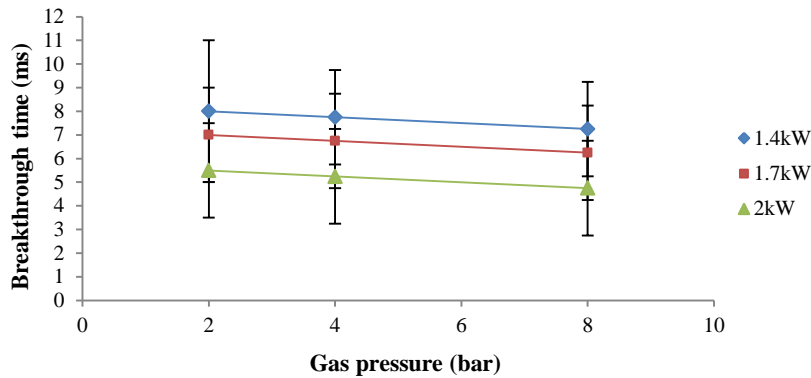


Figure 5.61- Pierce breakthrough times for variety of oxygen pressure and laser powers.

5.13.5.3 Overall, the hole diameter decreases with increasing power:

As presented in Figure 5.62, when the power is increased, the breakthrough time slightly decreases. Thus, there is less time for the hole to grow laterally as a result of heat conduction. Furthermore, when the breakthrough happens, the erosion of upper hole edge is stopped as a result of the change in the melt removal direction from the upward melt ejection to the downward melt ejection.

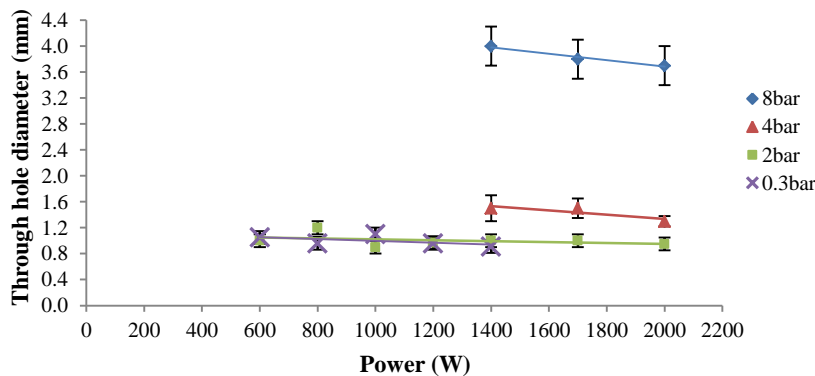


Figure 5.62- Upper pierce hole diameter for oxygen at a range of powers and gas pressures.

5.13.5.4 The hole diameter increases with increasing gas pressure.

When the oxygen pressure is increased, the rate of exothermic reaction between oxygen and melt increases thus, significant heat is yielded in the piercing zone enhancing the melting and hole diameter (Figure 5.62).

The reason why the hole shape gets worse with increase in the oxygen pressure might be related to the oxidation burning. During laser melting of mild steel the exothermic oxidation reaction between iron and oxygen to FeO inputs a large amount

of heat into the melting zone [9]. The thermal energy evolved by oxidation reaction is approximately 250 kJmol^{-1} . When the oxygen pressure is increased, the boiling point of Fe and dissociation temperature of FeO increases, however, the amount of heat evolved by oxidation reaction per mole (ΔH) is not affected [9]. When the oxygen pressure increases, a further mole of oxygen is added to the melting zone hence the oxidation energy released to the melting zone considerably increases resulting in a sudden melt extension and an increase in the melt temperature. Figure 5.63 indicates that when the oxygen pressure increases from 2 bar to 4 bar, the volumes of hole and melt increase. Moreover, FeO in the iron melt decreases the melt viscosity [9, 89], and as the temperature of the melt increases the viscosity of melt is further decreased resulting in an easy melt expulsion [9, 89]. Thus, the high pressure of oxygen easily ejects this very low viscosity hot melt from the melting zone resulting in a heavy fiery melt expulsion. It is found that piercing using a high pressure of oxygen (e.g. 8 bar) involves an uncontrollable melting zone therefore a big hole with a random shape and large entrance is achieved, resulting in the lowest quality of piercing (Figure 5.59-A and Figure 5.62). As the power increases, the MPD increases and so the breakthrough occurs at a shorter irradiation time. For example in 4 bar pressure, breakthrough with 2000 W happens at 4-6 ms while with 1400 W it occurs at 8 ms (Figure 5.60 and Figure 5.61). A comparison of 2 bar and 4 bar oxygen pressure using 2000 W laser power in terms of melt and hole volumes is presented in Figure 5.63. As is seen, the volumes of hole and melt increase when the gas pressure increases. Furthermore, the NEM (difference between hole and melt) increases as the oxygen pressure increases.

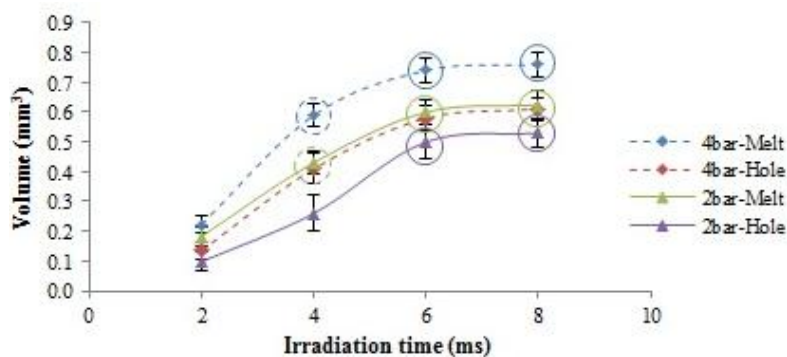


Figure 5.63- The volume of the melted zone and the hole volume versus irradiation time for two oxygen pressures at the power of 2000 W. Circles show through holes. Dash circles show sporadic penetration.

As is seen in Figure 5.64, the volumes of melt and hole at breakthrough using 1000 W are larger than those for 2000 W. Moreover, the NEM lining the surface of hole for 1000 W is larger than that for 2000 W.

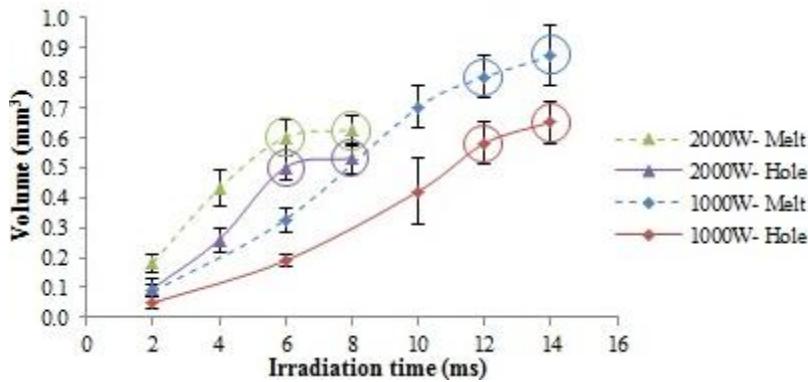


Figure 5.64- The volumes of melt and hole versus irradiation time when piercing with 2 bar oxygen pressure with powers of 1000 W and 2000 W. Circles show through holes.

To summarise in this section, the exothermic oxidation reaction between melt iron and oxygen affects the melt, adds FeO to the melt and decreases the viscosity of melt [9]. In laser piercing with oxygen, the additional energy and also the reduction of melt viscosity obviously affects the hole generation and causes some advantages and disadvantages. Due to the extra energy, melting of the material occurs rapidly and penetration of the laser to the sheet is accelerated hence breakthrough happens at shorter irradiation time. Moreover due to the low viscosity of melt, the melt ejection effectiveness enhances and this helps the laser beam penetrate the sheet quickly. However, the hole is not symmetrical and severe erosion at the upper edge of the pierced hole brings about a wide hole.

5.14 Hole characteristics

With regard to the characteristics of the holes pierced by oxygen and nitrogen, the EDS observation of the holes pierced at 100 W and 50 ms is presented. The line scan EDS of a hole pierced by oxygen confirmed the presence of a relatively thick oxide layer on the edge and inside the hole (Figure 5.65 and Figure 5.66).

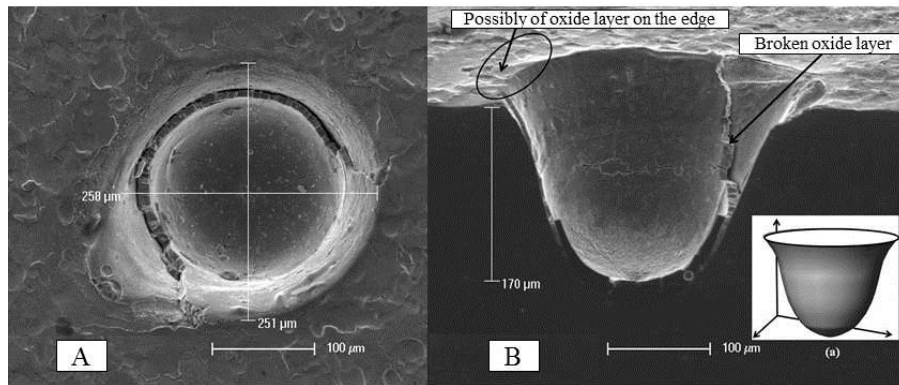


Figure 5.65- Indicating a hole accompanied by an oxide layer which is pierced by 100 W fibre laser-oxygen at 50 ms. Cross section of the hole is shown in B. The Gaussian curve to compare with the shape of the hole is shown.

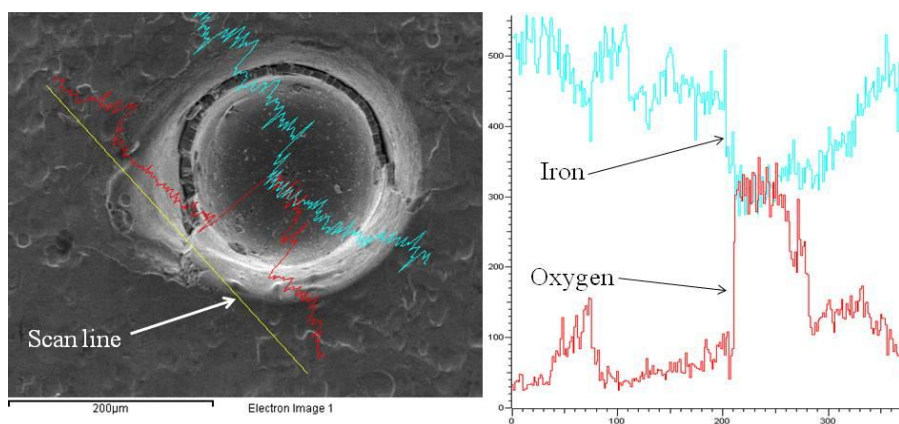


Figure 5.66- Showing the line scan EDS results at the edge of hole.

Micrograph of the hole pierced by nitrogen (Figure 5.67) showed that the hole is excluded from the oxide layer which could be seen in the hole produced by oxygen (compare with Figure 5.65-A). EDS examination qualitatively indicates that the amount of oxygen on the spatter near the hole edge is not significant in comparison with oxygen hole.

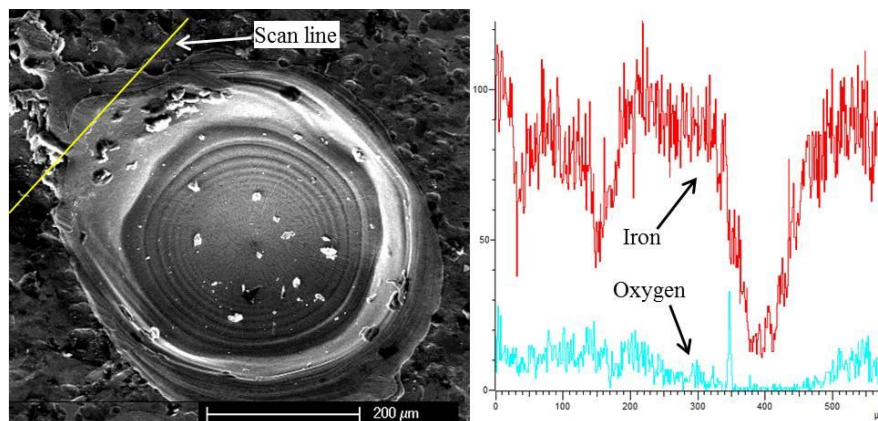


Figure 5.67- Showing a hole pierced by nitrogen with the EDS examination at the edge of the hole.

5.15 Summary of piercing results

The results of an experimental study on the CW fibre laser piercing of 2 mm-thick mild steel sheet with using oxygen and nitrogen as assist gases and different pressures from 0.3 bar to 12 bar at a variety of laser powers from 600 W to 2000 W were presented. The map of hole growth, hole dimensions, melt and hole volumes as a function of irradiation time were shown for a variety of piercing conditions. The results were studied in low, moderate and high power-pressure and then compared in terms of power, gas type and pressure. Some important results are presented as below.

According to our results, a brief comparison between oxygen and nitrogen regarding the effect of gas type and pressure on the melting zone has been gathered in Table 5.18. Some results are consistent with the literature given as the references.

Table 5.18- Showing a brief comparison between oxygen and nitrogen as assist gas.

Gas	Characteristics
2 bar O ₂	<ul style="list-style-type: none"> • Mechanical ability to eject molten material from the melting zone [1, 89]. • Exothermic oxidation reaction with molten iron adding more heat to the melting zone [9, 87]. • Change in melt component (Fe + FeO), might affect beam reflection [52, 87]. • Decrease in melt viscosity, ease melt ejection [89].
0.3 bar O ₂	<ul style="list-style-type: none"> • Limited mechanical ability to eject the melt, but hole was formed. So maybe it has a little effect or maybe there is another phenomenon. • Exothermic oxidation reaction with molten iron adding more heat to the melting zone [1, 89]. • Change in melt component (Fe + FeO), might affect beam reflection [52, 87]. • Decrease in melt viscosity, ease melt ejection [89].
2 bar N ₂	<ul style="list-style-type: none"> • Mechanical ability to expel molten material from the melting zone [1, 89, 119]. • No reaction with molten iron [1, 89, 119].
0.3 bar N ₂	<ul style="list-style-type: none"> • Limited mechanical ability to eject molten material, but hole was formed. So maybe it has a little effect or maybe there is another phenomenon. • No reaction with molten iron [89].

5.15.1 General results

- 1- The depths of hole and melt increase with irradiation time until breakthrough occurs.
- 2- The volumes of hole and melt gradually increases with irradiation time until breakthrough happens then they almost become constant just with a variation.
- 3- The upper hole width increases as the irradiation time increases until breakthrough occurs then it becomes almost constant.
- 4- The HAZ is usually observed around the NEM. The HAZ volume follows the melt volume.

- 5- Holes pierced by oxygen are considerably wider than those produced by nitrogen.
- 6- Efficient melt removal requires sufficient laser power and sufficient assist gas pressure.
- 7- When piercing with low gas pressure (e.g. 0.3 bar), in nitrogen piercing the melt is ejected by the melt surface vaporisation pressure but in oxygen piercing the gas pressure is still capable to remove the low viscosity melt.
- 8- Continued irradiation after initial piercing for a limited time can decrease the hole taper modifying the final hole shape.
- 9- A relatively thick oxide layer can be observed inside the hole pierced by oxygen whereas this feature cannot be observed in the hole pierced by nitrogen.

5.15.2 Nitrogen piercing results

- 1- When piercing with 2 to 12 bar, the breakthrough time decreases with increasing power but it increases with power when piercing with 0.3 bar.
- 2- With the same power, the breakthrough time significantly decreases when the pressure increases from 0.3 to 4 bar. Further increase in the gas pressure does not have significant effect in the breakthrough time reduction.
- 3- Piercing time reduces with increasing gas pressure up to a certain threshold (approximately 6 bar in this case). Above this threshold pressure the piercing time is unaffected by further increases in pressure.
- 4- When piercing with 2 to 12 bar, the hole and melt volumes at breakthrough decrease with increasing power while in piercing with 0.3 bar the volumes overall increase with power.
- 5- With the same power, overall, the hole and melt volumes at breakthrough decrease as the pressure increases from 0.3 to 12 bar.
- 6- With the same power at breakthrough the gap between hole and melt volumes (the NEM volume) decreases as the pressure increases.
- 7- When piercing with 2 to 12 bar, overall, the upper hole width at breakthrough decreases with increasing power while at 0.3 bar there is a variation in the hole width with increasing power.

- 8- Generally, with the same power the upper hole width at breakthrough slightly decreases with increasing pressure.

5.15.3 Oxygen piercing results

- 1- Overall, the breakthrough time decreases with increasing power.
- 2- With the same power, the breakthrough time decreases significantly when the gas pressure increases from 0.3 to 2 bar. With further increase in the oxygen pressure the breakthrough time slightly decreases.
- 3- Generally, the hole and melt volumes at breakthrough decrease with increasing power.
- 4- With the same power, the volumes of melt, hole and the NEM at breakthrough decrease when the gas pressure increases from 0.3 to 2 bar. With further increase in the oxygen pressure the volumes enlarge.
- 5- Overall, the upper hole width at breakthrough slightly decreases with increasing power.
- 6- In general, the upper hole width at breakthrough widens with increasing oxygen pressure.

5.16 Piercing with nitrogen - cutting with oxygen

At the beginning of this chapter, it was discussed that one of the main problems in oxygen laser cutting is that the width of start-up hole at the beginning of each cut generally exceeds the kerf width and thus this decreases the quality of the cut part edge. The ideal case would be for the diameter of the initial pierced hole to match the kerf width. There would then be no need for the pierced hole to lie off of the final cut line which would result in two benefits:

1. Cut parts could be placed closer together on the sheet, saving material.
2. The cut line from the pierce hole to the required profile would not be necessary, reducing process time.

Now, the aim of this section is to introduce a new invention to decrease the diameter of the initial hole at the beginning of oxygen laser cutting of mild steel.

From the results of piercing experiments it has been derived that the hole diameter in nitrogen piercing is smaller than that is in oxygen piercing. This might be a key to approaching the aim. A look on the kerf width results of the primary cut experiments (chapter 4) can get us closer to the goal. A comparison of through hole diameter and the range of kerf width when using nitrogen assist gas is presented in Figure 5.68. As can be seen, the range of average hole diameter is between 0.48 mm for 12 bar to 0.8 mm for 2 bar while the range of kerf width for nitrogen laser cutting is between 0.3 mm to 0.4 mm.

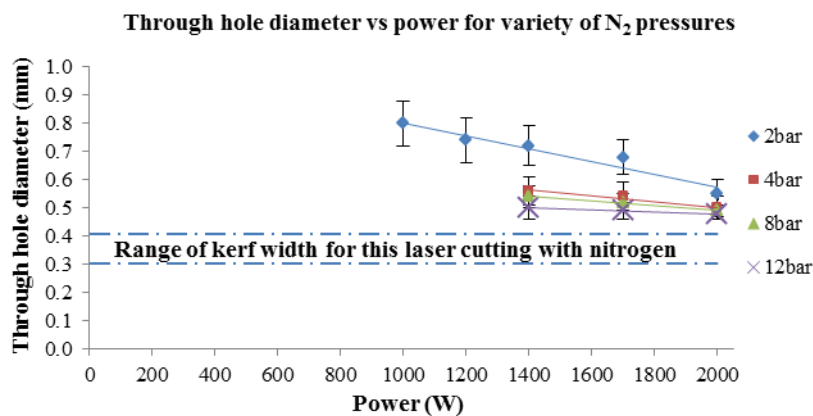


Figure 5.68- Upper pierced hole diameter for nitrogen at a range of powers and gas pressures.

Figure 5.69 indicates a comparison of through hole diameter and the range of kerf width with using oxygen assist gas. The range of upper hole diameter for different gas pressure is between 1 mm to 3 mm while the range of kerf width in oxygen laser cutting is between 0.4 mm to 0.7 mm.

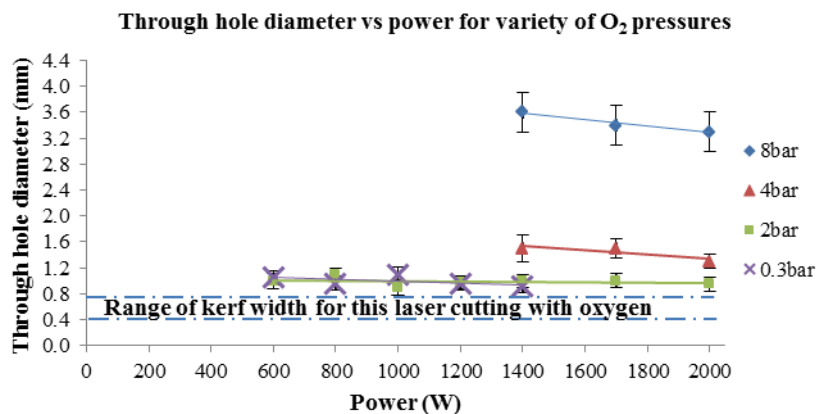


Figure 5.69- Upper pierced hole diameter for oxygen at a range of powers and gas pressures.

The results presented so far indicate that industrially realistic pressures and powers will not allow the pierced hole diameter to be less than the kerf width, so another

approach is needed. Comparison of Figure 5.68 and Figure 5.69 indicates that nitrogen assisted piercing can produce pierce holes that are of the same dimensions as oxygen kerf widths. This comparison briefly presented in Figure 5.70.

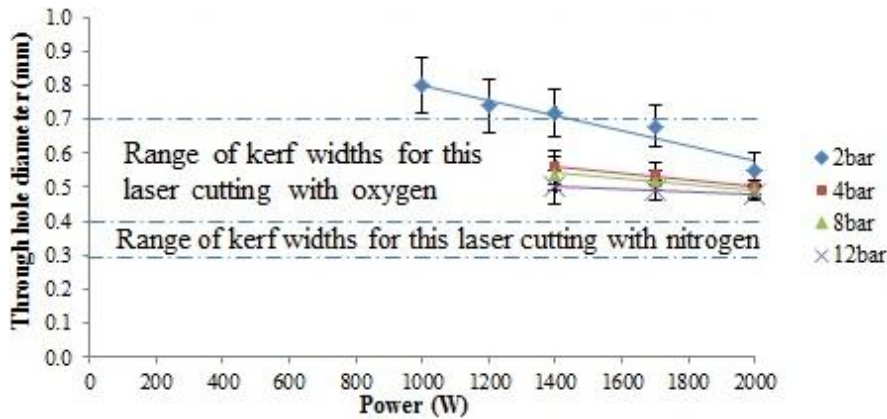


Figure 5.70- Showing that the kerf width in oxygen laser cutting is in the range of nitrogen piercing.

Having confirmed that the hole diameter in nitrogen piercing is in the range of kerf width of oxygen laser cutting, we can now introduce a new method in laser cutting which involves piercing on the cut line with nitrogen and cutting with oxygen. According to this hypothesis, a proof of principle experiment was carried out.

5.16.1 Results

The detail of doing this experiment is properly discussed in chapter 3; however, this is appropriate to briefly remind some important parameters as presented in Table 5.19 with the results of hole and kerf width measurements.

Table 5.19- The parameters of pre-piercing with 3bar pressure of nitrogen and cutting with 2 bar oxygen pressure (2 mm thick mild steel, 200µm spot size, 120mm optical length).

Piercing parameters			Cutting parameters			Dia/kerf
3 bar nitrogen pressure			2 bar oxygen pressure			
Power	Irradiation time	Dia.	Power	Cutting speed	Kerf width	
1200W	24ms	920µm	1000W	4000mm/min	510	1.8
1200W	28ms	800µm	1000W	4000mm/min	500	1.6
1200W	30ms	830µm	1000W	5000mm/min	480	1.7
1200W	32ms	920µm	1000W	6000mm/min	470	1.96
1500W	20ms	760µm	1500W	6000mm/min	750	1.01
1500W	20ms	740µm	1500W	5000mm/min	660	1.12
1500W	20ms	750µm	1500W	4000mm/min	570	1.3

A primary experiment in off axis piercing confirmed that with the employed inclined nozzle the minimum nitrogen pressure to pierce a through hole was 3bar and below

this pressure there was no breakthrough. Moreover, at the power of 1000 W and less there was no through hole. Overall, the breakthrough time increases in comparison with the normal piercing.

Figure 5.71-(A) indicates two holes pierced by an inclined nozzle with 3 bar pressure of nitrogen at power intensity of 1500 W and 20 ms irradiation time.

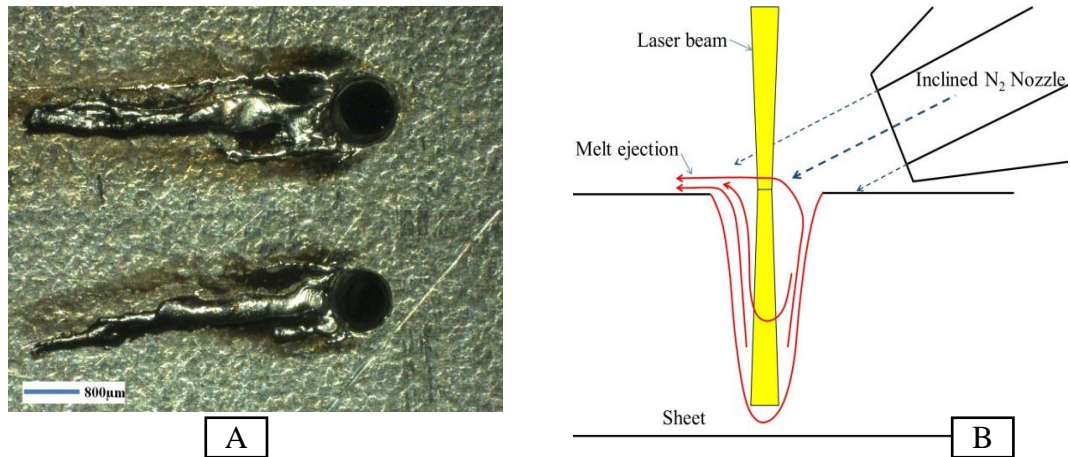


Figure 5.71- A) Showing two holes pierced by inclined nozzle. (3bar pressure of nitrogen, 1500 W, 20 ms). Directional spatter on the sheet is due to inclined nozzle. B) Possibility of decrease in the pressure at the entrance of the hole.

In off axis piercing a long spatter is observed on the sheet which is extended at one side of the hole entrance opposite to the inclined nozzle (Figure 5.71-A). This is due to the inclined nitrogen nozzle which is shown in Figure 5.71-B. The melt layer tends to move from one side of the hole to the other side in front of the inclined nozzle. While the melt is ejecting from the hole, the inclined gas pressure pushes the melt to the opposite side generating a directional spatter on the sheet (Figure 5.72).

The upward melt flow must be due to the pressure gradient inside the hole. An inclined nitrogen jet most likely can decrease the pressure inside the hole.

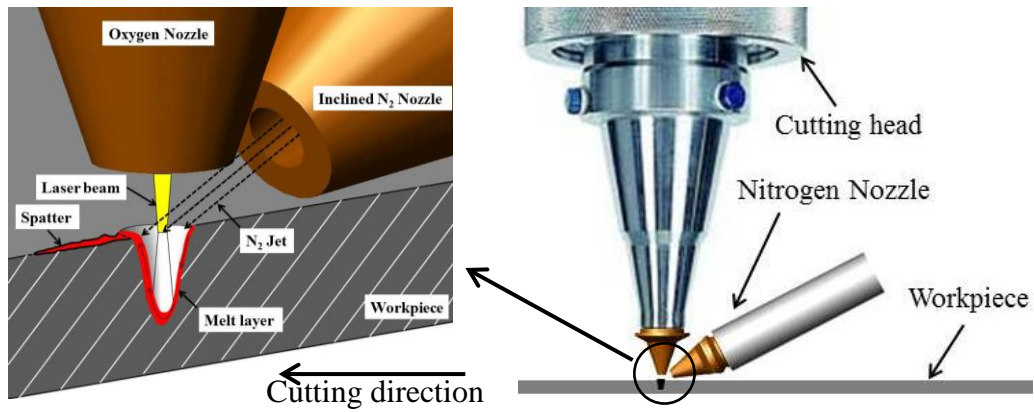


Figure 5.72- Showing off axis piercing with an inclined nitrogen nozzle.

A comparison between common laser-oxygen cutting with the new method is shown in Figure 5.73. As can be seen the start-up hole diameter in the new method (B) is lower than that in common laser cutting (A). Another characteristic of the nitrogen piercing-oxygen cutting is related to the difference in the oxidation mark on the surface of sheet. As is seen in Figure 5.73 nitrogen has not affected the surface around the start-up hole while a dark area can be observed in both sides of oxygen cut kerf.

Figure 5.73 (B) shows a cut which was produced by the new method.

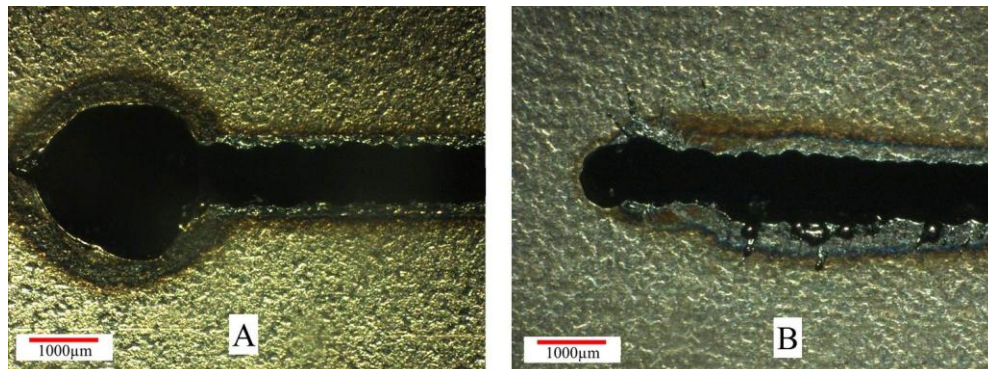


Figure 5.73- (A) Common laser-oxygen cutting (1500 W-6000 mm/min, 2 bar oxygen). (B) Nitrogen piercing-oxygen cutting method (Piercing parameters: 1500 W, 20 ms, 3 bar nitrogen and cutting parameters: 1500 W, 6000 mm/min, 2 bar oxygen).

As can be seen the start-up hole is well matched to the kerf width. Some variation is observed on the kerf's edges at the beginning of each cut where the kerf looks coarse. This is due to the acceleration of the CNC table and also the lack of steady state conditions. This shape of primary formation of the kerf is most likely related to the uncontrolled melting by cyclic oxidation burning which brings about an unsteady

state cutting [88]. The discrepancy between the laser velocity and cyclic oxidation burning rate might raise the unsteady laser cutting condition. At the middle of the cut path the cutting speed is constant and a steady state cutting dominates. Subsequently, the rough edges of the kerf disappear and a fine kerf with a narrower width (compared to the beginning part of cut) is achieved.

Another benefit of nitrogen piercing-oxygen cutting is that the spatter of piercing will be removed by laser cutting if the setup is as shown in Figure 5.72.

In order to directly compare the initial hole diameter and kerf width, a hole with off-axis nitrogen was pierced at the middle of the cut path before cutting as presented Figure 5.74.

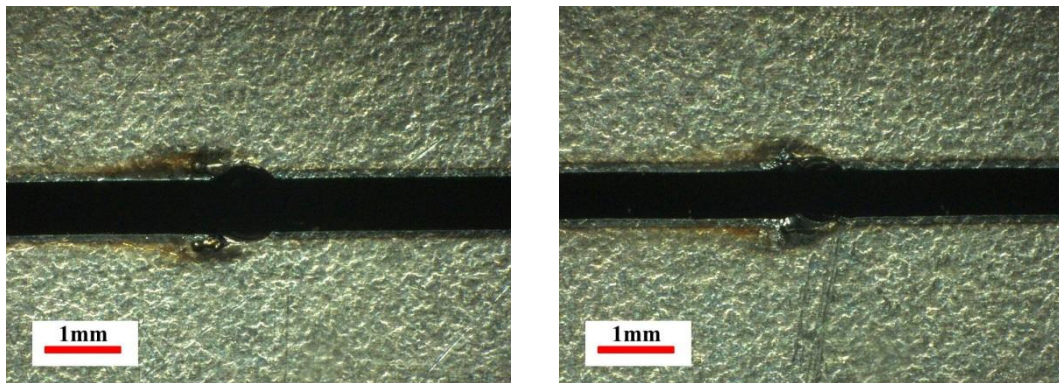


Figure 5.74- A hole with nitrogen was pierced at the middle of cut path before cutting by oxygen. (Left: piercing at 1500 W, 20 ms and cutting at 1500 W, 6000 mm/min – Right: piercing at 1500 W, 20 ms and cutting at 1500 W, 5000 mm/min.

As is seen in Figure 5.74, the off axis pierced holes have been well matched with the kerf width. Thus disregarding the effect of unsteady state cutting on the kerf formation at the beginning of each cut, it is clear that the use of this type of piercing could allow the piercing hole to lie on the cut line of the finished product. Obviously this use of two gases – nitrogen to pierce, followed by oxygen to cut, would need to be optimised in order to allow rapid pierce times and a lower entrance diameter. However there are many applications where the saving in material could be very worth-while – for example, when cutting interlocking parts with shared cut profiles, or when cutting rings within rings to produce sets of laser cut washers or shims.

6 Specific Point Energy

6.1 Introduction

This chapter presents a study of fibre laser cutting based on a novel experimental research method which was developed by Suder and Williams from Cranfield university to investigate fibre laser welding [11]. The investigation into the effects of laser material interaction parameters on laser welding by Cranfield has indicated that three basic laser material interaction parameters (i.e. power density, interaction time and specific point energy) allow the welding process to be defined regarding the depth of penetration and weld width. The aim of this chapter is to find out if these basic laser parameters can be used in a similar way for laser cutting.

Fibre lasers are very flexible in terms of power, beam diameter, power density and total energy delivered to a sheet, which makes them attractive for many applications such as welding and cutting. The beam diameter has a major influence in this energy flexibility, the importance of which is often underrated. In laser welding, the depth of penetration is a key parameter and laser welders usually need to adjust parameters for the material being welded. The same depth of penetration can be achieved with different combinations of system parameters, such as power and travel speed, which makes the parameter selection complicated. In most experimental research, the penetration depth has been studied based on the system parameters, such as the laser output power and the welding speed. Suder et al. [11] experimentally used a set of laser parameters to uniquely describe the characteristic of the heat source on the sheet. This is a new approach which allows welding to compose different welding systems working at different powers with different optics and different process speeds. They used an 8 kW fibre laser machine with different focussing lenses with focal lengths ranging from 150 to 300 mm to achieve different beam diameters ranging from 0.38 to 0.78 mm on the surface of sheet. A beam profiler was used to identify the beam diameter and focal point position. All welds were sectioned, polished and examined under an optical microscope in order to measure the depth of penetration.

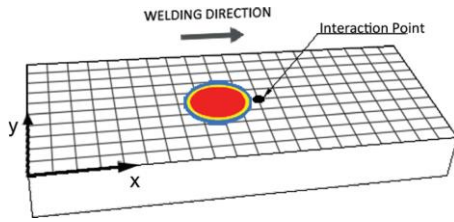


Figure 6.1- Schematic of interaction of laser beam with workpiece [12].

They found that at a constant beam diameter (e.g. 0.63 mm) the depth of penetration linearly increases with power density. In contrast, the depth of weld logarithmically increases with interaction time (interaction time = beam diameter divided by welding speed). In all cases, either with constant power density and increasing interaction time or with constant interaction time and increasing power density, the depth of weld increased with increasing beam diameter on the surface of sheet [11].

6.2 Basic laser material interaction parameters

The following section is a summary of the paper published by Suder et al. [12]. In order to understand the parameters controlling the depth of penetration and weld width it is essential to study the fundamental laser material interaction parameters. The interaction of a fibre laser beam with a sheet material is determined by power density (q_p), interaction time (T_i) and the size of heat source on the workpiece [12].

6.2.1 Power density

The average power density (q_p), of a laser beam, is specified by Equation 6.1 where P is laser power and A_s is the laser spot area on the sheet surface.

$$q_p = \frac{P}{A_s} \quad \{Wm^{-2}\} \quad 6.1$$

6.2.2 Interaction time

The interaction time defines the time during which a point on the workpiece is irradiated by the laser beam. Considering a point on the centreline of the weld, the interaction time T_i for a circular beam spot size with the diameter of d which moves with a constant cutting speed for a distance of d is given in Equation 6.2 and Figure 6.3. This definition explains the maximum interaction time on the cut centreline.

$$T_i = \frac{d}{V} \quad \{s\} \quad 6.2$$

6.2.3 Energy density

The average energy density, i.e. the energy delivered to the cutting zone per unit area, is the product of power density and interaction time and is defined by Equation 6.3.

$$q_E = q_p \cdot T_i = \frac{P \cdot d}{A_S \cdot V} \quad \{J m^{-2}\} \quad 6.3$$

6.2.4 Specific point energy

The usual consideration of power density and interaction time gives an incomplete analysis system to compare different combinations of laser parameters. This is because, with the same energy density (product of power density and interaction time) applied with different beam size, different energies will be delivered to the laser processing zone. Hence, a third factor is required. For the laser welding mechanism, it can be considered that laser welding is a periodic process whose cycle time is the interaction time. Then, the energy delivered to the welding zone in the interaction time of T_i is the specific point energy (E_{SP}) [11] which can be calculated by Equation 6.4.

$$E_{SP} = q_p \cdot T_i \cdot A_S = P \cdot T_i = \frac{P \cdot d}{V} \quad \{J\} \quad 6.4$$

Figure 6.2 shows a dependency of penetration depth on the specific point energy (SPE) for two levels of power density.

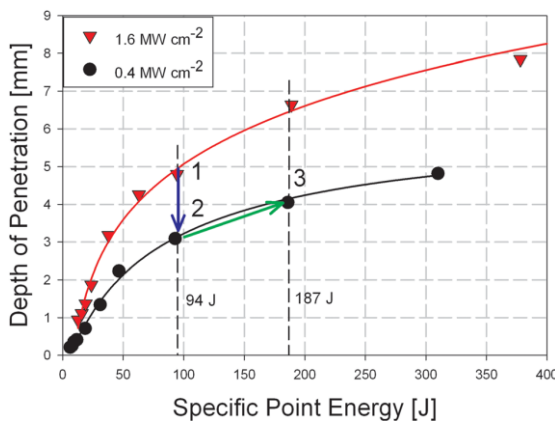


Figure 6.2- Effect of specific point energy on depth of penetration at low levels of power density: 1.6 MWcm⁻² (5 kW at 0.63 mm) and 0.4 MWcm⁻² (2 kW at 0.78 mm) [12].

Considering Figure 6.2, a change in power density from 1.6 MWcm^{-2} to 0.4 MWcm^{-2} could be achieved by either decreasing the laser power or increasing the spot size by changing the optical configuration. If, for example, the spot size is increased by using a different fibre, it could result in a move from point 1 to point 2 on the graph (decreasing the depth of penetration from 5 to 3 mm). However, this is counteracted by an increase in the interaction time because the spot size is increased. This increases the SPE, and results in an automatic shift from point 2 to point 3 (increasing the depth of penetration from 3 to 4 mm).

In summary, Suder et al. [12] showed that the depth of penetration is mainly controlled by the power density and the specific point energy (SPE) whilst the weld width is controlled by the interaction time.

In any case it is clear that the SPE approach is useful in gathering and composing different sets of data for laser welding. This chapter investigates this option for laser cutting.

In fibre laser cutting, the same sheet thickness can be cut with variety combination of laser parameters such as power, cutting speed, fibre diameter and focussed beam size which makes the parameter selection complicated. Since the purpose is to cut a sheet, it is important to know which laser parameters determine the cut sheet thickness. In commercial fibre laser cutting two laser parameters (power or cutting speed) can be changed in order to achieve a cut for a given system. Do the power density and specific point energy control the cut sheet thickness?

Since the kerf width is important, the laser parameters, e.g. focal spot size and cutting speed, can be adjusted and tuned to achieve the narrowest kerf size for a given optical system. Regarding the effect of beam diameter on the kerf size, it is well known that the larger the focussed beam diameter, the wider the kerf width [1, 10]. However for a given focussed beam diameter, if a different combination of laser parameters is used, different kerf sizes will be achieved. Does the interaction time control the kerf width?

A model, which is used to investigate the SPE approach in laser cutting, is shown in Figure 6.3.

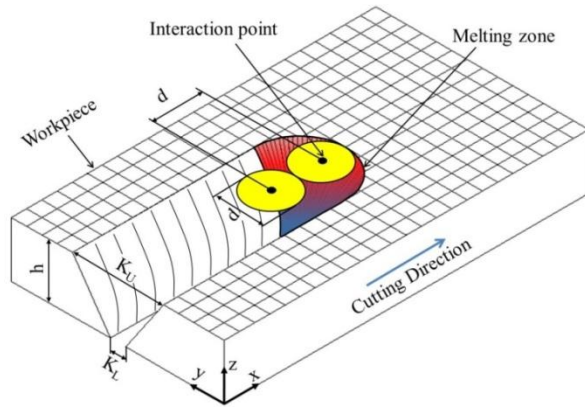


Figure 6.3- Schematic interaction of laser beam with workpiece in laser cutting.

In order to simplify the following discussion, it has been supposed that the interaction area equals the area of the focussed laser beam on the sheet surface. In reality, the interaction area is something like a half-pipe which is kinked and bent towards the bottom of the kerf and its shape and inclination angle are changed with the cutting speed [22, 37]. Figure 6.4 shows how the cutting speed affects the cutting front angle [22].

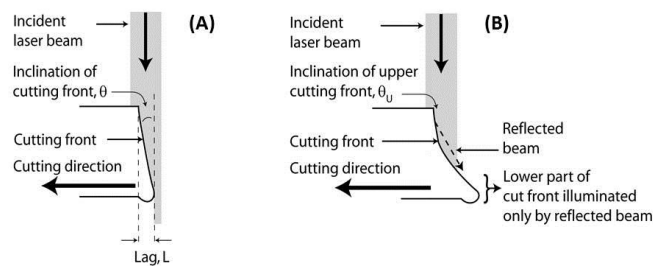


Figure 6.4- Showing cut front laser beam interaction geometries. (A) Slower cutting speed (steep cut front, some laser beam is lost), (B) Faster cutting speed (steeper cut front, all laser beam interacts with cut edge) [22].

In Equation 6.4, it is assumed that the laser cutting mechanism is performed by an energy (E_{SP}) with a uniform intensity distribution exerted to the cutting zone in a constant interaction time (T_i). The intensity distribution of the beam was investigated by a beam characterisation test (see chapter 3).

6.3 Cutting with maximum speed

For each laser power a relevant maximum cutting speed was identified. This use of the maximum speed made sure that energy losses out of the kerf would be minimised in all cases. Table 6.1 briefly shows the parameters used in maximum cutting speed experiments.

Table 6.1- Cutting parameters which were applied in maximum cutting speed experiments.

Focal length	Thickness	200 μm		400 μm		600 μm	
		Power (kW)	Speed (m/min)	Power (kW)	Speed (m/min)	Power (kW)	Speed (m/min)
120 mm	1 mm	0.14-0.32	0.12-2.4	0.16-0.7	0.22-4.55	0.25-1.55	0.36-6
	2 mm	0.25-0.8	0.12-2.4	0.3-1.6	0.22-4.55	0.375-1.67	0.36-3.6
	3 mm	0.35-1.425	0.12-2.4	0.42-1.52	0.22-2.2	0.55-1.35	0.36-1.6
	4 mm	0.48-1.7	0.12-1.7	0.55-1.7	0.22-1.45	0.68-1.55	0.36-1.2
	6 mm	0.75-1.4	0.15-0.6	0.9-1.15	0.22-0.55	1.3-1.6	0.45-0.6
80 mm	1 mm	0.12-0.21	0.09-1.8	0.14-0.47	0.156-3.12	-	-
	4 mm	0.45-1.1	0.09-0.9	0.51-1.79	0.156-1.56	-	-
	6 mm	0.7-1.7	0.09-0.6	0.8-1.5	0.195-0.52	-	-

The maximum speeds were confirmed by attempting to cut at slightly lower power. The results of cut/no cut are shown in Appendix Figure 10.1 to Figure 10.5. The small separation of the cut and no cut lines indicates the precision with which the maximum cutting speeds were determined. As can be seen, the border between cut and no cut is very narrow, indicating that the maximum cutting speeds used were accurate.

6.3.1 Kerf width

Kerf widths of all cuts were measured. Before going through the results of kerf width, it is appropriate to restate the diameters of focused beams which were measured by the focus monitor and used in this experiment (Table 6.2).

Table 6.2- Focussed beam diameter for each fibre and focal length (measured at power of 400-600 W).

Focal length	<i>Fibre diameter (μm)</i>		
	200 μm	400 μm	600 μm
120 mm	0.2 mm	0.37 mm	0.6 mm
80 mm	0.15 mm	0.26 mm	-

Upper kerf width results as a function of power for some cuts are indicated in Figure 6.5 to Figure 6.8. As can be seen, in most case the kerf width is close to the focused beam diameter. However, in some cases the kerf width was observed significantly larger than the focused spot size e.g. the kerf widths for 200 μm fibre lie in the range of 500 to 600 μm (see Figure 6.8).

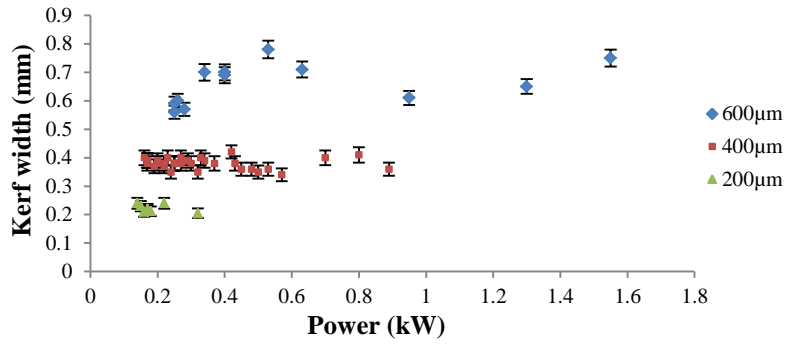


Figure 6.5- Kerf width versus power for different fibres (1 mm thick, 120 mm focal length).

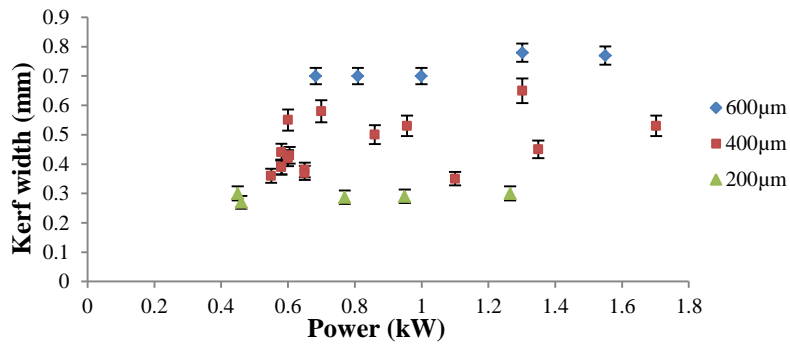


Figure 6.6- Kerf width versus power for different fibres (4 mm thick, 120 mm focal length).

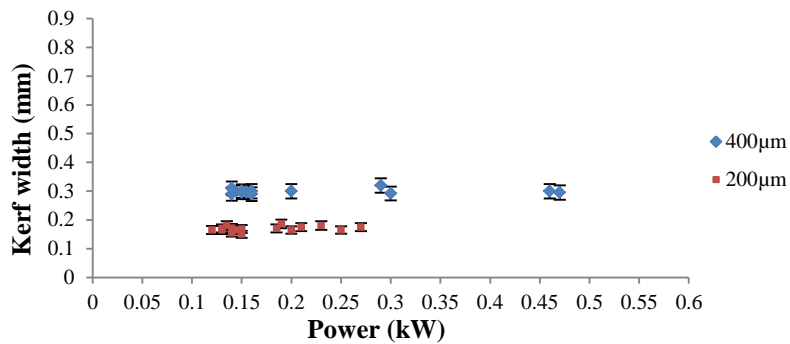


Figure 6.7- Kerf width versus power for different fibres (1 mm thick, 80 mm focal length).

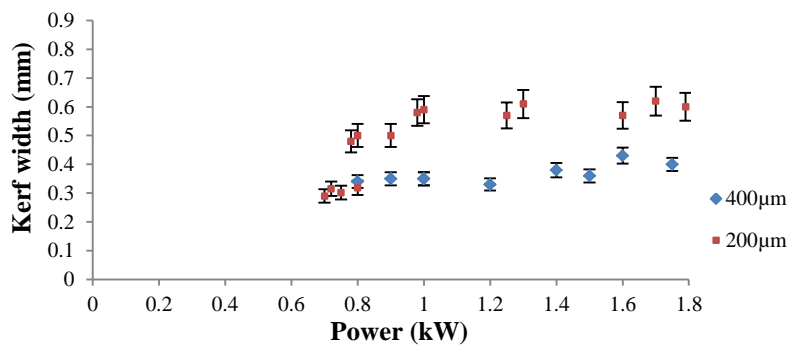


Figure 6.8- Kerf width versus power for different fibres (6 mm thick, 80 mm focal length).

6.4 Thermal lensing

During kerf width measurement, it was observed that in some cases the kerf width slightly increased along the cut line as shown in Figure 6.9. Moreover, from the results of kerf width (Figure 6.5 to Figure 6.8) it can be seen that some kerf widths are unusually much wider than the focused beam size. For example, when cutting 1 mm with using 400 μm the ratio of kerf width per spot size (K/S) is almost constant at 1.10 with increasing power from 0.14 kW to 0.47 kW, but when cutting 6 mm with using 200 μm , the K/S is more than 2 and rapidly increases to 4 as power is increased from 0.7 kW to 1.0 kW (Figure 6.32) This kerf width widening with increasing time and power created a suspicion that some of the results of this experiment were affected by the thermal lensing phenomenon.

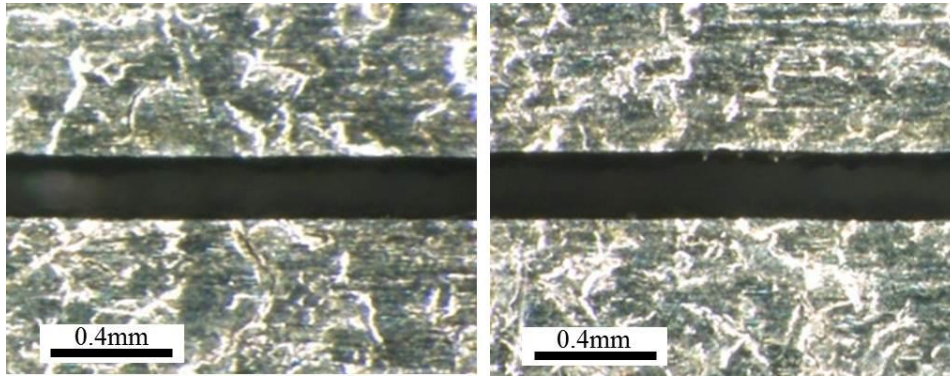


Figure 6.9- Kerf width widening due to thermal lensing. Kerf width slightly increases along the cut (left to right) from 0.195 mm to 0.22 mm (1 mm thick, fibre of 200 μm , 120 mm focal length, power of 310 W, 2.4 m/min).

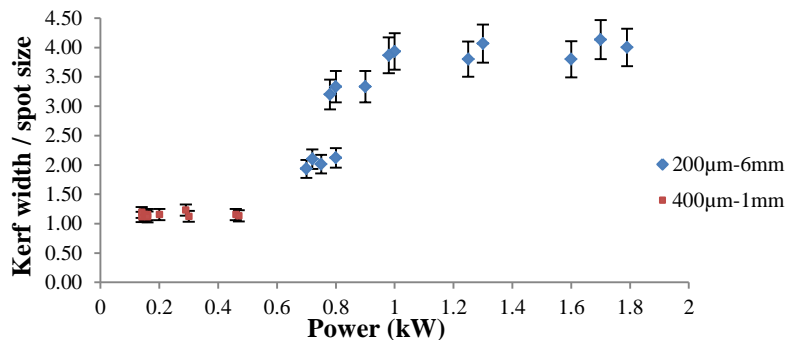


Figure 6.10- Example of kerf width per spot size ratio (K/S) versus power for different fibres and thicknesses. Kerf width for 200 μm fibre and 6 mm thickness is much bigger than that is achieved for 400 μm -1 mm, confirming thermal lensing (80 mm focal length).

Although today's optical lenses are made of fused silica material which is highly transmissive, there is still some radiation that is either absorbed or scattered within

the lens which causes it to heat up [100]. The presence of dust and scratches on the lens will also create lens heating [11, 70]. In our experiments visual inspection of the lens surface showed a surface without dust or any scratch marks, but it seems that thermal lensing did happen in some cases. For example, this thermal lensing effect can clearly be seen in the example shown in Figure 6.9 where the kerf width is bigger at the end of the cut that it was at the beginning.

In our results, thermal lensing had two effects on the kerf width for some samples:

- 1- Time dependent: the kerf width increases along the cut as the time increases at which the cutting speed is constant (Figure 6.33).
- 2- Power dependent: the kerf width is much bigger than the spot size when using higher power (Figure 6.32).

When the lens is warming, the refractive index and thickness of the lens both change [99]. Figure 6.11 schematically shows the effect of thermal lensing on the lens geometry, focal position and the focused spot size. The effect of thermal lensing on the spot size will directly affect the kerf width.

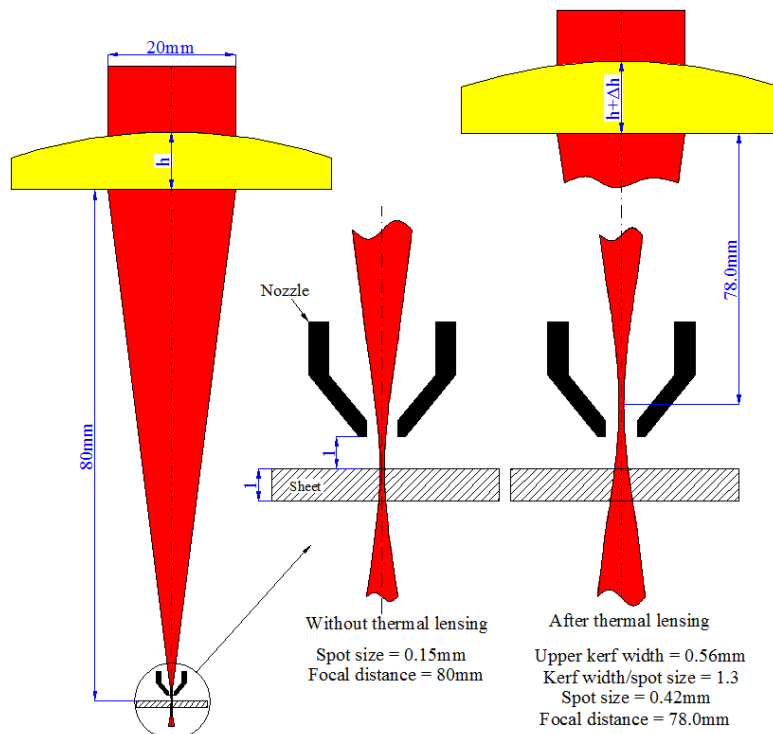


Figure 6.11- Schematically showing the effect of thermal lensing on the lens, focal distance and spot size for a lens with original focal length of 80 mm and raw beam diameter of 20 mm after collimation. Before thermal lensing, focused beam size at power of 400 W is 0.15 mm (measured by focus monitor). After thermal lensing, the lens volume increases and focal length decreases so the focussed spot size on the sheet surface increases, giving a bigger kerf width.

To remove results affected by thermal lensing only those with a K/S ratio less than or equal to 1.30 were accepted for thermal lensing. This means that several results, typically involving high powers and higher thicknesses, were removed from the original batch of results. From here onwards, only thermal lensing free results will be used.

6.5 The effect of beam diameter on kerf width

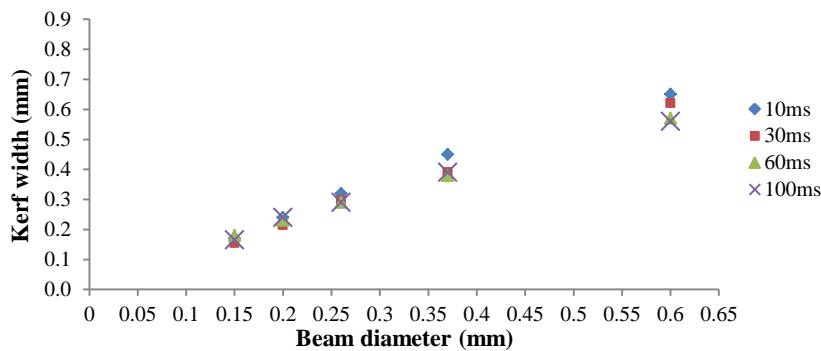


Figure 6.12- Kerf width versus beam diameter for different interaction times (1 mm-thick).

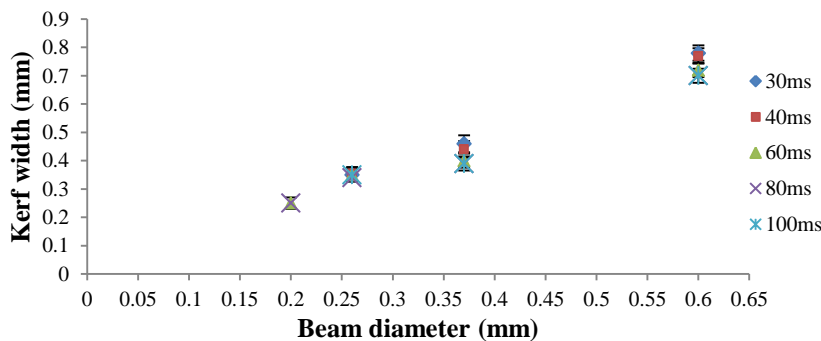


Figure 6.13- Kerf width versus beam diameter for different interaction time (4 mm-thick).

As can be seen in Figure 6.12 and Figure 6.13, the kerf width linearly increases with focussed beam diameter. Figure 6.14 also shows that there is only a slight increase in the kerf width with increasing interaction time. In Figure 6.12 the reverse slight relationship between interaction time and kerf width can be seen. In summary, interaction time has a negligible effect on the kerf width.

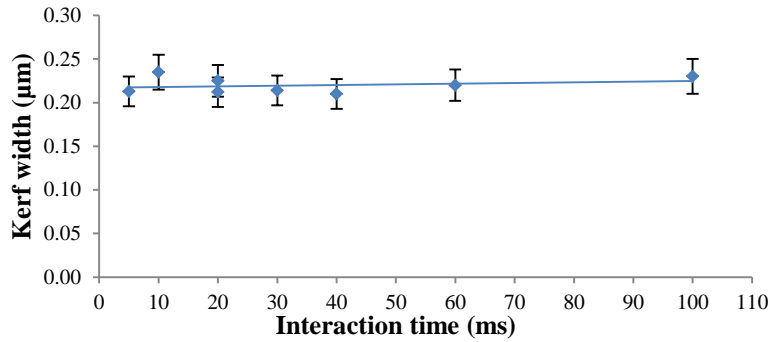


Figure 6.14- Showing kerf width slightly increases with interaction time (1 mm thick, 200 µm beam diameter, 120 mm focal length).

6.6 Effect of power density on kerf width

The effect of power density on the kerf width for different beam diameters is shown in Figure 6.15 and Figure 6.16 for thicknesses of 1 and 4 mm respectively. These graphs indicate that for a given beam diameter (e.g. 0.37 mm), the kerf width slightly increases with power density. This is probably because the top hat energy distribution of the beam is not exactly a top hat shape. As the power density of the beam increases the effective cutting diameter of the beam increases as illustrated in Figure 6.17.

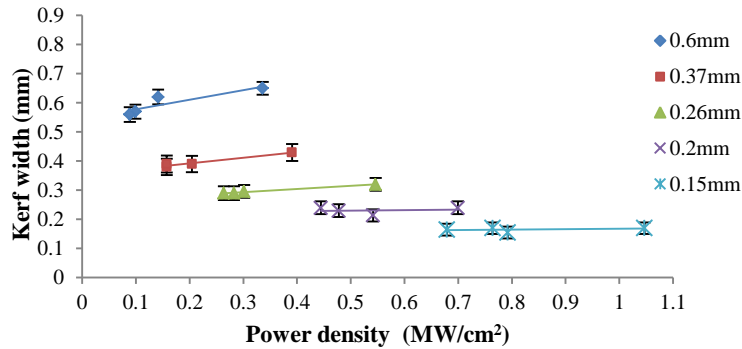


Figure 6.15- Kerf width versus power for different beam diameter (1mm-thick, power range of 120-950 W, cutting speed range of 0.09-3.6 m/min, SPE range of 1.85-25 J, K/S≤1.30).

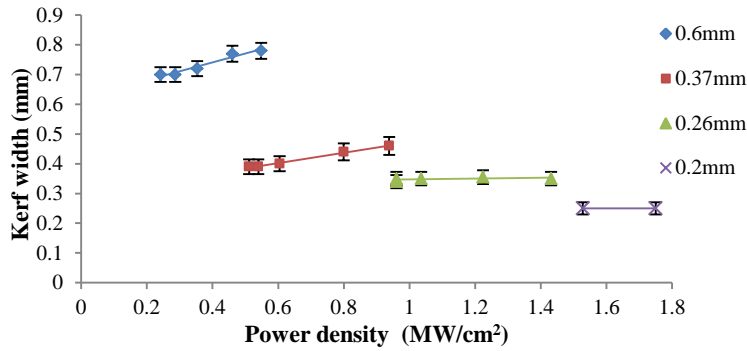


Figure 6.16- Kerf width versus power for different beam diameter (4mm-thick, power range of 480-1550 W, cutting speed range of 0.15-1.2 m/min, SPE range of 22.8-68.3 J, $K/S \leq 1.3$).

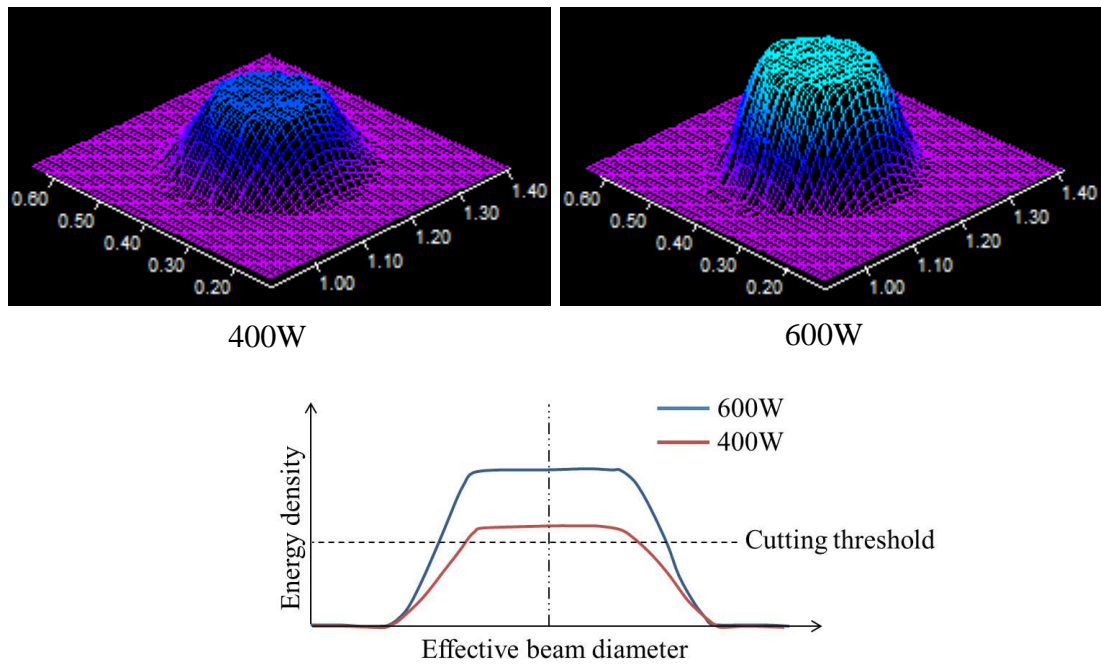


Figure 6.17- Energy distribution for two focused beams delivered by a fibre of 400µm at two powers of 400 W and 600 W. The energy distribution is not exactly a top hat. The energy density for the cutting threshold indicates that the effective beam diameter increases with power.

6.7 Effect of power density and SPE on the cut sheet thickness

The power densities, used in the maximum cutting experiments, are seen in Figure 6.18. In order to investigate the effect of power density on the cut sheet thickness for different combinations of laser cutting parameters, it is useful to separate the power density results into several batches, so that each batch consists of few power densities of very close values as shown in Figure 6.19.

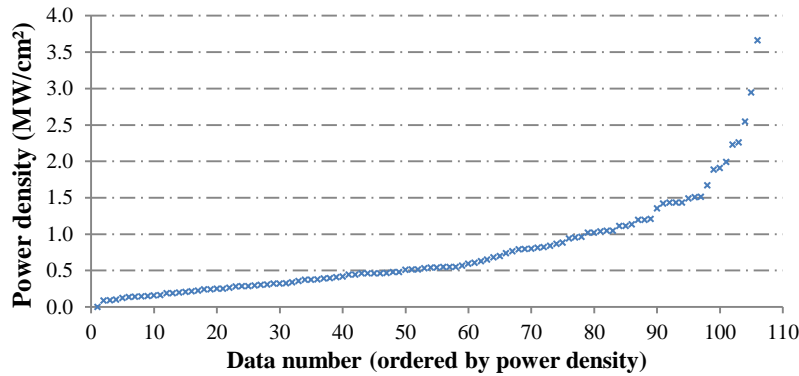


Figure 6.18- Power density results as a function of data number.

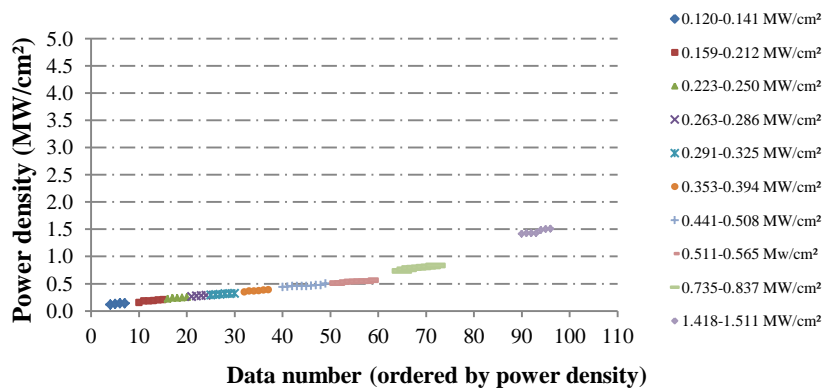


Figure 6.19- Showing power density batches used in following results.

The specific point energy (SPE) range was specified for each power density group and sheet thickness as shown in Table 6.3. As can be seen, each group of power density consists of several thicknesses which help us to evaluate the effect of power density and SPE on the cut sheet thickness.

Table 6.3- Showing the specific point energy for each sheet thickness and different power density range.

Power density (MWcm ⁻²)	Specific point energy (J)				
	1 mm	2 mm	3 mm	4 mm	6 mm
0.120-0.141	12.0-13.6	31.92-37.47	-	-	-
0.159-0.212	6.6-10.6	27.0	48.0-55.0	-	-
0.223-0.250	5.43-11.35	20.25	42.0	68.3	-
0.263-0.286	9.0-11.2	23.77	-	64.74	-
0.291-0.325	6.0-9.5	18.21	36.0	-	-
0.353-0.394	4.0-4.23	16.143	31.49-42.82	60.0	-
0.441-508	6.38-14.0	17.32	30.0-37.65	52.05	104.1
0.511-0.565	2.9-9.3	11.09	20.0-23.0	46.5-58.55	96.0
0.735-0.837	2.9-10.44	8.82	17.14	34.7	90.88
1.418-1.511	-	5.4-7.8	12.24-18.0	22.80	64.0

The effect of SPE on the cut sheet thickness (sheet thickness) for different power densities is indicated in Figure 6.20 and Figure 6.21. In order to compare welding and cutting processes with regard to the effect of SPE on the depth of penetration and cut sheet thickness, Figure 6.2 is duplicated as Figure 6.22.

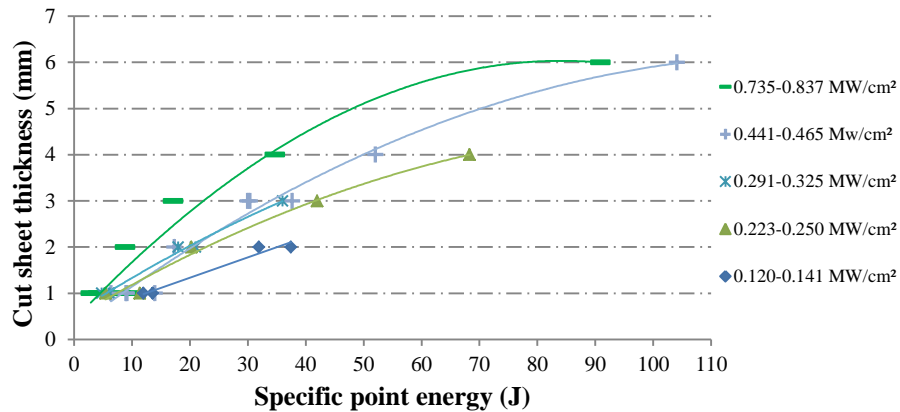


Figure 6.20- The effect of specific point energy on the cut sheet thickness for different power densities.

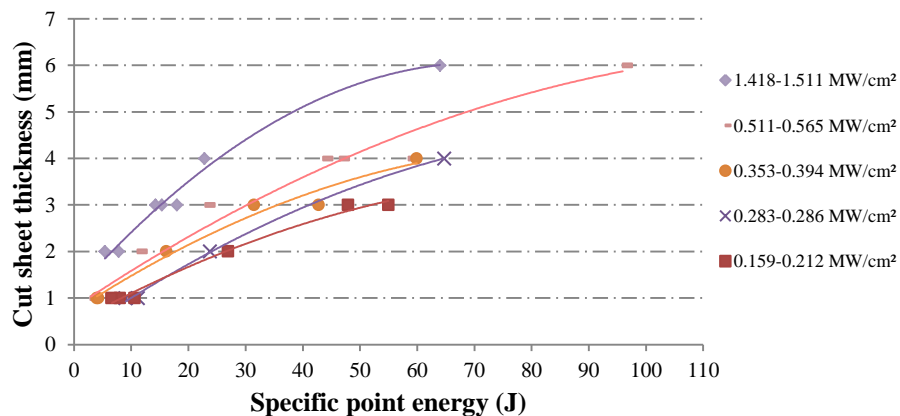


Figure 6.21- The effect of specific point energy on the cut sheet thickness for different power densities.

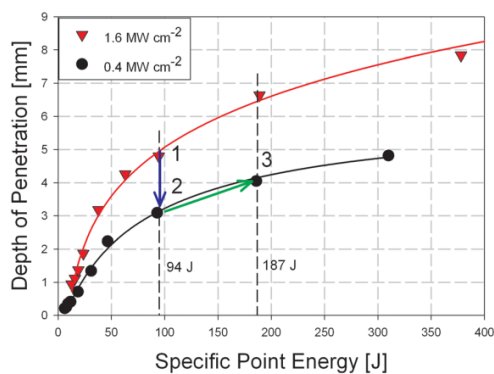


Figure 6.22- Duplication of Figure 6.2 to show the similarity of welding and cutting processes regarding the effect of SPE on the penetration depth and the cut sheet thickness.

As can be seen in Figure 6.20 and Figure 6.21, overall:

1. The same thickness can be cut by decreased SPE and increased power density. For example, with the same power and a decrease in the beam diameter, the cutting speed is increased, boosting the cutting efficiency.
2. With the same SPE, the cut sheet thickness can be increased with increasing power density.
3. With the same power density, the cut sheet thickness increases with increasing SPE.

6.8 Comparison of cutting and welding

There are some similarities and differences between laser welding and laser cutting as summarised in Table 6.4.

Laser welding	Laser cutting
<p>Depth of penetration:</p> <p>In laser welding the depth of penetration is a significant issue for the material being welded. It describes the quality and strength of a weld [11, 12].</p>	<p>Depth of cut (Cut sheet thickness):</p> <p>In laser cutting the cut sheet thickness represents the thickness of the plate being cut.</p>
<p>Depth of penetration:</p> <p>The depth of penetration is mainly controlled by the power density and the specific point energy (see Figure 6.22) [11].</p>	<p>Depth of cut (Cut sheet thickness):</p> <p>The same conclusion is valid for laser cutting (see Figure 6.20 & Figure 6.21).</p>
<p>Weld width:</p> <p>Weld width is important in the case of fit-up tolerance, residual stresses and distortions [11].</p>	<p>Cut width (kerf width):</p> <p>With a narrower kerf width, products with sharper corners can be cut. The narrower the kerf width, the more the detail of product's profile [3].</p>
<p>Weld width:</p> <p>The weld width is controlled by the interaction time [11, 12] (see Figure 6.23).</p>	<p>Cut width (Kerf width):</p> <p>The cut width is not controlled by the interaction time. This is because, unlike welding, laser cutting involves material leaving the laser-material interaction area. This ejected melt carries most of the energy of the process away from the cut zone. This prevents an increased interaction time from having a big effect on the cut width. In laser cutting, the cut width is generally controlled by the focused beam diameter (see Figure 6.23).</p>

Table 6.4- Comparison between laser cutting and laser welding.

Figure 6.23 is an example for difference between welding and cutting regarding the effect of interaction time on the weld/cut width.

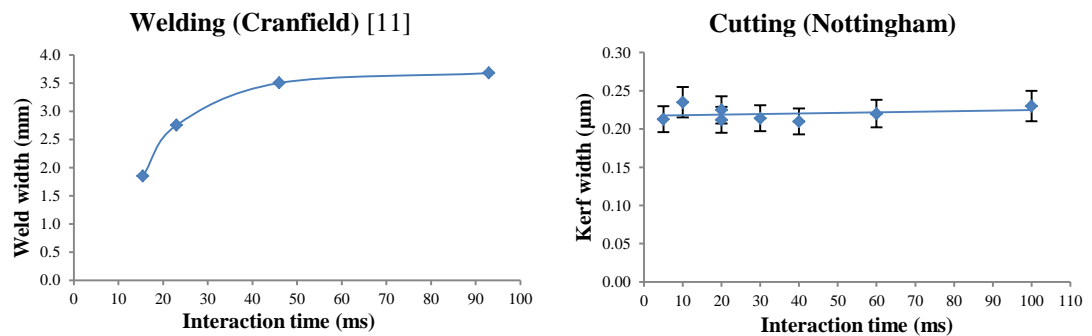


Figure 6.23- Weld width is controlled by the interaction time but the kerf width is not substantially change with increasing interaction time. Beam diameter for welding was 0.75 mm and for cutting was 0.2 mm.

6.9 Discussion

The similarity of Figure 6.20 and Figure 6.21 with Suder's figure (Figure 6.22) confirm that SPE analysis can be a useful tool in cutting as in welding.

This tool enables cuts generated with different optical systems to be compared, but what industrial laser cutters really want to know is how it could be exploited to improve the cutting process.

The cost of laser cutting can be approximated as being proportional to the energy input. For a given cut length the energy input is simply the laser power divided by the speed. As shown in Figure 6.24.

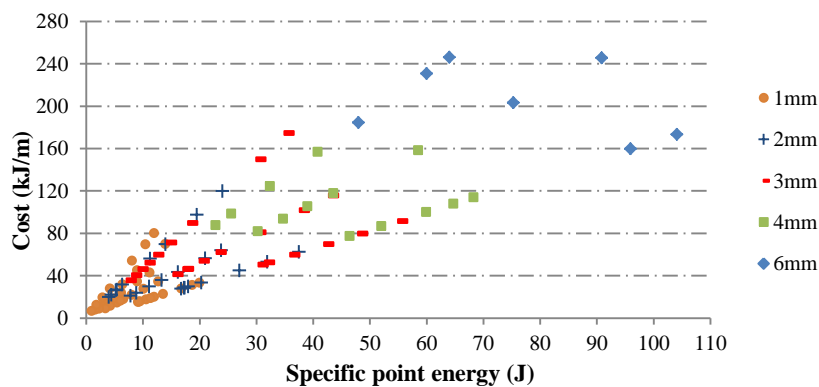


Figure 6.24- Cost (kJ/m) plotted against SPE (J) showing that data forms straight lines, data point markers correspond to material thickness.

A plot of this cost against SPE (Figure 6.25) shows that the data falls on a series of straight lines, with each line starting at the origin. Further consideration shows that this plot of cost, power/speed, against SPE, (power × beam diameter)/speed would be expected to produce a set of straight lines with the gradient of each line corresponding to 1/beam diameter. This is clearly seen in Figure 6.25 where data point markers correspond to beam diameter. This analysis does highlight that for any given value of SPE cost is decreased by using a larger beam diameter.

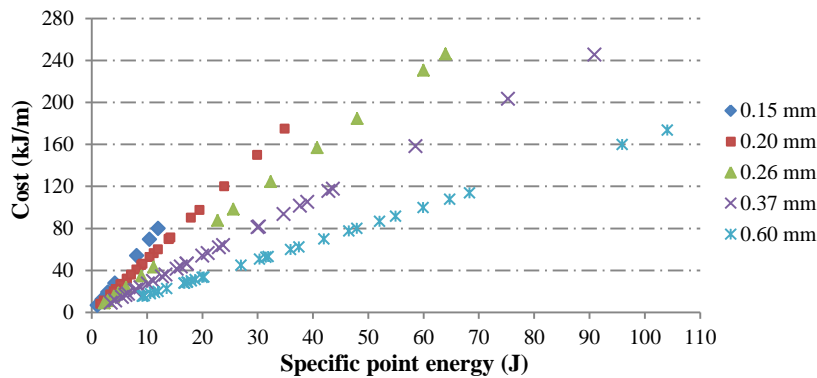


Figure 6.25- Cost (kJ/m) plotted against SPE (J) showing that data forms straight lines, with each line corresponding to a different beam diameter.

The analysis can also be expanded to include cutting efficiency. Cutting efficiency, C_{eff} , is defined here as the ratio of the area of cut surface generated per second to the energy input from the laser per second as indicated in equation 6.5:

$$C_{eff} = \frac{h * \frac{l}{t}}{\frac{E}{t}} = \frac{h * V}{P} \quad \{mm^2.J^{-1}\} \quad 6.5$$

Where:

h: Cut sheet thickness (mm)

l: Length of cut (mm)

t: Time of cut (sec)

E: Energy delivered to the cutting zoon

V: cutting speed (mm/s)

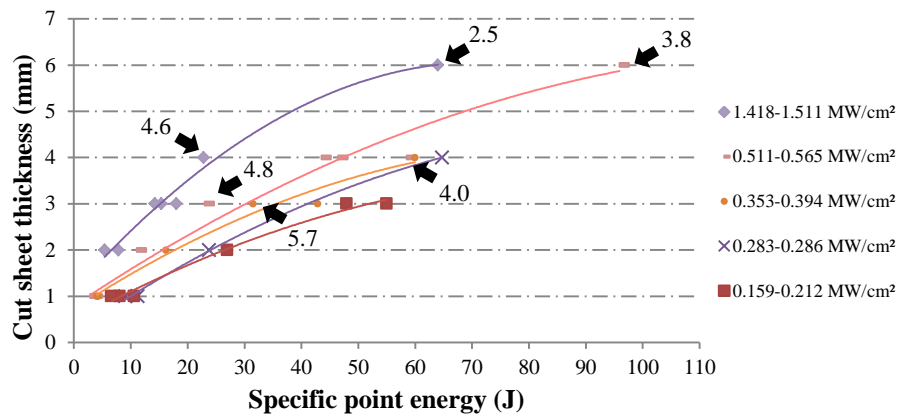


Figure 6.26- Showing Figure 6.21 with the C_{eff} values for selected data point superposed, units for C_{eff} are $10^{-8} \text{ m}^2 \text{ J}^{-1}$.

Selected C_{eff} values are superposed on the depth of cut versus SPE plot in Figure 6.26. Two trends relating to C_{eff} are observed:

- For a fixed cut sheet thickness, C_{eff} increases with SPE.
- For a given value of SPE, C_{eff} increases as cut sheet thickness decreases.

So, the highest cutting efficiencies will be achieved for thin section sheet cut with conditions that produce a high SPE. Powell [131] has discussed the fact that cutting efficiency is higher for thinner materials. The reason for this is that thin materials are cut at higher speeds. At these high speeds, there is less time for heat to be conducted away from the cut zone. This means that more of the laser energy can be used for melting and so cutting is more efficient.

This chapter has shown that part of the approach of Suder can be applied to laser cutting. The weld width – interaction time part of Suder’s work cannot be applied to laser cutting because the interaction time only has a minor effect on kerf width. However, Suder’s weld penetration depth - SPE work can be applied to laser cutting to give useful comparisons between different optical set ups. This will be a useful tool for comparing different laser cutting systems in the future.

7 Summary and conclusions

The work presented in this thesis has studied key characteristics of fibre laser cutting, including a study of striations on the cut edge. The piercing process, required to start a cut that does not start from the edge of a sheet, has been studied and a new, dual gas, process that minimises material wastage has been developed and demonstrated. The SPE analysis approach, developed by Suder and Williams at Cranfield University, has been shown to also be applicable to laser cutting.

The results reported in Chapter 6 revealed that thermal lensing had occurred for some cutting conditions. This largely explains the observations in Chapter 4 of kerf widths significantly exceeding the beam diameter. The high brightness beams of fibre lasers make them particularly likely to suffer from thermal lensing. It should be noted that whilst the cuts reported in Chapter 4 may not have been made under optimal conditions, the reported trends and analysis are still valid, albeit for a larger spot size than expected.

Specific key observations and conclusions are:

7.1 Characterisation of fibre laser cutting:

- The surface roughness for the oxygen laser cut edge is less than that for the nitrogen cut edge (on average 2.5 μm and 5 μm respectively).
- EDS and XRD examination of the cut edges indicate that the surface produced by oxygen laser cutting is covered by an oxide layer ($\text{FeO} + \text{Fe}_3\text{O}_4$). This feature is not seen for nitrogen laser cutting.
- In oxygen laser cutting, the striation patterns are much smoother than those observed for nitrogen laser cutting. This was evident from the results of surface roughness analysis.
- Some striations in oxygen laser cutting are due to the rippled oxide on top of the smooth surface roughness.
- After nitrogen laser cutting, the cut edge includes dross attachment while for oxygen laser cutting the cut edge is generally dross free.

- For both applied gases, the width of the HAZ on the lower part of cut edge is larger than that for the upper part.
- The amount of HAZ for laser-nitrogen cutting is 2 to 2.7 times larger than that for laser-oxygen cutting.
- The cross sectioned, polished and etched cut edge indicates that there is a relatively thick re-solidified melt material lining the cut edge after nitrogen cutting. This feature is not observed for the oxygen cut edge.

7.2 Piercing

- Piercing time reduces with both increasing laser power and assist gas pressure for both oxygen and nitrogen piercing.
- Increasing laser power has a more significant effect: a ~40% increase in power produces a 40–50% decrease in piercing time.
- The effect of increasing gas pressure is only significant at lower pressures, 2–4 bar, for oxygen piercing. For both gases, increasing pressure from 4 to 8 bar only decreases piercing time by about 10%.
- Holes pierced with oxygen are considerably wider than those cut with nitrogen.
- A combination of piercing with nitrogen and cutting with oxygen can allow the piercing hole to be positioned on the cut line, minimising material wastage.

7.3 Specific point energy (SPE) analysis:

- The SPE concept can be applied to laser cutting.
- Sheet cut thickness is mainly controlled by the power density and the specific point energy. This is in agreement with welding process.
- In laser welding, the weld width is controlled by the interaction time but for cutting the cut width is not controlled by the interaction time. This is because, unlike welding, laser cutting involves material leaving the laser-material interaction area. This ejected melt carries most of the energy of the process away from the cut zone. This prevents an increased interaction time from

having a big effect on the cut width. In laser cutting, the cut width is generally controlled by the focused beam diameter.

- The SPE results indicated the possibility that, for a given material thickness and any given value of SPE, cost could be decreased by using a larger beam diameter.
- For a given cut sheet thickness, cutting efficiency increases with SPE.
- For a given value of SPE, cutting efficiency increases as cut sheet thickness decreases.

8 Future Work

It has been shown that SPE analysis is applicable to laser cutting. To date all results considered have come from a single laser, albeit using a variety of optical set ups. Further work is required to investigate the broader application of this approach, specifically:

- 1 Collation of results from different laser systems to allow more wide ranging comparisons is required to fully examine the potential of this analysis approach.
- 2 Further experiments with different materials to fully observe the effect of material on the SPE analysis.
- 3 Further analysis is required to exploit the results of SPE analysis in optimisation of cutting cost and efficiency.

The influence of thermal lensing on the laser cutting in terms of kerf width has been highlighted in this work. Further examination of published fibre laser cutting results is required to determine the extent of this issue.

In order to gain further insight into striation generation it would be very interesting to obtain images of the cut front during cutting, and to correlate these with the resultant cut surface. Use of high speed imaging equipment could reveal the origin and evolution of surface features.

A new method of piercing with nitrogen-cutting with oxygen, has been demonstrated however further work is required to in order to fully understand the mechanism and to optimise the process. Specific areas of interest are:

- 1 Wider experimental investigation of effect of power intensity and inclined gas pressure on the breakthrough time and hole diameter.
- 2 Additional experimental work to separate the effects of using an inclined piercing gas source and a nitrogen piercing gas source and thereby determine if an inclined jet of oxygen would have any benefit.
- 3 For industrial applications a new cutting head could be developed, equipped with double coaxial nozzles and suitable valves to switch from nitrogen to

oxygen which is called NIPOC as shown in Figure 8.1. Optimisation of gas switching times could save process time and material.

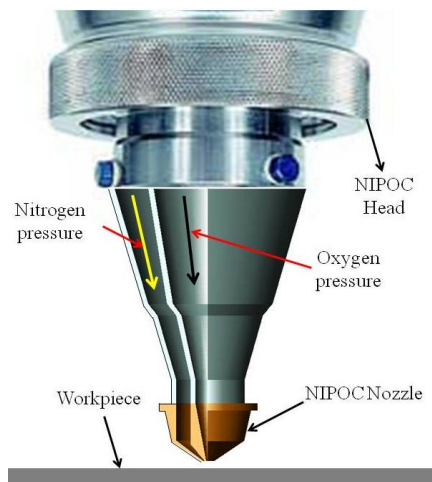


Figure 8.1- A developed NIPOC head with two coaxial nozzles (designed by the author).

9 References

- [1] Powell J. CO₂ Laser Cutting. 2nd, editor: Springer Verlag Inc; 1998.
- [2] Ion JC. Laser Processing of Engineering materials. Oxford: Elsevier Butterworth-Heinemann; 2005.
- [3] Powell J, Kaplan A. Laser cutting: from first principle to the state of the art. Proceedings of the 1st Pacific International Conference on Application of Lasers and Optics. 2004.
- [4] O'Neill W, Gabzdyl JT. New developments in laser-assisted oxygen cutting. Optics and Lasers in Engineering. 2000;34(4-6):355-67.
- [5] O'Neill W, Steen WM. A three-dimensional analysis of gas entrainment operating during the laser-cutting process. J Phys D: Appl Phys. 1995;28:12-8.
- [6] Seefeld T, O'Neill B. Cutting and welding with the new high brightness lasers. The laser users. 2008(50):24.
- [7] Powell J, Kaplan A. A comparison of fibre laser and CO₂ laser cutting. AILU-The lasers users. 2013(69):18-20.
- [8] Ivarson A, Powell J, Kamalu J, Broden G, Magnusson C. The effects of oxygen purity in laser cutting mild steel; a theoretical and experimental investigation. Lasers in Engineering. 1993;1:299.
- [9] Powell J, Petring D, Kumar RV, Al-Mashikhi SO, Kaplan A, Voisey KT. Laser–oxygen cutting of mild steel: the thermodynamics of the oxidation reaction. Journal of Physics D: Applied Physics. 2009;42:11pp.
- [10] Sparkes M, Gross M, Celotto S, Zhang T, O'Neill W. Practical and theoretical investigations into inert gas cutting of 304 stainless steel using a high brightness fiber laser. Journal of Laser Applications. 2008;20(1):59-67.
- [11] Suder WJ. Study of fundamental parameters in hybrid laser welding [Ph.D. Thesis]. Cranfield: School of applied Science, Cranfield University; 2012.
- [12] Suder WJ, Williams SW. Investigation of the effects of basic laser material interaction parameters in laser welding. Journal of laser applications. 2012;24(3):10.
- [13] FreakLasers. How laser works. <http://www.freaklasers.com/how-laser-works.html>; 2009 [cited 19/07/2011].
- [14] Gahan BC. New high-power fiber laser enables cutting edge research. Laser Technology. Winter 2004:29-31.

- [15] Shiner B. High-power fiber lasers impact material processing. *Industrial Laser Solutions*. 2003.
- [16] Bergstrom D, Powell J, Kaplan AFH. The absorptance of steels to Nd : YLF and Nd : YAG laser light at room temperature. *Applied Surface Science*. 2007;253(11):5017-28.
- [17] Niziev VG, Nesterov AV. Influence of beam polarization on laser cutting efficiency. *Journal of Physics D Applied Physics*. 1999;32:1455-61.
- [18] Weber R, Michalowski A, Abdou-Ahmed M, Onuseit V, Rominger V, Kraus M, Graf T. Effects of radial and tangential polarization in laser material processing. *Physics Procedia*. 2011;12:21-30.
- [19] Pasquet P, del Coso R, Boneberg J, Leiderer P, Oltra R, Boquillon JP. Laser cleaning of oxide iron layer: Efficiency enhancement due to electrochemical induced absorptivity change. *Applied Physics A, Materials, Science & Processing*. 1999;69:727-30.
- [20] Bergstrom D. The Absorptance of Metallic Alloys to Nd: YAG and Nd: YLF Laser Light [Ph.D. thesis]. Luleå, Sweden: Luleå University of Technology; 2005.
- [21] Mahrle A, Beyer E. Theoretical aspects of fibre laser cutting. *Journal OF Physics D: Applide Physics*. 2009;42(175507).
- [22] Powell J, Al-Mashikhi SO, Kaplan AFH, Voisey KT. Fibre laser cutting of thin section mild steel: An explanation of the 'striation free' effect. *Optics and Lasers in Engineering*. 2011;49:1069-75.
- [23] Kaplan AFH. Local absorptivity modulation of a 1.0 μm -laser beam through surface waviness. *Applied Surface Science*. 2012;258(24):9732-6.
- [24] Kaplan AFH. Absorptivity modulation on wavy molten steel surfaces: The influence of laser wavelength and angle of incidence. *Applied Physics Letters*. 2012;101.
- [25] Petring D, Schneider F, Wolf N, Nazery V. How beam quality power and wavelength influence laser cutting and welding processes. *Proceedings of LAMP2009 - the 5th international congress on laser advanced materials processing; Kobe, Japan; 2009*.
- [26] Fomin VM, Malikov AG, Orishich AM, Shulyat'ev VB. Similarity of heat fluxes upon laser oxygen cutting of steel. *Doklady Physics*. 2011;56(1):12-5.
- [27] Fomin VM, Malikov AG, Orishich AM, Shulyat'ev VB. Energy conditions of gas laser cutting of thick steel sheets. *Applied mechanics and technical physics* 2011;52(3):340-6.

- [28] Berkmanns J, Faerber M. Facts about laser technology - laser cutting. <http://www.laserdeal.com/techInfoFiles/>; 2005 [cited 05/09/2011]; 20].
- [29] Schulz W, Eppelt U. Basic concepts of laser drilling. Springer Series in Material Science. 2009;119:129-65.
- [30] Abdel Ghany K, Abdel Rafea H, Newishy M. Using a Nd:YAG laser and six axes robot to cut zinc-coated steel. Advanced Manufacturing Technology. 2006;28:1111-7.
- [31] Xiao Z. Fibre laser cutting of mild steel [Ph.D. Thesis]: Lapperanta University of Technology; 2007.
- [32] Berkmanns J, Faerber M. Laser cutting. The Surrey Research Park, Guildford, Surrey, BOC Industrial Gases UK,; http://www.boconline.co.uk/internet.lg.lg.gbr/en/images/laser-cutting410_39553.pdf; June 18, 2008 [cited 10/05/2012].
- [33] Steen. WM, Mazumder. J. Laser Material Processing, Fourth edition: Springer; 2010.
- [34] O'Neill W, Sparkes M, Varnham M, Horley R, Birch M, Woods S, Harker A. High power high brightness industrial fiber laser technology. In Proceedings of the 23rd International Congress on Applications of lasers and electro optics (ICALEO); San Francisco, USA; 2004. p. 1-7.
- [35] Hugel H. New solid-state lasers and their application potentials. Optics and Lasers in Engineering. 2000;34:213-29.
- [36] Scintilla LD, Tricarico L, Wetzigb A, Mahrlec A, Beyerb E. Primary losses in disk and CO₂ laser beam inert gas fusion cutting. Journal of Materials Processing Technology. 2011;211:2050-61.
- [37] Scintilla LD, Tricarico L, Wetzig A, Mahrle A, Beyerb E, editors. Experimental investigation on the cut front geometry in the inert gas laser fusion cutting with disk and CO₂ lasers. 30th international congress on applications of laseres & electro-optic; 2011; Orlando, FL, USA: ICALEO.
- [38] Tünnermann A. High-power cw Fiber Lasers – Present and future. Laser Technik Journal. 2007;2(2):54-6.
- [39] Gregorčič P. High power fiber lasers. Ljubljana: University of Ljubljana; 2009.
- [40] Hand DP, Jones JDC. Single-mode fiber delivery of Nd:YAG light for precision machining applications. Applied optics 1998;37(9):1602-6.
- [41] Shiner B, IPG Photonics. Fiber lasers for material processing processing. [Catalog]: http://nefc.com/IPG_06222011.pdf; 2011 [5/07/2011].

- [42] Shiner B, IPG Photonics. High power fiber Laser technology [Catalog]: <http://www-conf.slac.stanford.edu/lsow/2013-Presentations/BShiner-HighPowerFiberLasers.pdf>; 2013 [27/11/2013].
- [43] Platonov NS, Gapontsev DV, Gapontsev VP, Shumilin V, editors. 135W CW fiber laser with perfect single mode output. Lasers and Electro-Optics, 2002 CLEO '02 Technical Digest; 2002; Long beach, CA, USA.
- [44] Verhaeghe G, Hilton P. Battle of the sources - using a high-power Yb-fibre laser for welding steel and aluminium. 58th Annual Assembly and International Conference of International Institute of Welding, 14 - 15 July 2005; Prague, Czech Republic: TWI Ltd; 2005.
- [45] Wandera C. Performance of high power fibre laser cutting of thick-section steel and medium aluminium [Ph.D. thesis]. Finland: Lappeenranta University of Technology; 2010.
- [46] Baumeister m, Dickmann K, Hoult T. Fiber laser micro-cutting of stainless steel sheets. Applied Physics A: Materials Science & Processing. 2006;A 85:121-4.
- [47] Hand DP, Su D, Naeem M, Jones JDC. Fiber optic high-quality Nd:YAG beam delivery for materials processing. Optical Engineering. 1996;35(2):502-6.
- [48] Olsen F. An evaluation of the cutting potential of different types of high power. 25nd International Congress on Application of Lasers and Electro-Optics: ICALEO 2006, Laser Materials Processing Conferance; Orlando, FL : Laser Institute of America; 2006. p. 188-96.
- [49] Uslan I. CO₂ laser cutting: kerf width variation during cutting. Proceedings of the Institution of Mechanical Engineering Part B: Journal of Engineering Manufacturing. 2005;219:571-7.
- [50] Steen WM. Laser Material Processing, third edition: Springer; 2005.
- [51] Wandera C, Kujanpaa V, Salminen A. Laser power requirement for cutting of thick-section steel and effects of processing parameters on mild steel cut quality Journal of Engineering Manufacturing 2011;225(5):651-61.
- [52] Al-Mashikhi SO. Fibre laser cutting of thin section mild steel [Ph.D. Thesis]. Nottingham: The University of Nottingham; 2009.
- [53] Hirano K, Fabbro R. Experimental observation of hydrodynamics of melt layer and striation generation during laser cutting of steel. Physics Procedia 2011;12(Part A):555-64.
- [54] Chen K, Yao Y. Striation formation and melt removal in the laser cutting process. Journal of manufacturing processes. 1999;1(1):43-53.

- [55] Scintilla LD, Sorgente D, Tricarico L. Experimental investigation on fibre laser cutting of Ti6Al4V thin sheet. *Advanced Material Research*. 2011;264-265:1281-6.
- [56] Tani G, Tomesani L, Campana G, Fortunato A. Quality factors assessed by analytical modelling in laser cutting. *Thin solid films*. 2004;453-454:486-91.
- [57] Xie XZ, Li LJ, Wei X, Hu W. Distribution of the intensity absorbed by evaporative front in laser cutting nonmetallic material. *Optics and Lasers in Engineering*. 2008;46:604-13.
- [58] Petring D, Molitor T, Schneider F, Wolf N. Diagnostics, modeling and simulation: Three keys towards mastering the cutting process with fiber, disk and diode lasers. *Physics Procedia*. 2012;39:186-96.
- [59] Mahrle A, Lutke M, Beyer E. Fibre laser cutting: beam absorption characteristics and gas-free remote cutting. *Proceedings of the Institution of Mechanical Engineers Part C-Journal of Mechanical Engineering Science*. 2010;224(C5):1007-18.
- [60] Mahrle A, Badrb Y. Thermodynamic evaluation of inert-gas laser beam fusion cutting with CO₂, disk and fiber lasers. In *proceedings of the 28th International Congress on Applications of Lasers & Electro-Optics; Orlando, USA: ICALEO; 2009. p. 610-09.*
- [61] Scintilla LD, Tricarico L, Mahrle A, Wetzig A, Himmer T. A comparative study on fusion cutting with disk and CO₂ Lasers. *International Congress on Applications of Lasers & Electro Optics (ICALEO); Anaheim, California, USA, 2010.*
- [62] Scintilla LD, Tricarico L, Mahrle A, Wetzig A, Beyer E. A comparative study of cut front profiles and absorptivity behavior for disk and CO₂ laser beam inert gas fusion cutting. *Journal of Laser Applications*. 2012;24(5):6.
- [63] O'Neill B. Laser cutting: a technology with some surprise in store. *The laser users*. 2008(51):34-6.
- [64] Scintilla LD, Tricarico L, Wetzig A, Mahrle A, Beyer E. Primary losses in disk and CO₂ laser beam inert gas fusion cutting. *Journal of Materials Processing Technology*. 2011;211:2050-61.
- [65] Wandera C, Salminen A, Kujanpaa V. Inert gas cutting of thick-section stainless steel and medium-section aluminum using a high power fiber laser. *Journal of Laser Applications*. 2009;21(3):154-61.
- [66] Ermolaev GV, Kovalev OB, Zaitsev AV. Parameterization of hybrid laser-assisted oxygen cutting of thick steel plate. *Optics & Laser Technology*. 2013;47:95-101.

- [67] Schulz W, Kostykin V, Nieben M, Michel J, Petring D, Kreutz E, Poprawe R. Dynamics of ripple formation and melt flow in laser beam cutting. *Journal of Physics D: Applied Physics*. 1999;32:1219-28.
- [68] ISO9013:2002. European Committee for Standardization. Thermal cutting - Classification of thermal cuts, Geometrical product specification and quality tolerances. 2002.
- [69] Powell J, Ivarson A, Magnusson C, editors. An energy balance for inert gas laser cutting. In: *Proceedings of the SPIE (ICALEO'93)*, Vol 2306 1993; Orlando, USA.
- [70] Ready JF. *Handbook of Laser Materials Processing*: Laser Institute of America, USA; 2001.
- [71] Scintilla LD, Tricarico L, Wetzig A, Beyer E. Investigation on disk and CO₂ laser beam fusion cutting differences based on power balance equation. *International Journal of Machine Tools & Manufacture*. 2013;69:30-7.
- [72] Precitec. laser cutting. <http://www.precitec.com/2011> [cited 08/08/2011].
- [73] Meng H, Liao J, Zhou Y, Zhang Q. Laser micro-processing of cardiovascular stent with fiber laser cutting system. *Journal of optics and laser technology*. 2008;41:300-2.
- [74] Wedel B. Focusing high brightness laser-special requirements on laser processing heads. In *Proceedings of 26th International Congress on Applications of Lasers and Electro-Optics*; Orlando: ICALEO; 2007. p. 83.
- [75] Bautze T, Diepold K. Review of fundamental aspects of focal shift effects and countermeasures. In *Proceedings of 4th Pacific International Conference on Applications of Lasers and Optics*; Wuhan: PICALO; 2010.
- [76] Schuocker D. *High power lasers in production engineering*. London: Imperial College Press; 1999.
- [77] Wandera C, Kujanpaa V. Optimization of parameters for fiber laser cutting of a 10 mm stainless steel plate *Journal of Engineering Manufacturing*. 2011;225(5):641-9.
- [78] Miyamoto I. Applications of high power single-mode fiber lasers to novel microwelding and microcutting. *Proc LPM*; Nara, Japan; 2004.
- [79] Sparkes M, Gross M, Celotto S, Zhang T, O'Neill W. Inert cutting of medium section stainless steel using a 2.2 kW high brightness fibre laser. *International Congress on Applications of Lasers & Electro-Optics (ICALEO 2006)*; Scottsdale, AZ, US; 2006.
- [80] Caristan C. *Laser cutting guide for manufacturing*: SME; 2004.

- [81] Wandera C, Kujanpaa V. Characterization of the melt removal rate in laser cutting of thick-section stainless steel. *Journal of Laser Applications*. 2010;22(2):62-70.
- [82] Duan J, Man HC, Yue TM. Simulation of high pressure gas flow field inside a laser cut kerf. *Proceedings of ICALEO 2000 Section B; Laser Institute of America, Orlando, 2000*. p. 87–96.
- [83] Man HC, Duan J, Yue TM, Dong P. Design of supersonic nozzle for laser cutting with high pressure gas. *Proceedings of ICALEO 1997 Section B; Laser Institute of America, Orlando; 1997*. p. 118-27.
- [84] Man HC, Duan J, Yue TM. Behavior of supersonic and subsonic gas jets inside laser cut kerfs. *Proceedings of ICALEO 1997 Section B; Laser Institute of America, Orlando; 1997*. p. 27–36.
- [85] Chen S-L. The effect of high-pressure assistant-gas flow on high-power CO₂ laser cutting. *Journal of Materials Processing Technology*. 1997;88:57-66.
- [86] Golnabi H, Bahar M. Investigation of optimum condition in oxygen gas-assisted laser cutting. *Optics & Laser Technology*. 2009;41:454-60.
- [87] Ivarson I, Powell J, Magnusson C. Laser cutting of steels; analysis of the particles ejected during cutting. *Weld World*. 1992;30:116-25.
- [88] Ivarson A, Powell J, Kamalu J, Magnusson C. The oxidation dynamics of laser cutting of mild-steel and the generation of striations on the cut edge. *Journal of Materials Processing Technology*. 1994;40(3-4):359-74.
- [89] Miyamoto I, Maruo H. The mechanism of laser cutting. *Wilding in the world*. 1991;29(9/10):283-94.
- [90] Huagng MY. Characterization of laser cutting for adaptive control environment [Ph.D.]: Glasgow university; 1994.
- [91] Abdulhadi E, Pelletier JM, Larnbertin M. Metallurgical effects induced by laser cutting, experimental and theoretical investigation. Section B, ICALEO, LIA. 1997;83.
- [92] Hanadi G, Salema HG, Mohy S, Mansourb, Yehya Badrb, A. W, Abbasb. CW Nd:YAG laser cutting of ultra low carbon steel thin sheets using O₂ assist gas. *Journal of Materials Processing Technology*. 2008; 1 9 6:64-72.
- [93] Tirumala Rao B, Lttoop MO, Kukreja LM. A power ramped pulsed mode laser piercing technique for improved CO₂ laser profile cutting. *Optics and Lasers in Engineering*. 2009;47:1108-16.
- [94] Ng GKL, Li L. The effect of laser peak power and pulse width on the hole geometry repeatability in laser percussion drilling. *Optics & Laser Technology*. 2001;33:393-402.

- [95] Low DKY, Li L, Corfe AG. The influence of assist gas on the mechanism of material ejection and removal during laser percussion drilling. Proc Instn Mech Engrs. 2000;214(B):521-7.
- [96] McNally C, Folkes J, Pashby R. Laser drilling of cooling holes in engines: state of the art and future challenges. Materials Science and Technology. 2004;20:805-13.
- [97] Yilbas B, Sami M. Liquid ejection and possible nucleate boiling mechanisms in relation to the laser drilling process. Journal of Physics D: Applied of Physics. 1997;30(14):1996-2005.
- [98] Voisey KT, Kudesia SS, Rodden WSO, Hand DP, Jones JDC, Clyne TW. Melt ejection during laser drilling of metals. Materials Science and Engineering A. 2003;356:414-24.
- [99] PRIMES GmbH. Focus monitor / Beam monitor laser diagnostic software 2.73. Catalog. 2006.
- [100] Scaggs M, Haas G. Thermal lensing compensation objective for high power lasers. HAAS laser technologies Inc.: <http://www.haaslti.com/pdf/Thermal-Lensing-Compensation-Objective-High-Power-Lasers.pdf>; [5/09/2013].
- [101] Mearten O, Kramer R, Schwede H, Wolf S, Brandl V. Thermal characterization of focusing system for high power lasers with high beam quality. http://www.primes.de/download/support/f69_www%20PRIMES%20LP_EX_09_.pdf; 2009 [cited 25/12/2013].
- [102] Ophir Optronics. Products. www.ophiropt.com; [cited 11/11/2011].
- [103] PRIMES GmbH. Product Catalogue. www.primes.de; 2011 [cited 11/11/2011].
- [104] Photometrics L. Products. www.lambdaphoto.co.uk; [cited 11/11/2011].
- [105] ISO11554:2006. Optics and photonics - Lasers and laser-related equipment - Test methods for laser beam power, energy and temporal characteristics. 2006.
- [106] ISO11146-1:2005. Lasers and laser related equipment - Test methods and beam properties ratios - Part 1: Stigmatic and simple astigmatic beams. 2005.
- [107] ISO11146-2:2005. Lasers and laser related equipment - Test methods and beam properties ratios - Part 2: General astigmatic beams. 2005.
- [108] ISO/TR11146-3:2004. Lasers and laser related equipment - Test methods and beam properties ratios - Part 3: Intrinsic and geometrical laser beam classification, propagation and details of test methods. 2004.

- [109] Klein C, Williamson M, Kestian A. Industrial laser solution. <http://www.industrial-lasers.com/articles/2006/09/owning-the-process.html>; 2006 [cited 01/11/2012].
- [110] Kratky A, Schuocker D, Liedl G. Processing with kW fibre lasers - advantages and limits. XVII International Symposium on Gas Flow, Chemical Lasers, and High-Power Lasers: Proc. of SPIE; 2009.
- [111] Ophir Optronics Solutions Ltd. Optics for CO2 lasers. <http://www.ophiropt.com/co2-lasers-optics/focusing-lens/cutting-head-optics>; [cited 20/01/2013].
- [112] Tesatool. Surface roughness testing. http://tesatool.com/pdf_files/catalog_surface.pdf, ; 2012 [cited: 30/04/2012].
- [113] Simmons CH, Maguire D, Phelps N. Manual of engineering drawing : technical product specification and documentation to British and international standards. Oxford: Butterworth-Heinemann; 2012.
- [114] Gindis E. Up and running with AutoCAD 2011 : 2D and 3D drawing and modeling: Oxford academic press; 2011.
- [115] Arata Y, Maruo H, Miyamoto I, Takeuchi S. Dynamic behavior in laser gas cutting of mild steel. Transactions of JWRI by Welding research institute of Osaka University. 1979;8(2):15-26.
- [116] Sobih M, Crouse PL, Li L. Striation-free fibre laser cutting of mild steel sheets. Applied Physics A: Materials, Science & Processing. 2008;90:171-4.
- [117] Wells AA. Oxygen cutting. British welding journal. 1961;8:86.
- [118] Wells AA. Further studies of iron-oxygen combustion in gas cutting British welding journal. 1961;8:79.
- [119] Ivarson A, Powell J, Magnusson C. Factors affecting the efficiency of inert gas laser cutting. Laser in Engineering. 1993;2:169-80.
- [120] Gross MS, O'Neill W. New aspects of melt flow phenomena through narrow kerfs. JOURNAL OF PHYSICS D: APPLIED PHYSICS. 2007;40:1201-5.
- [121] Poprawe R, Schulz W, Schmitt R. Hydrodynamics of material removal by melt expulsion: Perspectives of laser cutting and drilling. Physics Procedia. 2010;5(A):1-18.
- [122] Overton J. Fibre laser cutting of engineering materials. 3rd year individual project. Report. Department of Mechanical, Materials & Manufacturing Engineering; 2009.
- [123] Petring D, Schneider F, Wolf N, Nazery N. The relevance of brightness for high power laser cutting and welding. ICALEO; 2008. p. 95-103.

- [124] Low DKY, Li L, Byrd PJ. The influence of temporal pulse train modulation during laser percussion drilling. *Optics and Lasers in Engineering*. 2001;35:149-64.
- [125] Okasha MM, Mativenga PT, Driver N, Li L. Sequential laser and mechanical micro drilling of Ni superalloy for aerospace application. *CIRP Annals - Manufacturing Technology*. 2010;59:199-202.
- [126] Leigh S, Sezer K, Li L, Grafton-Reed C, Cuttall M. Statistical analysis of recast formation in laser drilled acute blind holes in CMSX-4 nickel superalloy. *International Journal of Advanced Manufacturing Technology*. 2009;43(1094-1105).
- [127] Low DKY, Li L. An investigation into melt flow dynamics during repetitive pulsed drilling of transparent media. *Optics & Laser Technology*. 2001;33(7):515-22.
- [128] Zhanguo L, Jingjing L, Daimin C. The effect research of laser power on carbon steel drilling. *International Conference on Computer, Mechanics, Control and Electronic Engineering (CMCE): IEEE*; 2010. p. 196-9.
- [129] Yao CY, Tam SC, Jana S, Lau MWS. A technical review of the laser drilling of aerospace materials. *Journal of Materials Processing Technology*. 1994;42(1):15-49.
- [130] Dubey AK, Yadava V. Experimental study of Nd:YAG laser beam machining-An overview. *Journal of Materials Processing Technology*. 2008;195:15-26.
- [131] Powell J. The Influence of Material Thickness on the Efficiency of Laser Cutting and Welding. In *proceedings of 6th International Conference on Lasers in Manufacturing: ISBN 1-85423-047-6*; 1989. p. 215-21.

10 Appendix

Table 10.1- The effect of different parameters on the kerf width/spot size for stainless steel [73].

No	Laser	Power	Material	Assistant gas	Speed	Spot size	Kerf width	K/S
1	Pulsed Fibre	6 W	0.11 mm, St. St.	O ₂ ,Ø0.4, 0.3 MPa	4.8 mm/s	0.012 mm	0.019 mm	1.58
2	Pulsed Fibre	6 W	0.11 mm, St. St.	O ₂ ,Ø0.4, 0.3 MPa	6.5 mm/s	0.012 mm	0.0184 mm	1.53
3	Pulsed Fibre	6 W	0.11 mm, St. St.	O ₂ ,Ø0.4, 0.3 MPa	8 mm/s	0.012 mm	0.0183 mm	1.525
4	Pulsed Fibre	6 W	0.11 mm, St. St.	O ₂ ,Ø0.4, 0.3 MPa	9.7 mm/s	0.012 mm	0.0182 mm	1.52
5	Pulsed Fibre	6 W	0.11 mm, St. St.	O ₂ ,Ø0.4, 0.3 MPa	11.3 mm/s	0.012 mm	0.0181 mm	1.5
6	Pulsed Fibre	7.5 W	0.11 mm, St. St.	O ₂ ,Ø0.4, 0.3 MPa	4.8 mm/s	0.012 mm	0.023 mm	1.92
7	Pulsed Fibre	7.5 W	0.11 mm, St. St.	O ₂ ,Ø0.4, 0.3 MPa	6.5 mm/s	0.012 mm	0.0229 mm	1.91
8	Pulsed Fibre	7.5 W	0.11 mm, St. St.	O ₂ ,Ø0.4, 0.3 MPa	8 mm/s	0.012 mm	0.0228 mm	1.9
9	Pulsed Fibre	7.5 W	0.11 mm, St. St.	O ₂ ,Ø0.4, 0.3 MPa	9.7 mm/s	0.012 mm	0.0227 mm	1.89
10	Pulsed Fibre	7.5 W	0.11 mm, St. St.	O ₂ ,Ø0.4, 0.3 MPa	11.3 mm/s	0.012 mm	0.0226 mm	1.88
11	Pulsed Fibre	9 W	0.11 mm, St. St.	O ₂ ,Ø0.4, 0.3 MPa	4.8 mm/s	0.012 mm	0.0265 mm	2.21
12	Pulsed Fibre	9 W	0.11 mm, St. St.	O ₂ ,Ø0.4, 0.3 MPa	6.5 mm/s	0.012 mm	0.0264 mm	2.2
13	Pulsed Fibre	9 W	0.11 mm, St. St.	O ₂ ,Ø0.4, 0.3 MPa	8 mm/s	0.012 mm	0.0262 mm	2.18
14	Pulsed Fibre	9 W	0.11 mm, St. St.	O ₂ ,Ø0.4, 0.3 MPa	9.7 mm/s	0.012 mm	0.026 mm	2.17
15	Pulsed Fibre	9 W	0.11 mm, St. St.	O ₂ ,Ø0.4, 0.3 MPa	11.3 mm/s	0.012 mm	0.0258 mm	2.15

Table 10.2- The effect of different parameters on the kerf width/spot size for stainless steel [46].

No	Laser	Power	Material	Assistant gas	Speed	Spot size	Kerf width	K/S
1	Fibre	9 W	0.1 mm St. St.	O ₂ ,Ø0.5,10 bar	50 mm/s	0.02 mm	0.02 mm	1
2	Fibre	16 W	0.1 mm St. St.	O ₂ ,Ø0.5,10 bar	50 mm/s	0.02 mm	0.027 mm	1.35
3	Fibre	25 W	0.1 mm St. St.	O ₂ ,Ø0.5,10 bar	50 mm/s	0.02 mm	0.028 mm	1.4
4	Fibre	34 W	0.1 mm St. St.	O ₂ ,Ø0.5,10 bar	50 mm/s	0.02 mm	0.034 mm	1.7
5	Fibre	41 W	0.1 mm St. St.	O ₂ ,Ø0.5,10 bar	50 mm/s	0.02 mm	0.043 mm	2.15
6	Fibre	50 W	0.1 mm St. St.	O ₂ ,Ø0.5,10 bar	50 mm/s	0.02 mm	0.045 mm	2.25
7	Fibre	59 W	0.1 mm St. St.	O ₂ ,Ø0.5,10 bar	50 mm/s	0.02 mm	0.047 mm	2.35
8	Fibre	66 W	0.1 mm St. St.	O ₂ ,Ø0.5,10 bar	50 mm/s	0.02 mm	0.055 mm	2.75
9	Fibre	75 W	0.1 mm St. St.	O ₂ ,Ø0.5,10 bar	50 mm/s	0.02 mm	0.056 mm	2.8
10	Fibre	84 W	0.1 mm St. St.	O ₂ ,Ø0.5,10 bar	50 mm/s	0.02 mm	0.065 mm	3.25
11	Fibre	16 W	0.2 mm St. St.	O ₂ ,Ø0.5,10 bar	20 mm/s	0.02 mm	0.022 mm	1.1
12	Fibre	25 W	0.2 mm St. St.	O ₂ ,Ø0.5,10 bar	20 mm/s	0.02 mm	0.026 mm	1.3
13	Fibre	34 W	0.2 mm St. St.	O ₂ ,Ø0.5,10 bar	20 mm/s	0.02 mm	0.03 mm	1.5
14	Fibre	41 W	0.2 mm St. St.	O ₂ ,Ø0.5,10 bar	20 mm/s	0.02 mm	0.034 mm	1.7
15	Fibre	50 W	0.2 mm St. St.	O ₂ ,Ø0.5,10 bar	20 mm/s	0.02 mm	0.036 mm	1.8
16	Fibre	59 W	0.2 mm St. St.	O ₂ ,Ø0.5,10 bar	20 mm/s	0.02 mm	0.038 mm	1.9
17	Fibre	66 W	0.2 mm St. St.	O ₂ ,Ø0.5,10 bar	20 mm/s	0.02 mm	0.041 mm	2.05
18	Fibre	75 W	0.2 mm St. St.	O ₂ ,Ø0.5,10 bar	20 mm/s	0.02 mm	0.042 mm	2.1
19	Fibre	84 W	0.2 mm St. St.	O ₂ ,Ø0.5,10 bar	20 mm/s	0.02 mm	0.048 mm	2.4
20	Fibre	16 W	0.3 mm St. St.	O ₂ ,Ø0.5,10 bar	20 mm/s	0.02 mm	0.018 mm	0.9
21	Fibre	25 W	0.3 mm St. St.	O ₂ ,Ø0.5,10 bar	20 mm/s	0.02 mm	0.022 mm	1.1
22	Fibre	34 W	0.3 mm St. St.	O ₂ ,Ø0.5,10 bar	20 mm/s	0.02 mm	0.028 mm	1.4
23	Fibre	41 W	0.3 mm St. St.	O ₂ ,Ø0.5,10 bar	20 mm/s	0.02 mm	0.033 mm	1.65
24	Fibre	50 W	0.3 mm St. St.	O ₂ ,Ø0.5,10 bar	20 mm/s	0.02 mm	0.036 mm	1.8
25	Fibre	59 W	0.3 mm St. St.	O ₂ ,Ø0.5,10 bar	20 mm/s	0.02 mm	0.038 mm	1.9
26	Fibre	66 W	0.3 mm St. St.	O ₂ ,Ø0.5,10 bar	20 mm/s	0.02 mm	0.047 mm	2.35
27	Fibre	75 W	0.3 mm St. St.	O ₂ ,Ø0.5,10 bar	20 mm/s	0.02 mm	0.048 mm	2.4
28	Fibre	84 W	0.3 mm St. St.	O ₂ ,Ø0.5,10 bar	20 mm/s	0.02 mm	0.058 mm	2.9

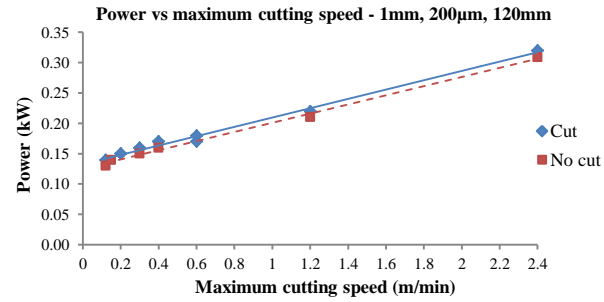
Table 10.3- The effect of different parameters on the kerf width/spot size for zinc steel [30].

No	Laser	Power	Material	Assistant gas	Speed	Spot size	Kerf width	K/S
1	Nd:Yag -Fib- CW	600 W	1 mm, Zinc St.	O2, Ø1.2, 6 bar	2 m/min	0.18 mm	0.25 mm	1.39
2	Nd:Yag -Fib- CW	600 W	1 mm, Zinc St.	O2, Ø1.2, 6 bar	3 m/min	0.18 mm	0.23 mm	1.28
3	Nd:Yag -Fib- CW	600 W	1 mm, Zinc St.	O2, Ø1.2, 6 bar	4 m/min	0.18 mm	0.2 mm	1.11
4	Nd:Yag -Fib- CW	600 W	1 mm, Zinc St.	O2, Ø1.2, 6 bar	5 m/min	0.18 mm	0.19 mm	1.06
5	Nd:Yag -Fib- CW	600 W	1 mm, Zinc St.	O2, Ø1.2, 6 bar	6 m/min	0.18 mm	0.17 mm	0.94
6	Nd:Yag -Fib- CW	600 W	1 mm, Zinc St.	N2, Ø1.2, 6 bar	2 m/min	0.18 mm	0.225 mm	1.25
7	Nd:Yag -Fib- CW	600 W	1 mm, Zinc St.	N2, Ø1.2, 6 bar	3 m/min	0.18 mm	0.19 mm	1.06
8	Nd:Yag -Fib- CW	600 W	1 mm, Zinc St.	N2, Ø1.2, 6 bar	4 m/min	0.18 mm	0.19 mm	1.06
9	Nd:Yag -Fib- CW	600 W	1 mm, Zinc St.	N2, Ø1.2, 6 bar	5 m/min	0.18 mm	0.175 mm	0.97
10	Nd:Yag -Fib- CW	600 W	1 mm, Zinc St.	N2, Ø1.2, 6 bar	6 m/min	0.18 mm	-	-
11	Nd:Yag -Fib- CW	600 W	1 mm, Zinc St.	Air, Ø1.2, 6 bar	2 m/min	0.18 mm	0.225 mm	1.25
12	Nd:Yag -Fib- CW	600 W	1 mm, Zinc St.	Air, Ø1.2, 6 bar	3 m/min	0.18 mm	0.22 mm	1.22
13	Nd:Yag -Fib- CW	600 W	1 mm, Zinc St.	Air, Ø1.2, 6 bar	4 m/min	0.18 mm	0.2 mm	1.11
14	Nd:Yag -Fib- CW	600 W	1 mm, Zinc St.	Air, Ø1.2, 6 bar	5 m/min	0.18 mm	0.18 mm	1
15	Nd:Yag -Fib- CW	600 W	1 mm, Zinc St.	Air, Ø1.2, 6 bar	6 m/min	0.18 mm	0.165 mm	0.92
16	Nd:Yag-Fib- Pul	600 W	1 mm, Zinc St.	O2, Ø1.2, 6 bar	2 m/min	0.18 mm	0.225 mm	1.25
17	Nd:Yag-Fib- Pul	600 W	1 mm, Zinc St.	O2, Ø1.2, 6 bar	3 m/min	0.18 mm	0.2 mm	1.11
18	Nd:Yag-Fib- Pul	600 W	1 mm, Zinc St.	O2, Ø1.2, 6 bar	4 m/min	0.18 mm	0.21 mm	1.17
19	Nd:Yag-Fib- Pul	600 W	1 mm, Zinc St.	O2, Ø1.2, 6 bar	5 m/min	0.18 mm	0.2 mm	1.11
20	Nd:Yag-Fib- Pul	600 W	1 mm, Zinc St.	O2, Ø1.2, 6 bar	6 m/min	0.18 mm	0.18 mm	1
21	Nd:Yag-Fib- Pul	600 W	1 mm, Zinc St.	N2, Ø1.2, 6 bar	2 m/min	0.18 mm	0.175 mm	0.97
22	Nd:Yag-Fib- Pul	600 W	1 mm, Zinc St.	N2, Ø1.2, 6 bar	3 m/min	0.18 mm	0.17 mm	0.94
23	Nd:Yag-Fib- Pul	600 W	1 mm, Zinc St.	N2, Ø1.2, 6 bar	4 m/min	0.18 mm	0.15 mm	0.83
24	Nd:Yag-Fib- Pul	600 W	1 mm, Zinc St.	N2, Ø1.2, 6 bar	5 m/min	0.18 mm	0.14 mm	0.78
25	Nd:Yag-Fib- Pul	600 W	1 mm, Zinc St.	N2, Ø1.2, 6 bar	6 m/min	0.18 mm	-	-
26	Nd:Yag-Fib- Pul	600 W	1 mm, Zinc St.	Air, Ø1.2, 6 bar	2 m/min	0.18 mm	0.21 mm	1.17
27	Nd:Yag-Fib- Pul	600 W	1 mm, Zinc St.	Air, Ø1.2, 6 bar	3 m/min	0.18 mm	0.2 mm	1.11
28	Nd:Yag-Fib- Pul	600 W	1 mm, Zinc St.	Air, Ø1.2, 6 bar	4 m/min	0.18 mm	0.175 mm	0.97
29	Nd:Yag-Fib- Pul	600 W	1 mm, Zinc St.	Air, Ø1.2, 6 bar	5 m/min	0.18 mm	0.16 mm	0.89
30	Nd:Yag-Fib- Pul	600 W	1 mm, Zinc St.	Air, Ø1.2, 6 bar	6 m/min	0.18 mm	0.15 mm	0.83

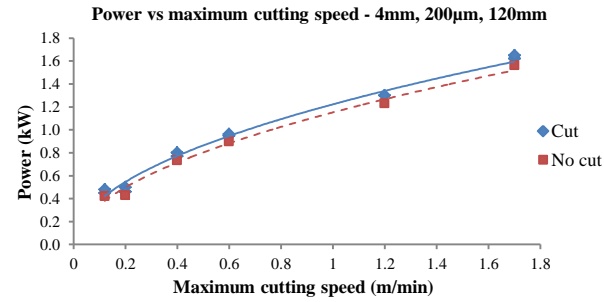
Table 10.4- The effect of different parameters on the kerf width/spot size for stainless steel [46].

Power	Material	Assistant gas	Speed	Spot size	Kerf width	K/S
16 W	0.1 mm St. St.	N2,Ø0.5,10 bar	50 mm/s	0.02 mm	0.026 mm	1.3
25 W	0.1 mm St. St.	N2,Ø0.5,10 bar	50 mm/s	0.02 mm	0.025 mm	1.25
34 W	0.1 mm St. St.	N2,Ø0.5,10 bar	50 mm/s	0.02 mm	0.036 mm	1.8
41 W	0.1 mm St. St.	N2,Ø0.5,10 bar	50 mm/s	0.02 mm	0.047 mm	2.35
50 W	0.1 mm St. St.	N2,Ø0.5,10 bar	50 mm/s	0.02 mm	0.055 mm	2.75
59 W	0.1 mm St. St.	N2,Ø0.5,10 bar	50 mm/s	0.02 mm	0.058 mm	2.9
66 W	0.1 mm St. St.	N2,Ø0.5,10 bar	50 mm/s	0.02 mm	0.065 mm	3.25
75 W	0.1 mm St. St.	N2,Ø0.5,10 bar	50 mm/s	0.02 mm	0.071 mm	3.55
84 W	0.1 mm St. St.	N2,Ø0.5,10 bar	50 mm/s	0.02 mm	0.070 mm	3.5
34 W	0.2 mm St. St.	N2,Ø0.5,10 bar	50 mm/s	0.02 mm	0.031 mm	1.55
42.5 W	0.2 mm St. St.	N2,Ø0.5,10 bar	50 mm/s	0.02 mm	0.040 mm	2
50 W	0.2 mm St. St.	N2,Ø0.5,10 bar	50 mm/s	0.02 mm	0.041 mm	2.05
59 W	0.2 mm St. St.	N2,Ø0.5,10 bar	50 mm/s	0.02 mm	0.045 mm	2.25
66 W	0.2 mm St. St.	N2,Ø0.5,10 bar	50 mm/s	0.02 mm	0.052 mm	2.6
75 W	0.2 mm St. St.	N2,Ø0.5,10 bar	50 mm/s	0.02 mm	0.057 mm	2.85
84 W	0.2 mm St. St.	N2,Ø0.5,10 bar	50 mm/s	0.02 mm	0.064 mm	3.2
42 W	0.3 mm St. St.	N2,Ø0.5,10 bar	20 mm/s	0.02 mm	0.045 mm	2.25
51 W	0.3 mm St. St.	N2,Ø0.5,10 bar	20 mm/s	0.02 mm	0.065 mm	3.25
58 W	0.3 mm St. St.	N2,Ø0.5,10 bar	20 mm/s	0.02 mm	0.052 mm	2.6
68 W	0.3 mm St. St.	N2,Ø0.5,10 bar	20 mm/s	0.02 mm	0.053 mm	2.65
76 W	0.3 mm St. St.	N2,Ø0.5,10 bar	20 mm/s	0.02 mm	0.066 mm	3.3
84 W	0.3 mm St. St.	N2,Ø0.5,10 bar	20 mm/s	0.02 mm	0.071 mm	3.55

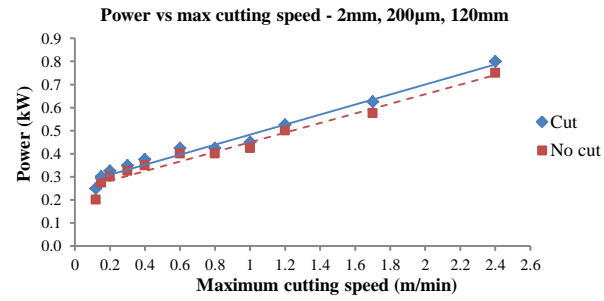
1 mm



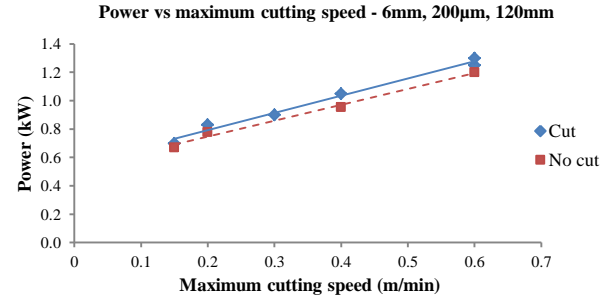
4 mm



2 mm



6 mm



3 mm

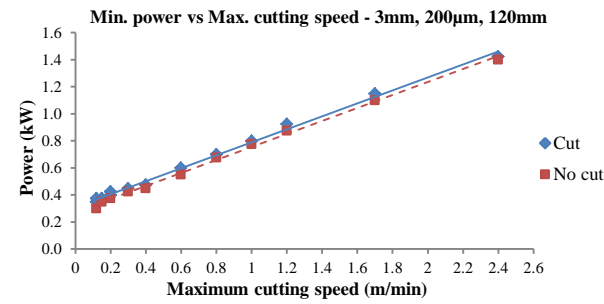


Figure 10.1- Power versus maximum cutting speed for different thicknesses (200 μ m fibre diameter, 120 mm focal length, 12 bar nitrogen).

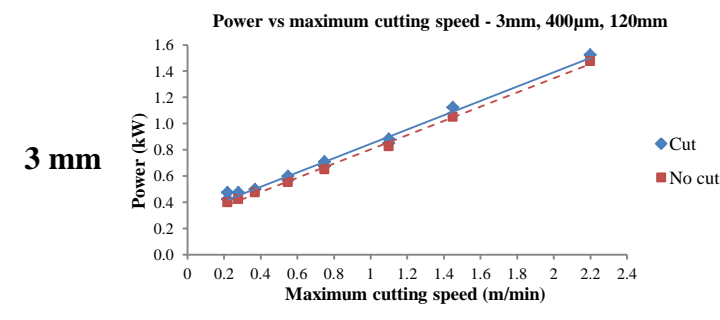
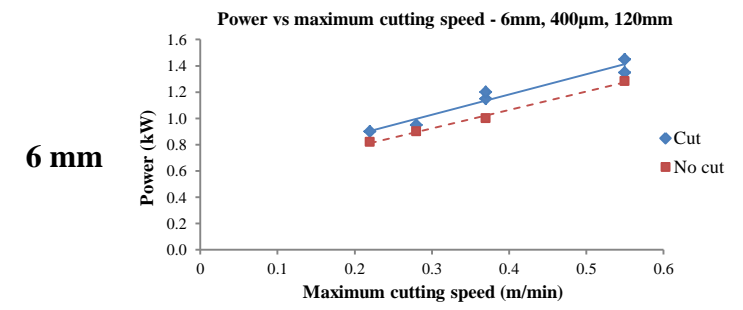
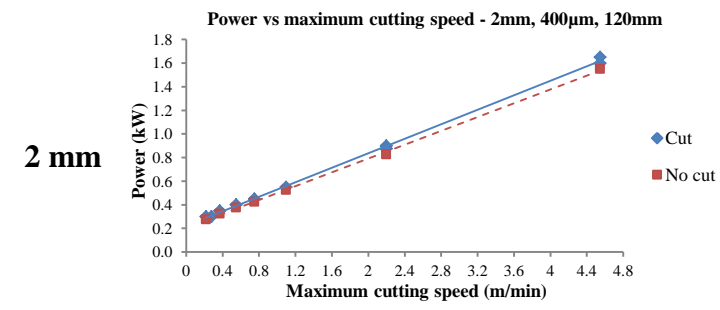
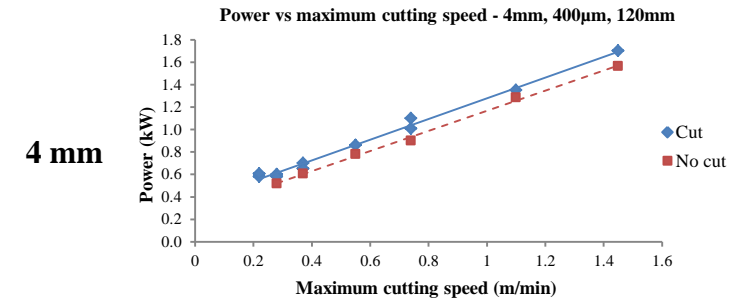
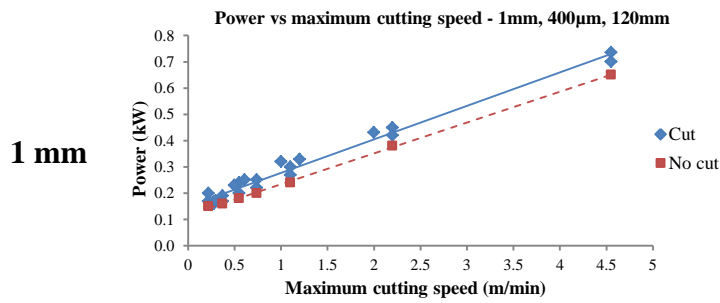
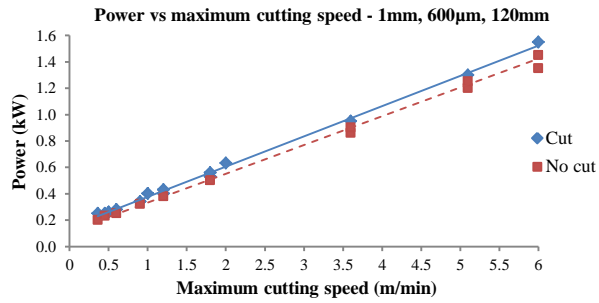
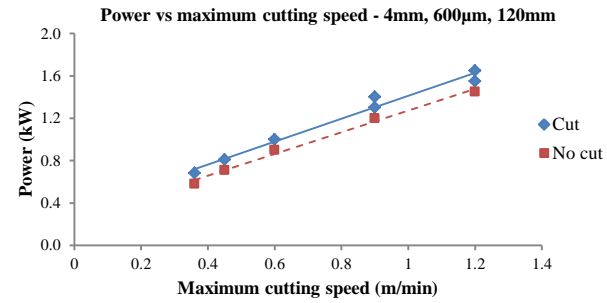


Figure 10.2- Power versus maximum cutting speed for different thicknesses (400 μ m fibre diameter, 120 mm focal length, 12 bar nitrogen).

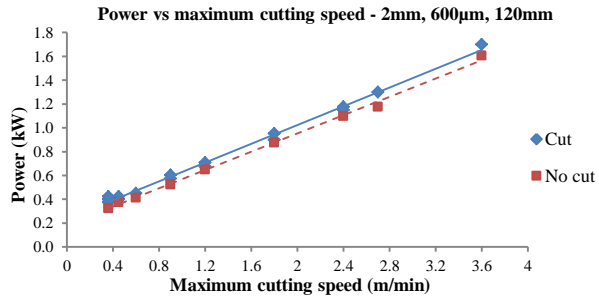
1 mm



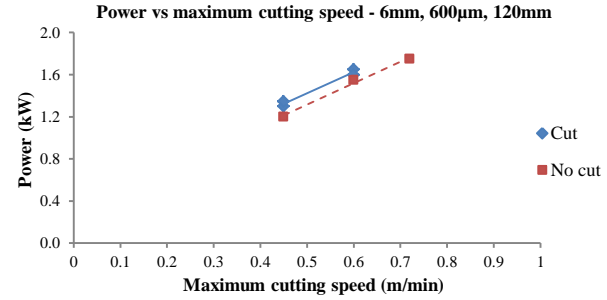
4 mm



2 mm



6 mm



3 mm

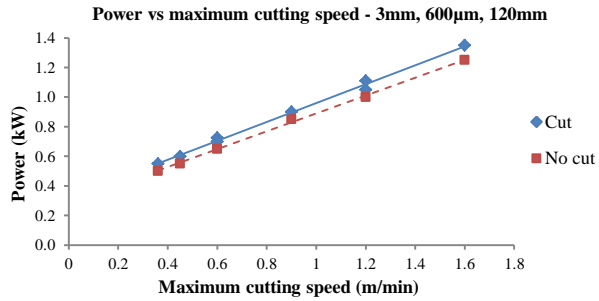
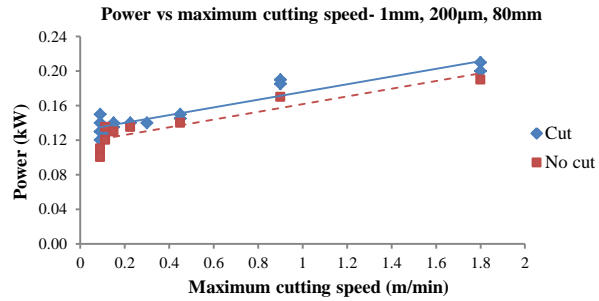
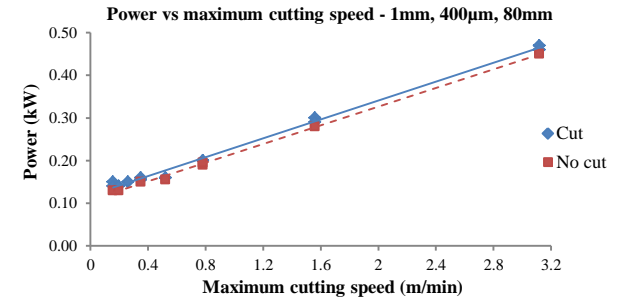


Figure 10.3- Power versus maximum cutting speed for different thicknesses (600 μ m fibre diameter, 120 mm focal length, 12 bar nitrogen).

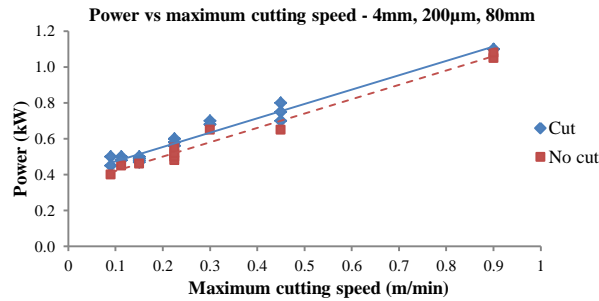
1 mm



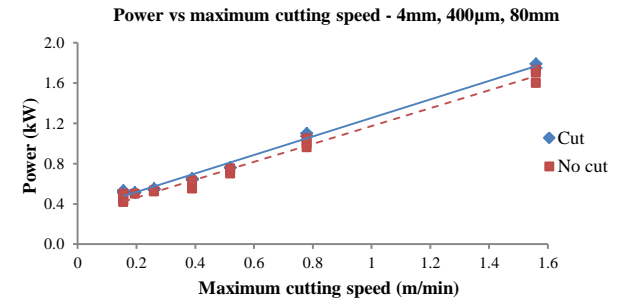
1 mm



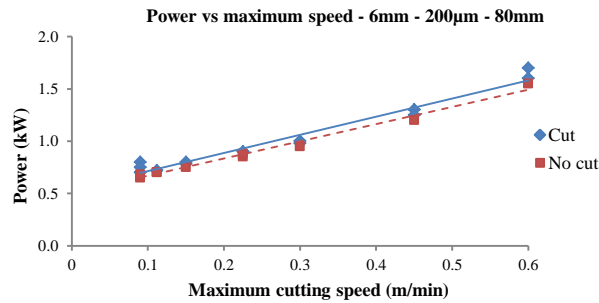
4 mm



4 mm



6 mm



6 mm

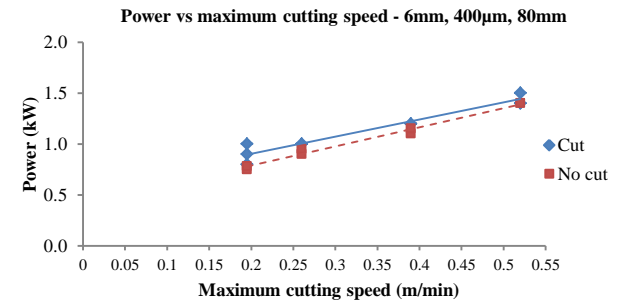


Figure 10.4- Power vs max cutting speed for different thicknesses (200 µm, 80 mm focal length, 12 bar nitrogen).

Figure 10.5- Power vs max cutting speed for different thicknesses (400 µm, 80 mm focal length, 12 bar nitrogen).

